95194

N.I.

Nonlinear Combustion Instability in Liquid-Propellant Rocket Motors

Samuel Z. Burstein and Wallace Chinitz

Third Quarterly Report

to

Jet Propulsion Laboratory

April 30, 1968

Mathematical Applications Group, Inc.

180 South Broadway

White Plains, New York

Nonlinear Combustion Instability in Liquid-Propellant Rocket Motors

Samuel Z. Burstein and Wallace Chinitz

Third Quarterly Report

to

Jet Propulsion Laboratory

April 30, 1968

JPL Contract
951946

"This work was performed for the Jet Propulsion Laboratory, California Institute of Technology, as sponsored by the National Aeronautics and Space Administration under Contract NAS7-100."

"This report contains information prepared by Mathematical Applications Group, Inc. (MAGI) under JPL subcontract. Its content is not necessarily endorsed by the Jet Propulsion Laboratory, California Institute of Technology, or the National Aeronautics and Space Administration."

TABLE OF CONTENTS

INTRODUCTION

During the third quarter progress continued along two fronts, the fluid dynamic model and the flame model of droplet combustion. This quarterly report describes some of the effort that is being generated in these two model building areas.

The first section describes some numerical experiments carried out with the fluid dynamic pancake model of the combustor The experiments include both non-reacting and reacting flow conditions. The status of program COMB is also discussed.

The second section describes recent work in producing a simplified droplet evaporation and combustion analysis. Some recent results towards completing the Peskin-Wise model relating to the modified flame surface analysis are presented.

The authors would like to again acknowledge the creative programming effort that Harold Schechter has provided during the course of this research program.

I. Fluid Dynamic Model

A. Finite Amplitude Transverse Waves in a Cylindrical Chamber

We have continued exploring and analyzing the nonlinear motion of finite amplitude waves in the transverse plane of a cylindrical channel. In the last quarterly report (number 2) we reported on a calculation which exhibited continuous behavior of the fluid properties for all time. The initial data is prescribed by relations(traveling wave solution to the wave equation in cylindrical coordinates)which are presented on page 19 of quarterly report number 2. The initial pressure field and velocity field are shown in figures 1 and 2 and correspond to finite values for the amplitude parameter in the above equations. It should be noted that to obtain the dimensional value of pressure the nondimensional pressure is to be multiplied by γp_∞. In this test case, however, the maximum value of the pressure is 590 psia while the minimum value is 10 psia (here p_∞ = 300 psia and γ = 1.2). The numerical values shown in figures 1 and 2 correspond to this case. For the previous reported calculation the maximum (minimum) pressure was 450 (250) while p_∞ = 300 psia, and there the solution remained continuous for all time.

As figure 3 shows, for the present calculation, a shock wave has formed after about 1.22 units of nondimensional time (time is normalized by R/a_∞ ~ .131 millisec). The wave is strongest at the wall and decreases in strength as it curves inward into the chamber. Swirls seen behind the wave are due to numerical oscillations, a

feature inherent in these finite difference equations. Figure 4 shows the strong discontinuous behavior of the velocity field in the neighborhood of the shock. Now figure 5, taken at 400 cycles of computation, is an intermediate stage of the flow field development. Two pressure peaks are evident at a nondimensional radius of R = 1 of the combustion chamber. There is also a vast region of the chamber where the pressure is approximately uniform and it is clear that figure 6 shows a strong induced velocity field which is predominently tangential in direction. The pressure field shown in figure 7 shows clearly a symmetric compression/rarefaction wave with a peak pressure of about 1120 psia. The associated velocity field, shown in figure 8, is also locally symmetric about the pressure wave. Velocities increase and then decrease uniformly in the direction of motion while the maximum velocity is at the boundary.

One also notices that the velocity vectors on the leading edge of the wave point towards the wall while those at the trailing edge tend to point away from the wall.

Figures 9 and 10 show essentially the same picture as in the two previous plots; here the peak pressure is 1250 psia while the minimum pressure is 160 psia. The uniform portion of the flow field has a mean pressure level of about 220 psia. The wave has now undergone about one and two thirds rotations in 0.694 milliseconds. Figures 11 through 14 again show that the wave has the same basic structure as seen before, however, the peak pressure is decreasing to 1018 psia.

Figures 15 and 16 show the pressure field with multiple waves, waves which then seem to coalesce and lead to the flow field given by the next three figures.

It should be noted that the 'rev' counter value given at the bottom of the accompanying figures is computed from the relative position of the velocity vector at r = 0 from its starting position. For small values of the amplitude of the pressure wave, the vector rotates in phase with the wave. However, for large values of the amplitude, the fluid motion no longer is locked onto this convenient measure, but rather, there is in general a variation in phase between the rotation of the wave and the velocity vector at r = 0. At 2200 cycles (figure 18 corresponds to a physical time of 1.94 millisec) the wave has rotated about 4.8 times and the maximum amplitude has gone back up to 1350 psia. It is striking that the picture of the whole flow field again looks quite like that in figure 9. Apparently the fluid exhibits time wise dependent periodic behavior with waves of finite amplitude. The average period can be computed and is found to be 405 μ-sec.

Figures 20 and 21 give the dimensional pressure on the wall of the combustion chamber for selected values of time corresponding to some of the previous figures. The curves are labeled with three numbers. The first is the nondimensional time; the second is the rotation counter enclosed in parenthesis; and the third is the computation cycle count.

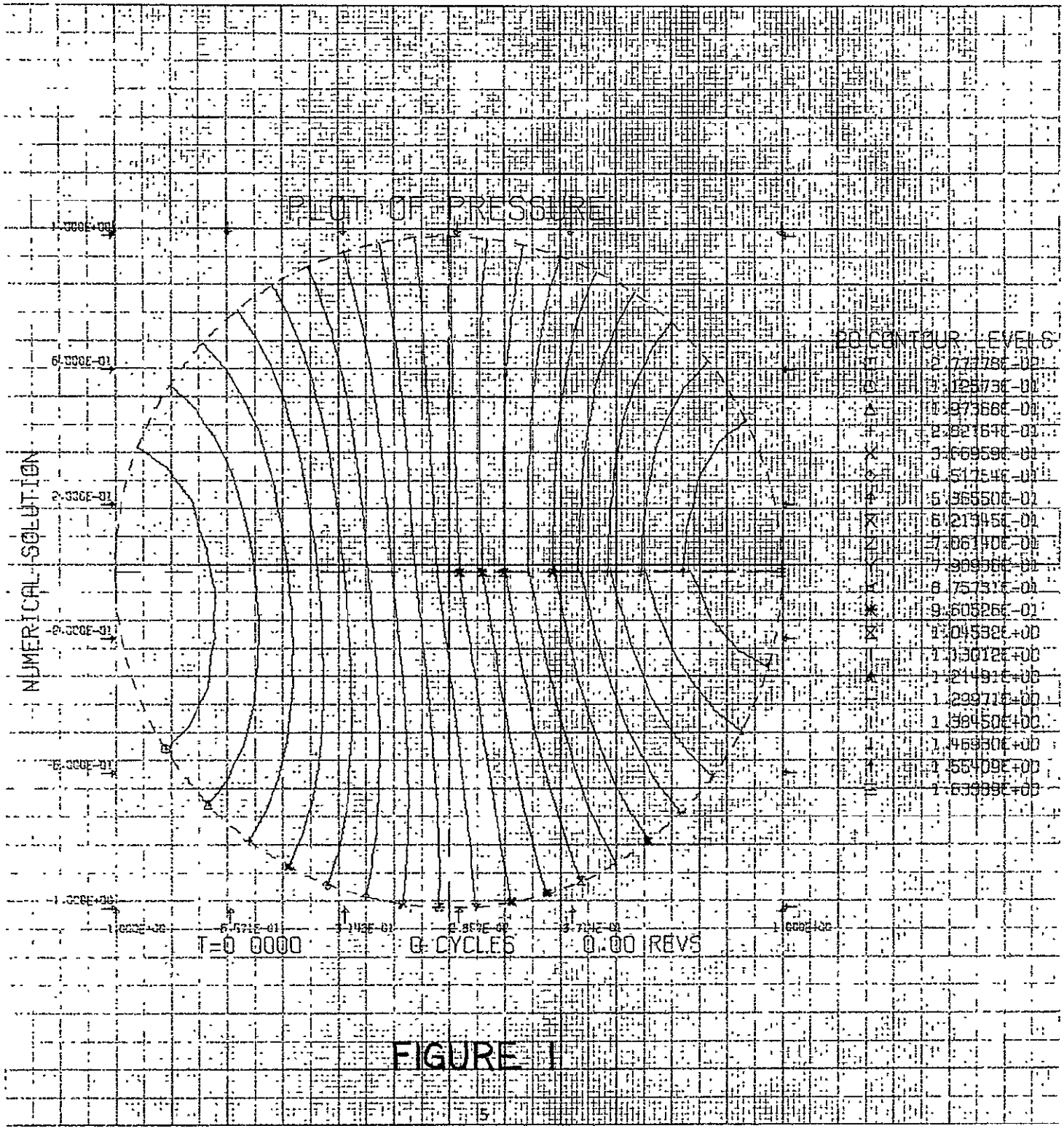
PLOT OF PRESSURE
NUMERICAL SOLUTION
20 CONTOUR LEVELS
T=0 0000
0 CYCLES
0.00 REVS

FIGURE 1

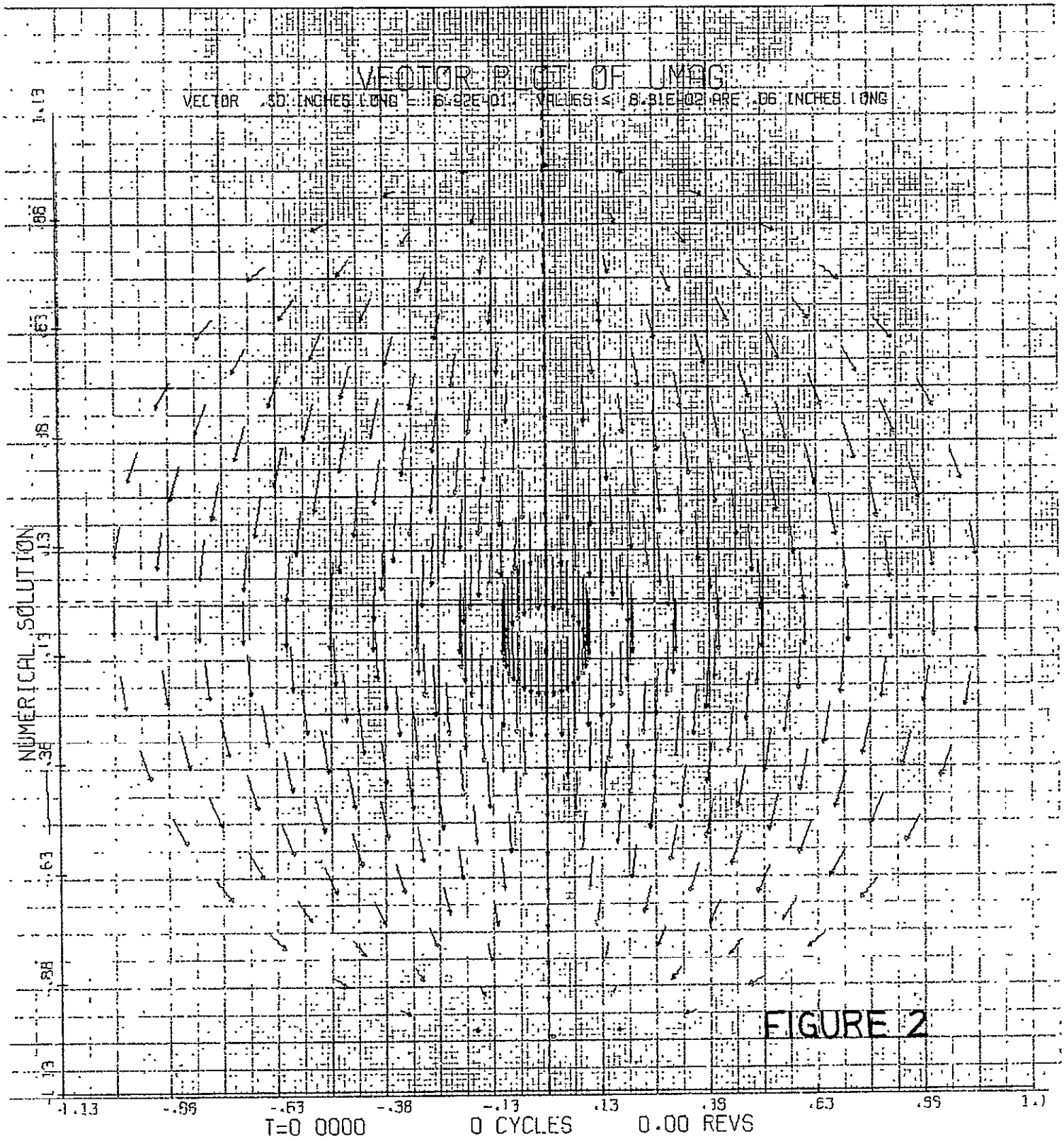
VECTOR PLOT OF UMAG
VECTOR .50 INCHES LONG = 6.92E-01 VALUES ≤ 8.81E-02 ARE .06 INCHES LONG
NUMERICAL SOLUTION
-1.13
-.88
-.63
-.38
-.13
.13
.38
.63
.88
1.13
T=0 0000 0 CYCLES 0.00 REVS

FIGURE 2

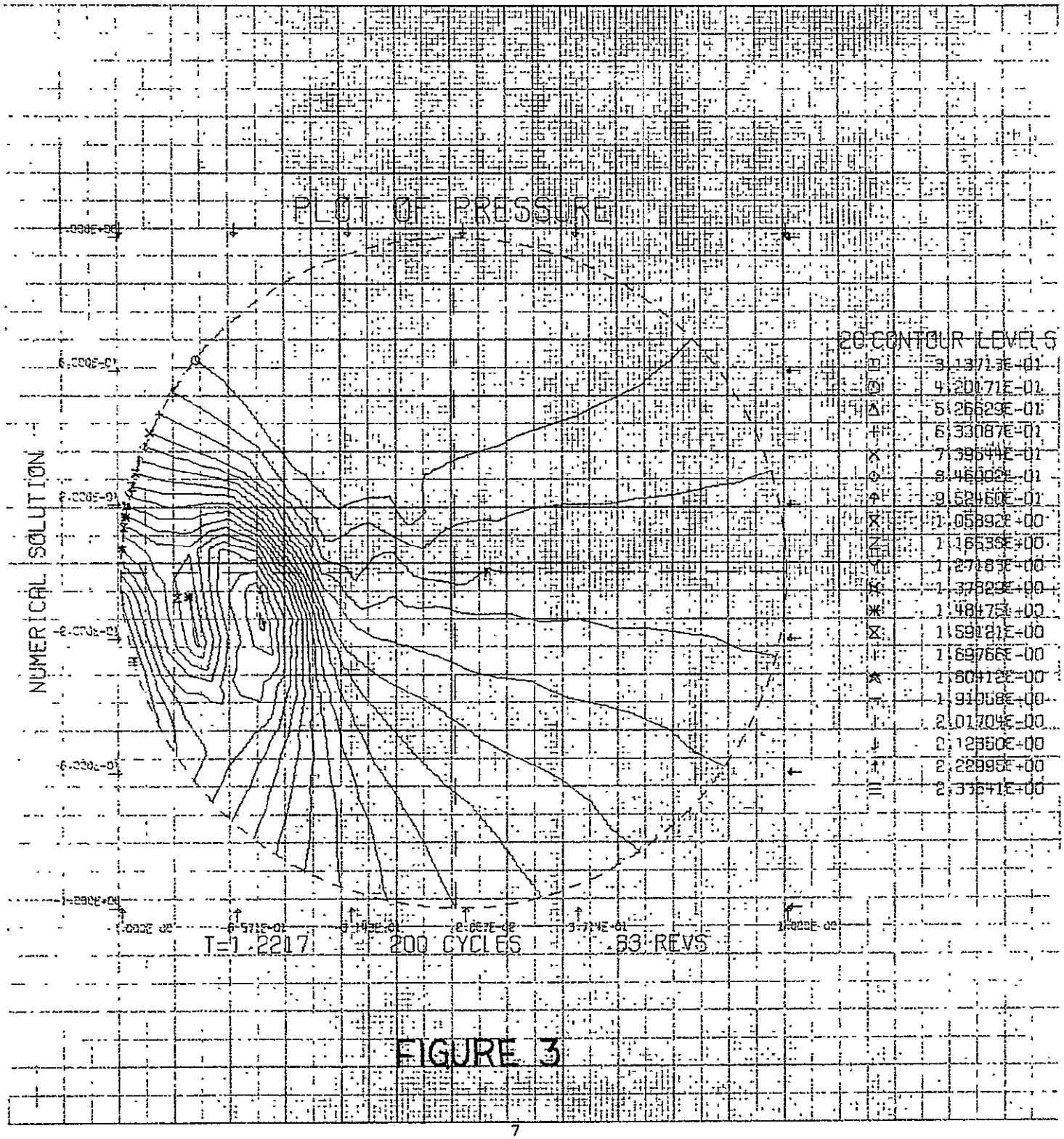
PLOT OF PRESSURE
NUMERICAL SOLUTION
20 CONTOUR LEVELS
3 1.13713E-01
4 1.20171E-01
5 1.26629E-01
6 1.33087E-01
7 1.39544E-01
8 1.46002E-01
9 1.52460E-01
1 1.05392E+00
1 1.16538E+00
1 1.27683E+00
1 1.38829E+00
1 1.49975E+00
1 1.59121E+00
1 1.69766E+00
1 1.80912E+00
1 1.91058E+00
2 2.01704E+00
2 2.12850E+00
2 2.22995E+00
2 2.33141E+00
T=1.2217 200 CYCLES 83 REVS

FIGURE 3

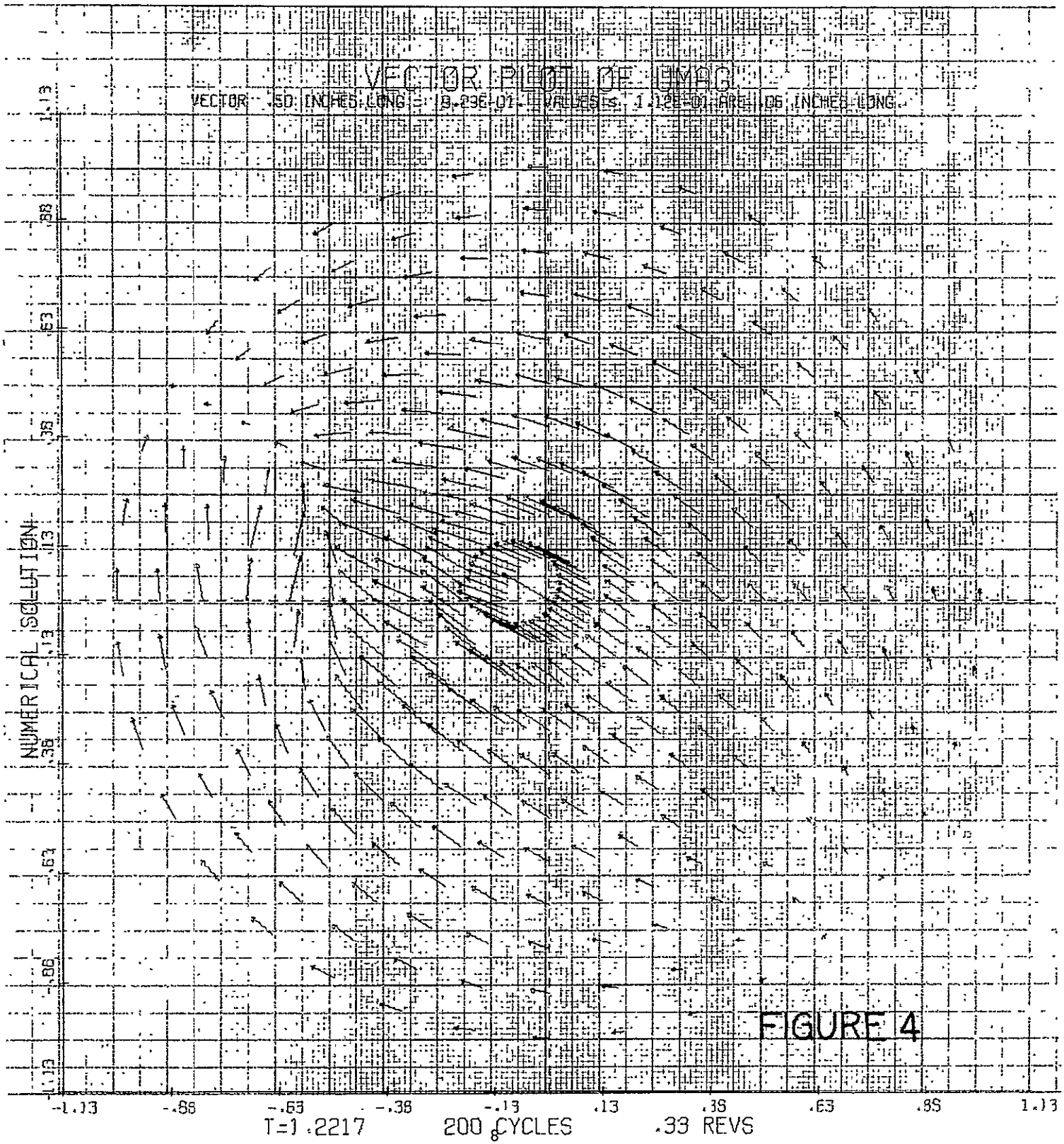
VECTOR PLOT OF VMAG
VECTOR .50 INCHES LONG = 8.23E-01 VALUES ≤ 1.12E-01 ARE .06 INCHES LONG
NUMERICAL SOLUTION
1.13
.88
.63
.38
.13
-.13
-.38
-.63
-.88
-1.13
-1.13
-.88
-.63
-.38
-.13
.13
.38
.63
.88
1.13
T=1.2217
200 CYCLES
.33 REVS

FIGURE 4

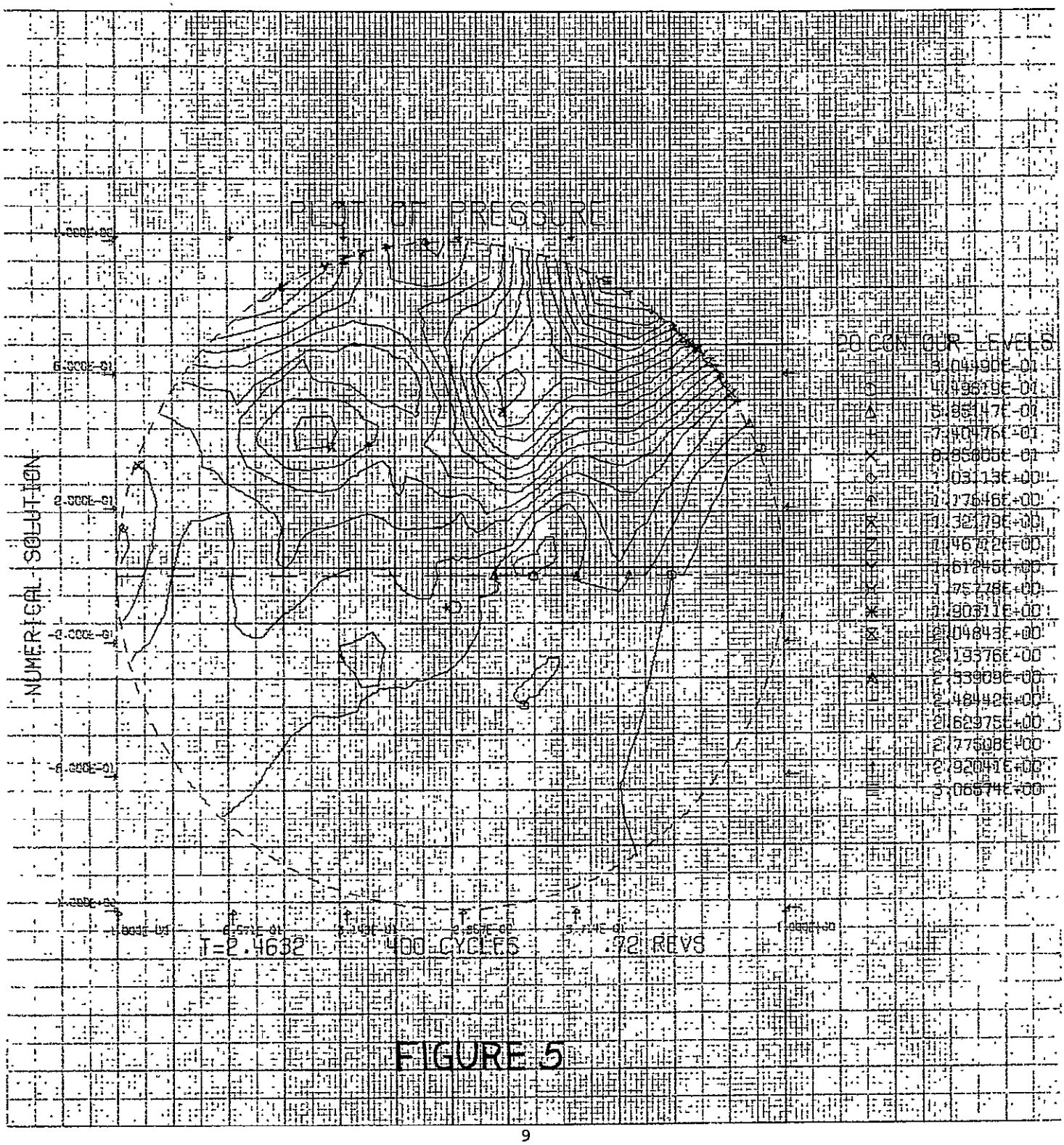
PLOT OF PRESSURE
NUMERICAL SOLUTION
T=2.4632
400 CYCLES
72 REVS

FIGURE 5

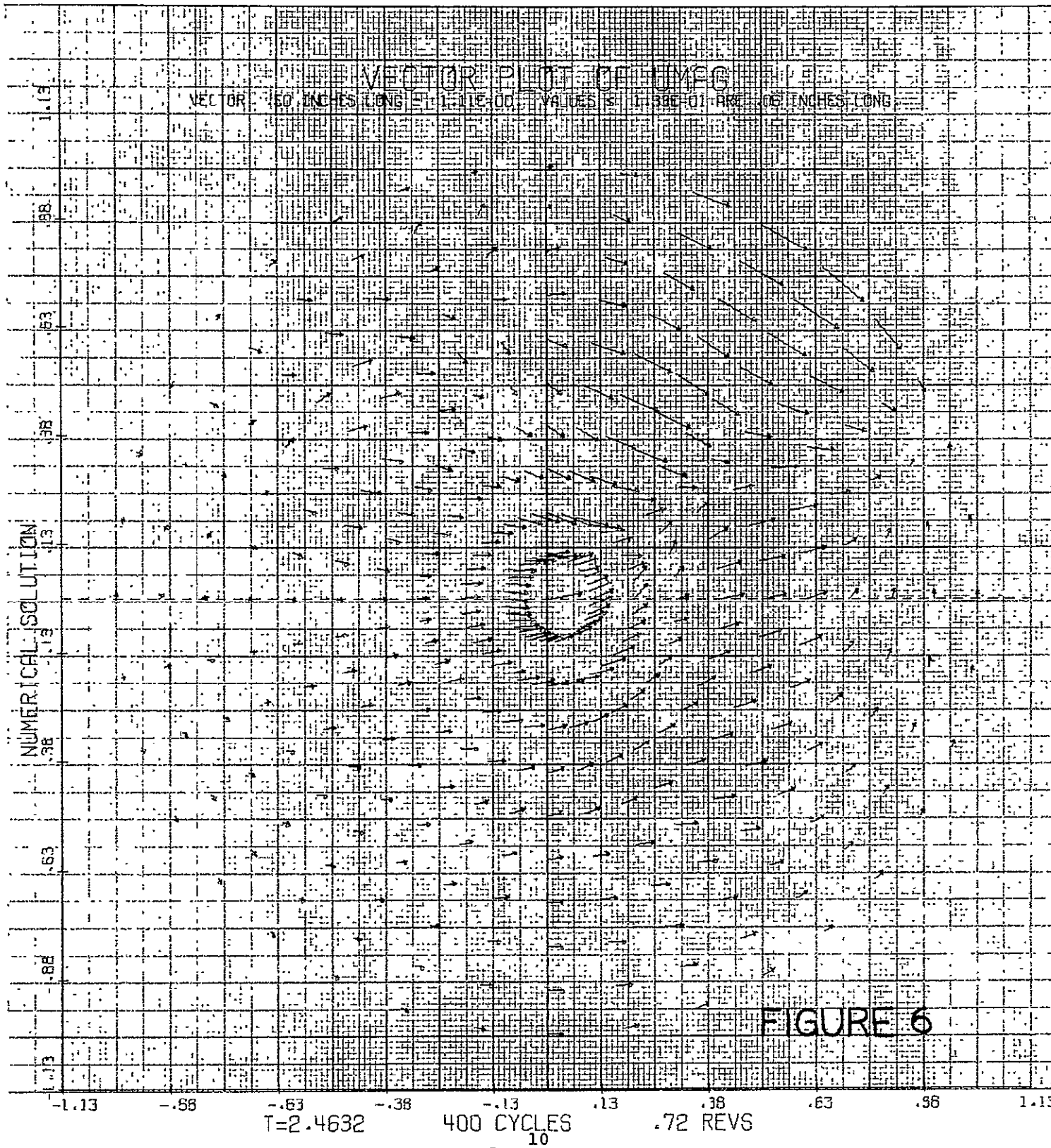
VECTOR PLOT OF UMEG
VECTOR .50 INCHES LONG = 1.11E-00 VALUES = 1.38E-01 ARE .06 INCHES LONG
NUMERICAL SOLUTION
1.13
.88
.63
.38
.13
-.13
-.38
-.63
-.88
-1.13
-1.13
-.88
-.63
-.38
-.13
.13
.38
.63
.88
1.13
T=2.4632
400 CYCLES
.72 REVS

FIGURE 6

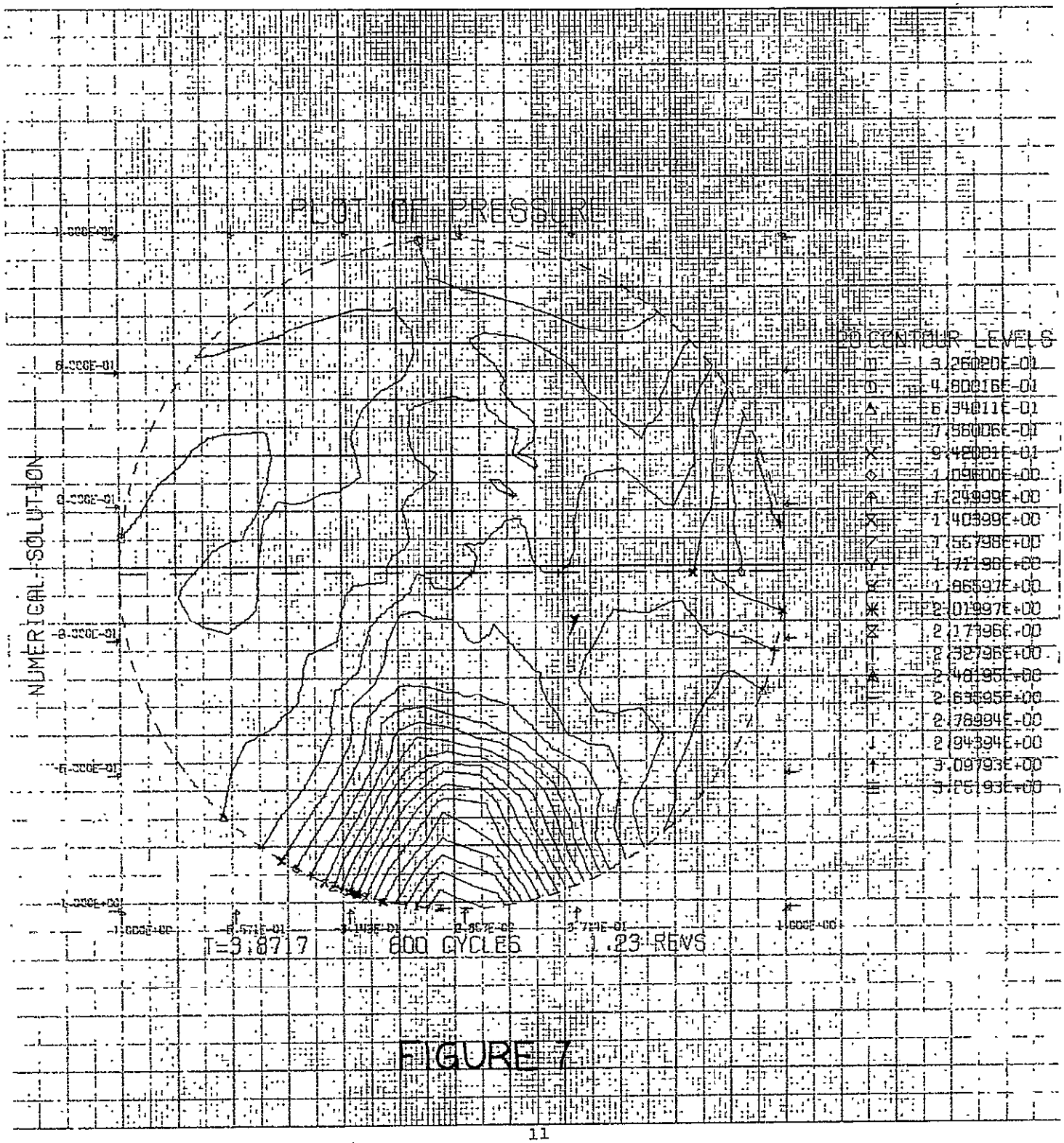
PLOT OF PRESSURE
NUMERICAL SOLUTION
20 CONTOUR LEVELS
3.260820E-01
4.808816E-01
6.340811E-01
7.860806E-01
9.420801E-01
1.096800E+00
1.249999E+00
1.403999E+00
1.557998E+00
1.711996E+00
1.865997E+00
2.019997E+00
2.177996E+00
2.327996E+00
2.481995E+00
2.635995E+00
2.789994E+00
2.943994E+00
3.097993E+00
3.251993E+00
T=3.8717
800 CYCLES
1.23 REVS

FIGURE 7

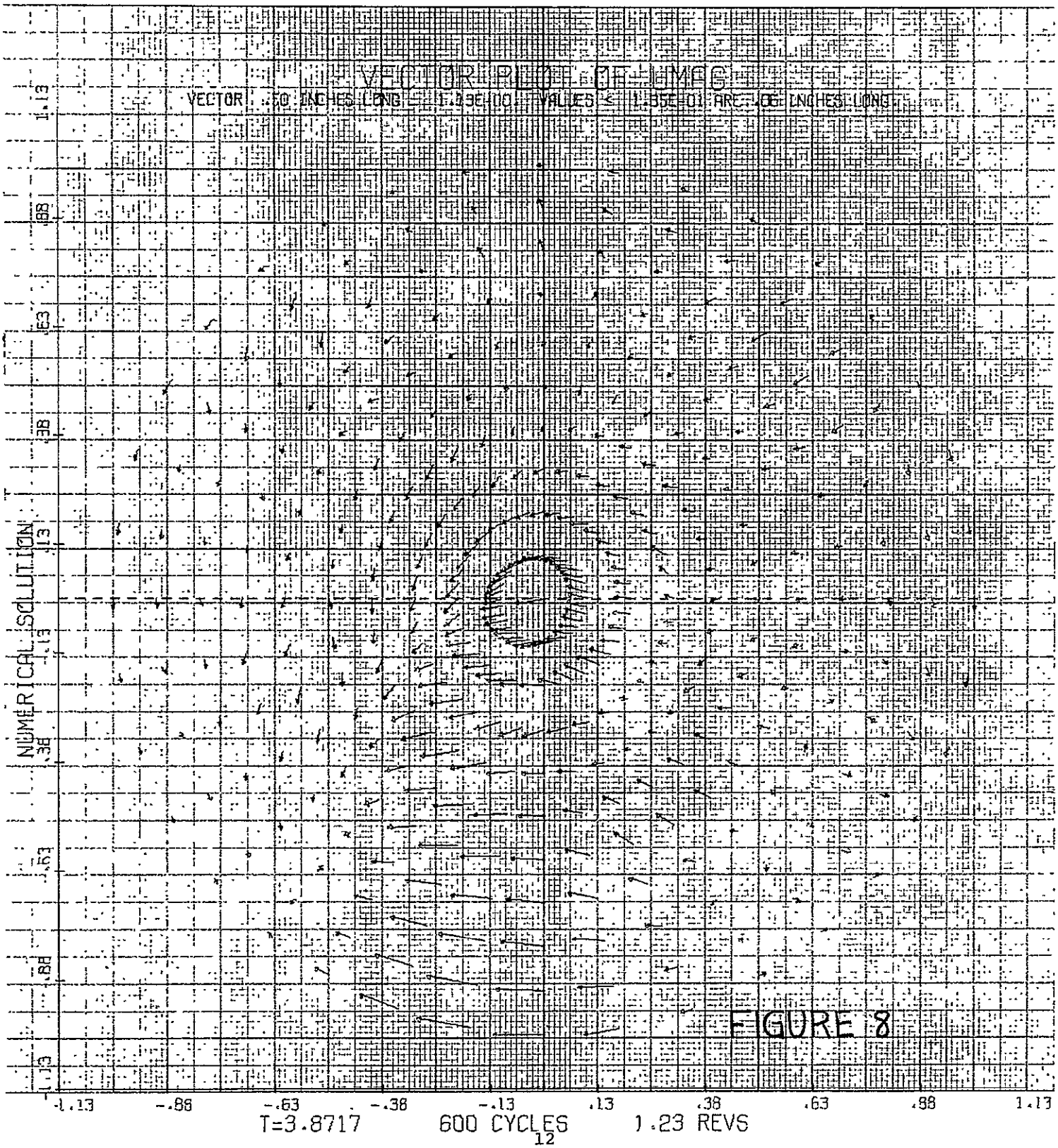
VECTOR PLOT MAP
VECTOR = .50 INCHES LONG = 1.49E 00 VALUES = 1.85E 01 ARE .06 INCHES LONG
NUMERICAL SOLUTION
1.13
.88
.63
.38
.13
-.13
-.38
-.63
-.88
-1.13
-1.13
-.88
-.63
-.38
-.13
.13
.38
.63
.88
1.13
T=3.8717
600 CYCLES
1.23 REVS

FIGURE 8

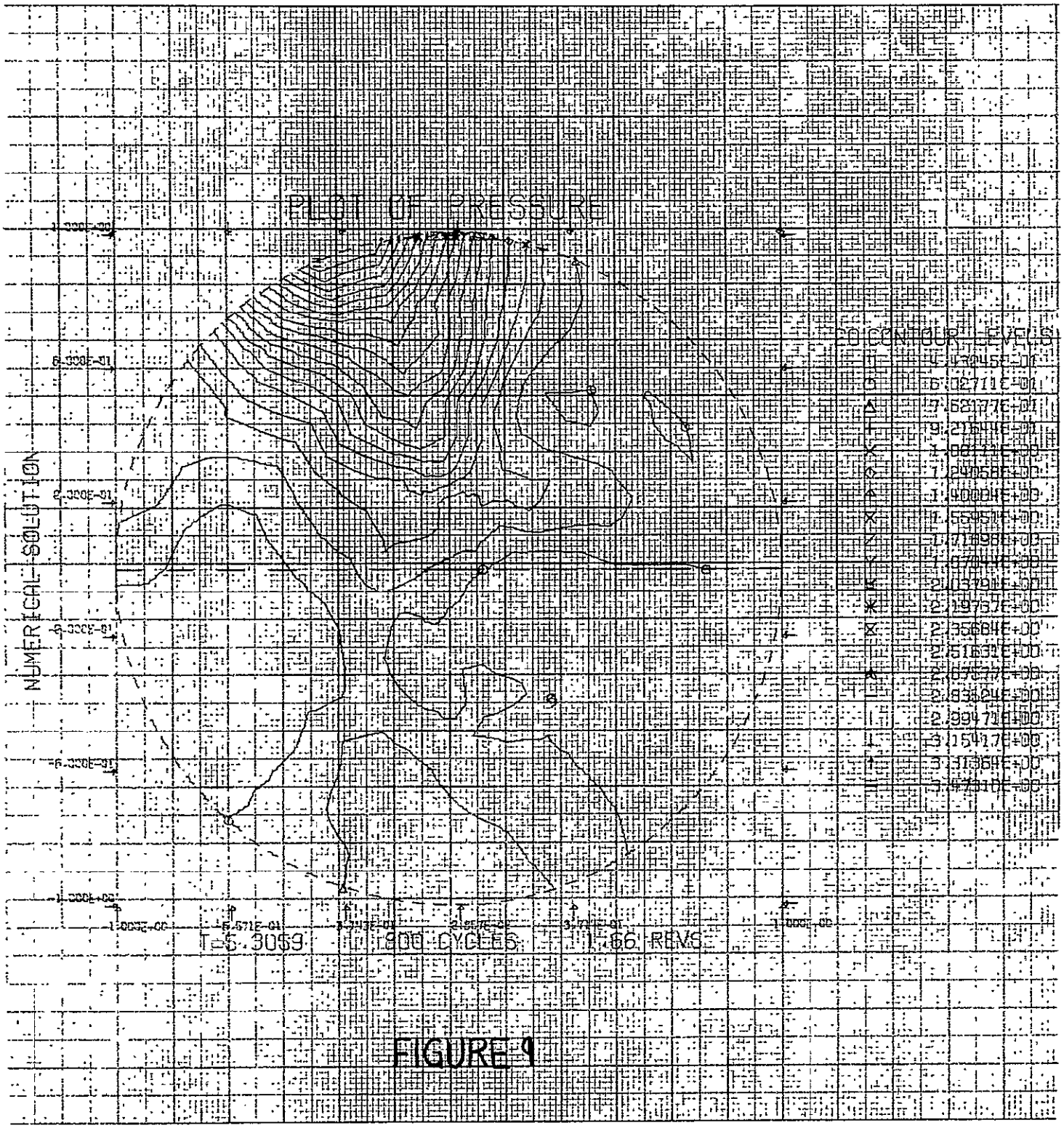
PLOT OF PRESSURE
NUMERICAL SOLUTION
T=5.3059
800 CYCLES
1.66 REVS

FIGURE 9

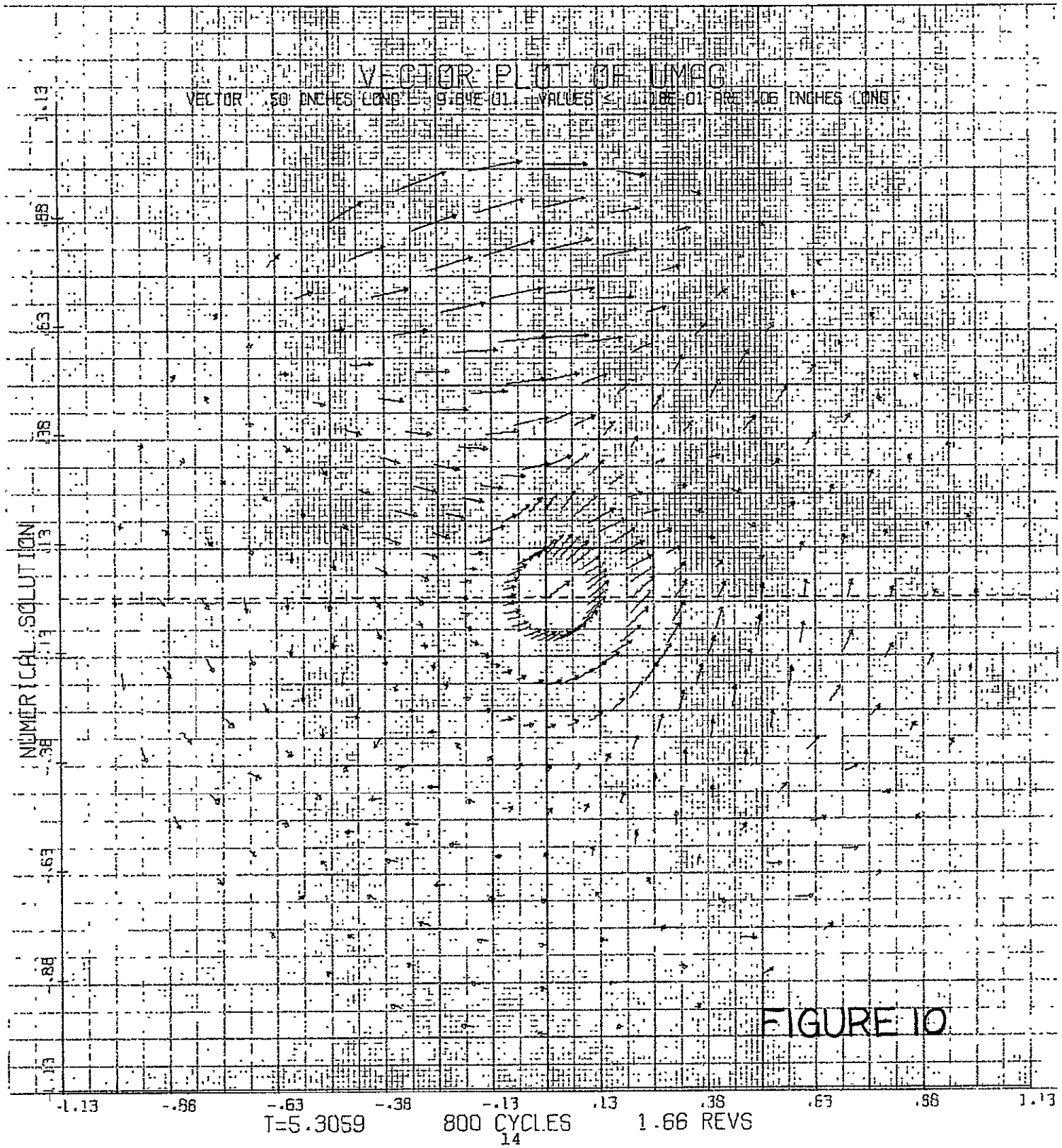
VECTOR PLOT OF UMAG
VECTOR .50 INCHES LONG = 9.64E-01 VALUES < 1.0E-01 ARE .06 INCHES LONG
NUMERICAL SOLUTION
1.13
.88
.63
.38
.13
-.13
-.38
-.63
-.88
-1.13
-1.13
-.88
-.63
-.38
-.13
.13
.38
.63
.88
1.13
T=5.3059
800 CYCLES
1.66 REVS

FIGURE 10

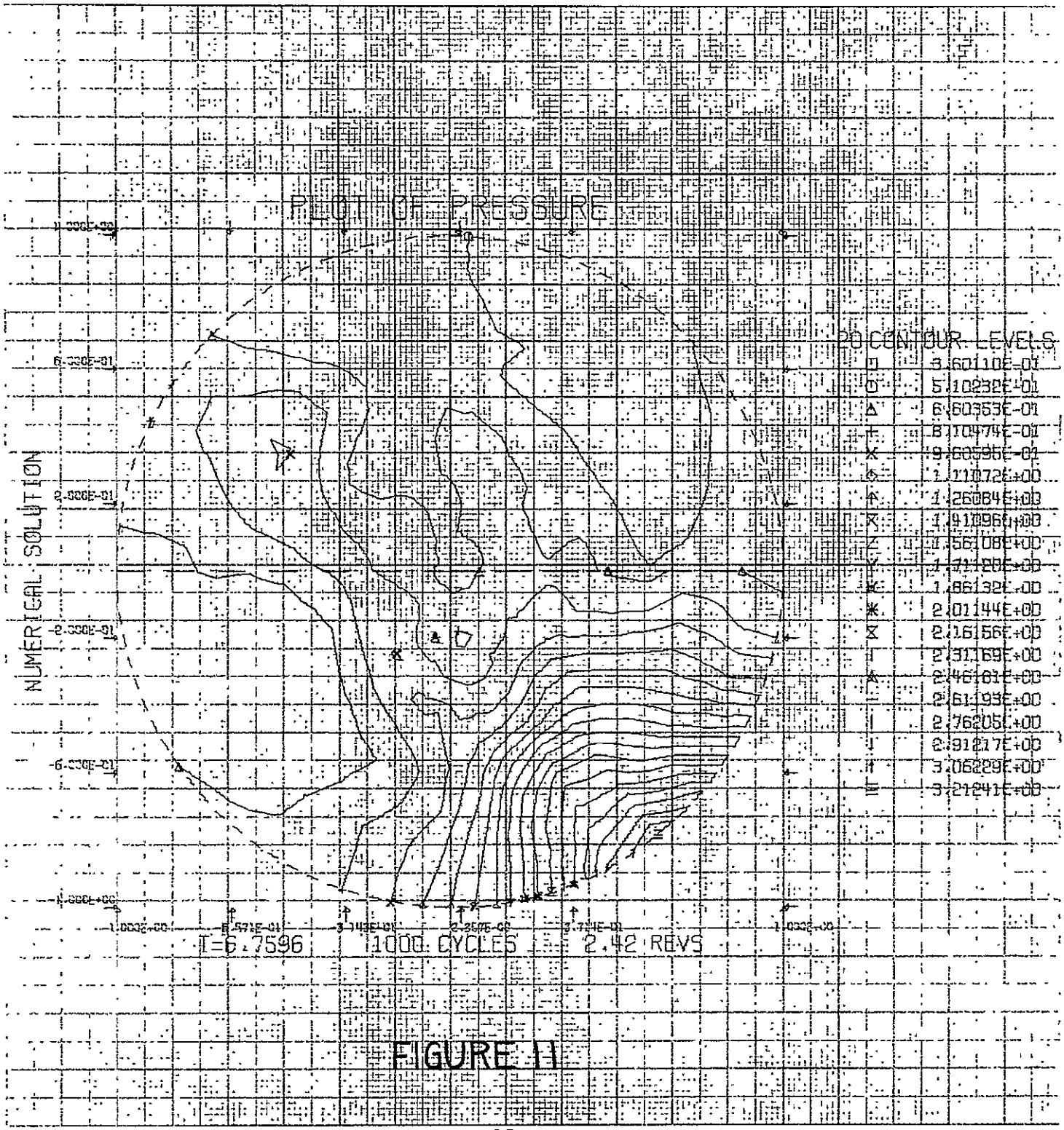
PLOT OF PRESSURE
NUMERICAL SOLUTION
PO CONTOUR LEVELS
3.60110E-01
5.10232E-01
6.60353E-01
8.10474E-01
9.60595E-01
1.11072E+00
1.26084E+00
1.41096E+00
1.56108E+00
1.71120E+00
1.86132E+00
2.01144E+00
2.16156E+00
2.31169E+00
2.46181E+00
2.61193E+00
2.76205E+00
2.91217E+00
3.06229E+00
3.21241E+00
T=6.7596
1000 CYCLES
2.42 REVS

FIGURE 11

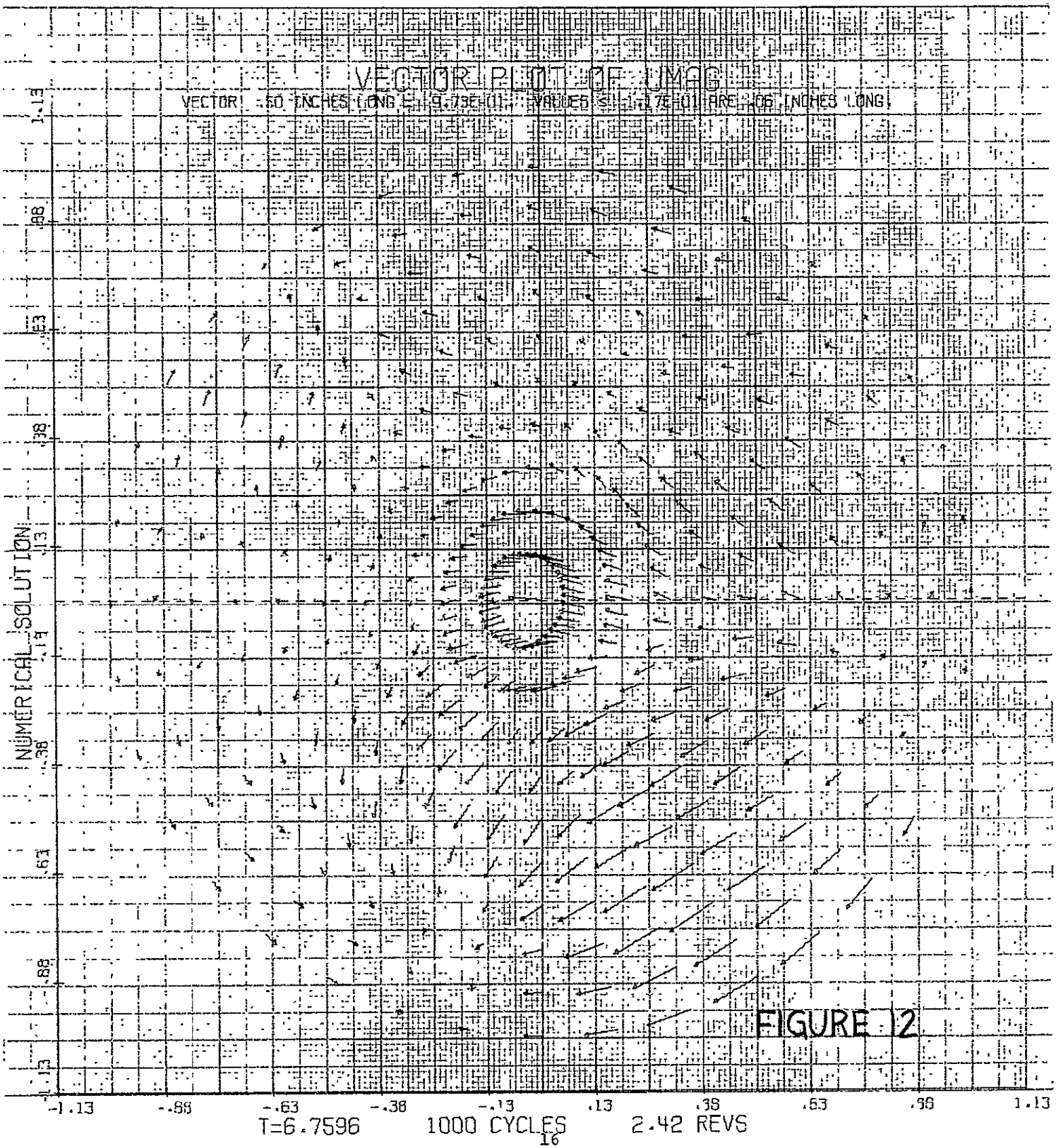
VECTOR PLOT OF UMAG
VECTOR = .50 INCHES LONG = 9.73E-01 VALUES = 1.17E-01 ARE .06 INCHES LONG
NUMERICAL SOLUTION
1.13
.88
.63
.38
.13
-.13
-.38
-.63
-.88
-1.13
T=6.7596 1000 CYCLES 2.42 REVS

FIGURE 12

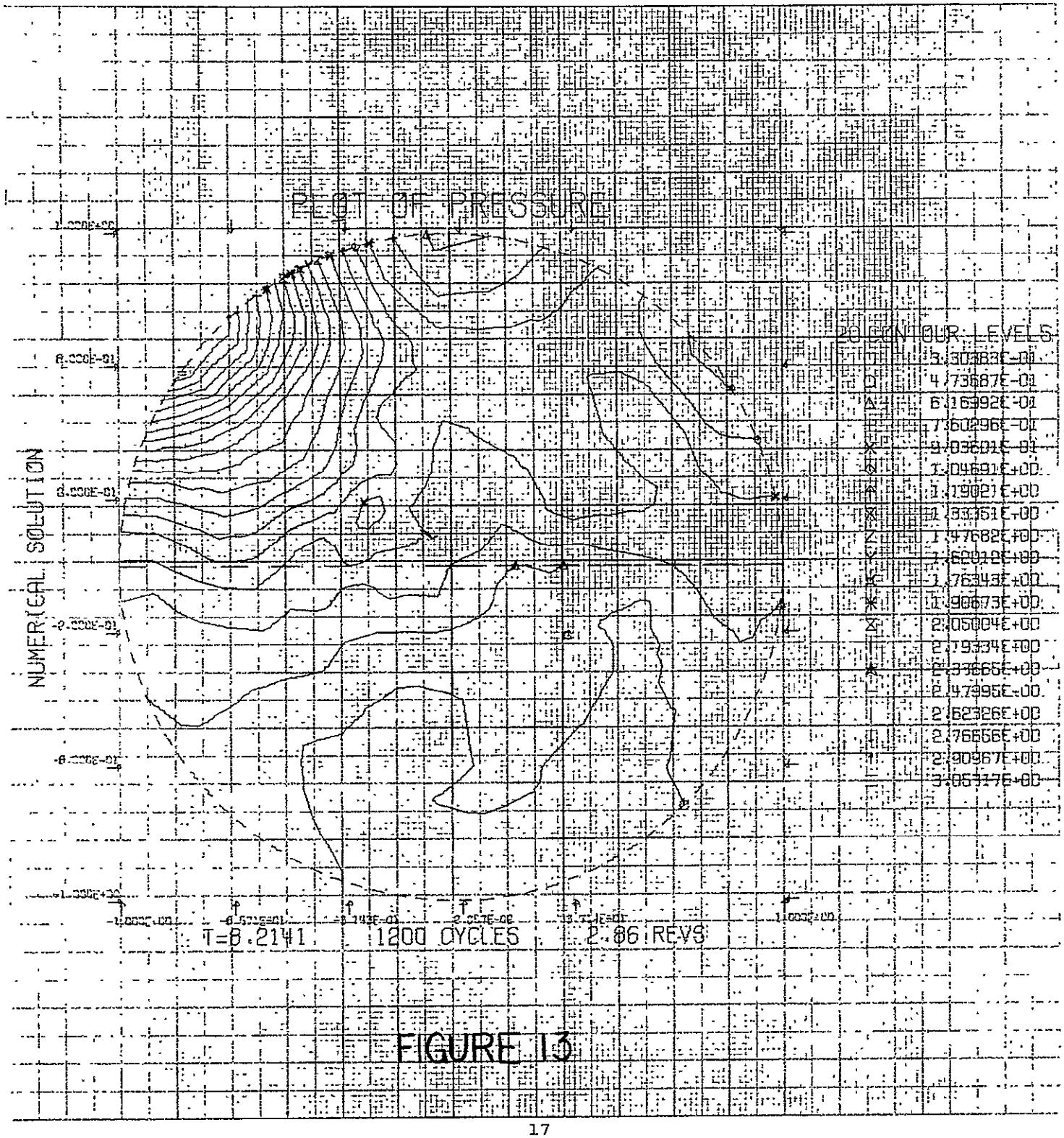
PLOT OF PRESSURE
NUMERICAL SOLUTION
20 CONTOUR LEVELS
3.303883E-00
4.736687E-01
6.169492E-01
7.602296E-01
9.035101E-01
1.046791E+00
1.190071E+00
1.333351E+00
1.476632E+00
1.619912E+00
1.763193E+00
1.906473E+00
2.049754E+00
2.193034E+00
2.336315E+00
2.479595E+00
2.622876E+00
2.766156E+00
2.909437E+00
3.052717E+00
T=8.2141
1200 CYCLES
2.86 REVS

FIGURE 13

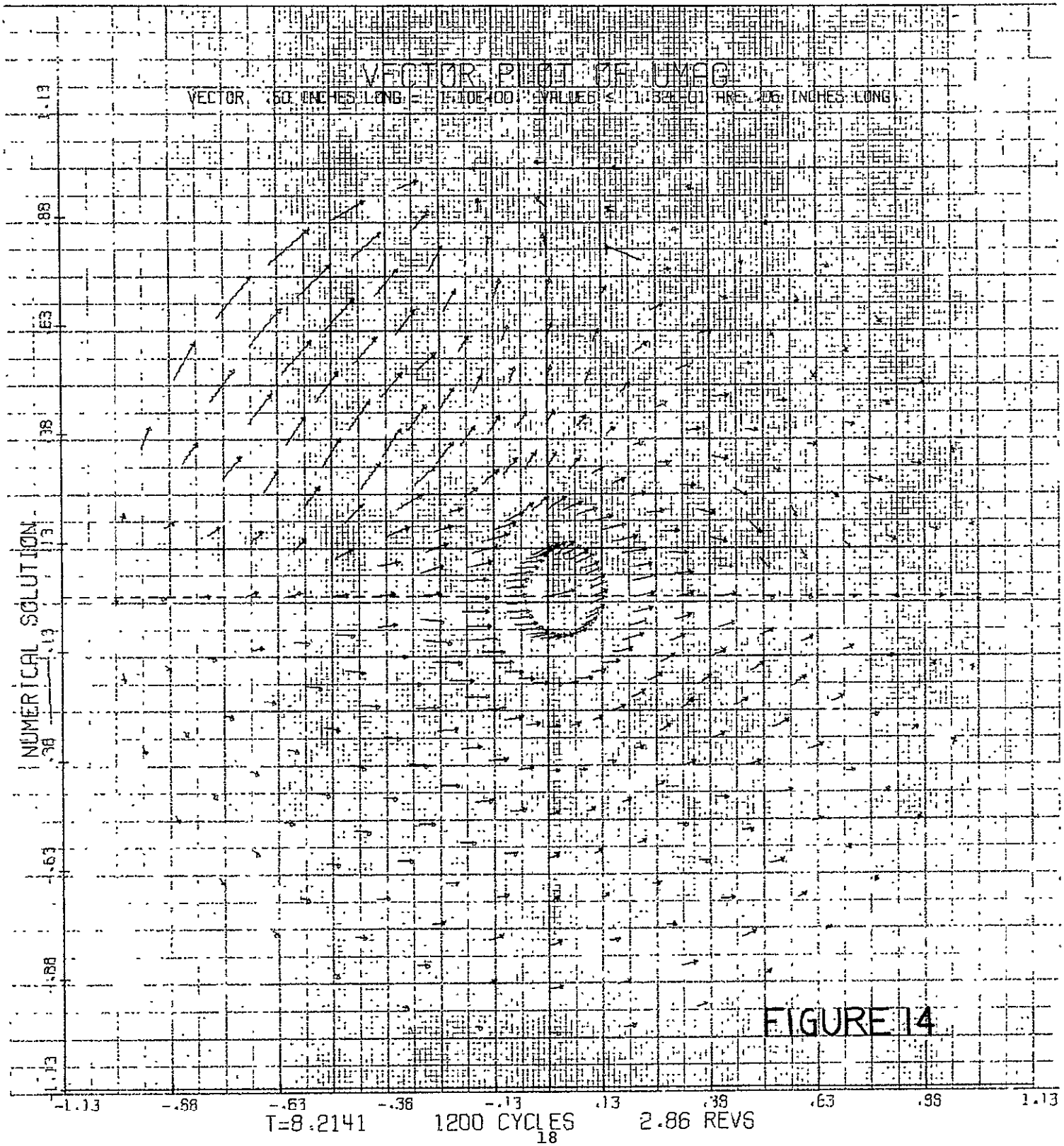
VECTOR PLOT OF UMAG
VECTOR .60 INCHES LONG = 1.0E+00 VALUES
1.32E+01 ARE .60 INCHES LONG
NUMERICAL SOLUTION
-1.13
-.88
-.63
-.38
-.13
.13
.38
.63
.88
1.13
T=8.2141 1200 CYCLES 2.86 REVS

FIGURE 14

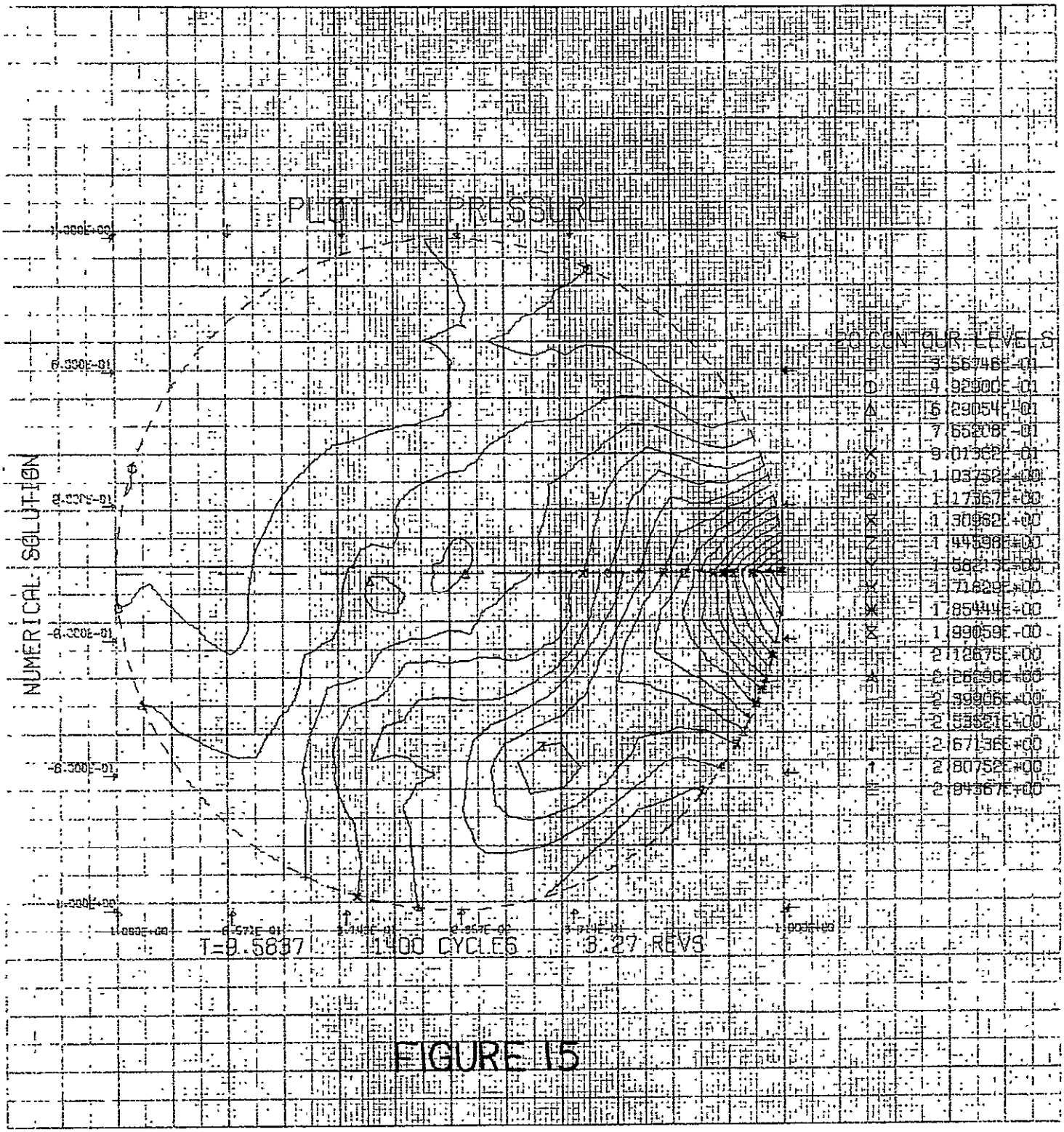
PLOT OF PRESSUR
NUMERICAL SOLUTION
T=0.5837
1400 CYCLES
3.27 REVS
CONTOUR LEVELS
3.56746E-01
9.92900E-01
2.80054E-01
7.65208E-01
9.01362E-01
1.03752E+00
1.17567E+00
1.30962E+00
1.44598E+00
1.58213E+00
1.71829E+00
1.85444E+00
1.99059E+00
2.12675E+00
2.26290E+00
2.39906E+00
2.53521E+00
2.67136E+00
2.80752E+00
2.94367E+00

FIGURE 15

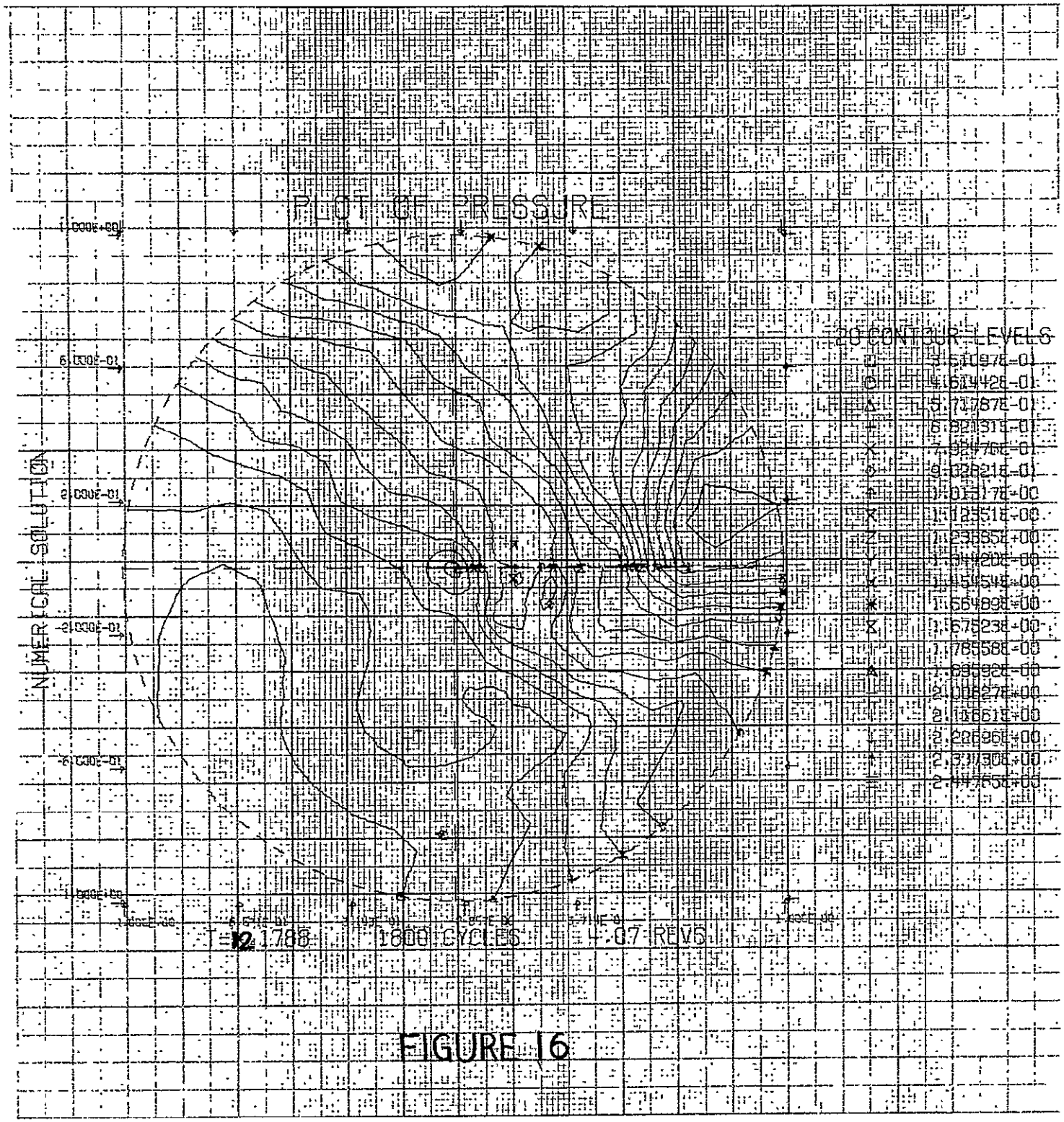
PLOT OF PRESSURE
NUMERICAL SOLUTION
20 CONTOUR LEVELS
3.510978E-01
4.614428E-01
5.717878E-01
6.821315E-01
7.924765E-01
9.028215E-01
1.013178E+00
1.123551E+00
1.233885E+00
1.344240E+00
1.454595E+00
1.564898E+00
1.675238E+00
1.785588E+00
1.895925E+00
2.006278E+00
2.116615E+00
2.226966E+00
2.337306E+00
2.447655E+00
T=2.1788
1800 CYCLES
4.07 REVS

FIGURE 16

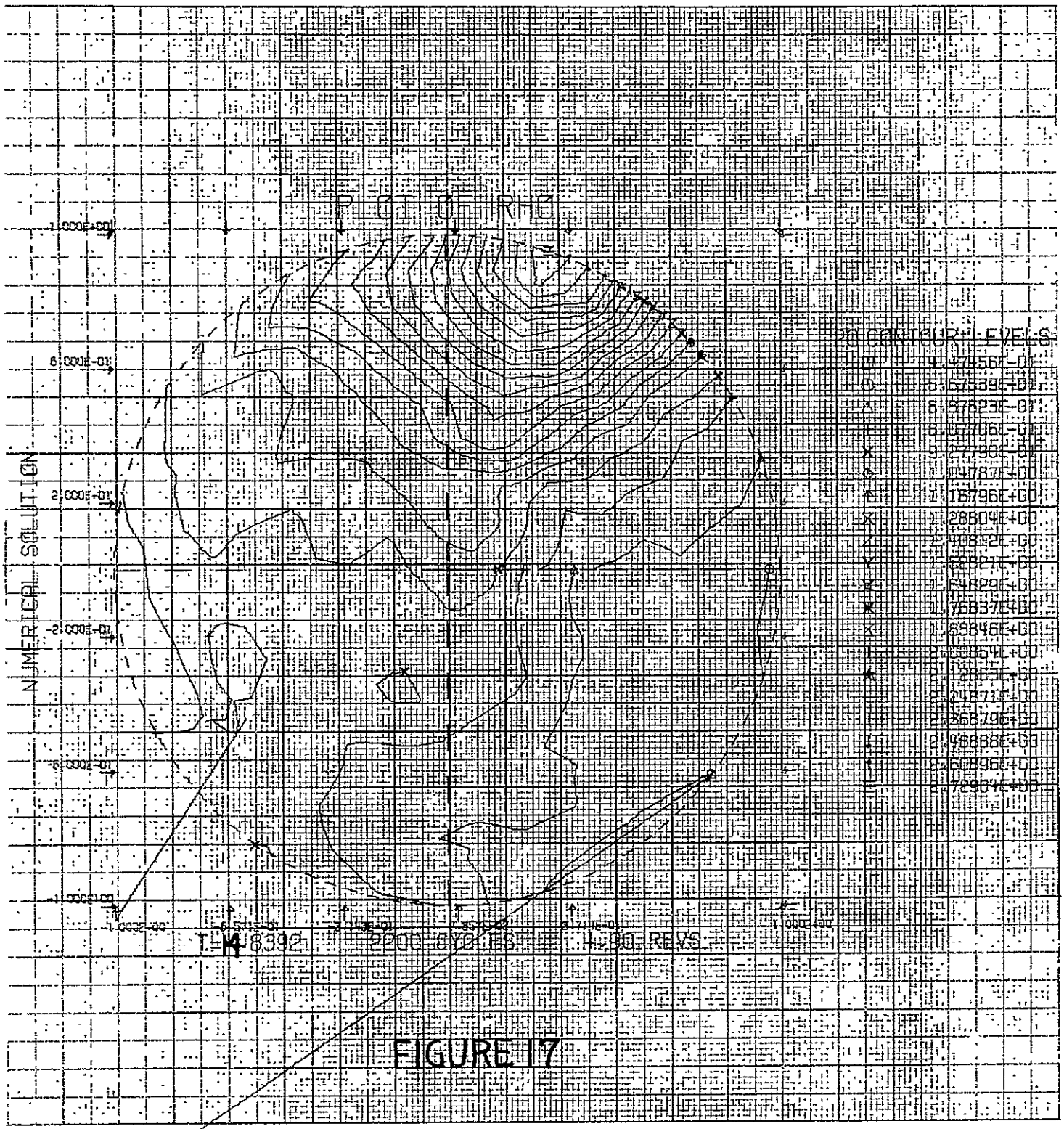

FIGURE 17

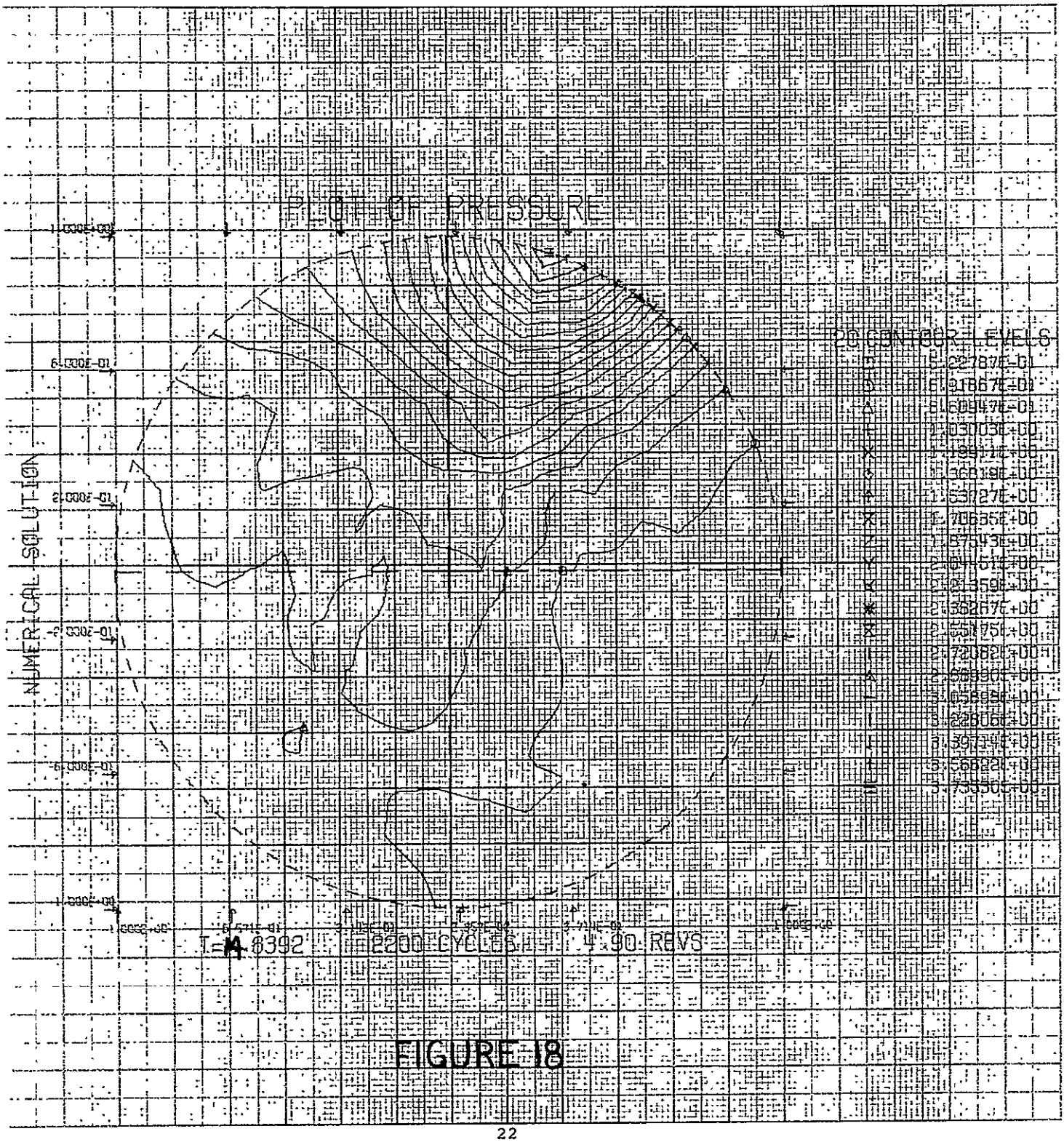
NUMERICAL SOLUTION
PLOT OF PRESSURE
20 CONTOUR LEVELS
T=4.8392
2200 CYCLES
4.90 REVS

FIGURE 18

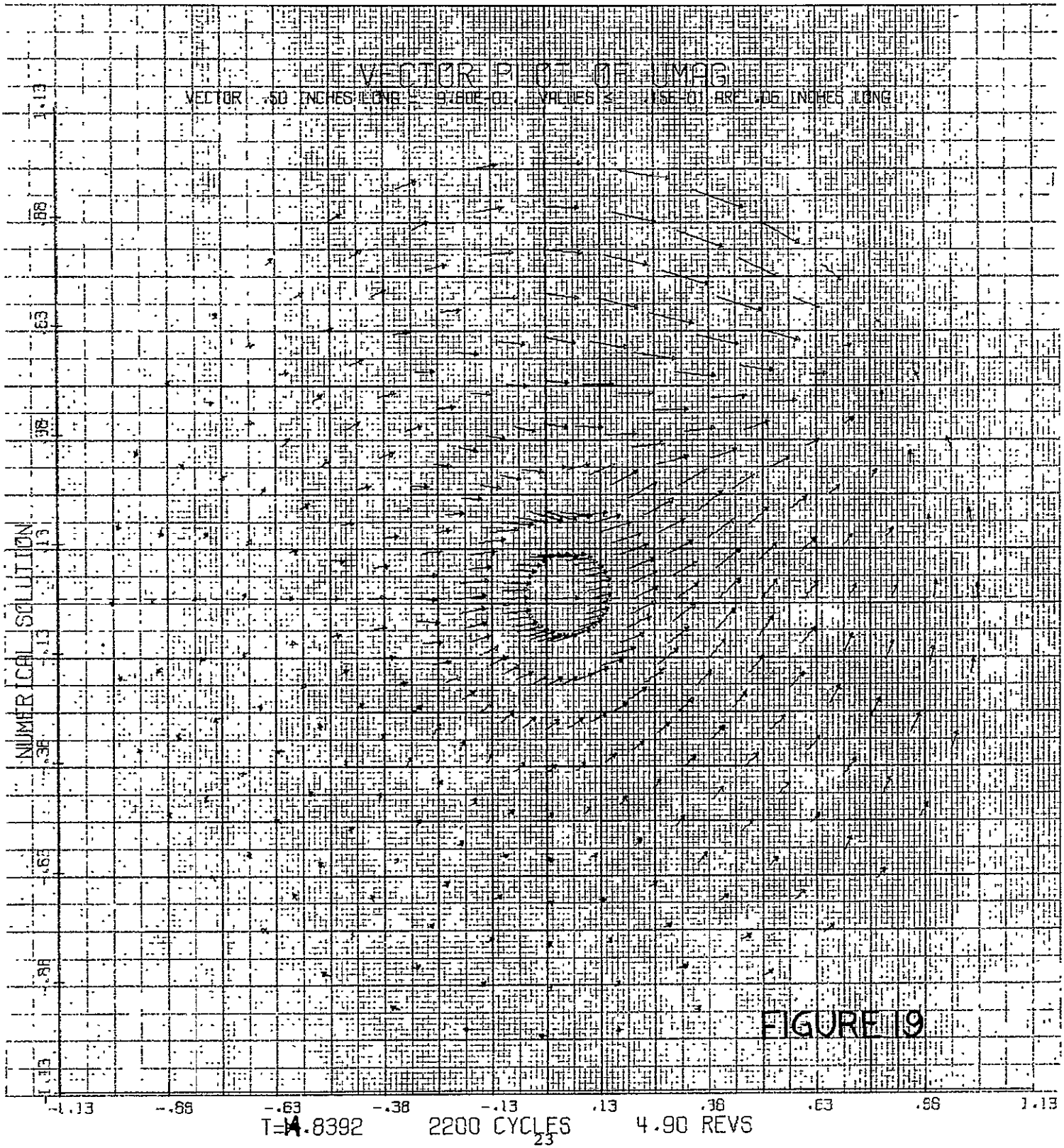
VECTOR PLOT OF UMAG
VECTOR .50 INCHES LONG = 9.18DE-01. VALUES < 1.5E-01 ARE .06 INCHES LONG
NUMERICAL SOLUTION
1.13
.88
.63
.38
.13
-.13
-.38
-.65
-.88
-1.13
-1.13
-.88
-.63
-.38
-.13
.13
.38
.63
.88
1.13
T=4.8392 2200 CYCLES 4.90 REVS

FIGURE 19

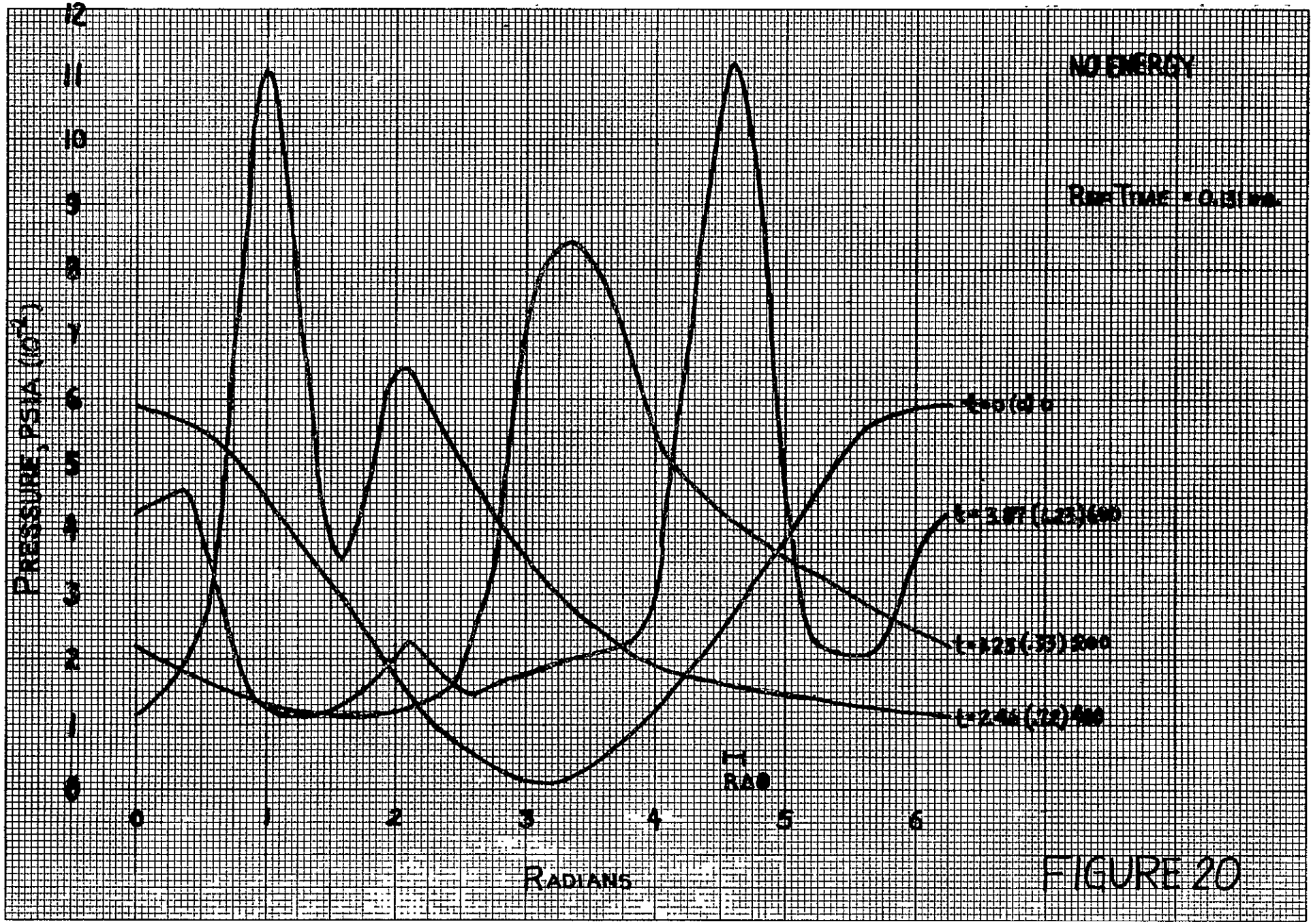
NO ENERGY
PRESSURE, PSIA (10⁻⁷)
RADIANS
FIGURE 20

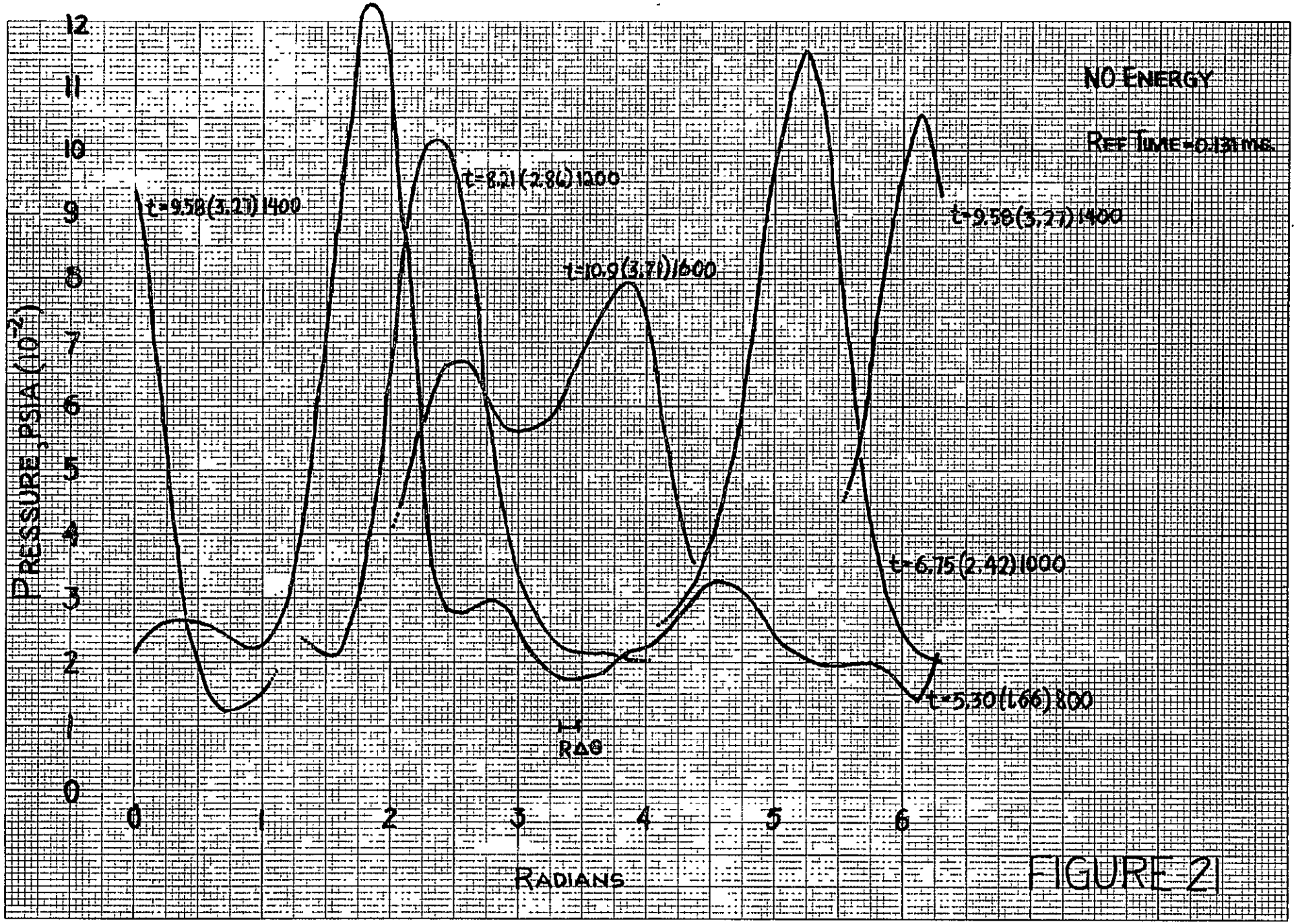
NO ENERGY
REF TIME=0.131 MS.
t=9.58(3.27)1400
t=8.21(2.84)1200
t=10.9(3.71)1600
t=9.58(3.27)1400
t=6.75(2.42)1000
t=5.30(1.66)800
RΔθ
PRESSURE, PSIA (10⁻²)
RADIANS
0
1
2
3
4
5
6
7
8
9
10
11
12

FIGURE 2

B. Energy Release in a Fluid with Finite Amplitude Waves, Simple Energy Source

We have carried out to completion the calculation started in the second quarterly report and described on page 26 of that report.

The calculation consists of adding an energy source term to the energy equation. There is no associated mass source term in the continuity equation. The energy term is dependent on the local pressure via

$$\dot{E} = \text{const}\,|(p-1)|^{\nu}\cdot\mu, \quad \nu=\tfrac{1}{2} \text{ if } p<1$$

$$\nu=1 \text{ otherwise}$$

It is also assumed that a velocity effect can be included by allowing μ to depend on the magnitude of the velocity $|\vec{u}| = (u^2+v^2)^{\frac{1}{2}}$ via

$$\mu = 1 \quad \text{if } |\vec{u}| \geq \delta$$

$$\mu = 0 \quad \text{otherwise}$$

We chose δ to be large enough so that the energy release occurred within the region of the pressure wave and nowhere else.

Finally, with the experience gained with the calculation described in section E of the second quarterly, we turn on the energy source slowly, i.e., the actual term used in the difference equation is $\omega\dot{E}$ where ω is monitonically increasing and satisfies $0\leq\omega\leq1$. We take ω to be the value of the 'rev' counter during the first rotation of the wave, it is taken as unity for all subsequent rotations.

The calculation starts off exactly as in the last section. Figures 22 and 23 show the extent of the development of the wave after about 1.8 rotations of the wave (note the velocity vector

at r = 0, the rev counter, has just passed the starting position $\theta = -\pi/2$ for the second time) and it is clear that the structure is quite similar to the non-reactive case. However, the peak pressure is 4350 psia. The velocity field is also similar to the non-reactive case. The maximum velocity in the wave corresponds to 9800 ft/sec. Of course, as the calculation proceeds, the pressure amplitude continues to grow reaching a value approximately thirty times the reference pressure while the maximum velocity reaches a value six times the reference sound speed after just four hundred more cycles of calculation.

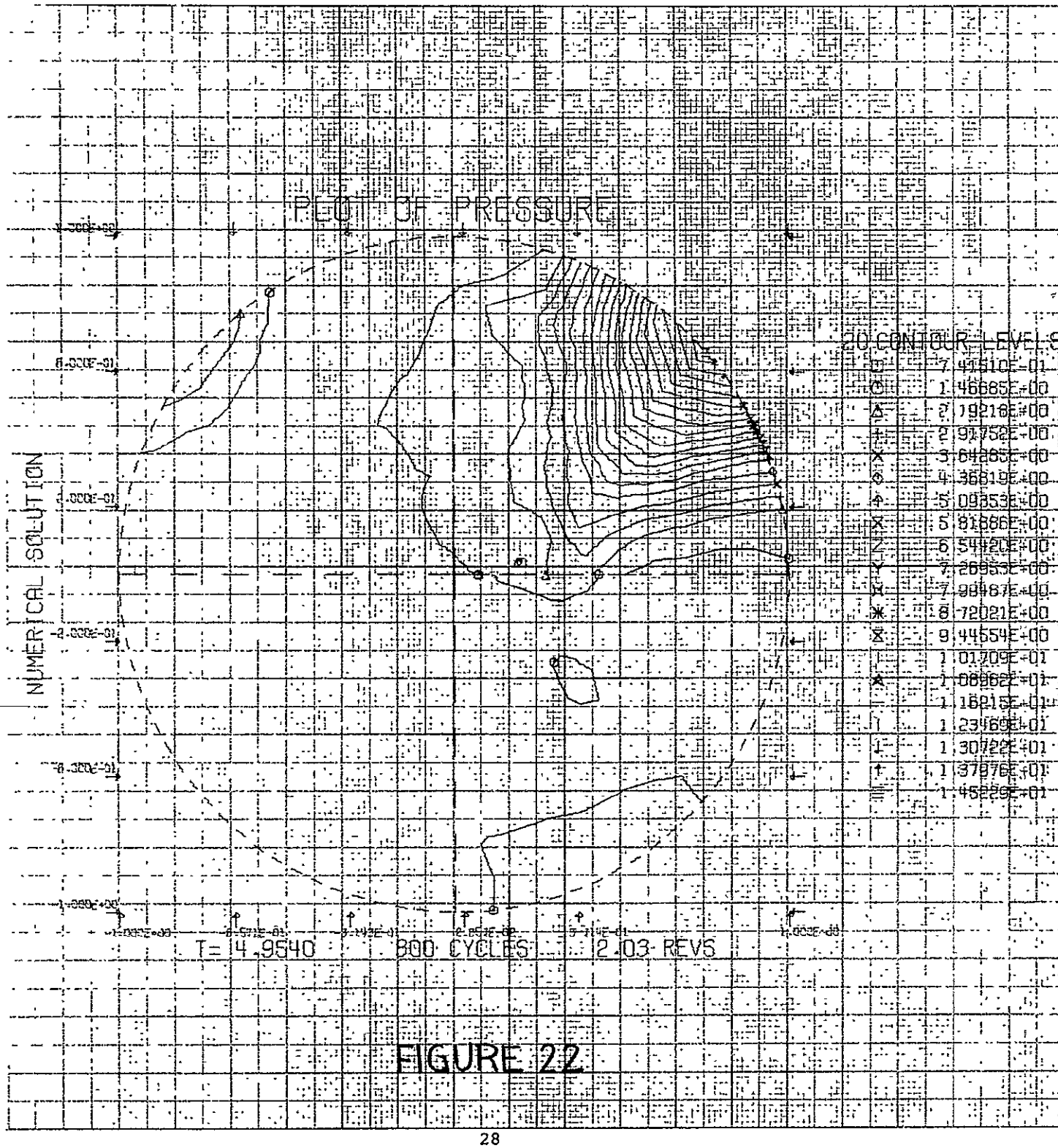
PLOT OF PRESSURE
NUMERICAL SOLUTION
20 CONTOUR LEVELS
7 41510E-01
1 46685E-00
2 19216E+00
2 91752E+00
3 64285E+00
4 36819E+00
5 09353E+00
5 81886E+00
6 54420E+00
7 26953E+00
7 99487E+00
8 72021E+00
9 44554E+00
1 01709E+01
1 08962E+01
1 16215E+01
1 23469E+01
1 30722E+01
1 37976E+01
1 45229E+01
T= 4.9540 800 CYCLES 2.03 REVS

FIGURE 22

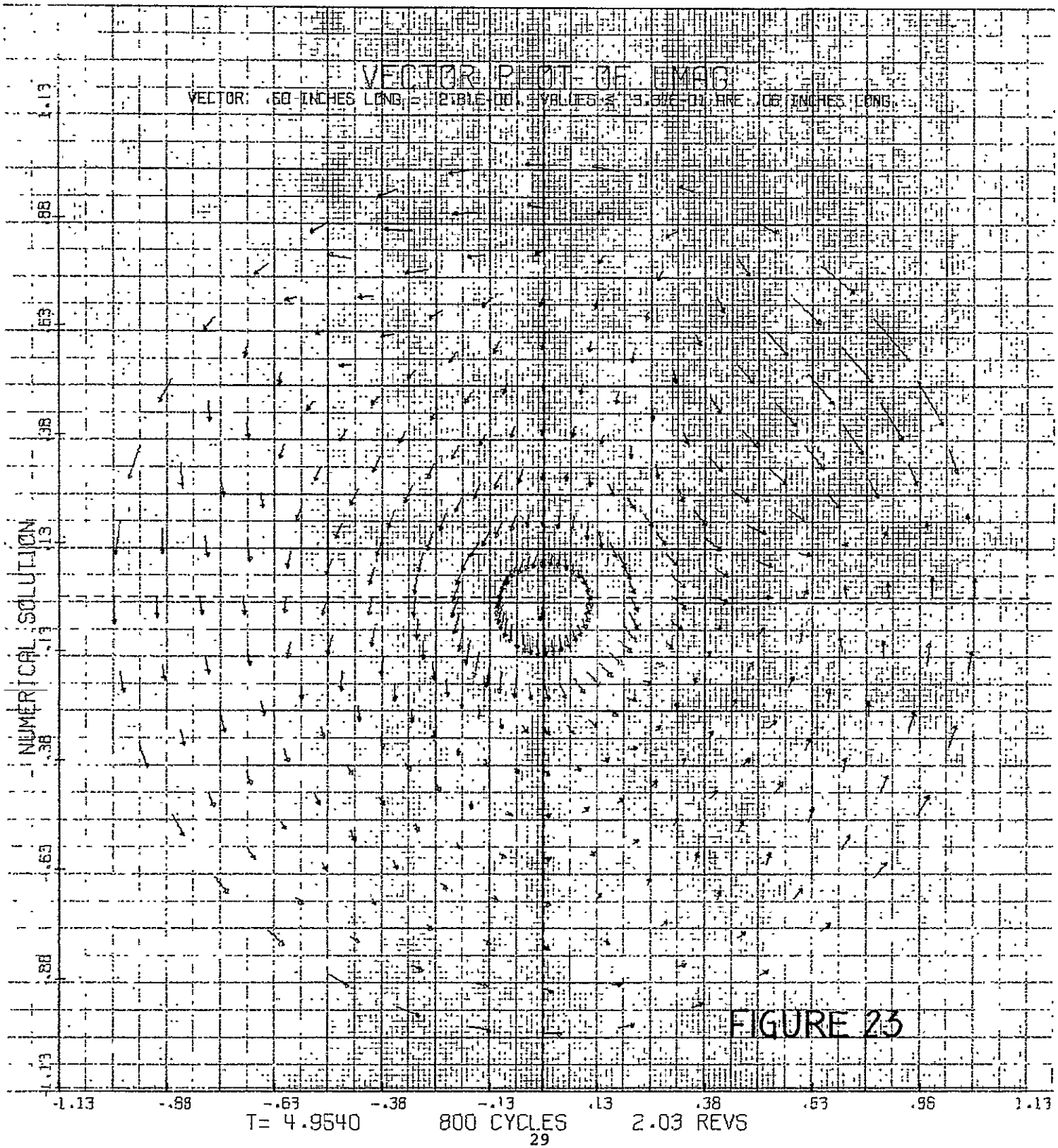
VECTOR PLOT OF UMAG
VECTOR .60 INCHES LONG = 2.81E-00 VALUES & 3.38E-01 ARE .06 INCHES LONG
NUMERICAL SOLUTION
1.13
.88
.63
.38
.13
-.13
-.38
-.63
-.88
-1.13
-1.13
-.88
-.63
-.38
-.13
.13
.38
.63
.88
1.13
T= 4.9540
800 CYCLES
2.03 REVS

FIGURE 23

C. Energy Release in a Fluid with Finite Amplitude Waves (Including the Axial Flux Calculation)

It is clear from the last section that unless energy is allowed to leave the system convectively, the pressure (as well as the specific internal energy) will continue to increase monotonically. Program COMB was then modified to include, in an approximate way, a value for the axial flux of energy.

Several approximations were tried. The first method, and perhaps the most obvious, involved in essentially finding the total energy (and mass) contained in the r-θ plane for each cycle of computation. The excess due to accumulation is parceled equally so that at each mesh point there exists a contribution to outflow which will exceed the inflow by just the amount that is accumulated. It was found that this procedure seems to work for small amplitude waves where only slight spatial variations in the energy release exist. However, for finite amplitude waves which initiate locally large influxes of mass and energy (due to increased transport processes on the droplet spray) this procedure fails to work. Some regions of the flow field where little reaction occurs see, according to this procedure, a relatively large outflow of energy (or mass). If this occurs for a sufficient number of time steps, the flow pressure (or density) can become negative locally and indeed this has been our observation. It is clear that a weighting of the outflow according to the inflow would be more desirable.

This was done for the simple energy release model given in the last section; the results being given below. The energy that was input due to combustion was allowed to reside in the r, θ

plane for one time step and then it was immediately considered to contribute to the axial flux. The following table gives a quick comparison of the value of $p_{max}/\gamma p_\infty$ of three calculations. The first column is an inert calculation with no energy term, the second with the simple energy model including an energy flux in the axial direction, and finally the third calculation is with the simple energy model but no convective flux in the z direction, i.e., the energy is locked in.

Wave Amplitude ($P_{max}/\gamma P_\infty$)

Cycle	Inert Case	With Axial Flux	Trapped Case
0	1.63	1.63	1.63
600	3.25	3.73	7.18
1000	3.21	3.53	19.57
1200	3.05	3.45	29.65
1400	2.84	3.91	-----

The final row of data corresponds to approximately 3.27 rotations of the wave and it is clear that by including the axial flux, the rapid growth of the wave is controlled while the energy source itself supplies energy to the wave.

It was found that for values of ten times the constant in the energy law in section B, the solution could not be continued beyond 300 cycles. This value is consistent with a physically real energy release near the injector. It is clear that the evaluation of the axial flux is quite critical and indeed, the problem really requires a third dimension so as to mathematically pose the calculation correctly.

D. Finite Amplitude Waves and Simplified Modified Godsave Analysis

In this section we show the results of a tangential pressure wave interacting with a system of droplets (mean diameter = 75μ) which evaporates and burns according to the simplified Godsave analysis presented in Section II of this report. Hence, there is both an energy source for the energy equation as well as a mass source included in the continuity equation. However, there is no axial flux calculation included in this section.

The calculation consisted in specifying the flow field at $t = 0$. It is similiar to that given in figures 1 and 2 except that the maximum (minimum) pressure is 550 psia (50 psia). The calculation proceeds without energy addition for as long as it takes the wave to make one complete rotation. Then the calculation incorporates the relations developed in Section II of this report for the evaporation and combustion of the droplets. The energy and mass source is turned on completely just as the wave is starting its second period of rotation. Figures 24 and 25 give the fluid dynamic field just before the droplets start interacting (excuse the extraneous hash for this series of pictures which is due to a malfunctioning solenoid valve hooked onto the pen on the Calcomp Plotter). For this series of pictures the pressure is normalized with p_∞ (rather than γp_∞ as before). Figure 26 gives the dimensional pressure $p(R,\theta)$ at $t = 3.3259$ units at the outer wall of the chamber ($r = R$), again just before the energy is switched on. The wave is moving from right to left.

The next two figures, 27 and 28, show the initial transient as the energy is switched on. Due to large radial components, figure 28, the pressure pulse moves inward, but still undergoing rotation as the next four figures indicate (figures 29-32). The next sequence of figures (figures 33-38) show the transition to the compression/rarefaction pulse traveling along the chamber wall (except that strong radial motion flattens the pulse against the wall). This is seen from figure 39 to the final figure 44. As can be seen from figures 28 and 30, strong radial motion is generated by the large release of energy and persists as transverse motion is interacting with the tangential motion. The resultant 'steady' or time periodic pattern would require additional calculation.

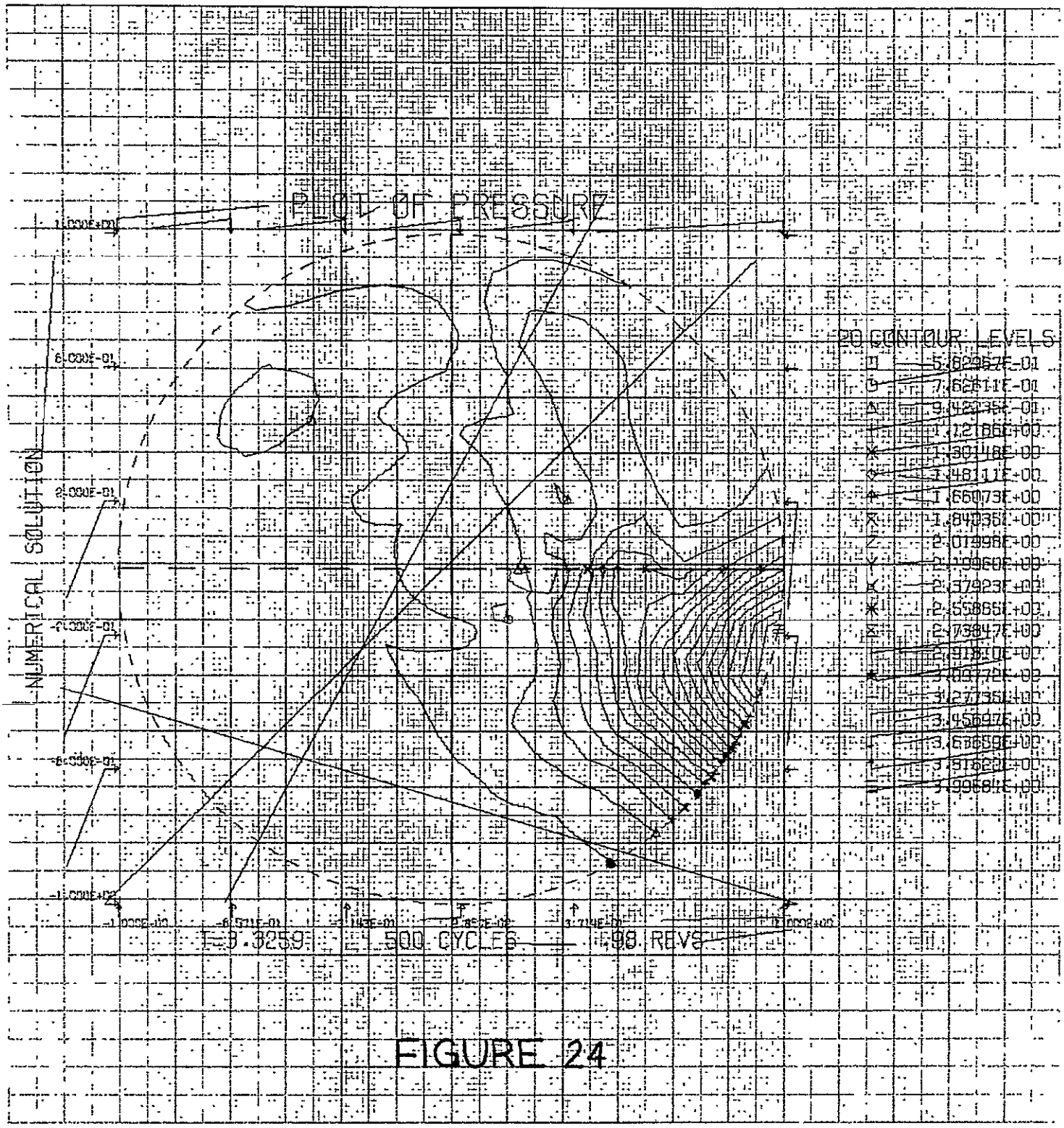
PLOT OF PRESSURE
NUMERICAL SOLUTION
20 CONTOUR LEVELS
5.82967E-01
7.62811E-01
9.42235E-01
1.12186E+00
1.30148E+00
1.48111E+00
1.66073E+00
1.84036E+00
2.01998E+00
2.19960E+00
2.37923E+00
2.55886E+00
2.73847E+00
2.91810E+00
3.09772E+00
3.27735E+00
3.45697E+00
3.63659E+00
3.81622E+00
3.99584E+00
T=9.3259 E+ 500 CYCLES 98 REVS

FIGURE 24

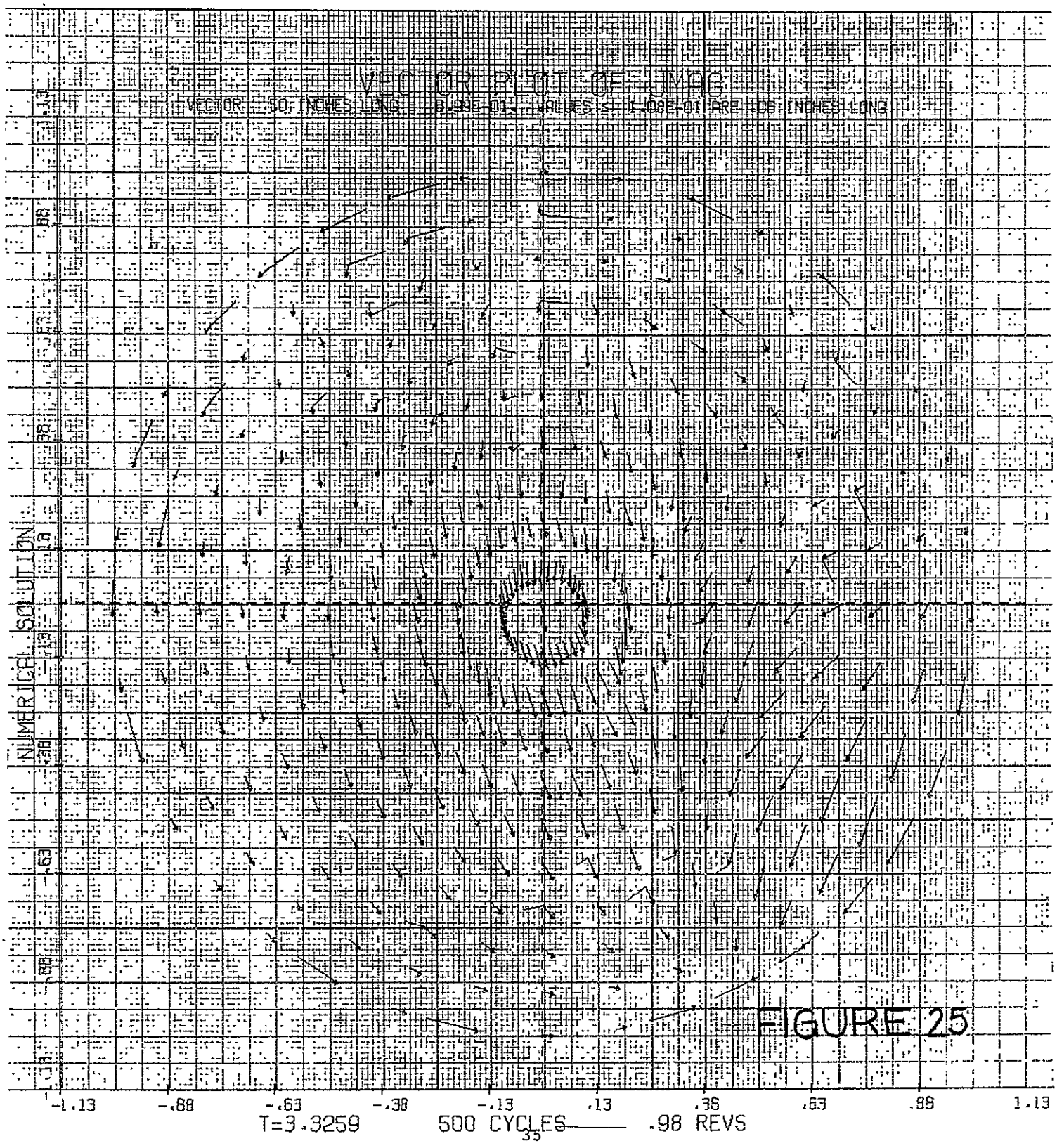
VECTOR PLOT OF MAG
VECTOR = 50 INCHES LONG = 8.99E-01 VALUES <= 1.08E-01 ARE .06 INCHES LONG
NUMERICAL SOLUTION
.13
.38
.63
.88
1.13
-1.13
-.88
-.63
-.38
-.13
.13
.38
.63
.88
1.13
T=3.3259
500 CYCLES
.98 REVS

FIGURE 25

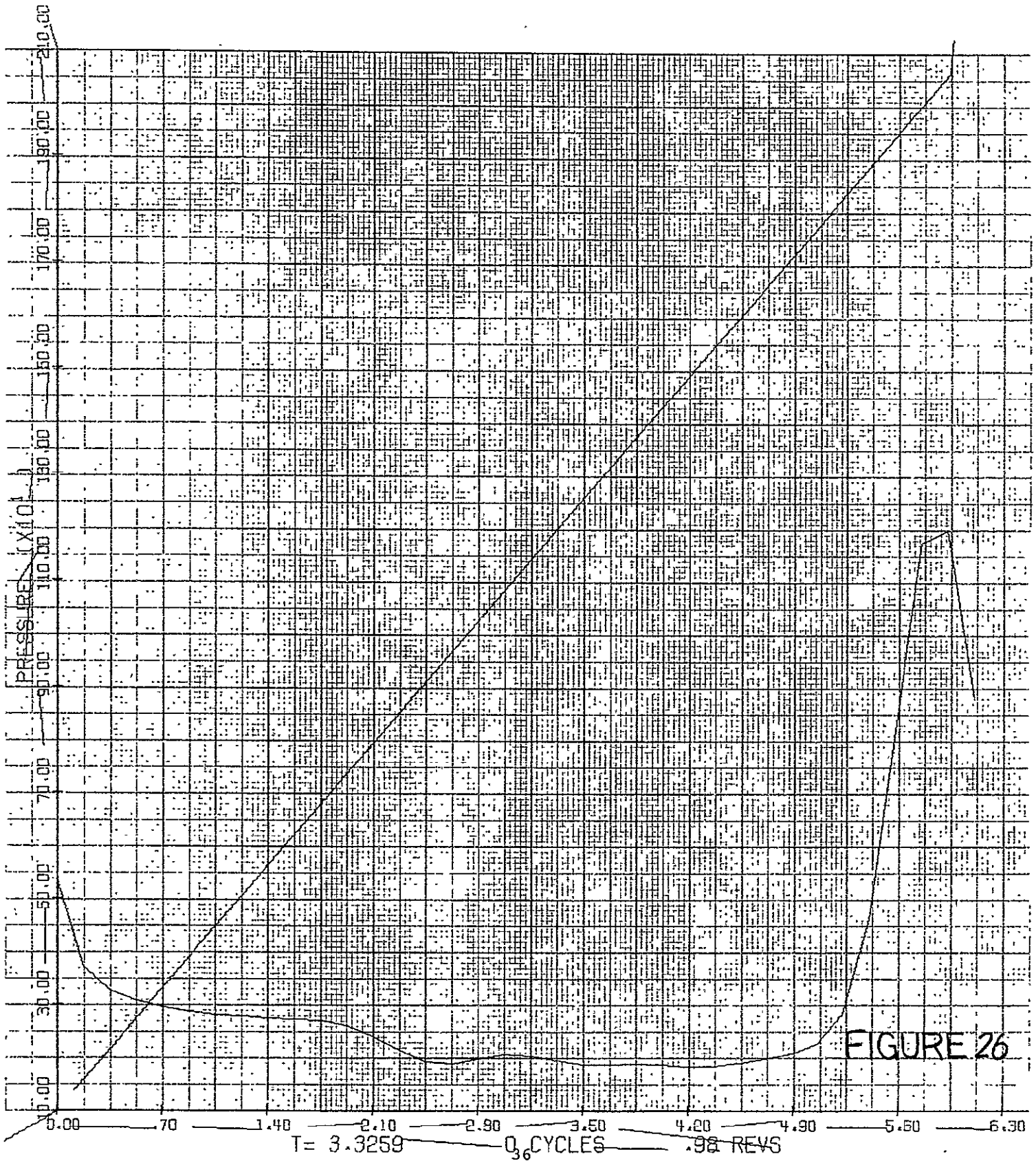
PRESSURE (X10 1)
210.00
190.00
170.00
150.00
130.00
110.00
90.00
70.00
50.00
30.00
0.00
0.00
.70
1.40
2.10
2.90
3.50
4.20
4.90
5.60
6.30
T= 3.3259
0 36 CYCLES
.98 REVS

FIGURE 26

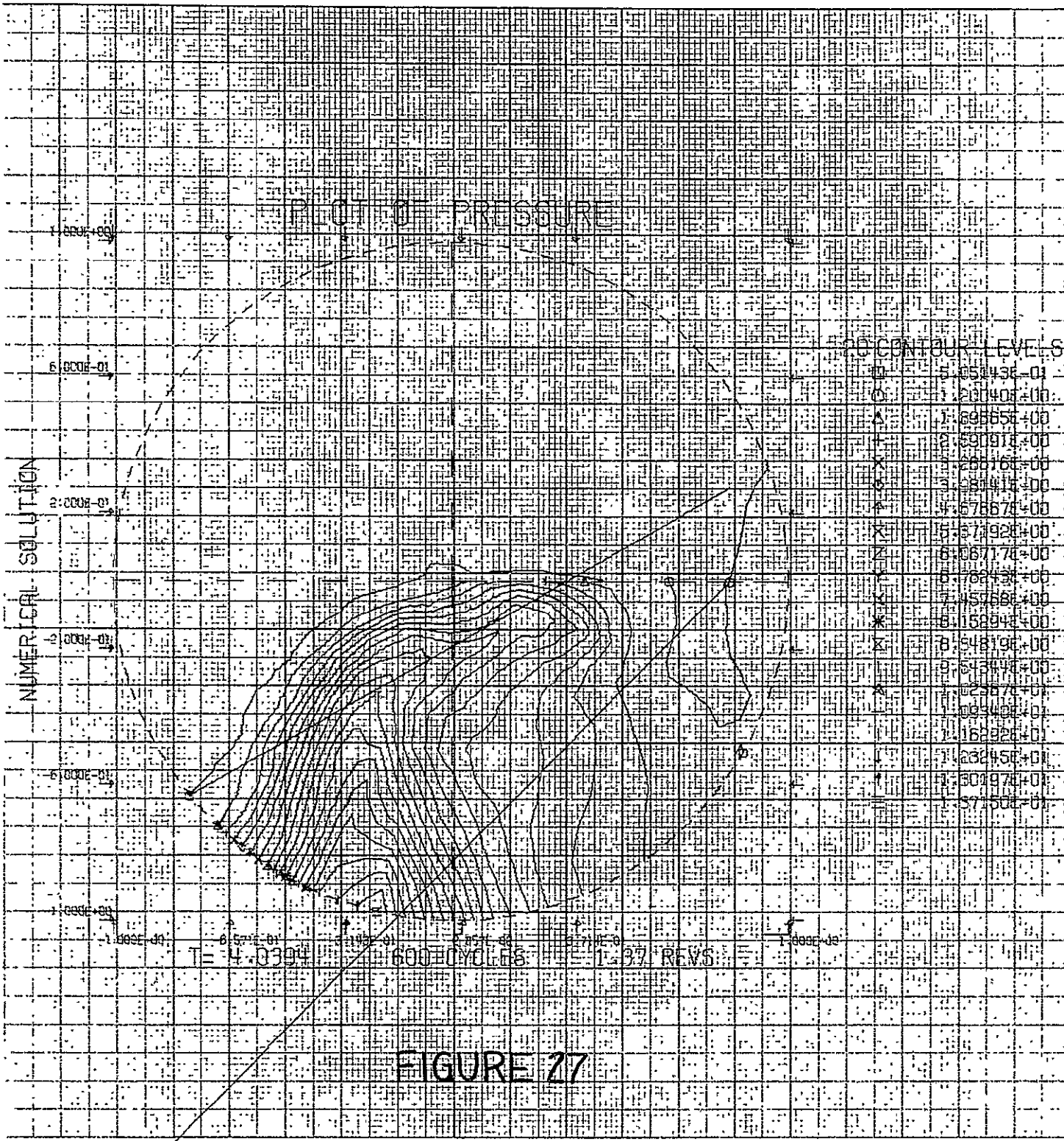
PLOT OF PRESSURE
NUMERICAL SOLUTION
20 CONTOUR LEVELS
T= 4.0394
600 CYCLES
1.37 REVS

FIGURE 27

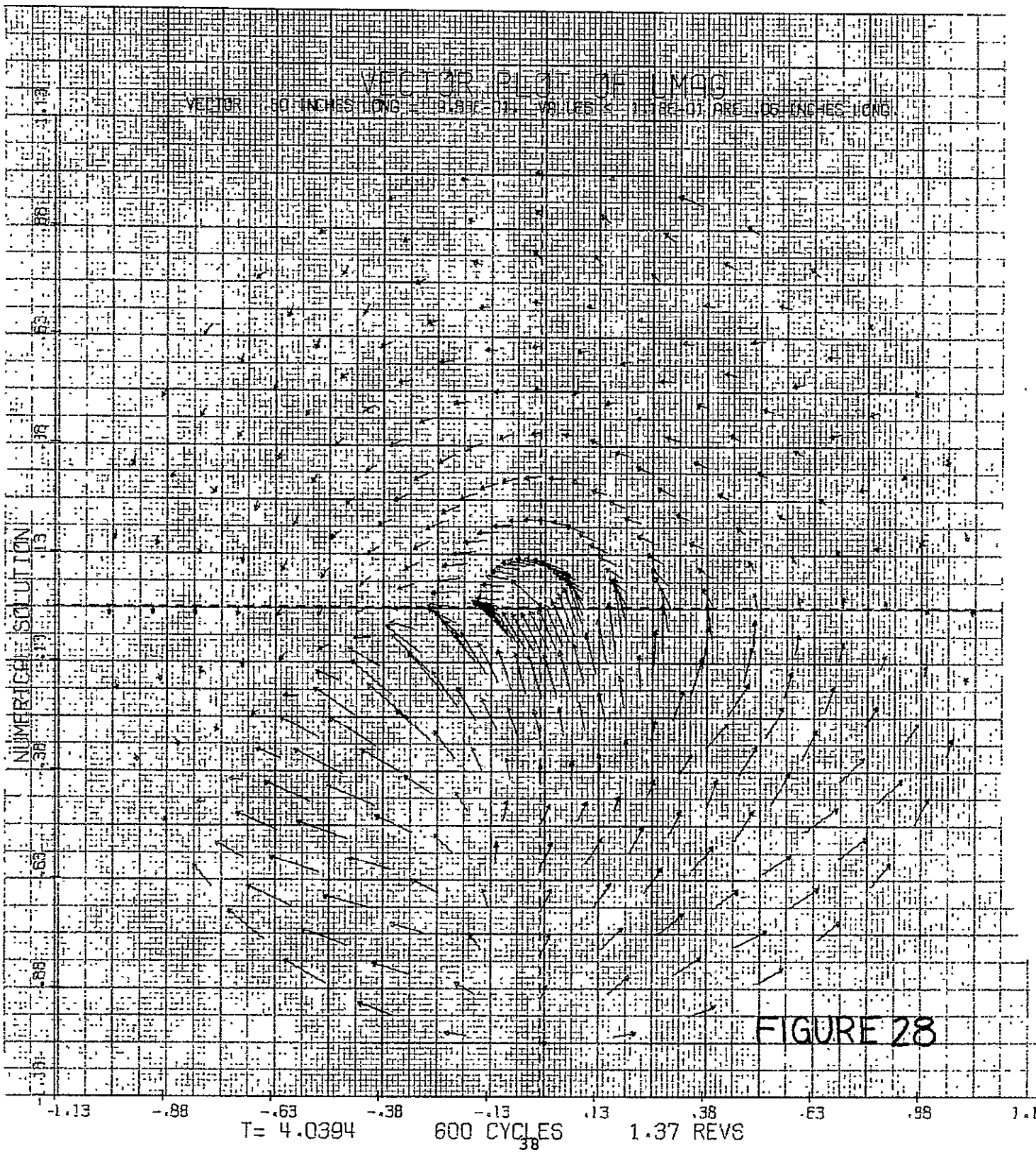
VECTOR PLOT OF UMOG
VECTOR = 80 INCHES LONG - BASE = 0; VALUES < 1.0E-07 ARE .06 INCHES LONG
NUMERICAL SOLUTION
-1.13
-.88
-.63
-.38
-.13
.13
.38
.63
.88
1.13
T= 4.0394
600 CYCLES
1.37 REVS

FIGURE 28

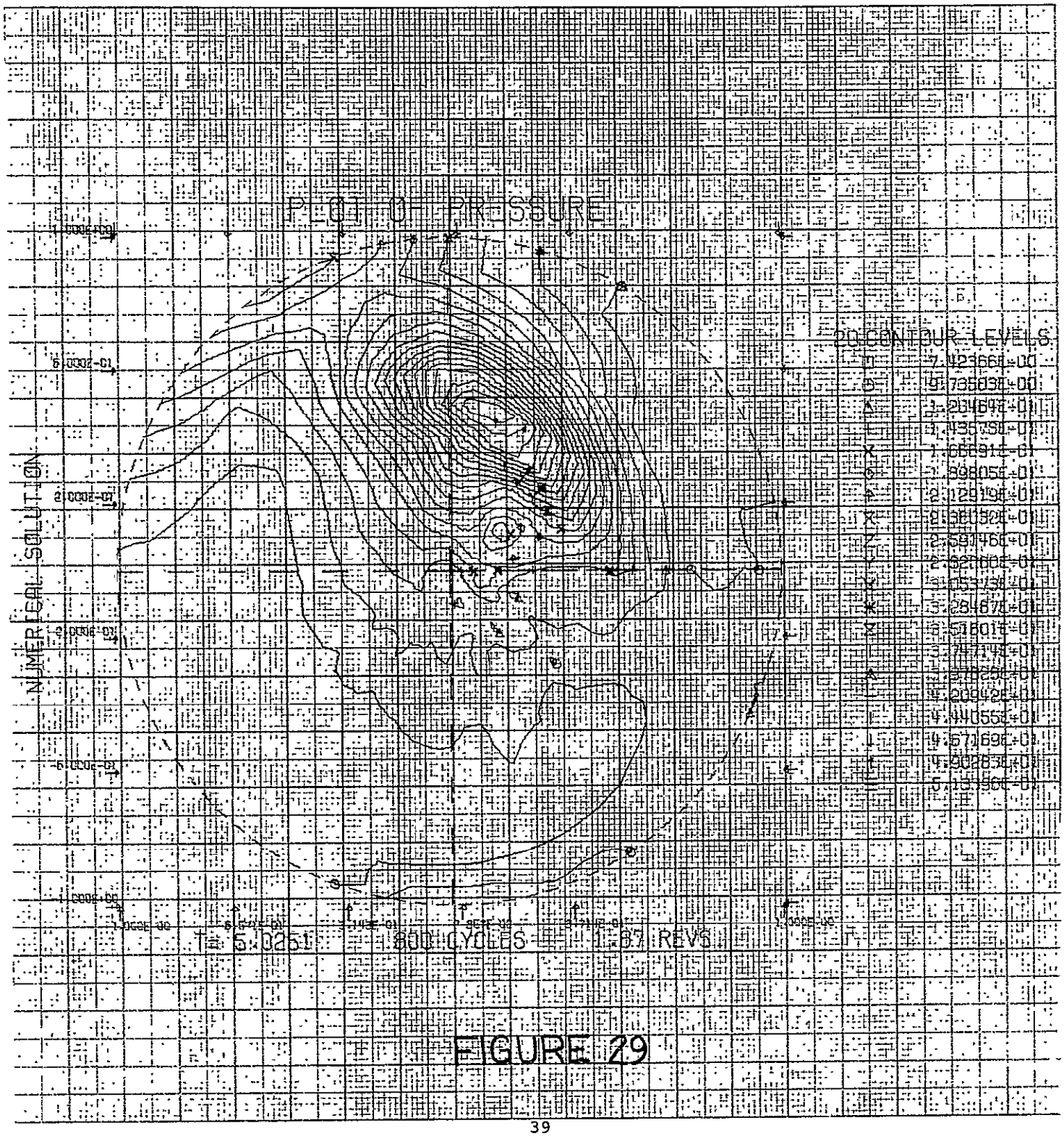
PLOT OF PRESSURE
NUMERICAL SOLUTION
20 CONTOUR LEVELS
MAXIMUM 7.423666E+00
MINIMUM 9.735035E+00
3.234694E+01
1.435758E+01
1.668914E+01
1.898054E+01
2.129198E+01
2.358152E+01
2.591466E+01
2.822606E+01
3.053738E+01
3.284878E+01
3.516015E+01
3.747149E+01
3.978286E+01
4.209425E+01
4.440552E+01
4.671696E+01
4.902836E+01
5.133966E+01
T = 5.0251 800 CYCLES 1.87 REVS

FIGURE 29

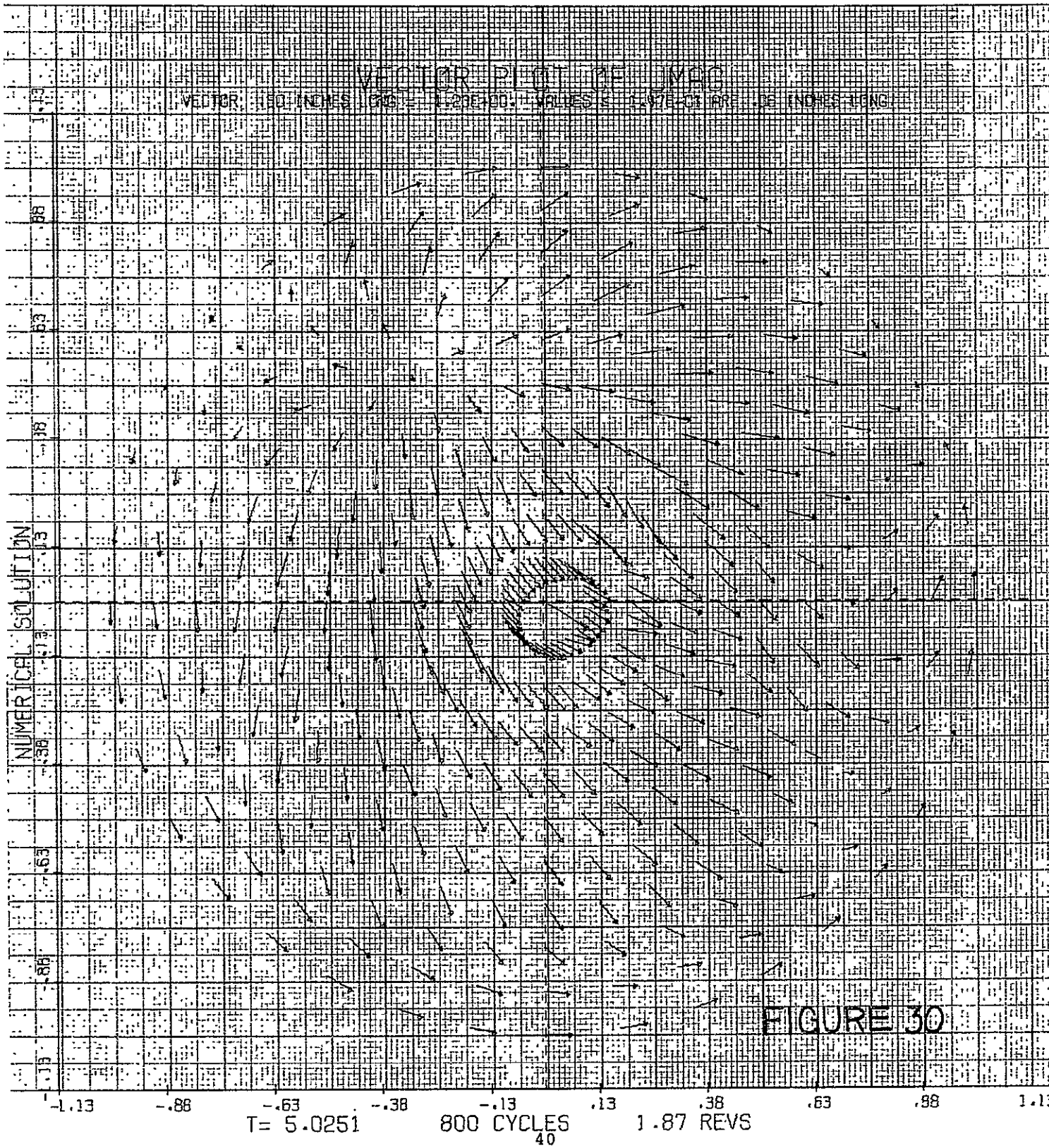
VECTOR PLOT OF MEG
VECTOR LEG INCHES (CM) = 1.20E+00. VALUES = 1.97E-01 PER .08 INCHES LONG
NUMERICAL SOLUTION
1.13
.88
.63
.38
.13
-.13
-.38
-.63
-.88
-1.13
-1.13
-.88
-.63
-.38
-.13
.13
.38
.63
.88
1.13
T= 5.0251
800 CYCLES
1.87 REVS

FIGURE 30

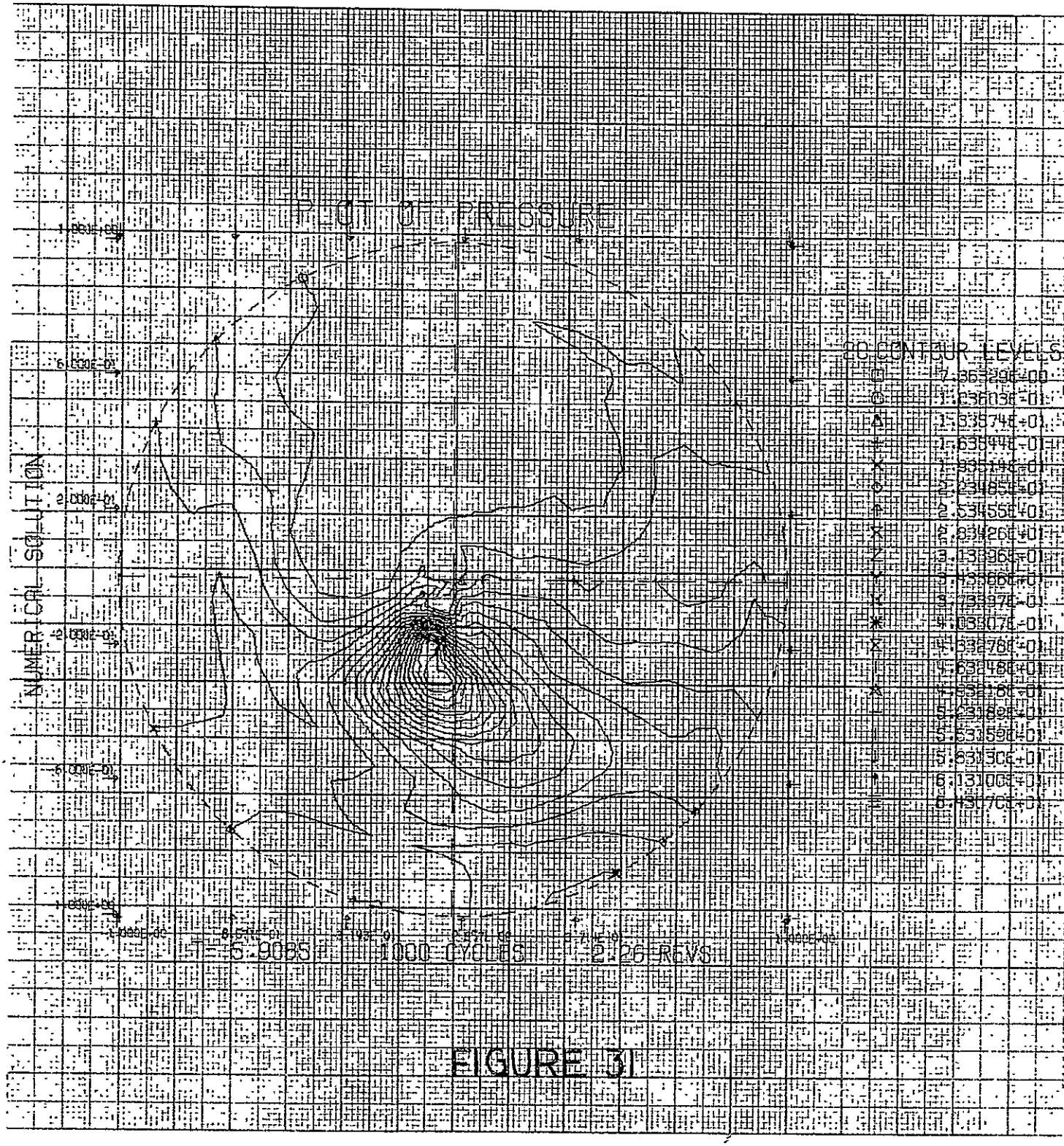
NUMERICAL SOLUTION
PLOT OF PRESSURE
20 CONTOUR LEVELS
7.363796E+00
1.236036E+01
1.335746E+01
1.635946E+01
1.935196E+01
2.234856E+01
2.534556E+01
2.834266E+01
3.133966E+01
3.433666E+01
3.733376E+01
4.033076E+01
4.332786E+01
4.632486E+01
4.932186E+01
5.231896E+01
5.531596E+01
5.831306E+01
6.131006E+01
6.430706E+01
T= 5.9085 1000 CYCLES 2.26 REVS

FIGURE 31

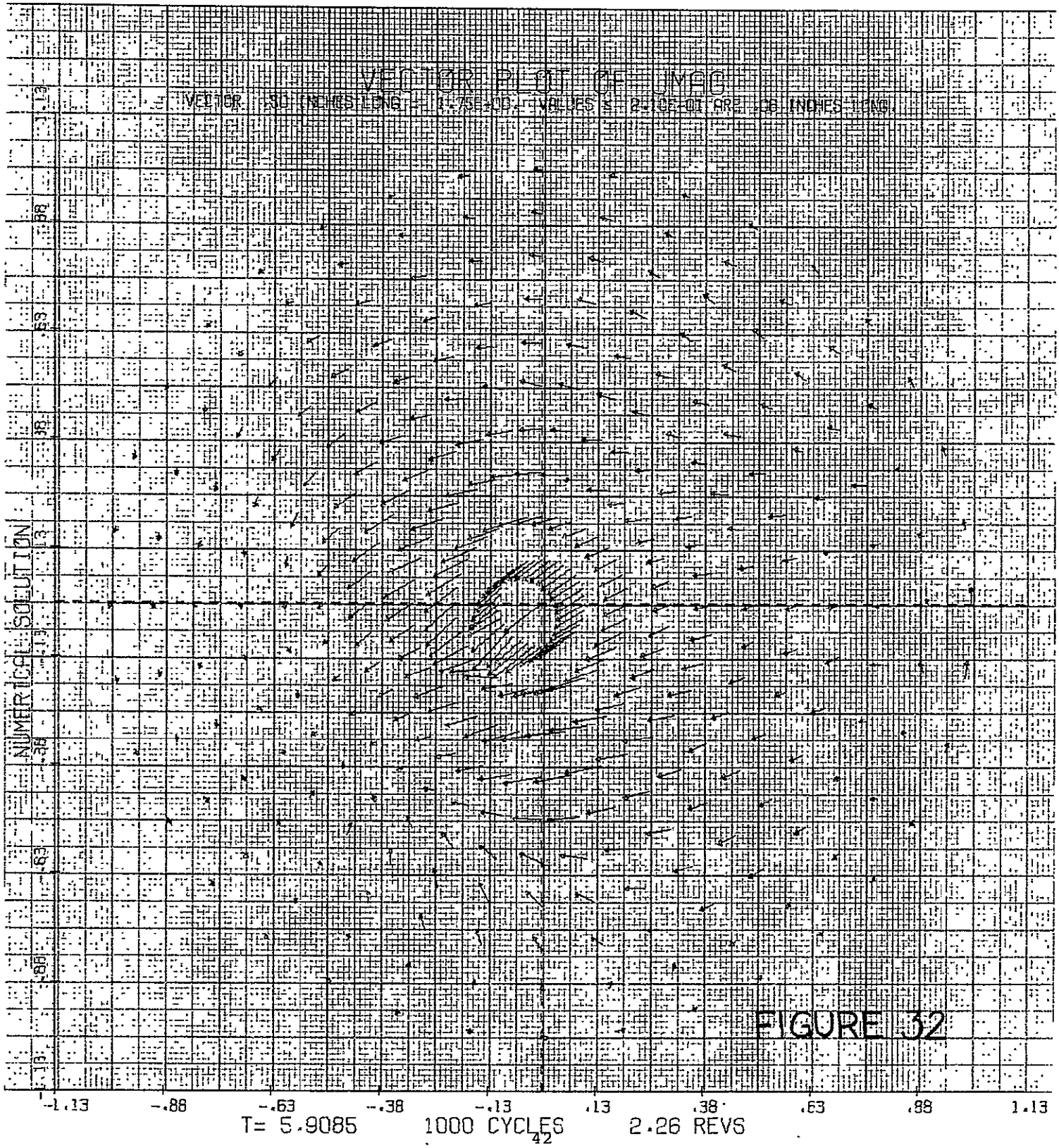
VECTOR PLOT OF VEC
VECTOR = 30 INCHES LONG = 0.75E+00 VALUES = 2.10E-01 ARE 30 INCHES LONG
NUMERICAL SOLUTION
-1.13
-.88
-.63
-.38
-.13
.13
.38
.63
.88
1.13
T= 5.9085 1000 CYCLES 2.26 REVS

FIGURE 32

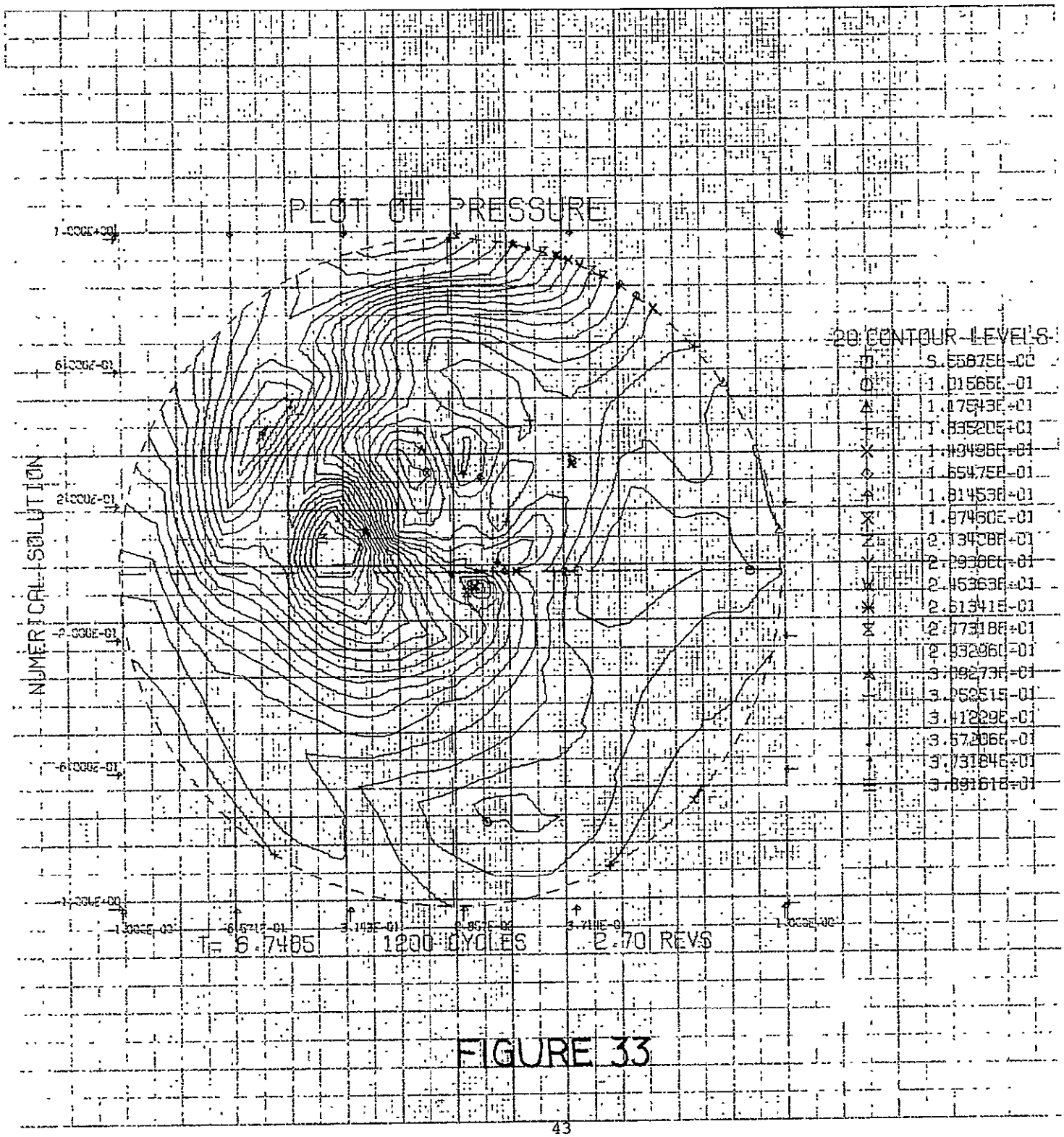
PLOT OF PRESSURE
NUMERICAL SOLUTION
20 CONTOUR LEVELS
T= 6.7485
1200 CYCLES
2.70 REVS

FIGURE 33

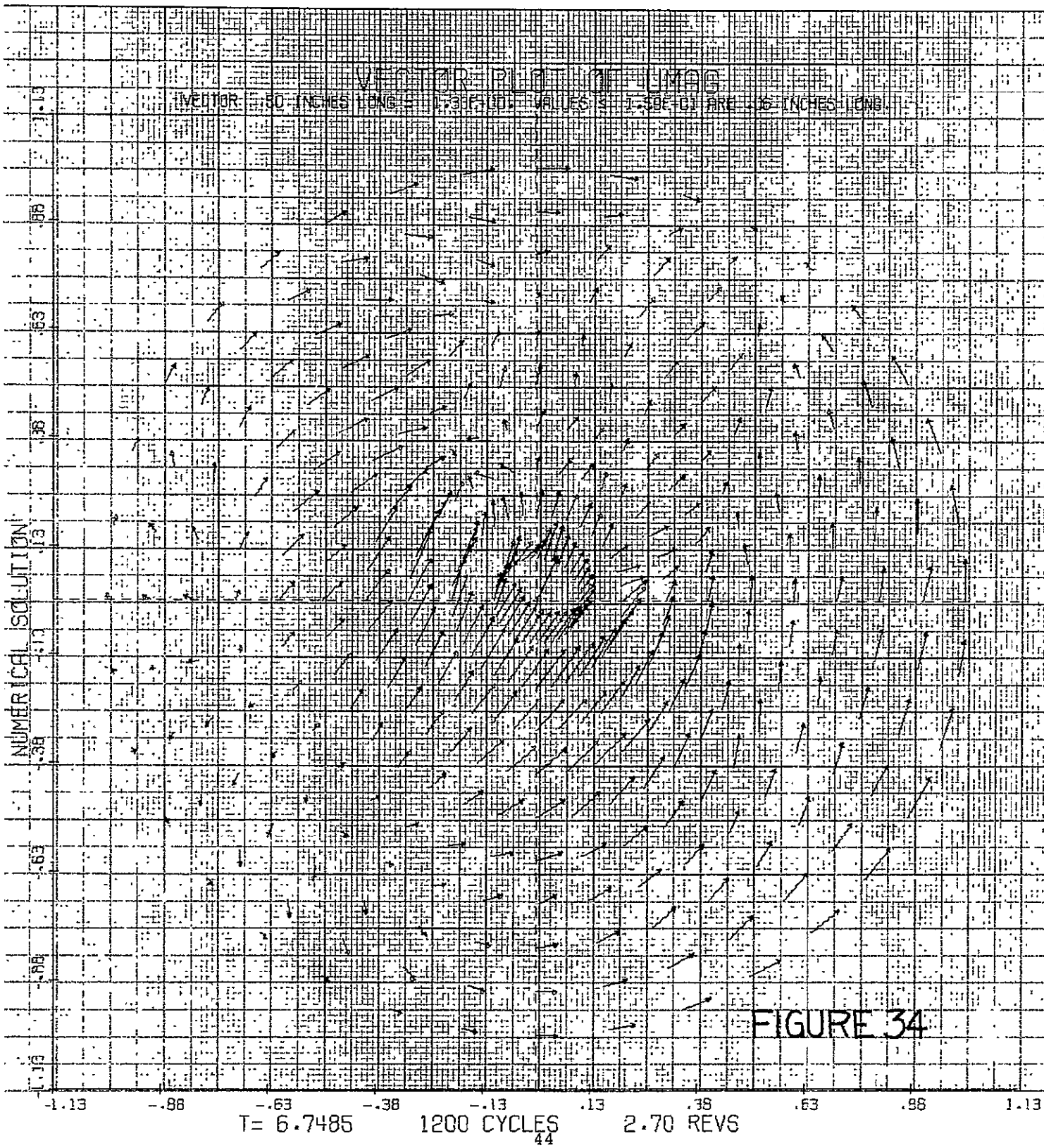
VECTOR PLOT
VECTOR 50 INCHES LONG = 1.30E+00 VALUES 1.50E-01 ARE 16 INCHES LONG
NUMERICAL SOLUTION
-1.13
-.88
-.63
-.38
-.13
.13
.38
.63
.88
1.13
T= 6.7485 1200 CYCLES 2.70 REVS

FIGURE 34

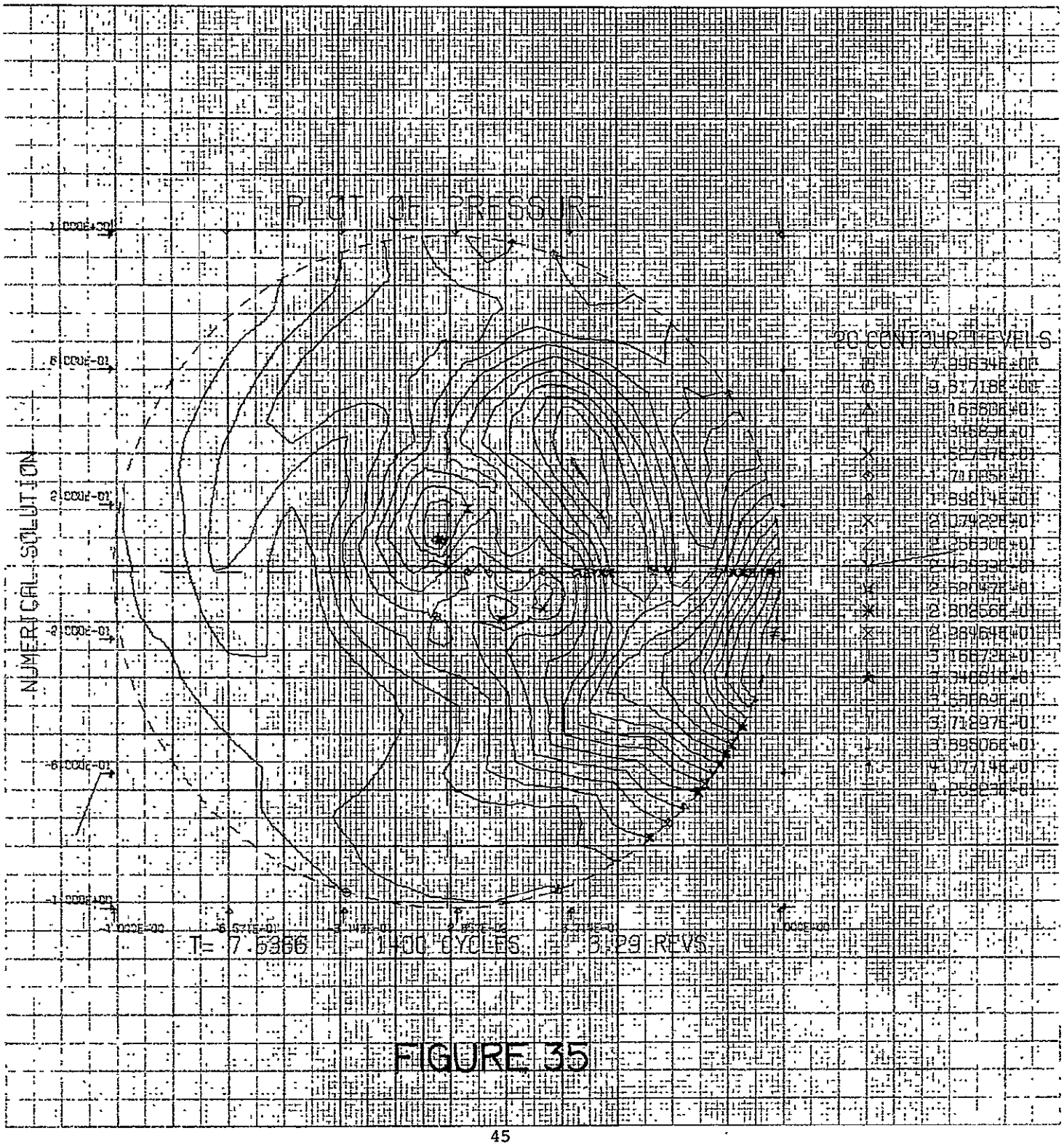
PLOT OF PRESSURE
NUMERICAL SOLUTION
20 CONTOUR LEVELS
T= 7.5366 1400 CYCLES 3.29 REVS

FIGURE 35

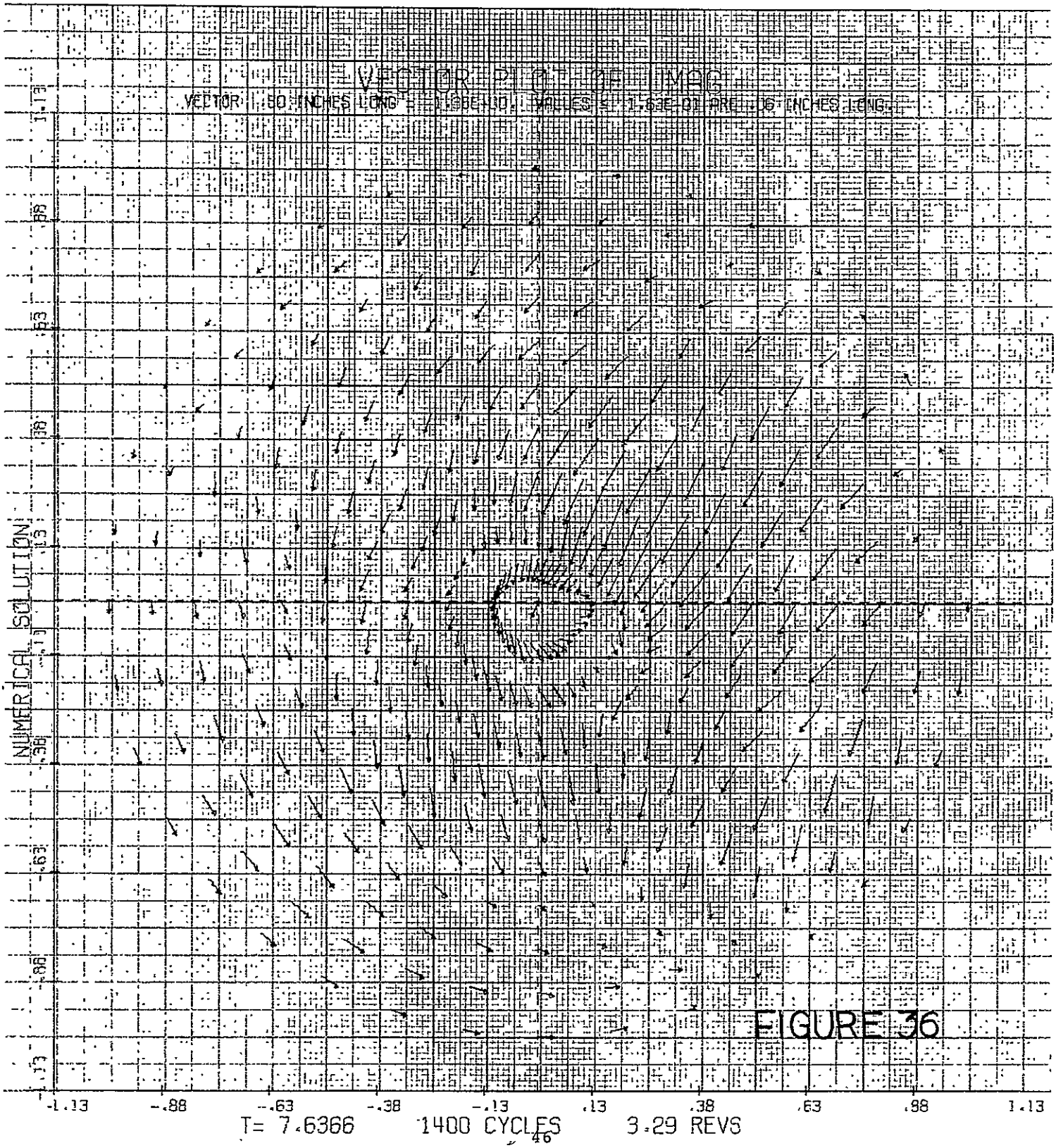
VECTOR PLOT OF MAG
VECTOR 50 INCHES LONG = 1.00E+00. VALUES > 1.63E-01 ARE 16 INCHES LONG
NUMERICAL SOLUTION
1.13
.88
.63
.38
.13
-.13
-.38
-.63
-.88
-1.13
-1.13
-.88
-.63
-.38
-.13
.13
.38
.63
.88
1.13
T= 7.6366 1400 CYCLES 3.29 REVS

FIGURE 36

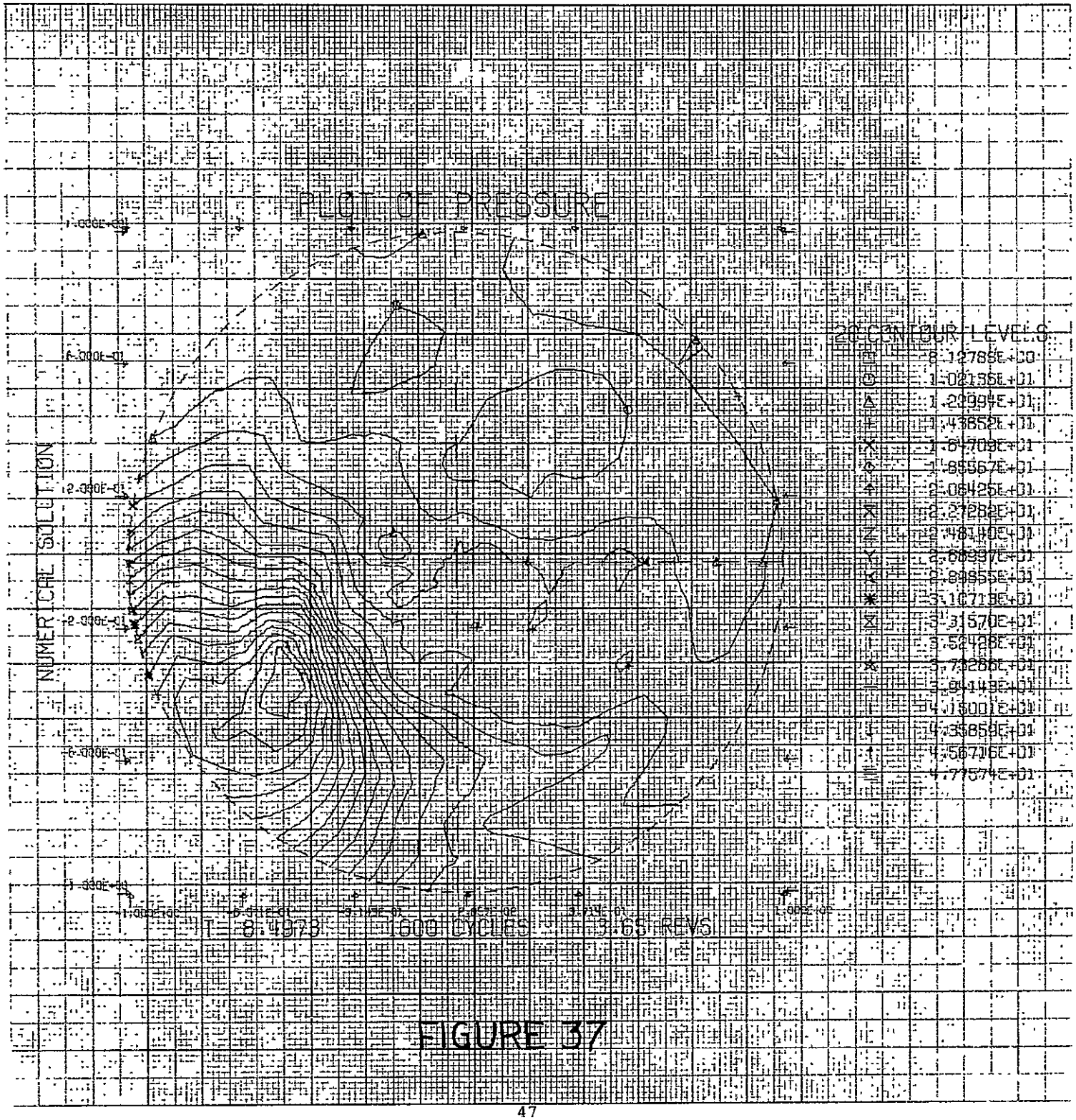
PLOT OF PRESSURE
NUMERICAL SOLUTION
20 CONTOUR LEVELS
T = 8.49378
600 CYCLES
3.65 REVS

FIGURE 37

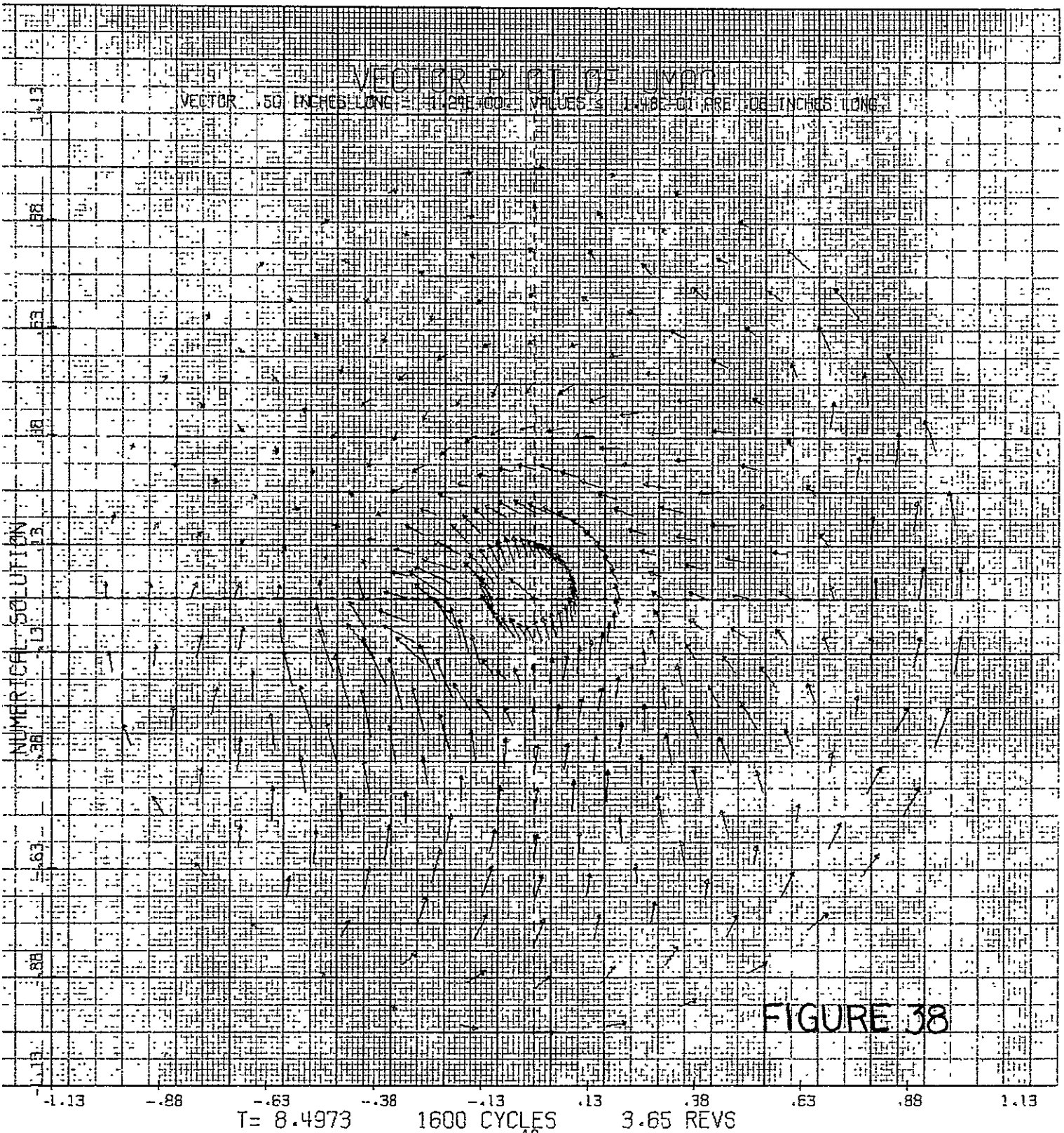
VECTOR PLOT OF JVEC
VECTOR = .50 INCHES LONG = 11.248 VALUES = 1.48E-01 ARE .06 INCHES LONG
NUMERICAL SOLUTION
1.13
.88
.63
.38
.13
-.13
-.38
-.63
-.88
-1.13
-1.13
-.88
-.63
-.38
-.13
.13
.38
.63
.88
1.13
T= 8.4973 1600 CYCLES 3.65 REVS

FIGURE 38

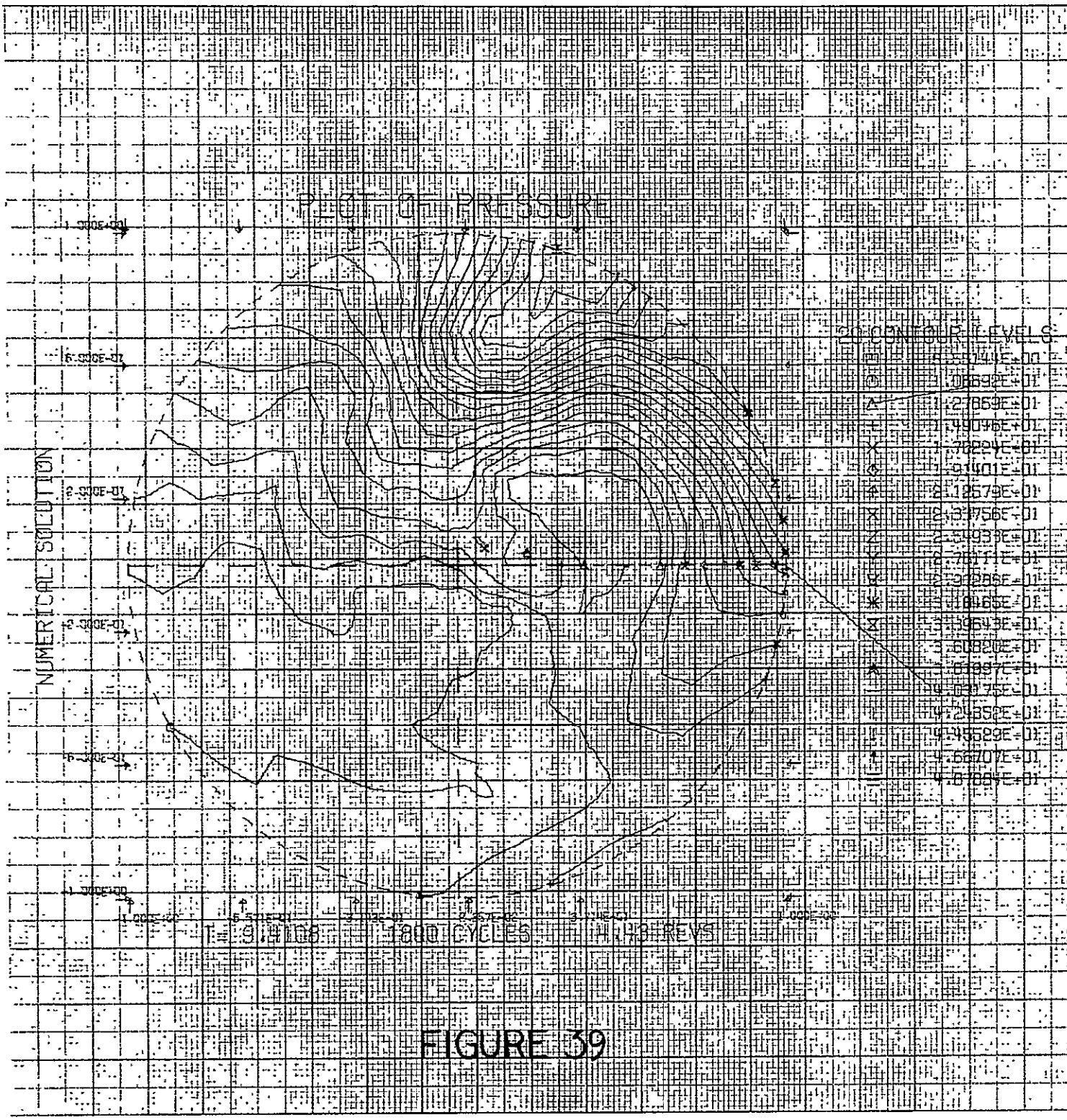

FIGURE 39

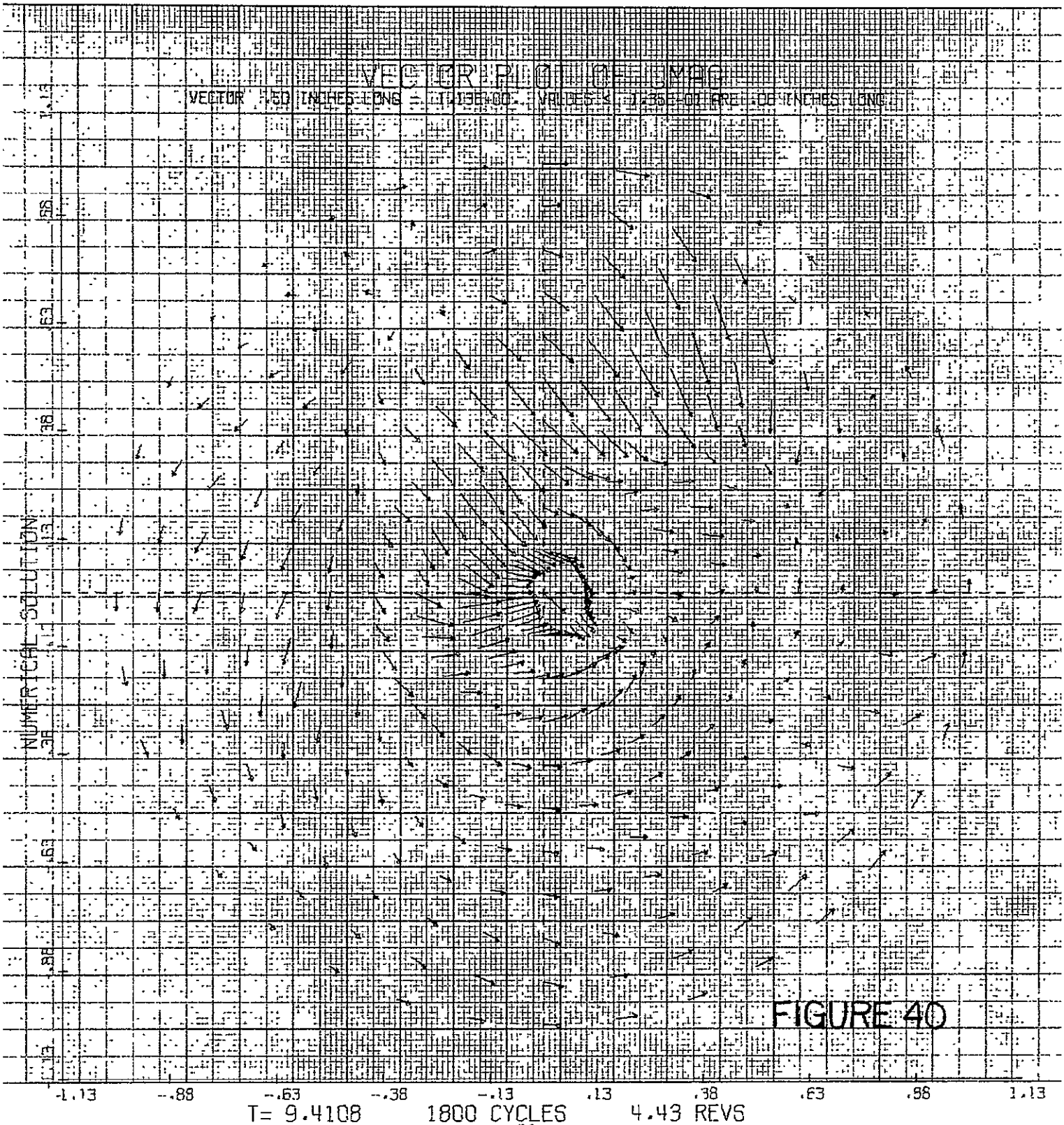
VECTOR PLOT OF UMAG
VECTOR .50 INCHES LONG = 1.1300 VALUES X 1.35-01 ARE .08 INCHES LONG
NUMERICAL SOLUTION
1.13
.88
.63
.38
.13
-1.13
-.88
-.63
-.38
-.13
.13
.38
.63
.88
1.13
T= 9.4108 1800 CYCLES 4.43 REVS

FIGURE 40

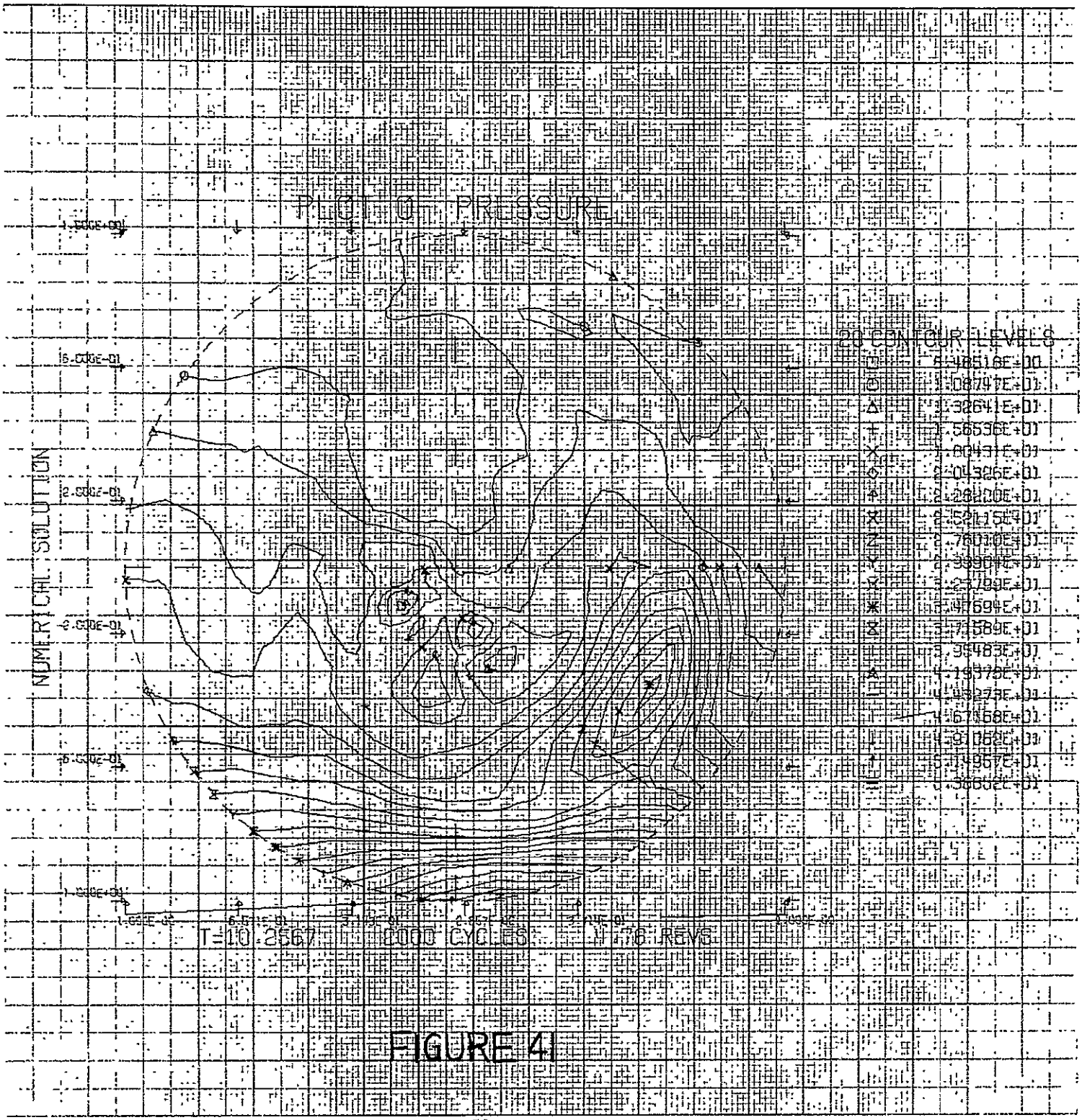
PLOT OF PRESSURE
NUMERICAL SOLUTION
20 CONTOUR LEVELS
T=10.2567 6000 CYCLES 76 REVS

FIGURE 41

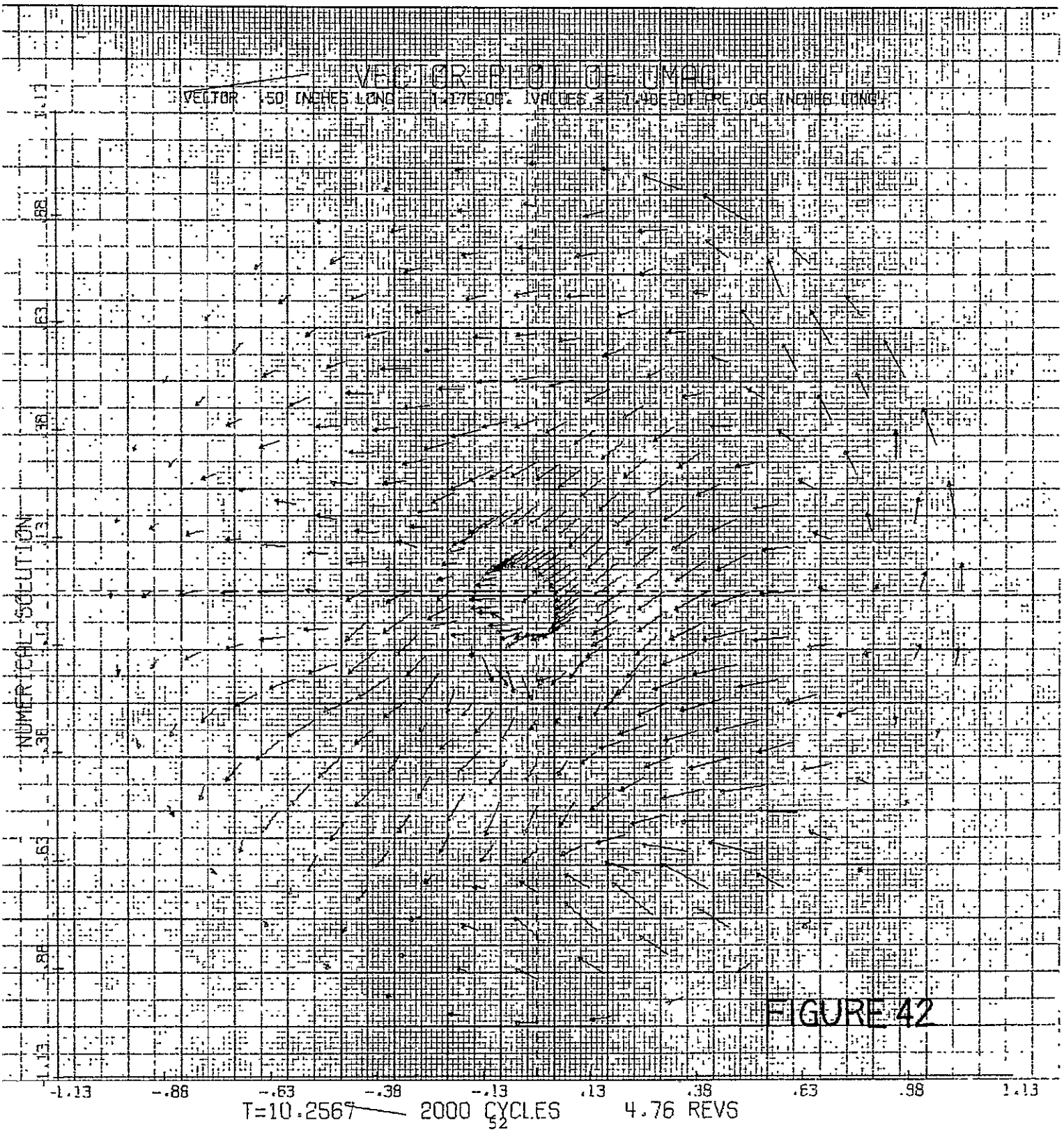
VECTOR PLOT OF UMPO
VECTOR .50 INCHES LONG = 1.17E-05. VALUES < 1.40E-06 ARE TOO SMALL TO BE SHOWN.
NUMERICAL SOLUTION
1.13
.88
.63
.38
.13
-.13
-.38
-.63
-.88
-1.13
-1.13
-.88
-.63
-.38
-.13
.13
.38
.63
.88
1.13
T=10.2567 2000 CYCLES 4.76 REVS

FIGURE 42

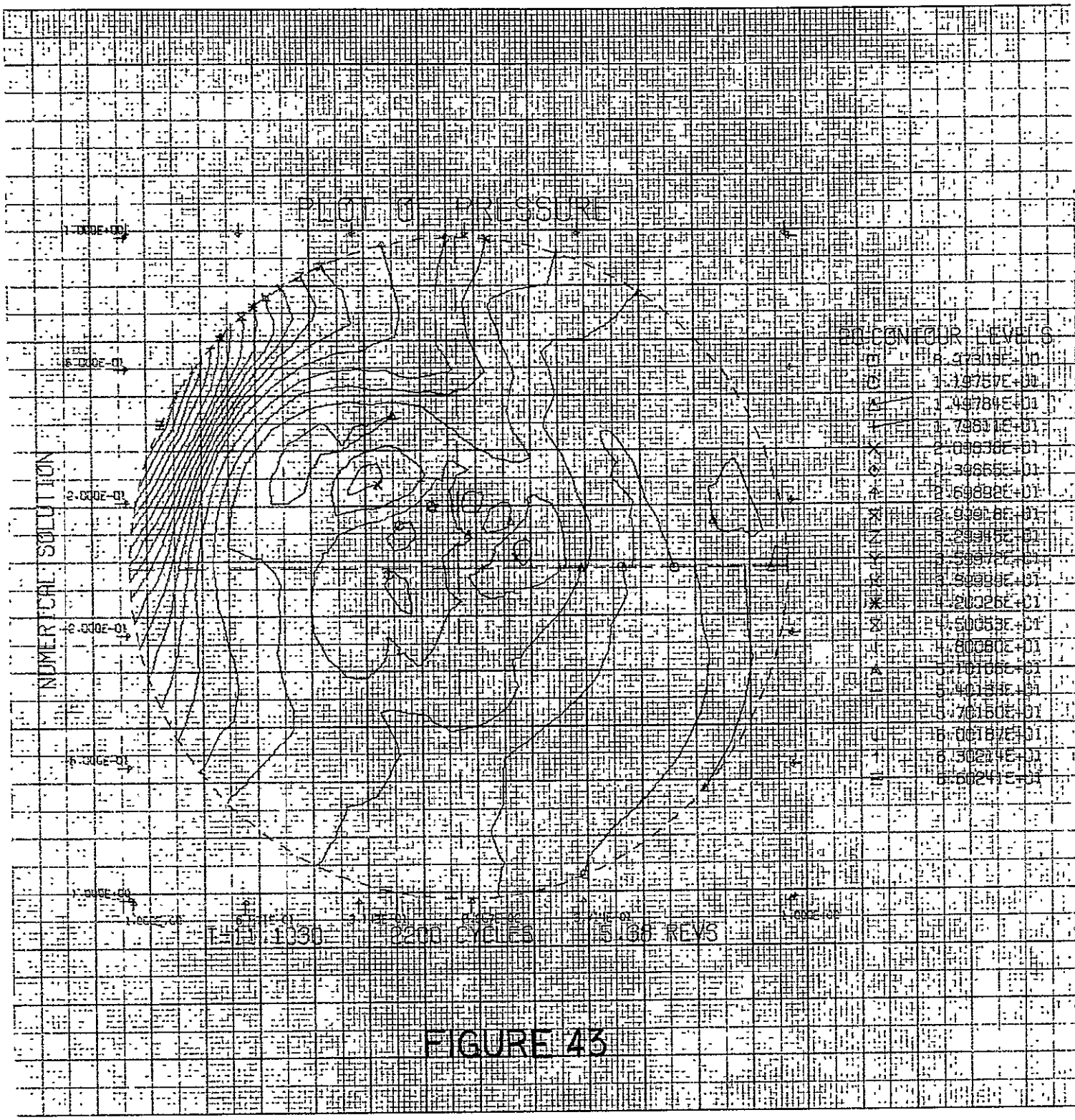
PLOT OF PRESSURE
NUMERICAL SOLUTION
60 CONTOUR LEVELS
T = 1030 2200 CYCLES 5.68 REVS

FIGURE 43

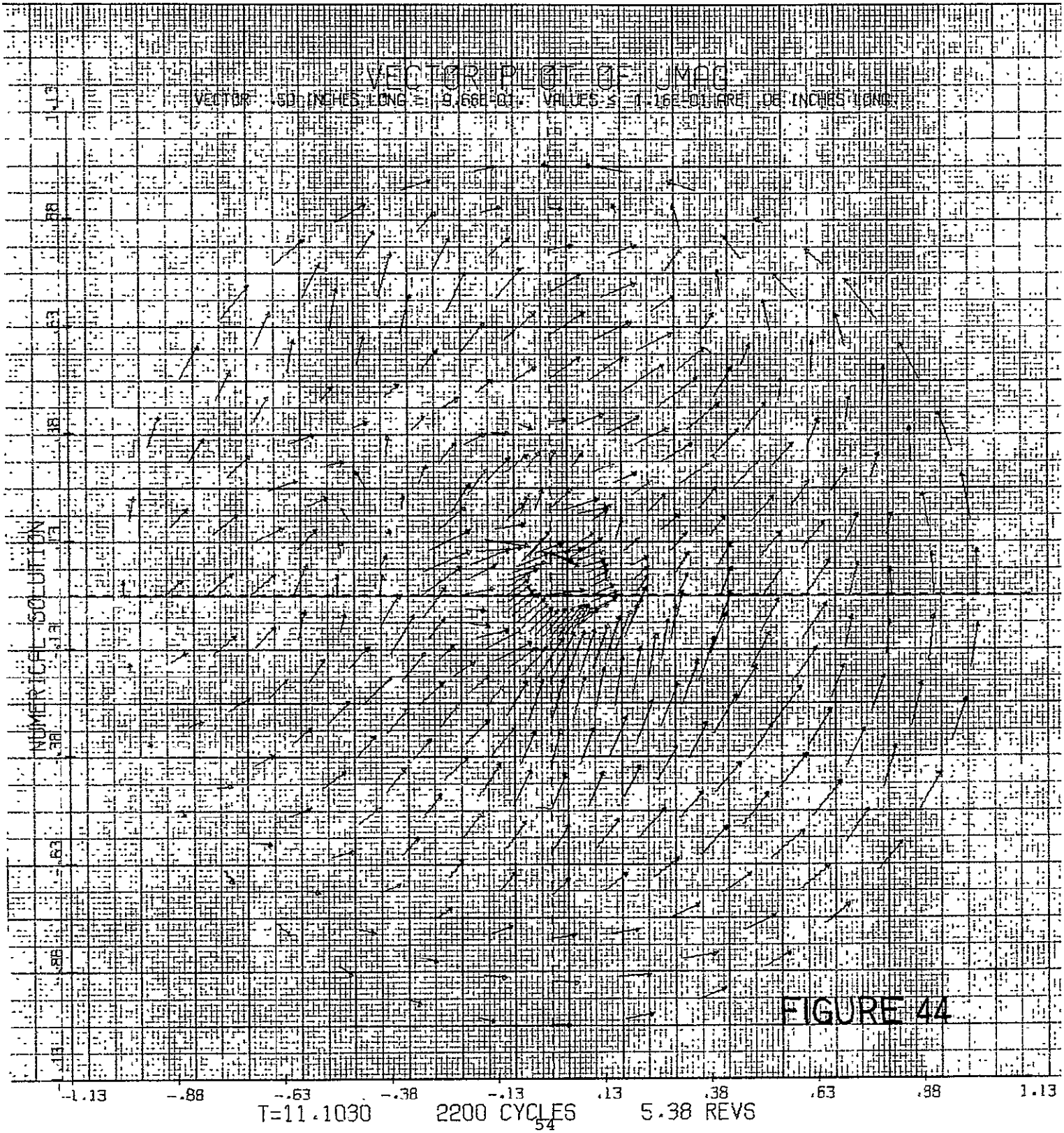
VECTOR PLOT OF UMAG
VECTOR = .50 INCHES LONG = 9.668E-01 VALUES = 1.16E-01 ARE .06 INCHES LONG
NUMERICAL SOLUTION
1.13
.88
.63
.38
.13
-1.13
-.88
-.63
-.38
-.13
.13
.38
.63
.88
1.13
T=11.1030 2200 CYCLES 5.38 REVS

FIGURE 44

E. Program COMB Status

As is shown by figure 26, we have incorporated the ability to selectively plot the tangential pressure distribution at any value of radius and at any time. This feature adds flexibility to the program for ease in interpretation of the computed results.

It is anticipated that the final report will contain some instantaneous streakline pictures of 'particles' moving in the r-θ plane. The resultant motion is shown plotted as separate pictures after, say, one complete rotation of the wave. It is hoped that correlations can be made with these computed results and photographic techniques to be attempted by the JPL rocket combustion group.

The toroidal motor model is almost debugged. Tests are now being run to establish a steady state flow in the θ-z direction with given arbitrary initial data. A simple approach has been taken so as to simulate a converging diverging nozzle. That it is necessary to incorporate a supersonic boundary condition at the outflow plane of this toroidal geometry is evident. For a liquid propellant motor the only other required boundary condition is that the normal component of velocity shall vanish on the injector face. Plotting routines have been written which will be used to see isobars and vector fields in this geometry. Some preliminary results have been obtained at this time but are too incomplete in nature to present.

II. Droplet Evaporation and Combustion Analyses*

A. The Rate of the N_2H_4/N_2O_4 Reaction

It will be recalled that in order to utilize the modified flame surface analysis of Peskin and Wise (Ref. 1), some estimate is required of the overall (i.e., 'global') reaction rate constant for the N_2H_4/N_2O_4 reaction (Ref. 2). That is, assuming the reaction proceeds according to

$$N_2H_4 + NO_2 \xrightarrow{k_f} \frac{3}{2}N_2 + 2H_2O \qquad (1)$$

some estimate of k_f is required. (NO_2 is considered the oxidant rather than N_2O_4 as a result of the high level of dissociation of the latter under most engine operating conditions.)

This estimate can be obtained from the streamtube analysis developed in Ref. 2, wherein the relevant equations and assumptions are detailed. For reference purposes, the streamtube equations are summarized here as well:

Energy Conservation

$$\frac{dh}{dt} = 0\,,\ h = \text{constant} \qquad (2)$$

Species Conservation

$$\frac{dY_i}{dt} = \frac{r_i}{\rho} \qquad (3)$$

Equation of State

$$\rho = \frac{pM}{RT} \qquad (4)$$

* Figures in this section again start with the number 1.

Auxiliary Equations

$$h = \sum_i Y_i h_i \tag{5}$$

$$M = \left(\sum_i \frac{Y_i}{M_i} \right)^{-1} \tag{6}$$

$$h_i = \Delta_i + \bar{c}_{p_i} (T - T_{REF}) \tag{7}$$

where h_i = enthalpy (sensible plus chemical) of species i

r_i = rate of appearance (or disappearance) of species i

Y_i = mass fraction of species i

M_i = molecular weight of species i

ρ = mass density of the gas mixture

p = pressure of the mixture

T = temperature of the mixture

Δ_i = reference enthalpy of species i

$\bar{c}_{p_i}$ = average specific heat of species i

T_{REF} = reference temperature (1000°K)

t = time

Preliminary results were shown in Ref. 2. More complete results are presented in figure 1. Defining the ignition delay time (t_{ID}) qualitatively as the time required for the principal oxidation reactions to occur, figure 1 yields the anticipated result that t_{ID} is a strong function of the initial mixture temperature. On the other hand, these results indicate that in the range examined, t_{ID} is nearly independent of the pressure. As can be seen, at the higher pressures, the second-order reactions (which become more significant at higher pressures) produce an initial partial oxidation which results in a slight temperature increase. However, a leveling-off period is seen to subsequently

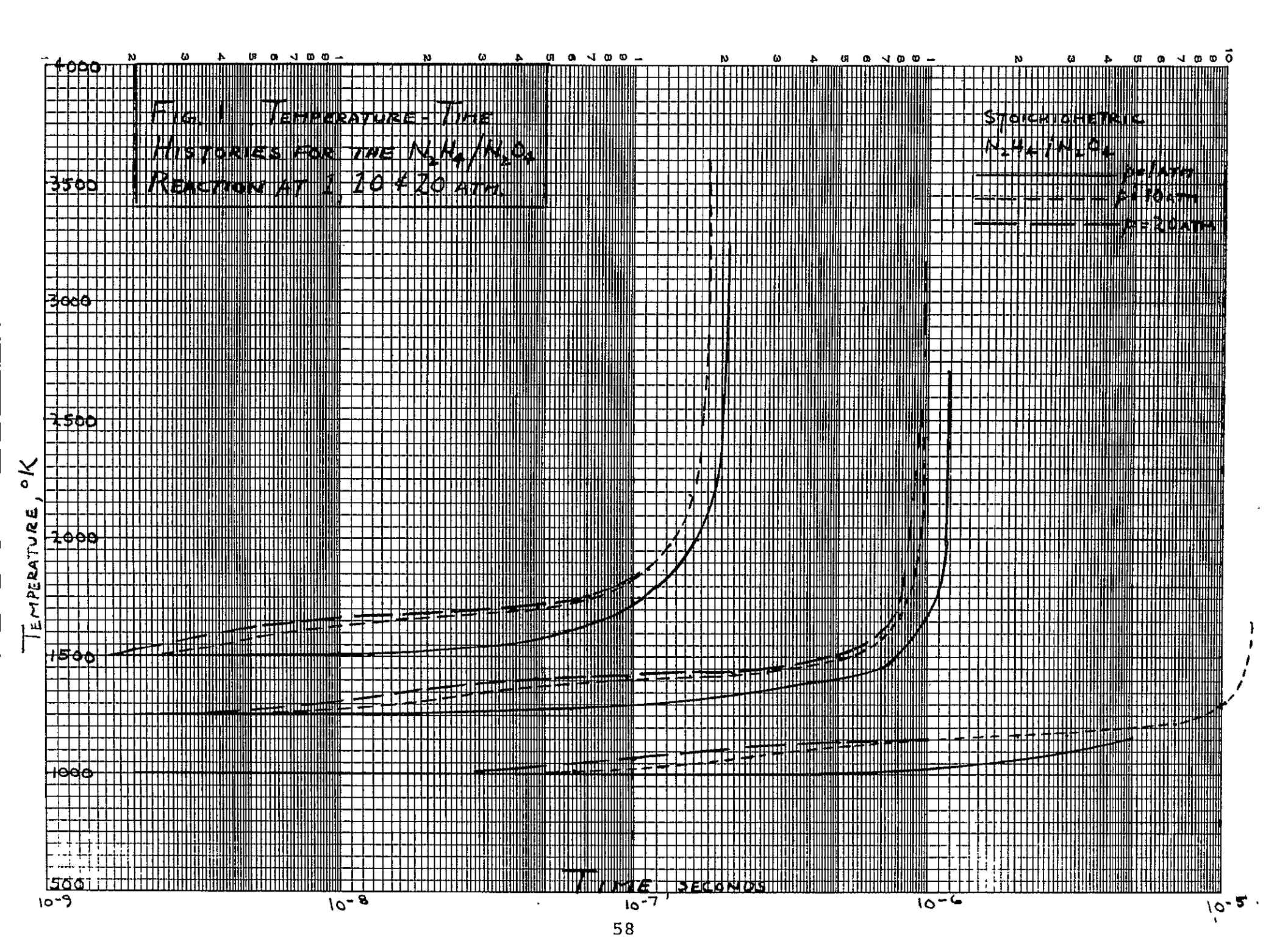
FIG. 1 TEMPERATURE - TIME HISTORIES FOR THE N_2H_4/N_2O_4 REACTION AT 1, 10 & 20 ATM.
STOICHIOMETRIC N_2H_4 - N_2O_4
P = 1 ATM
P = 10 ATM
P = 20 ATM
TEMPERATURE, °K
4000
3500
3000
2500
2000
1500
1000
500
TIME, SECONDS
10^{-9}
10^{-8}
10^{-7}
10^{-6}
10^{-5}

occur, followed by the principal, first-order oxidation processes which drive the reaction to completion.

As a result, the reaction may be said to be first-order, with ignition delay times (taken from figure 1) as shown in figure 2. In this latter figure, T_i is the initial mixture temperature. The approximate straight line behavior of ln t_{ID} when plotted against reciprocal initial temperature is in accordance with elementary chemical kinetic thoery which predicts a function of the form

$$t_{ID} = \alpha \cdot \exp\ (E/RT_i) \qquad (8)$$

where α is a constant and E is an overall activation energy. From figure 2, E was determined to be about 26,800 calories/mole.

As an initial estimate, the pre-exponential factor in the overall reaction rate constant was chosen to be the average of the pre-exponential factors for the N_2H_4 oxidation reactions as deduced by Sawyer (see Ref. 2, Table I). From this and the result obtained above, the initial estimate of the overall reaction rate constant was

$$k_f = 1.2 \times 10^{10}\ \exp\ (-26{,}800/RT) \qquad (9)$$

To check this estimate, results using eq. 9 were checked against results obtained using the complete streamtube analysis. The comparison was made at high pressure (20 atm), where the first-order approximation and eq. 9 would be least accurate. The results are shown in figure 3, with the streamtube result labeled 'exact'. The global model does not, of course, predict the initial reactions or the leveling off period after the initial second-order

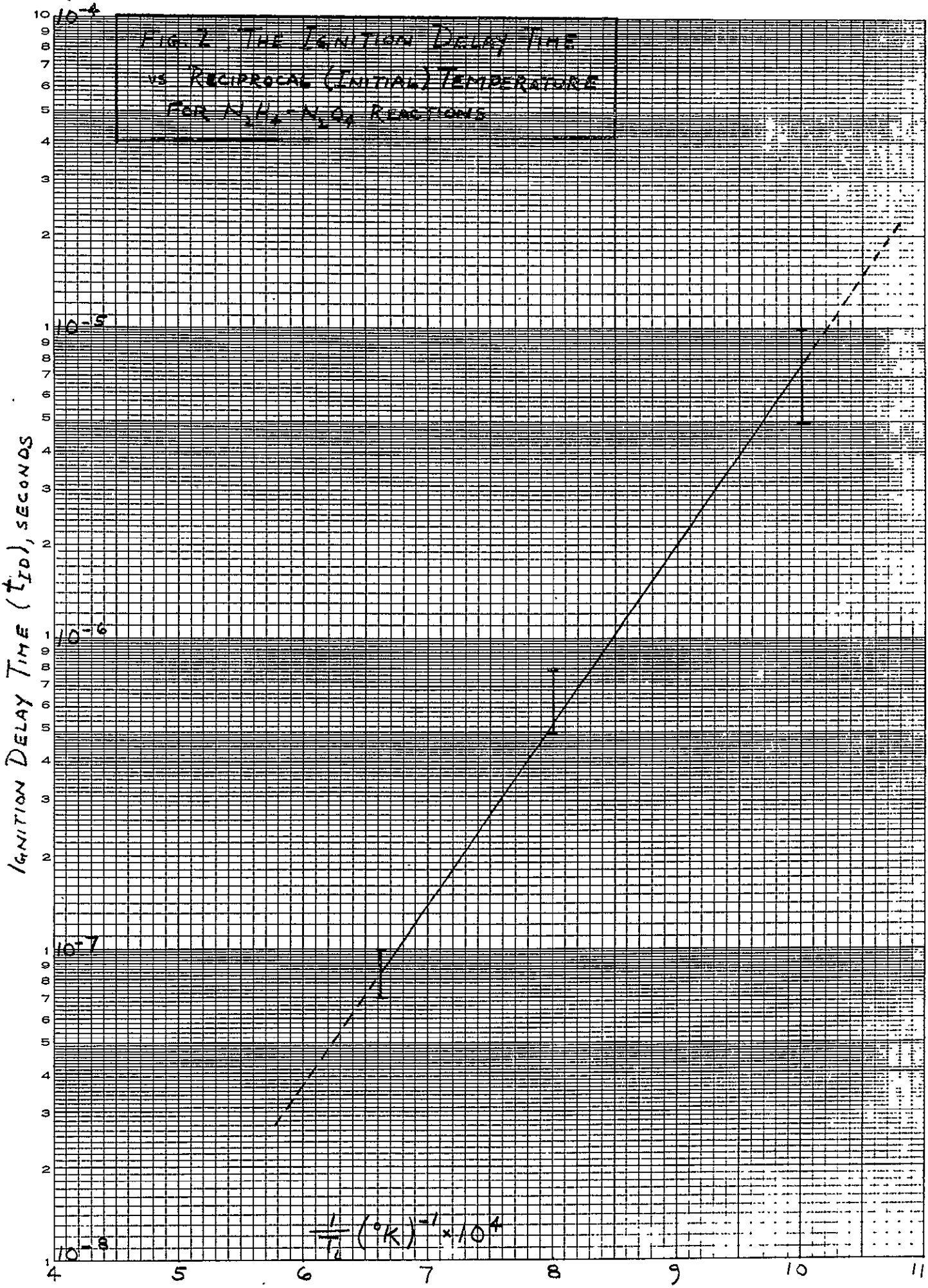
FIG. 2 THE IGNITION DELAY TIME VS RECIPROCAL (INITIAL) TEMPERATURE FOR N_2H_4-N_2O_4 REACTIONS
IGNITION DELAY TIME (t_{ID}), SECONDS
10^{-4}
10^{-5}
10^{-6}
10^{-7}
10^{-8}
$\frac{1}{T_i}(°K)^{-1} \times 10^4$
4
5
6
7
8
9
10
11

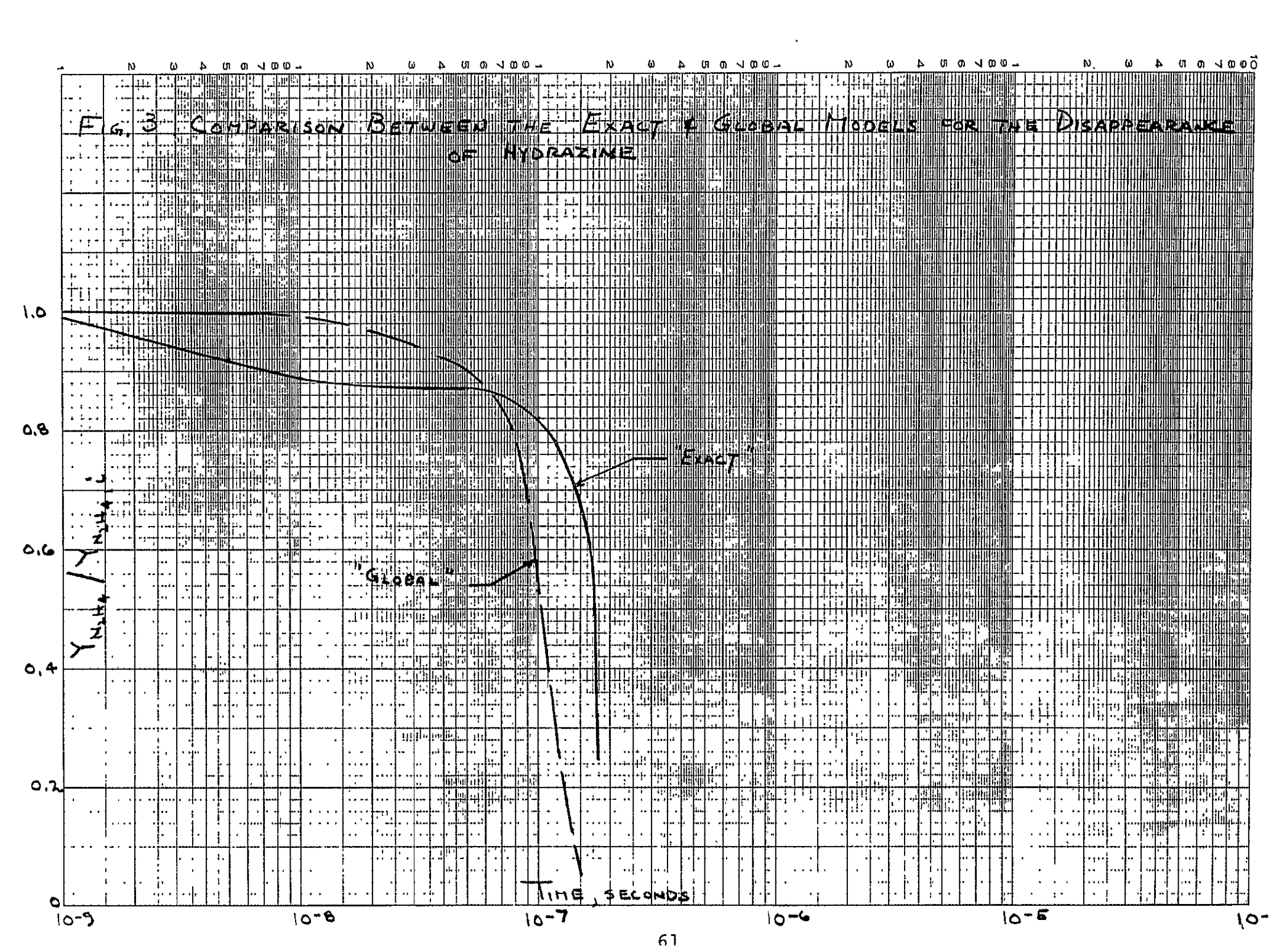
FIG. 3 COMPARISON BETWEEN THE EXACT & GLOBAL MODELS FOR THE DISAPPEARANCE OF HYDRAZINE
$Y_{N_2H_4} / Y_{N_2H_4}^{\circ}$
1.0
0.8
0.6
0.4
0.2
0
"EXACT"
"GLOBAL"
TIME, SECONDS
10^{-9}
10^{-8}
10^{-7}
10^{-6}
10^{-5}

reactions have occurred, but the general behavior and the delay time appears to be reasonable. Although the result for this particular case could have been improved by adjustment of the pre-exponential factor in eq. 9, this was felt to be unwarranted, and eq. 9 was selected as a suitably accurate overall reaction rate constant for inclusion in the modified flame surface analysis.

B. The Modified Flame Surface Analysis

Under the assumptions inherent in the modified flame surface analysis, as detailed in Refs. 2 and 3, the species conservation and energy equations were shown to reduce to

$$a\frac{dY_i}{d\eta} - \frac{d}{d\eta}\left(\eta^2 \frac{dY_i}{d\eta}\right) = - i_i \eta^2 b Y_F^{N_F} Y_o^{N_O} \tag{10}$$

$$a\frac{dt}{d\eta} - \frac{d}{d\eta}\left(\eta 2 \frac{dt}{d\eta}\right) = \eta^2 b Y_F^{N_F} Y_O^{N_O} \tag{11}$$

where a = dimensionless mass burning rate = $\dot{m}_F^o/(4\pi r_D k/c_p)$

$\dot{m}_F^o$ = mass burning rate in stagnant surrounding

r_D = fuel droplet radius

k = thermal conductivity

η = r/r_D

i_i = $\nu_i M_i/\nu_F M_F$

ν_i = stoichiometric coefficient of species i

N_F, N_O = reaction orders with respect to fuel and oxidizer

b = $k_f r_D^2/D$

D = binary diffusion coefficient

t = $(T-T_\infty)/(Q/c_p)$

Q = heat of reaction

T_∞ = temperature in the ambient gas mixture

On the basis of the conclusions drawn in the previous section, $N_O = 0$ and k_f is given by eq. 9. When eq. 10 is written first for the fuel and then for the oxidizer, and the resulting equations subtracted, an integrable ordinary differential equation results

subject to the following boundary conditions:

$$\left.\frac{d}{d\eta} Y_O\right]_{\eta=1} = a\, Y_O\Big]_{\eta=1}$$

$$\left.\frac{d}{d\eta} Y_F\right]_{\eta=1} = a\, Y_F\Big]_{\eta=1} - a$$

$$Y_F\Big]_{\eta\to\infty} = 0$$

When eq. 10 written for the fuel is added to eq. 11, another integrable ordinary differential equation results subject to these boundary conditions:

$$\left.\frac{dt}{d\eta}\right]_{\eta=1} = \frac{L}{Q}\, a$$

$$t\Big]_{\eta\to\infty} = 0$$

The resulting equations can be manipulated to yield the following expression for the dimensionless mass burning rate:

$$a = \ln\left[\frac{1 - \frac{L}{Q} + t_s}{1 - \frac{L}{Q} - Y_{F,s}}\right] \qquad (12)$$

where L = latent heat of vaporization of the fuel

t_s = dimensionless droplet surface temperature

$Y_{F,s}$ = mass fraction of fuel at the droplet surface

We now introduce the additional assumption that the flame zone of finite thickness can be replaced by an infinitessimal one represented by a Driac-delta function located such that the fuel and oxidant react stoichiometrically. As a consequence, the right-hand-sides of eqs. 10 (written for the fuel) and 11 become

$$\eta^2 b\, Y_F^* \cdot \delta(\eta-\eta^*)$$

where the asterisks refer to the values at the hypothetical flame surface, and δ is the delta function. (Note that the fact that $N_O = 0$ has been used in writing this term.)

Peskin (Ref. 1) shows that a solution to equation 10 with this right-hand-side is given by generalized function theory as

$$Y_F = \frac{b^*}{a}\ Y_F^*\ \eta^{*2}\ e^{-a/\eta} \begin{cases} 1-e^{a/\eta} & \text{for} \eta>\eta^* \\ 1-e^{a/\eta^*} & \text{for} \eta<\eta^* \end{cases} + 1-e^{-a/\eta} \tag{13}$$

Therefore, for $\eta=\eta^*$, $Y_F=Y_F$ and eq. 13 becomes

$$Y_F^* = \frac{(1-e^{-a/\eta^*})}{1+\frac{b^*}{a}\eta^{*2}(1-e^{-a/\eta^*})} \tag{14}$$

Now when eq. 13 is solved for $\eta=1$, $Y_F=Y_{FS}$, and eq. 14 is used, the result is

$$Y_{FS} = \frac{\frac{b^*}{a}\eta^{*2}\ e^{-a}\ (1-e^{a/\eta^*})\ (1-e^{-a/\eta^*})}{1+\frac{b^*}{a}\ \eta^{*2}\ (1-e^{-a/\eta^*})} + 1-e^{-a} \tag{15}$$

From the difference between eq. 10 written for the fuel and the oxidizer, and using the appropriate boundary conditions, the following expression is obtained for η^*:

$$\eta^* = \frac{a}{\ln\left[\frac{i_O\ Y_{Fs} + Y_O\ (\infty)}{Y_O\ (\infty)\ e^{-a} + i_O\ Y_{Fs}}\right]} \tag{16}$$

From the sum of equations 10 (written for the fuel) and 11, again subject to the appropriate boundary conditions, the following expression can be derived for t*:

$$t^* = \frac{(Y_{FS} + t_s)\ (e^{-a/\eta^*}-1)}{e^{-a}-1} - \frac{(1-e^{-a/\eta^*})}{1+\frac{b^*}{a}\,\eta^{*2}\,(1-e^{-a/\eta^*})} \qquad (17)$$

in which equation 14 was also used.

Finally, using the result of the previous section, b* can be written

$$b^* = \frac{r_D^2}{D}\left[1.2 \times 10^{10} \cdot \exp(-26{,}800/RT^*)\right] \qquad (18)$$

Equations 12, 15, 16, 17, and 18 constitute five equations in the five unknowns a, Y_{FS}, η^*, T^*, and b^*. (Unlike Peskin (Refs. 1, 4, 5), we are not interested here in species and temperature profiles surrounding the droplet, but in the mass burning rate a; as a consequence, the equations developed above are particularly suited to this purpose.)

Results using this analysis have been obtained for the following values of the parameters:

$Y_O(\infty) = 0.25$

$D = 10^{-4}\ \frac{ft^2}{sec}$

$i_O = \frac{23}{16}$ (see eq. 1)

Q was calculated from the enthalpies obtained from eq. 7; L was obtained from the Clausius-Clapeyron equation using the vapor pressure data in Ref. 6; in going from a to $\dot{m}_F^O$, k was obtained from Ref. 6 and c_p from Ref. 7.

Results are shown in figures 4, 5, and 6. In figure 4, the results are compared with the previous results obtained from the Godsav analysis (Ref. 2) and the experimental results of Ref. 8. As can be seen, the current analysis yields results which are about 80% higher over most of the range of r_D than the corresponding Godsav value. This is due, at least in part, to the values chosen for $Y_O(\infty)$ and D, as well as the differences inherent in the two approaches. It is interesting to note, however, that the line corresponding to $T = 1035^{\circ}K$, $p = 300$ psia (Curve B) passes right through the experimental points of Ref. 8. Unfortunately, Ref. 8 does not indicate the level of pressure at which these experiments were conducted, leaving this possible correlation unresolved. However, the linear dependence of the burning rate on droplet diameter is retained by the modified flame surface analysis, in accordance with the experimental results.

Figure 5 contrasts the ambient temperature dependence of this analysis and the Godsav analysis for the particular conditions noted. It was pointed out in Ref. 2, and can be seen in figure 5, that the Godsav analysis yields a very weak, almost linear ambient temperature dependence. Most experimental work indicates a stronger, non-linear dependence. The modified flame surface analysis does yield this latter type of dependence. It may be justifiably said, however, that the differences between the two analyses at these particular conditions are not sufficiently great to warrant using the current analysis in the fluid dynamics program. In particular, no evidence of extinction can be seen down

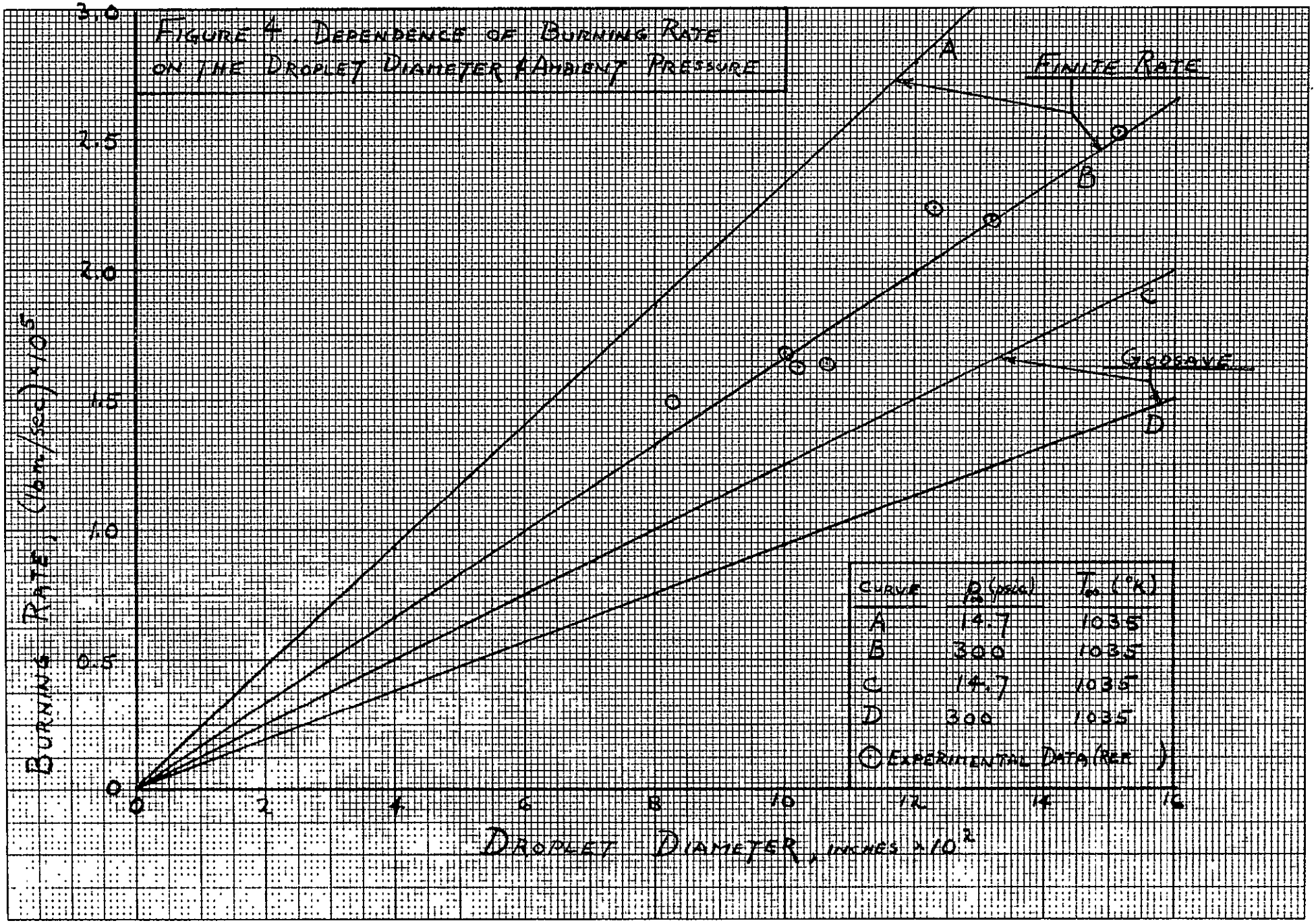
FIGURE 4 DEPENDENCE OF BURNING RATE ON THE DROPLET DIAMETER & AMBIENT PRESSURE
BURNING RATE, (gm/sec) x 10^5
DROPLET DIAMETER, INCHES x 10^2
3.0
2.5
2.0
1.5
1.0
0.5
0
0
2
4
6
8
10
12
14
16
A
B
C
D
FINITE RATE
GODSAVE
CURVE
P_∞ (psia)
T_∞ (°K)
A 14.7 1035
B 300 1035
C 14.7 1035
D 300 1035
EXPERIMENTAL DATA (REF)

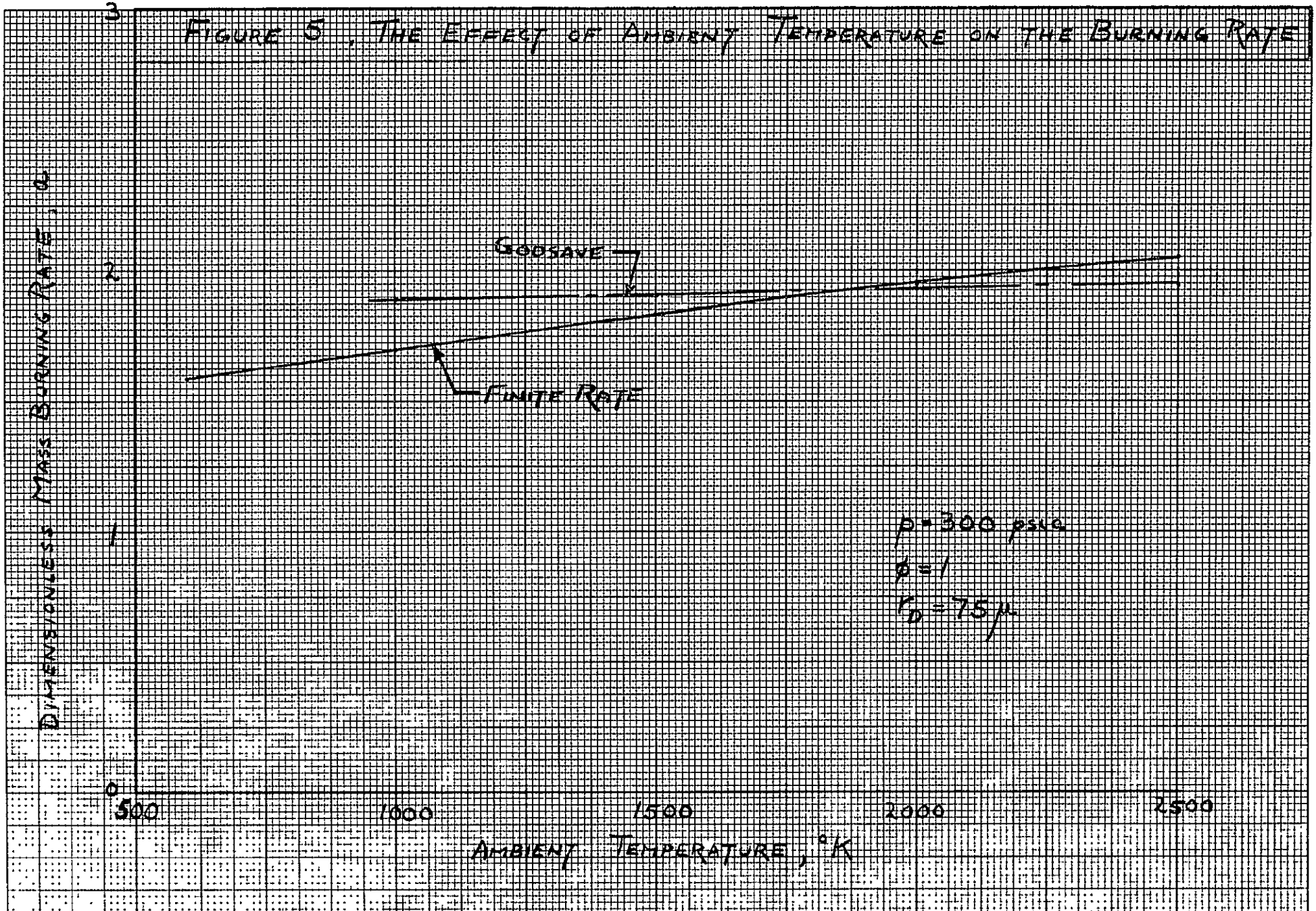
FIGURE 5, THE EFFECT OF AMBIENT TEMPERATURE ON THE BURNING RATE
DIMENSIONLESS MASS BURNING RATE, $\frac{\rho_p r_b}{\rho_p r_{b_{ref}}}$
3
2
1
0
GODSAVE
FINITE RATE
$P = 300$ PSIA
$\phi = 1$
$r_D = 75\mu$
500
1000
1500
2000
2500
AMBIENT TEMPERATURE, °K

to ambient temperatures near the boiling point of the fuel. If this same result is discovered at other values of the ambient pressure as well, this will constitute ample justification for the use of the simpler Godsav analysis.

The effect of ambient temperature on the values of Y_{FS}, η^* and T^* are shown in figure 6. The value of $Y_{FS} \to 1$ as T_∞ increases, in accordance with the assumption of the Godsav, diffusion-flame approximation ($Y_{FS=1}$). The hypothetical flame surface moves away from the droplet as T_∞ increases; this stems from the fact that in order to sustain a stoichiometric combustion process, the flame location must move away from the flame surface where a larger quantity of fuel vapor (Y_{FS}) is being produced. Finally, T^* exhibits a linear dependence on T_∞.

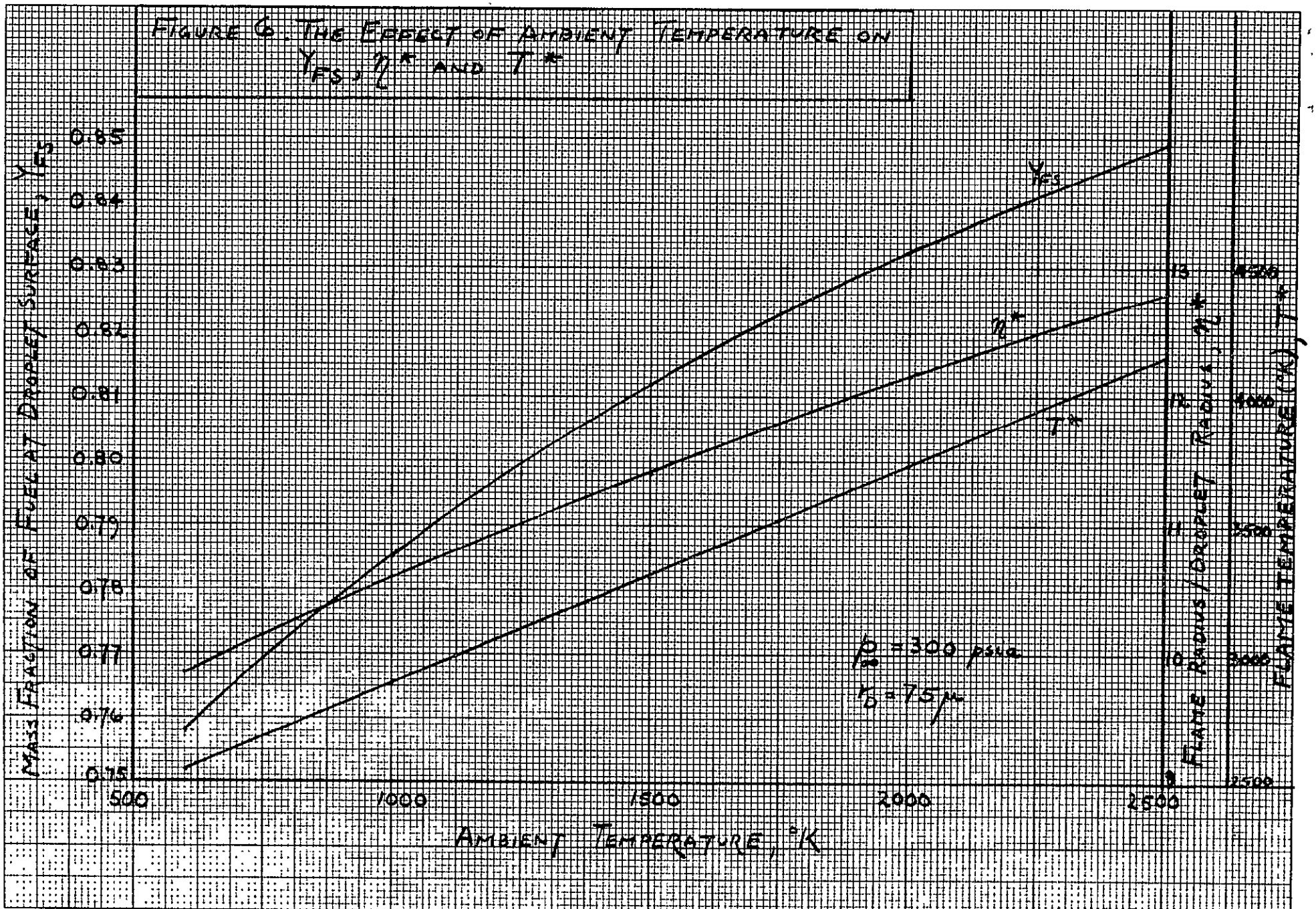
FIGURE 6. THE EFFECT OF AMBIENT TEMPERATURE ON Y_{FS}, η^* AND T^*
MASS FRACTION OF FUEL AT DROPLET SURFACE (Y_{FS})
0.85
0.84
0.83
0.82
0.81
0.80
0.79
0.78
0.77
0.76
0.75
500
1000
1500
2000
2500
AMBIENT TEMPERATURE, °K
Y_{FS}
η^*
T^*
P_∞ = 300 psia
r_D = 75 μ
FLAME RADIUS / DROPLET RADIUS, η^*
FLAME TEMPERATURE (°K), T^*
15
12
11
10
9
4500
4000
3500
3000
2500

C. The Reduced Godsav Analysis

Preliminary runs which coupled the complete Godsav analysis to the fluid dynamics program indicated that the running times were excessively long. (Roughly, five times slower than with the elementary energy term previously used.) As a consequence, the results obtained to date from the Godsav analysis (Ref. 2) were used to formulate the following simplified version of this analysis:

The weak, almost linear, temperature dependence of the dimensionless mass burning rate can be approximately expressed as

$$a_{300} = (3.73 \times 10^{-5}) \ (T_\infty) + 1.855 \tag{19}$$

where a_{300} is the dimensionless burning rate at a chamber pressure dependence is approximately given by

$$\frac{a_p}{a_{300}} = \left(\frac{p_\infty}{300}\right)^{0.0108} \tag{20}$$

Once a_p is computed, the burning rate in stationary surroundings is obtained from

$$\dot{m}_F^o = \frac{2\pi k}{c_p} \ d_L \ a_p \tag{21}$$

where d_L is the drop diameter, and the thermal conductivity and specific heat are functions of the liquid drop temperature.

The drop temperature, T_L, which is the boiling temperature at the chamber pressure, can be obtained to a good approximation from the integrated Clausius-Clapeyron equation

$$\ln \frac{p}{2131} = (8.7 \times 10^3)\left(\frac{1}{1176} - \frac{1}{T_L}\right) \tag{22}$$

where p is in psia, T_L is in ^oR, and the critical point conditions are 2131 psia, 1176 ^oR.

Knowing T_L, K is obtained from a linear curve fit of the data in Ref. 6:

$$\dot{K} = \frac{1}{3600}\left[(-8.33 \times 10^{-5})\ (T_L - 460) + 0.2107\right] \tag{23}$$

and c_p is obtained from Ref. 7:

$$c_p = 0.138 + 0.527 \times 10^{-3}\ T_L - 0.120 \times 10^{-6}\ T_L^{\ 2} \tag{24}$$

From $\dot{m}_F^o$, the burning rate in the convective environment is then obtained from (see Ref. 3, eq. 21):

$$\frac{\dot{m}_F}{\dot{m}_F^o} = 1 + 0.276\ (Re)^{\frac{1}{2}}\ (Pr)^{1/3} \tag{25}$$

Under the engine conditions of interest, the following constant values are reasonable:

$$Pr^{1/3} = 0.6$$

$$L_F = 540\ \frac{Btu}{lbm}$$

$$L_o = 178.2\ \frac{Btu}{lbm}$$

$$Q = 12{,}400\ \frac{Btu}{lbm}$$

where L_F is the latent heat of the fuel, L_o is the latent heat of the oxidizer, and Q is the heat of reaction. The appropriate terms in the ψ-vector of the fluid dynamics program may now be obtained as shown in Ref. 3 (eq. 22). Results obtained using this approximate formulation are shown elsewhere in this report.

REFERENCES

1. Peskin, R. L. and Wise, H., AIAA Journal, 4, 1646 (1966).

2. Burstein, S. Z. and Chinitz, W., "Nonlinear Combustion Instability in Liquid-Propellant Rocket Motors", 2nd Quarterly Report, Mathematical Applications Group, Inc., January 30, 1968.

3. IBID, 1st Quarterly Report, October 30, 1967.

4. Peskin, R. L., et.at., AIAA Journal, 5, 2173 (1967).

5. Polymeropoulos, C. E. and Peskin, R. L., "Theoretical Calculations of Fuel Drop Ignition and Extinction", Paper USCI-67-5, Western States Section/The Combustion Institute, April, 1967.

6. Aerojet-General Corporation Report on Properties of Propellants

7. Haws, J. L. and Harden, D. G., J. Spacecraft and Rockets, 2, 972 (1965).

8. Dynamic Science Report No. SN-95-4, Monthly Progress Report under Contract No. NAS7-567, 1967.

Nonlinear Combustion Instability in Liquid-Propellant Rocket Motors

Samuel Z. Burstein and Wallace Chinitz

Third Quarterly Report

to

Jet Propulsion Laboratory

April 30, 1968

GPO PRICE $ _____

CFSTI PRICE(S) $ _____

Hard copy (HC) 3.00

Microfiche (MF) _____

ff 653 July 65

Mathematical Applications Group, Inc.

180 South Broadway

White Plains, New York

Nonlinear Combustion Instability in Liquid-Propellant Rocket Motors

Samuel Z. Burstein and Wallace Chinitz

Third Quarterly Report

to

Jet Propulsion Laboratory

April 30, 1968

JPL Contract
951946

"This work was performed for the Jet Propulsion Laboratory, California Institute of Technology, as sponsored by the National Aeronautics and Space Administration under Contract NAS7-100."

"This report contains information prepared by Mathematical Applications Group, Inc. (MAGI) under JPL subcontract. Its content is not necessarily endorsed by the Jet Propulsion Laboratory, California Institute of Technology, or the National Aeronautics and Space Administration."

TABLE OF CONTENTS

INTRODUCTION

During the third quarter progress continued along two fronts, the fluid dynamic model and the flame model of droplet combustion. This quarterly report describes some of the effort that is being generated in these two model building areas.

The first section describes some numerical experiments carried out with the fluid dynamic pancake model of the combustor. The experiments include both non-reacting and reacting flow conditions. The status of program COMB is also discussed.

The second section describes recent work in producing a simplified droplet evaporation and combustion analysis. Some recent results towards completing the Peskin-Wise model relating to the modified flame surface analysis are presented.

The authors would like to again acknowledge the creative programming effort that Harold Schechter has provided during the course of this research program.

I. Fluid Dynamic Model

A. Finite Amplitude Transverse Waves in a Cylindrical Chamber

We have continued exploring and analyzing the nonlinear motion of finite amplitude waves in the transverse plane of a cylindrical channel. In the last quarterly report (number 2) we reported on a calculation which exhibited continuous behavior of the fluid properties for all time. The initial data is prescribed by relations(traveling wave solution to the wave equation in cylindrical coordinates)which are presented on page 19 of quarterly report number 2. The initial pressure field and velocity field are shown in figures 1 and 2 and correspond to finite values for the amplitude parameter in the above equations. It should be noted that to obtain the dimensional value of pressure the nondimensional pressure is to be multiplied by γp_∞. In this test case, however, the maximum value of the pressure is 590 psia while the minimum value is 10 psia (here p_∞ = 300 psia and γ = 1.2). The numerical values shown in figures 1 and 2 correspond to this case. For the previous reported calculation the maximum (minimum) pressure was 450 (250) while p_∞ = 300 psia, and there the solution remained continuous for all time.

As figure 3 shows, for the present calculation, a shock wave has formed after about 1.22 units of nondimensional time (time is normalized by R/a_∞ ~ .131 millisec). The wave is strongest at the wall and decreases in strength as it curves inward into the chamber. Swirls seen behind the wave are due to numerical oscillations, a

feature inherent in these finite difference equations. Figure 4 shows the strong discontinuous behavior of the velocity field in the neighborhood of the shock. Now figure 5, taken at 400 cycles of computation, is an intermediate stage of the flow field development. Two pressure peaks are evident at a nondimensional radius of R = 1 of the combustion chamber. There is also a vast region of the chamber where the pressure is approximately uniform and it is clear that figure 6 shows a strong induced velocity field which is predominently tangential in direction. The pressure field shown in figure 7 shows clearly a symmetric compression/rarefaction wave with a peak pressure of about 1120 psia. The associated velocity field, shown in figure 8, is also locally symmetric about the pressure wave. Velocities increase and then decrease uniformly in the direction of motion while the maximum velocity is at the boundary.

One also notices that the velocity vectors on the leading edge of the wave point towards the wall while those at the trailing edge tend to point away from the wall.

Figures 9 and 10 show essentially the same picture as in the two previous plots; here the peak pressure is 1250 psia while the minimum pressure is 160 psia. The uniform portion of the flow field has a mean pressure level of about 220 psia. The wave has now undergone about one and two thirds rotations in 0.694 milliseconds. Figures 11 through 14 again show that the wave has the same basic structure as seen before, however, the peak pressure is decreasing to 1018 psia.

Figures 15 and 16 show the pressure field with multiple waves, waves which then seem to coalesce and lead to the flow field given by the next three figures.

It should be noted that the 'rev' counter value given at the bottom of the accompanying figures is computed from the relative position of the velocity vector at r = 0 from its starting position. For small values of the amplitude of the pressure wave, the vector rotates in phase with the wave. However, for large values of the amplitude, the fluid motion no longer is locked onto this convenient measure, but rather, there is in general a variation in phase between the rotation of the wave and the velocity vector at r = 0. At 2200 cycles (figure 18 corresponds to a physical time of 1.94 millisec) the wave has rotated about 4.8 times and the maximum amplitude has gone back up to 1350 psia. It is striking that the picture of the whole flow field again looks quite like that in figure 9. Apparently the fluid exhibits time wise dependent periodic behavior with waves of finite amplitude. The average period can be computed and is found to be 405 μ-sec.

Figures 20 and 21 give the dimensional pressure on the wall of the combustion chamber for selected values of time corresponding to some of the previous figures. The curves are labeled with three numbers. The first is the nondimensional time; the second is the rotation counter enclosed in parenthesis; and the third is the computation cycle count.

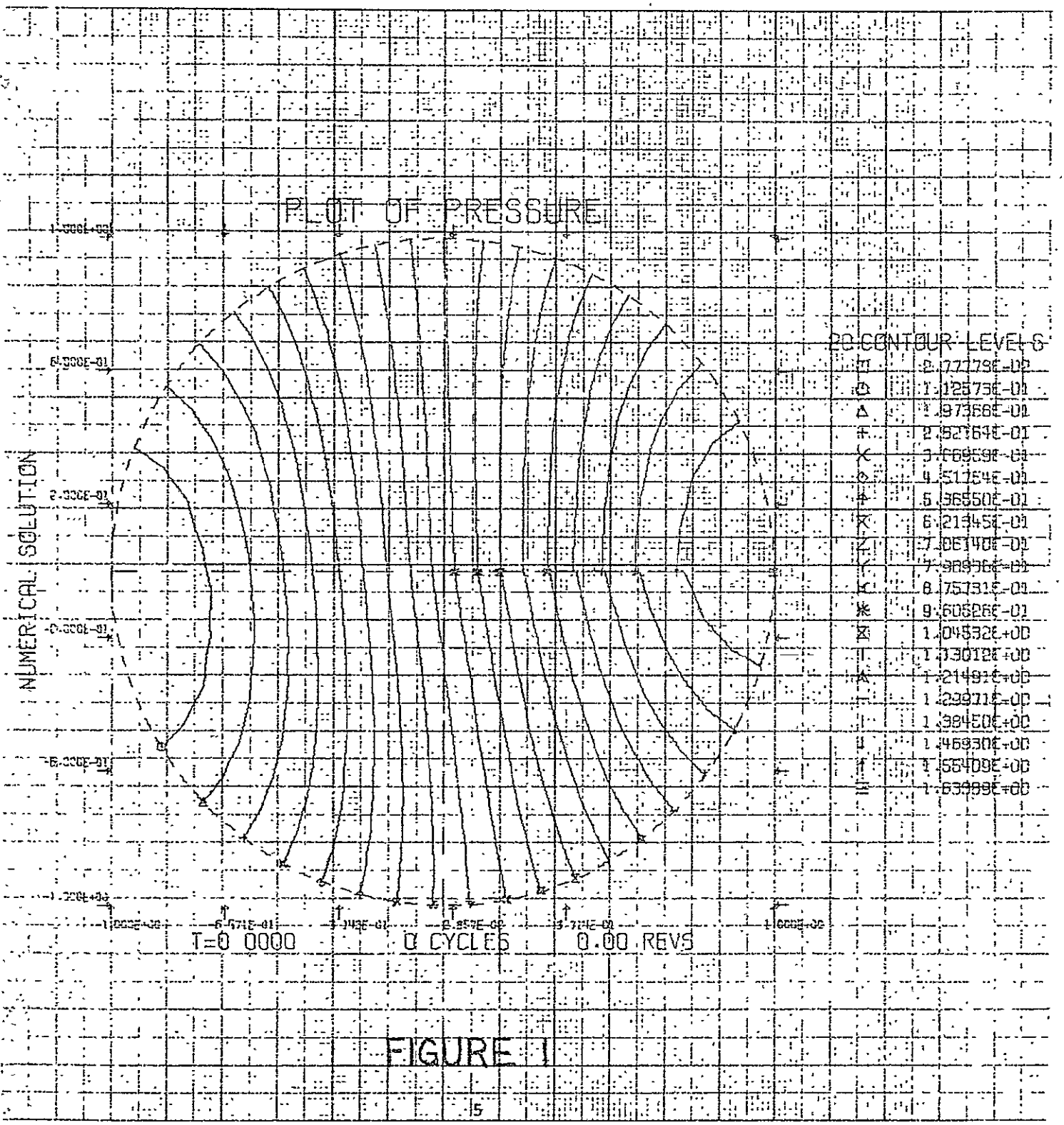
PLOT OF PRESSURE
NUMERICAL SOLUTION
20 CONTOUR LEVELS
T=0 0000
0 CYCLES
0.00 REVS

FIGURE 1

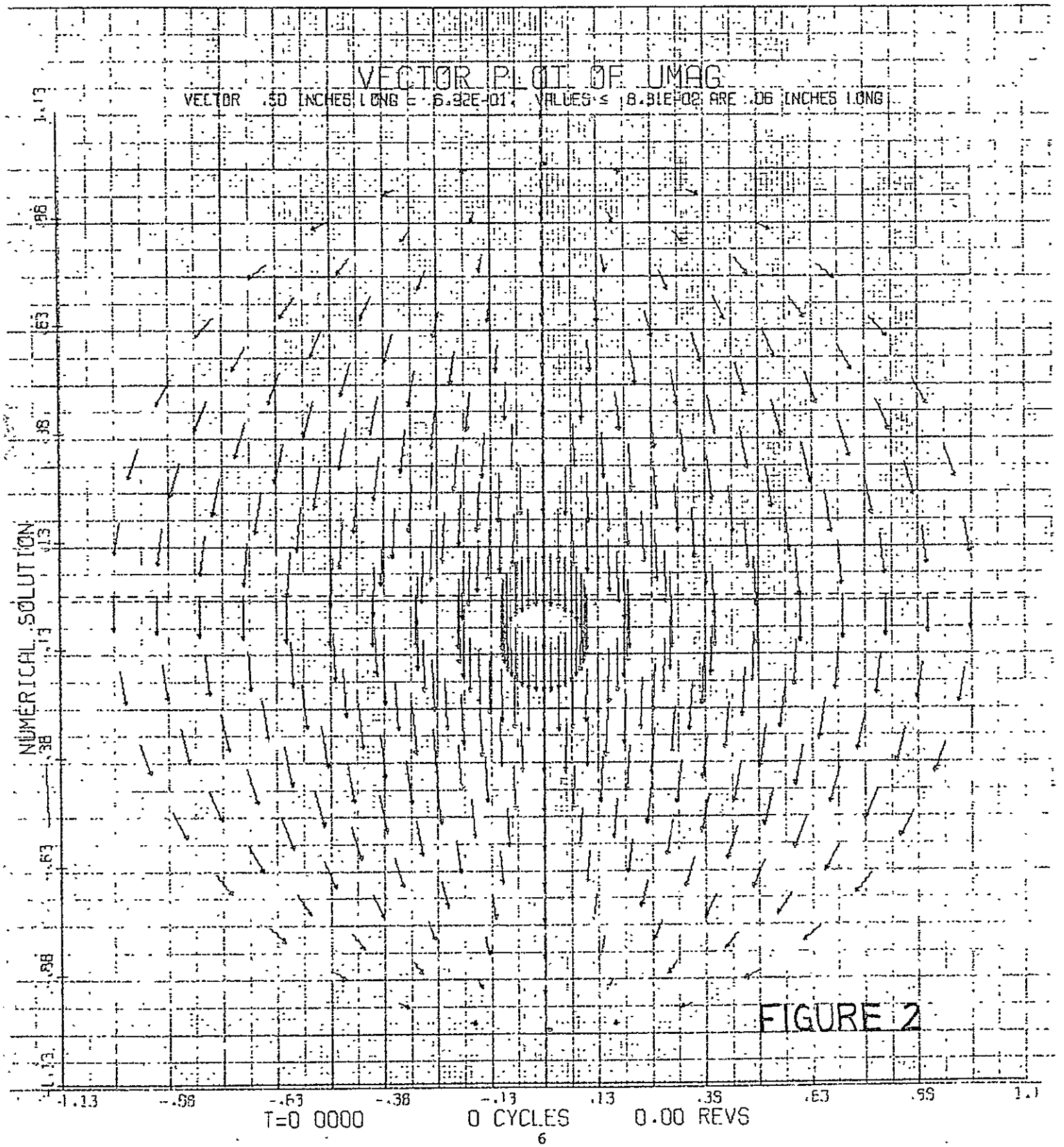
VECTOR PLOT OF UMAG
VECTOR .50 INCHES LONG = 6.32E-01, VALUES ≤ 8.81E+02 ARE .06 INCHES LONG
NUMERICAL SOLUTION
-1.13
-.88
-.63
-.38
-.13
.13
.38
.63
.88
1.13
T=0 0000
0 CYCLES
0.00 REVS

FIGURE 2

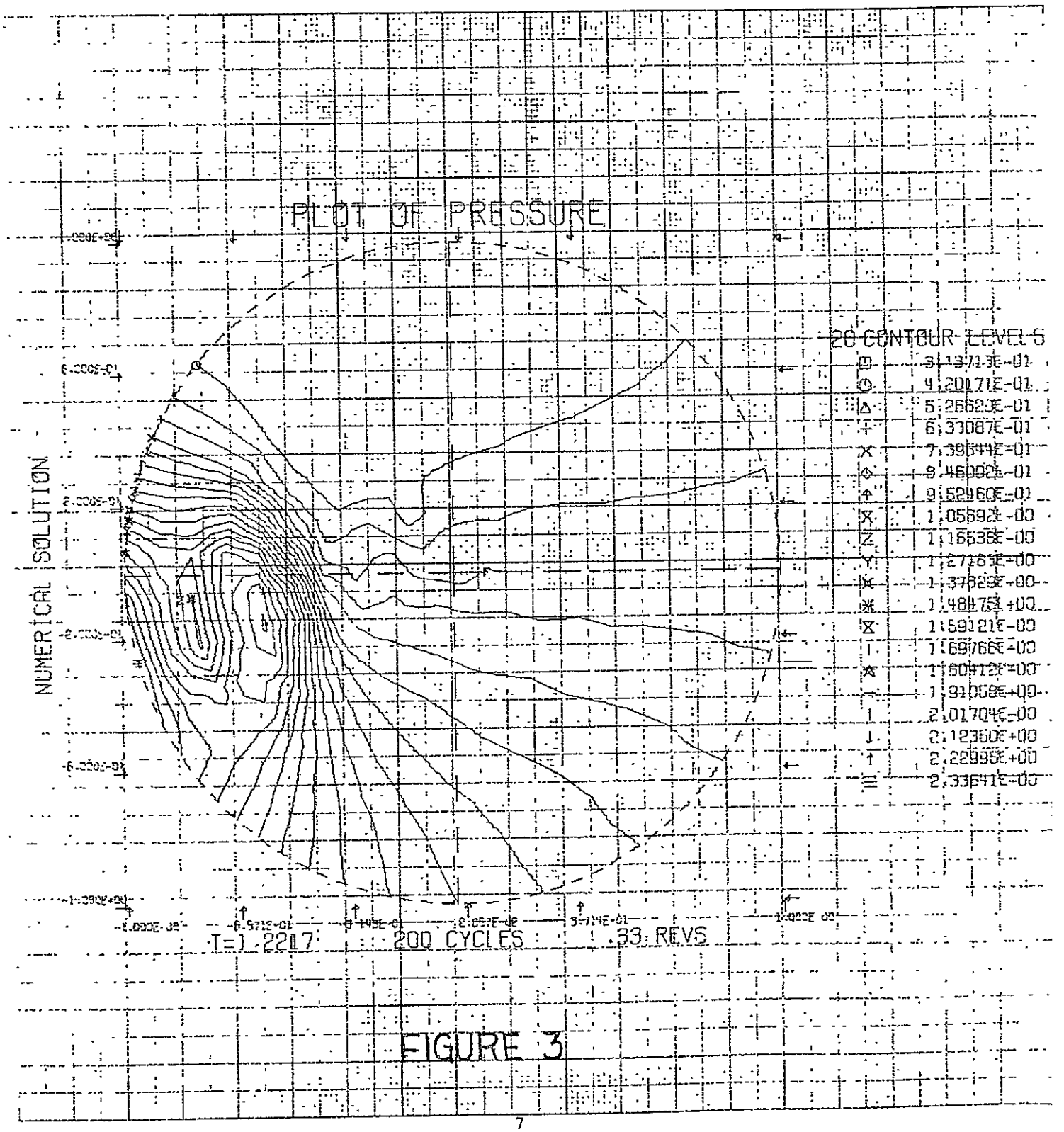
PLOT OF PRESSURE
NUMERICAL SOLUTION
20 CONTOUR LEVELS
3.13713E-01
4.20171E-01
5.26629E-01
6.33087E-01
7.39544E-01
8.46002E-01
9.52460E-01
1.05892E-00
1.16538E-00
1.27184E-00
1.37829E-00
1.48475E-00
1.59121E-00
1.69766E-00
1.80412E-00
1.91058E+00
2.01704E-00
2.12350E+00
2.22995E+00
2.33641E-00
T=1.2217
200 CYCLES
33 REVS

FIGURE 3

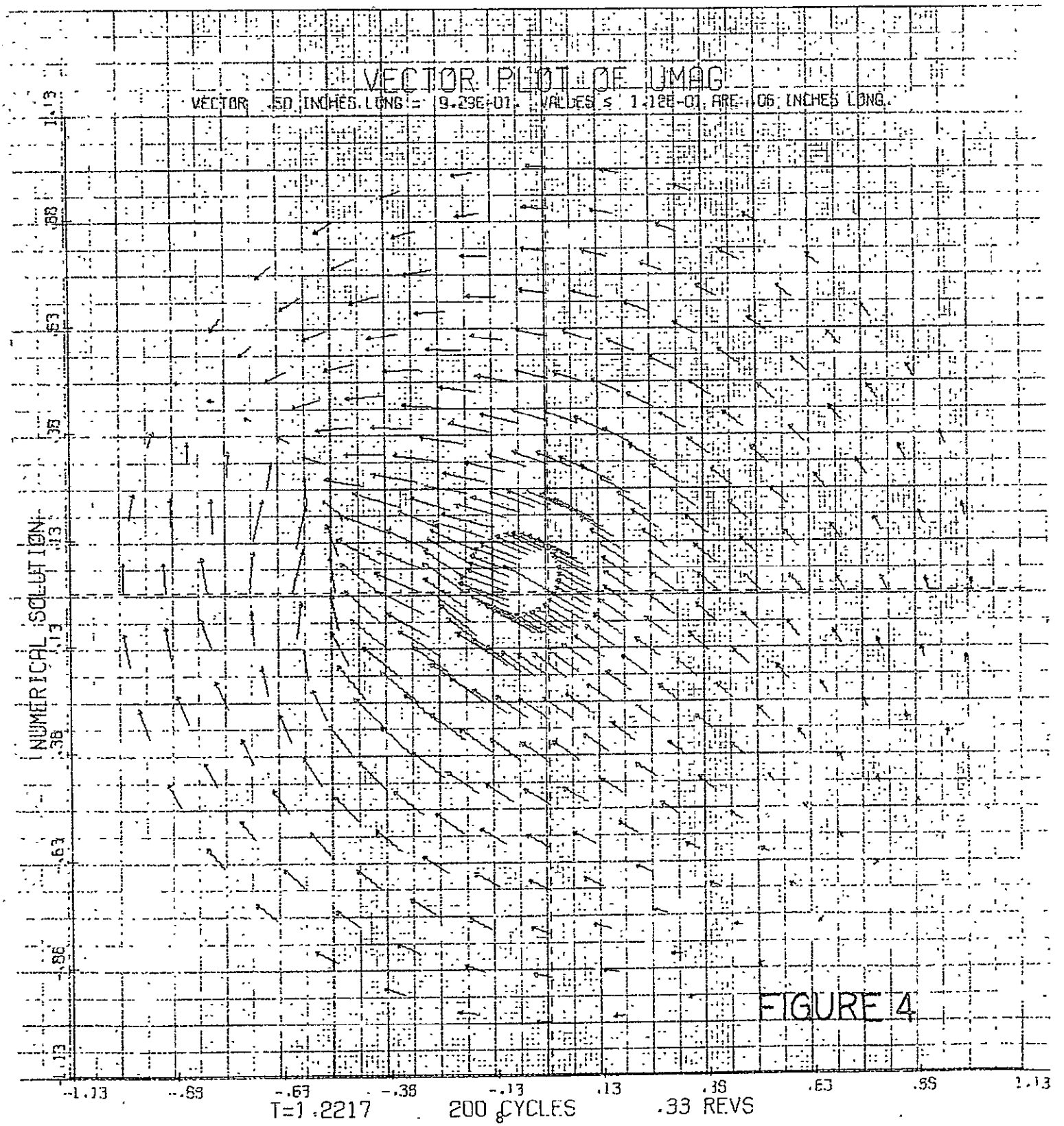
VECTOR PLOT OF UMAG
VECTOR .50 INCHES LONG = 9.23E-01 VALUES = 1.12E-01 ARE .06 INCHES LONG
NUMERICAL SOLUTION
1.13
.88
.63
.38
.13
-.13
-.38
-.63
-.88
-1.13
-1.13
-.88
-.63
-.38
-.13
.13
.38
.63
.88
1.13
T=1.2217
200 CYCLES
.33 REVS

FIGURE 4

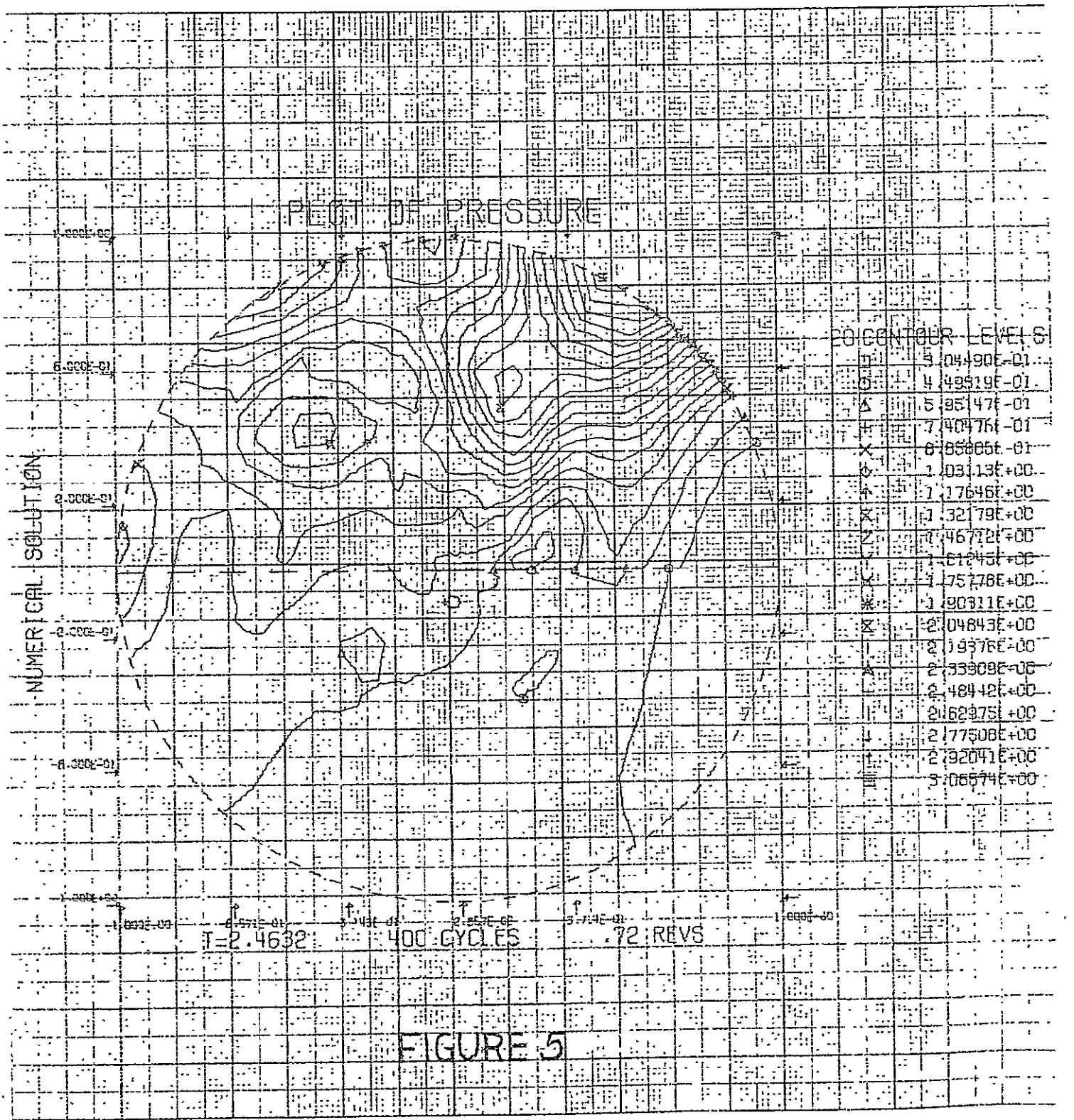
PLOT OF PRESSURE
NUMERICAL SOLUTION
20 CONTOUR LEVELS
5.04490E-01
4.49819E-01
3.95147E-01
3.40476E-01
2.85805E-01
2.31134E+00
1.76462E+00
1.21791E+00
6.71178E+00
1.24445E+00
1.75778E+00
2.90311E+00
2.04843E+00
2.19376E+00
2.33909E+00
2.48442E+00
2.62975E+00
2.77508E+00
2.92041E+00
3.06574E+00
T=2.4632
400 CYCLES
72 REVS

FIGURE 5

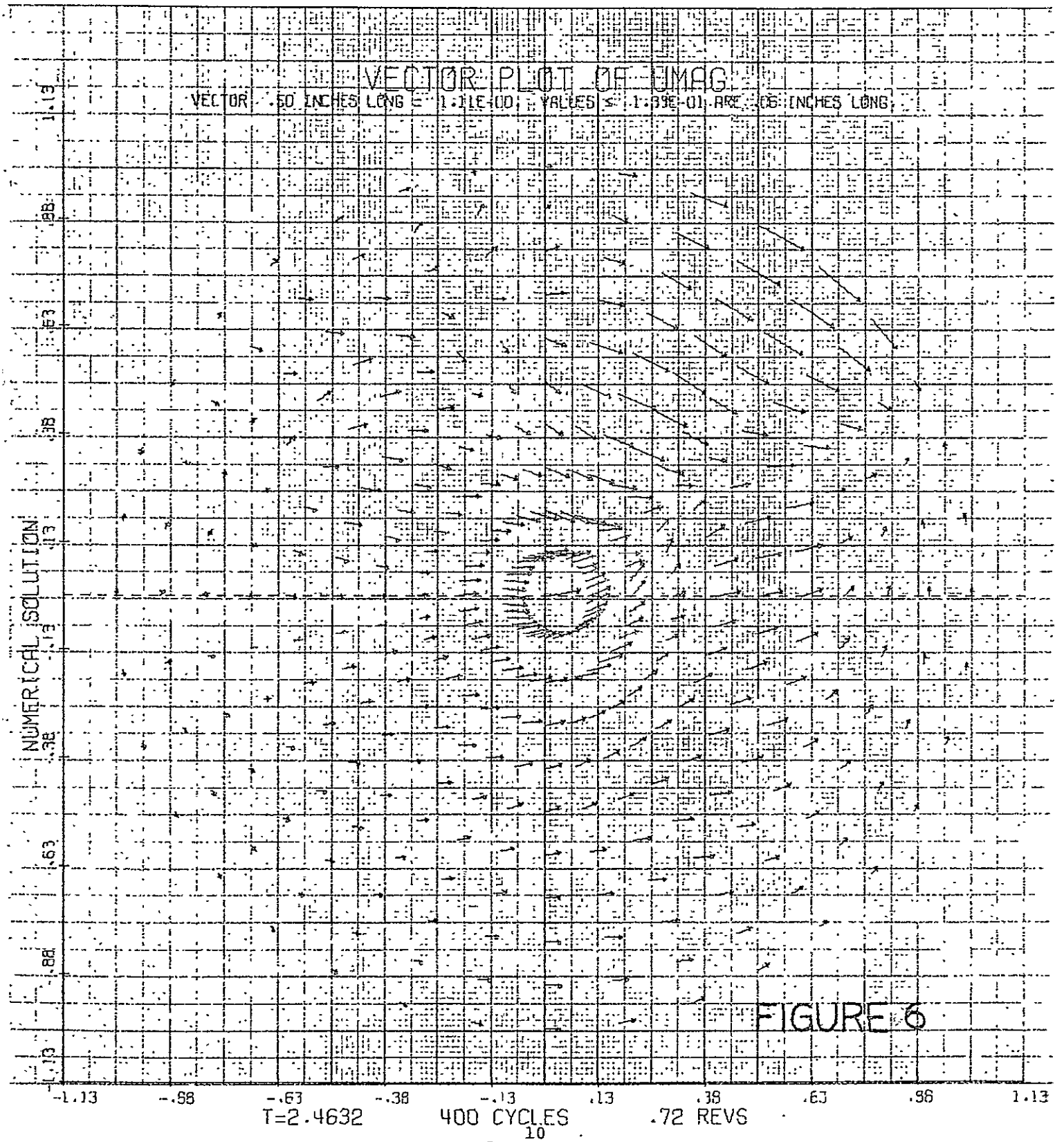
VECTOR PLOT OF UMAG
VECTOR .50 INCHES LONG = 1.1E-00, VALUES < 1.39E-01 ARE .06 INCHES LONG.
NUMERICAL SOLUTION
1.13
.88
.63
.38
.13
-.13
-.38
-.63
-.88
-1.13
-1.13
-.88
-.63
-.38
-.13
.13
.38
.63
.88
1.13
T=2.4632
400 CYCLES
.72 REVS

FIGURE 6

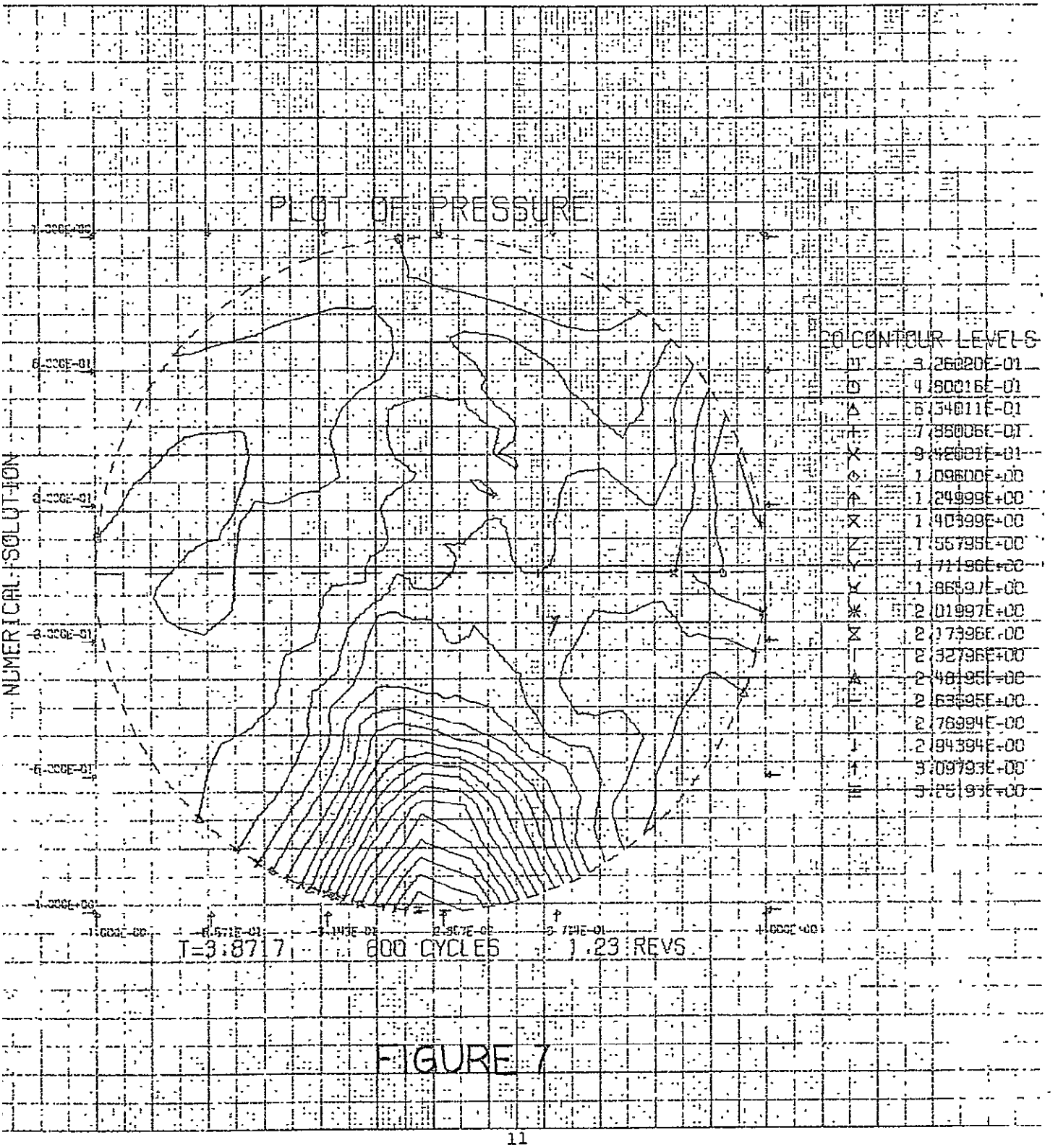
PLOT OF PRESSURE
NUMERICAL SOLUTION
20 CONTOUR LEVELS
3 26020E-01
4 80016E-01
6 34011E-01
7 85006E-01
9 42021E-01
1 09600E+00
1 24999E+00
1 40399E+00
1 55795E+00
1 71196E+00
1 86591E+00
2 01997E+00
2 17396E+00
2 32796E+00
2 48195E+00
2 63595E+00
2 78994E+00
2 94394E+00
3 09793E+00
3 25193E+00
T=3.8717
800 CYCLES
1.23 REVS

FIGURE 7

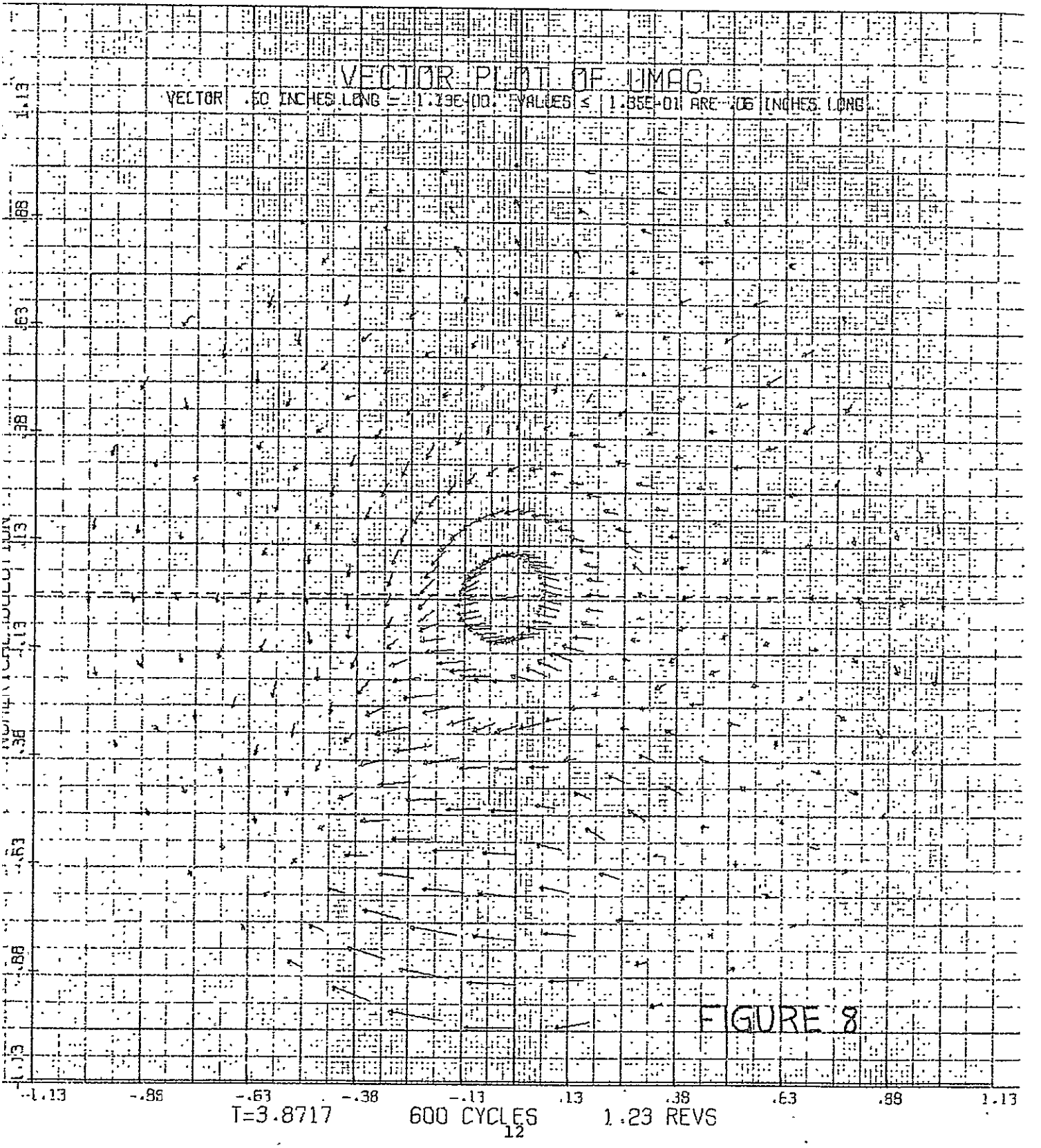
VECTOR PLOT OF UMAG
VECTOR .50 INCHES LONG = 1.23E+00. VALUES ≤ 1.85E-01 ARE .06 INCHES LONG.
1.13
.88
.63
.38
.13
-.13
-.38
-.63
-.88
-1.13
-1.13
-.88
-.63
-.38
-.13
.13
.38
.63
.88
1.13
T=3.8717
600 CYCLES
1.23 REVS

FIGURE 8

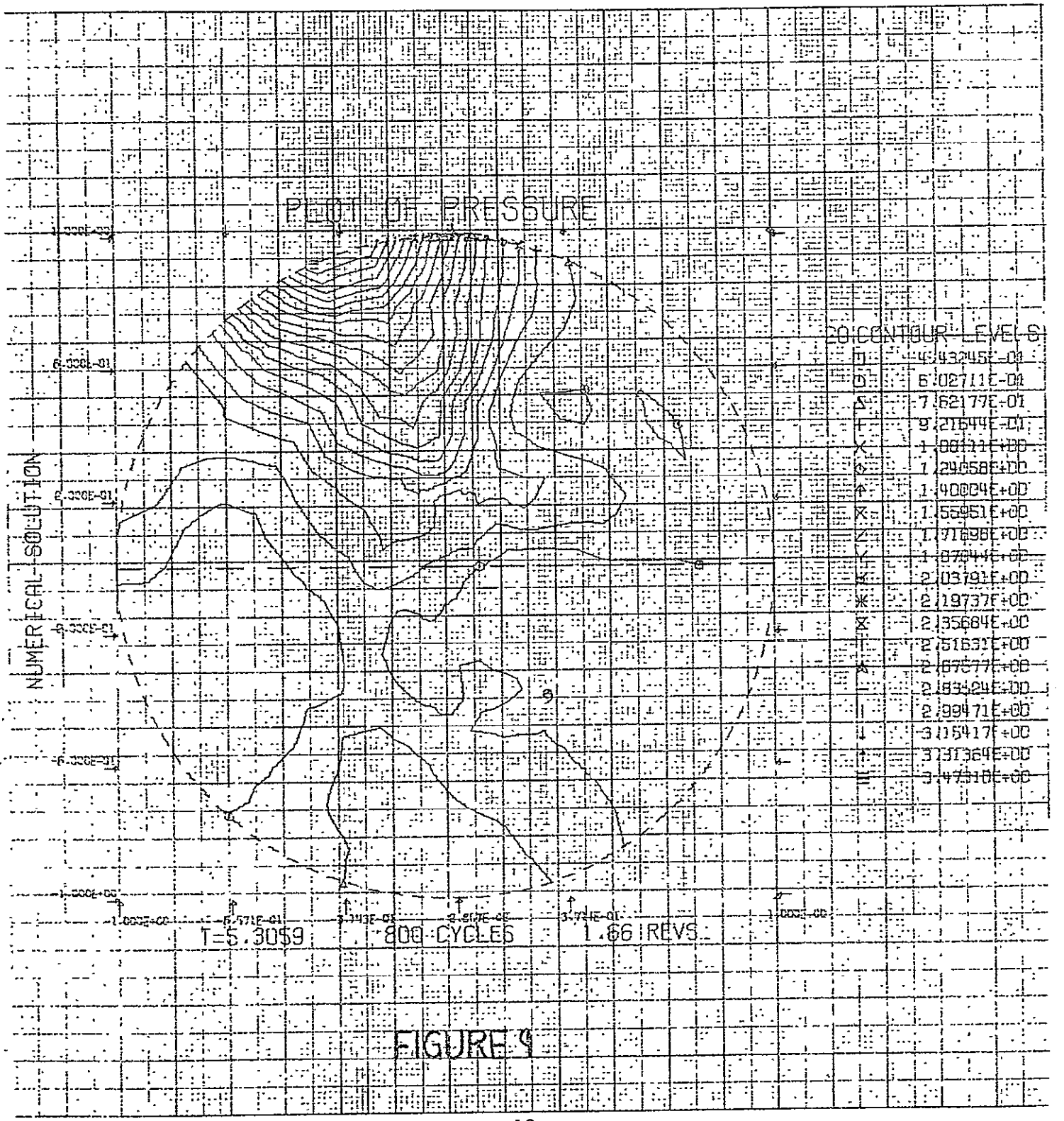
PLOT OF PRESSURE
NUMERICAL-SOLUTION
20 CONTOUR LEVELS
4.43245E-01
6.02711E-01
7.62177E-01
9.21644E-01
1.08111E+00
1.24058E+00
1.40004E+00
1.55951E+00
1.71898E+00
1.87844E+00
2.03791E+00
2.19737E+00
2.35684E+00
2.51631E+00
2.67577E+00
2.83524E+00
2.99471E+00
3.15417E+00
3.31364E+00
3.47310E+00
T=5.3059
800 CYCLES
1.66 REVS

FIGURE 9

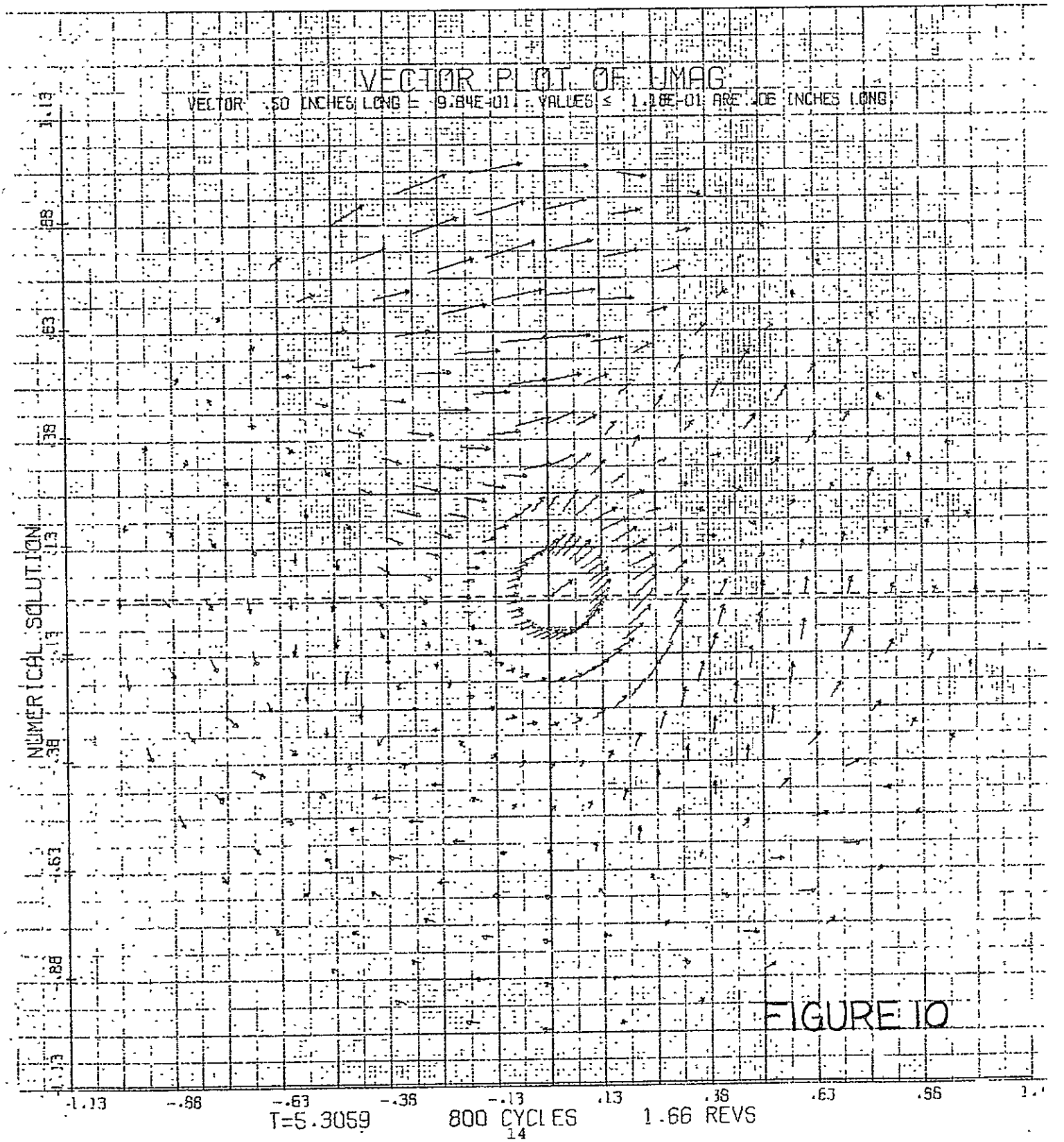
VECTOR PLOT OF UMAG
VECTOR .50 INCHES LONG = 9.84E-01 VALUES ≤ 1.18E-01 ARE .06 INCHES LONG
NUMERICAL SOLUTION
1.13
.88
.63
.38
.13
-.13
-.38
-.63
-.88
-1.13
-.86
-.63
-.36
-.13
.13
.36
.63
.86
T=5.3059
800 CYCLES
1.66 REVS

FIGURE 10

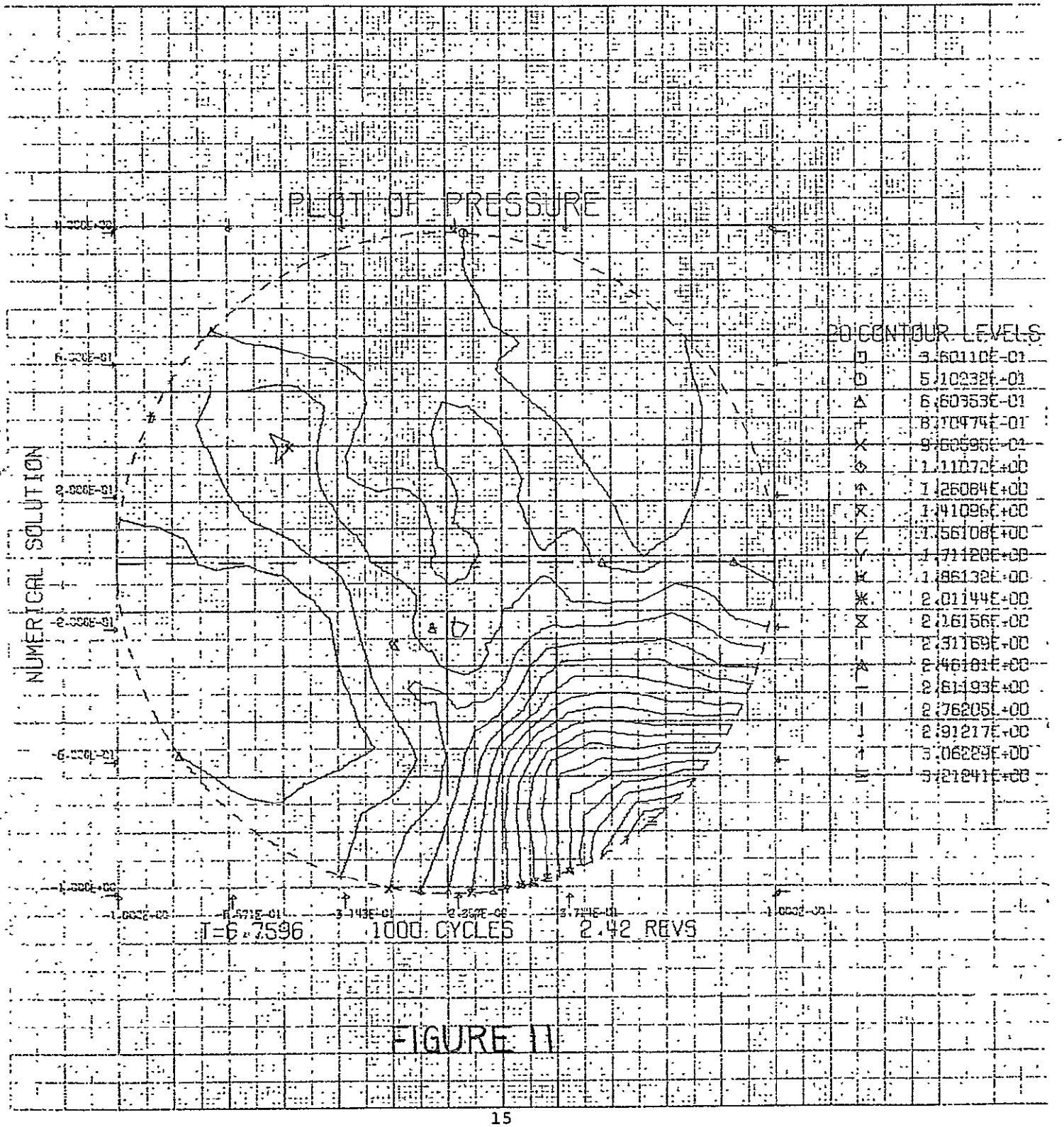
PLOT OF PRESSURE
NUMERICAL SOLUTION
20 CONTOUR LEVELS
3.60110E-01
5.10232E-01
6.60353E-01
8.10474E-01
9.60595E-01
1.11072E+00
1.26084E+00
1.41096E+00
1.56108E+00
1.71120E+00
1.86132E+00
2.01144E+00
2.16156E+00
2.31169E+00
2.46181E+00
2.61193E+00
2.76205E+00
2.91217E+00
3.06229E+00
3.21241E+00
T=6.7596
1000 CYCLES
2.42 REVS

FIGURE 11

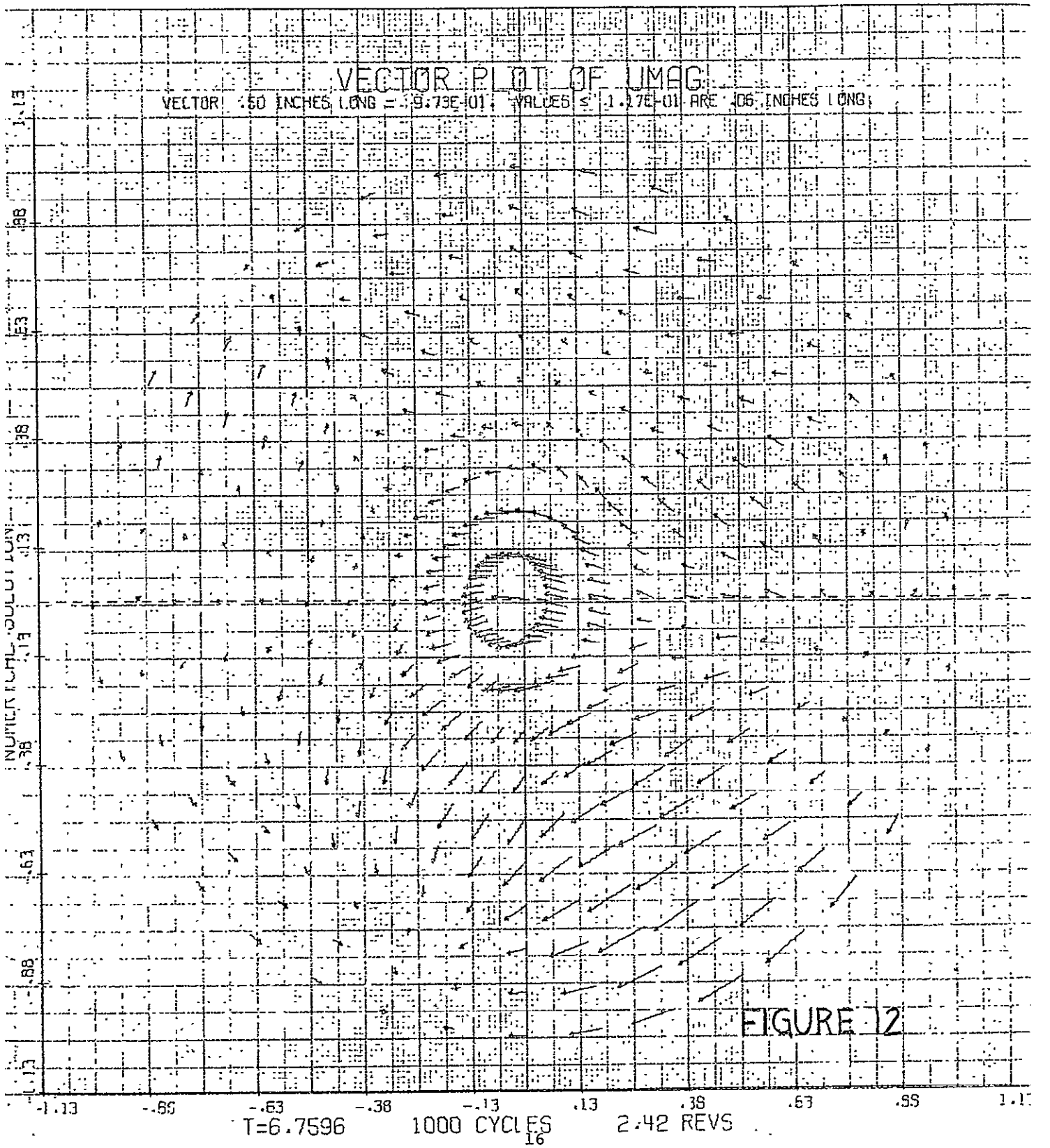
VECTOR PLOT OF UMAG
VECTOR .50 INCHES LONG = 9.73E-01 VALUES ≤ 1.27E-01 ARE .06 INCHES LONG
-1.13
-.88
-.63
-.38
-.13
.13
.38
.63
.88
1.13
T=6.7596 1000 CYCLES 2.42 REVS

FIGURE 12

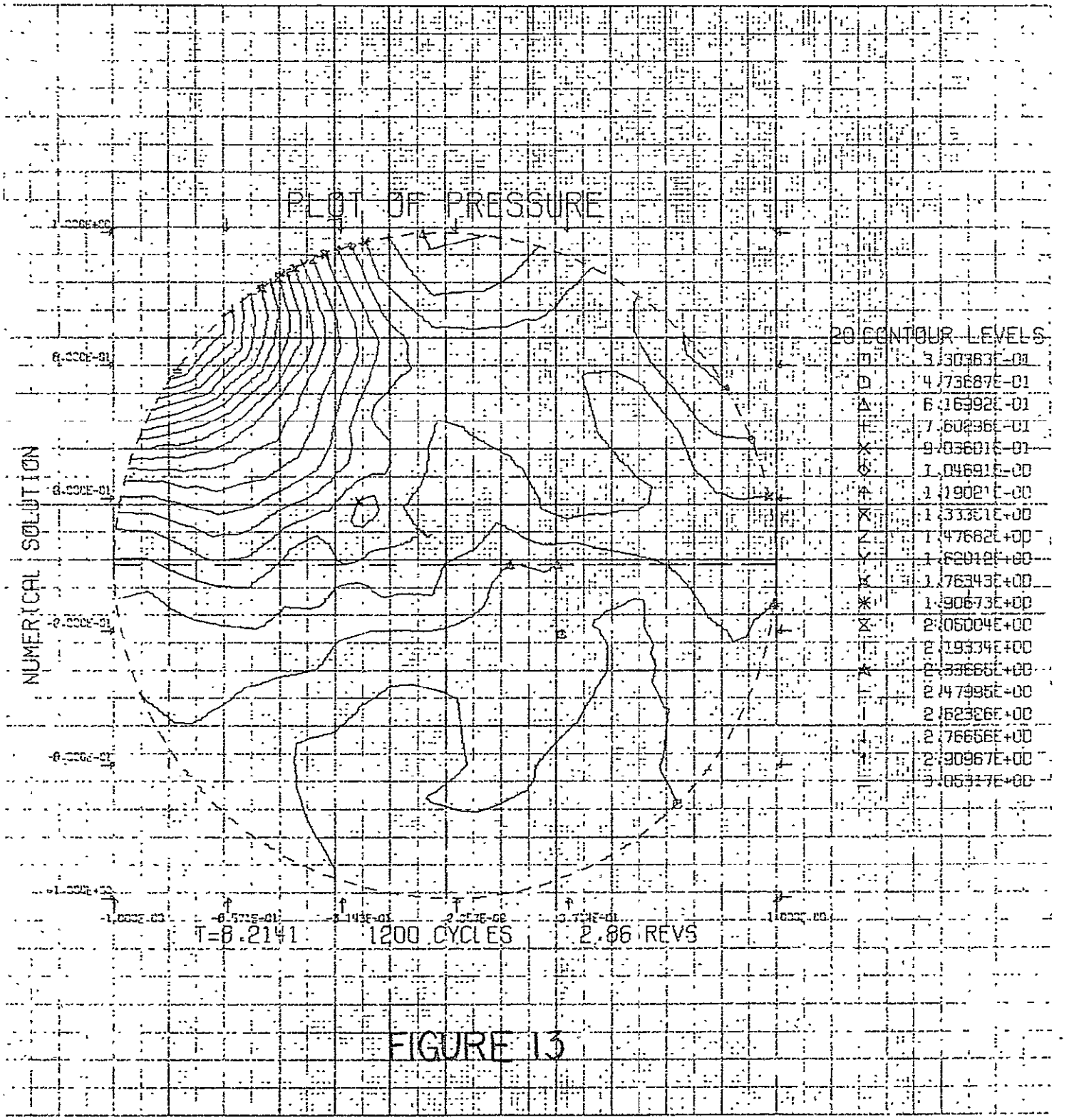
PLOT OF PRESSURE
NUMERICAL SOLUTION
20 CONTOUR LEVELS
3.30363E-01
4.73687E-01
6.16992E-01
7.60296E-01
9.03601E-01
1.04691E+00
1.19021E+00
1.33351E+00
1.47682E+00
1.62012E+00
1.76343E+00
1.90673E+00
2.05004E+00
2.19334E+00
2.33665E+00
2.47995E+00
2.62326E+00
2.76656E+00
2.90987E+00
3.05317E+00
T=8.2141
1200 CYCLES
2.86 REVS

FIGURE 13

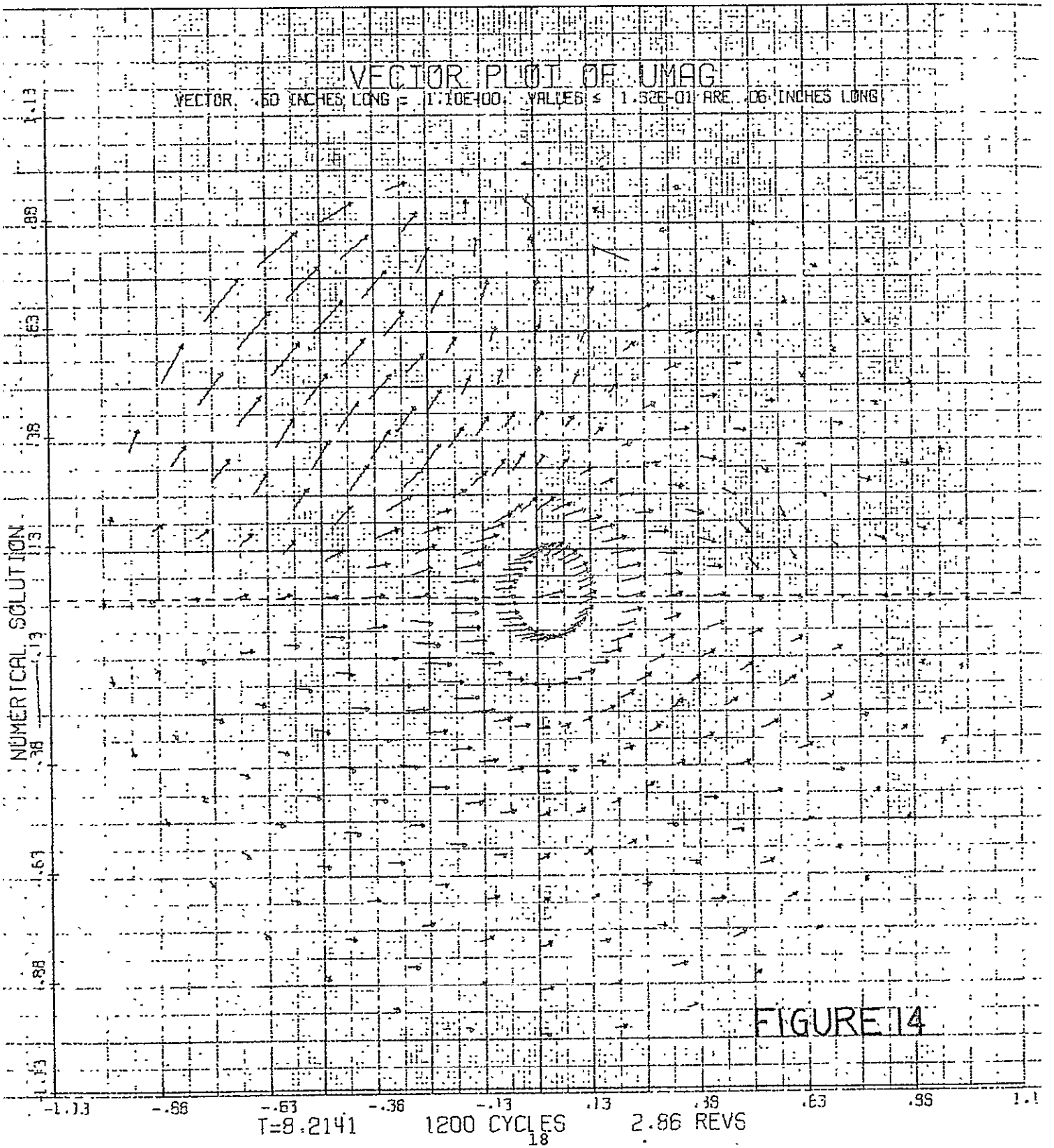
VECTOR PLOT OF UMAG
VECTOR, .60 INCHES LONG = 1.10E+00, VALUES ≤ 1.32E-01 ARE .06 INCHES LONG
NUMERICAL SOLUTION
-1.13
-.88
-.63
-.38
-.13
.13
.38
.63
.88
1.1
T=8.2141 1200 CYCLES 2.86 REVS

FIGURE 14

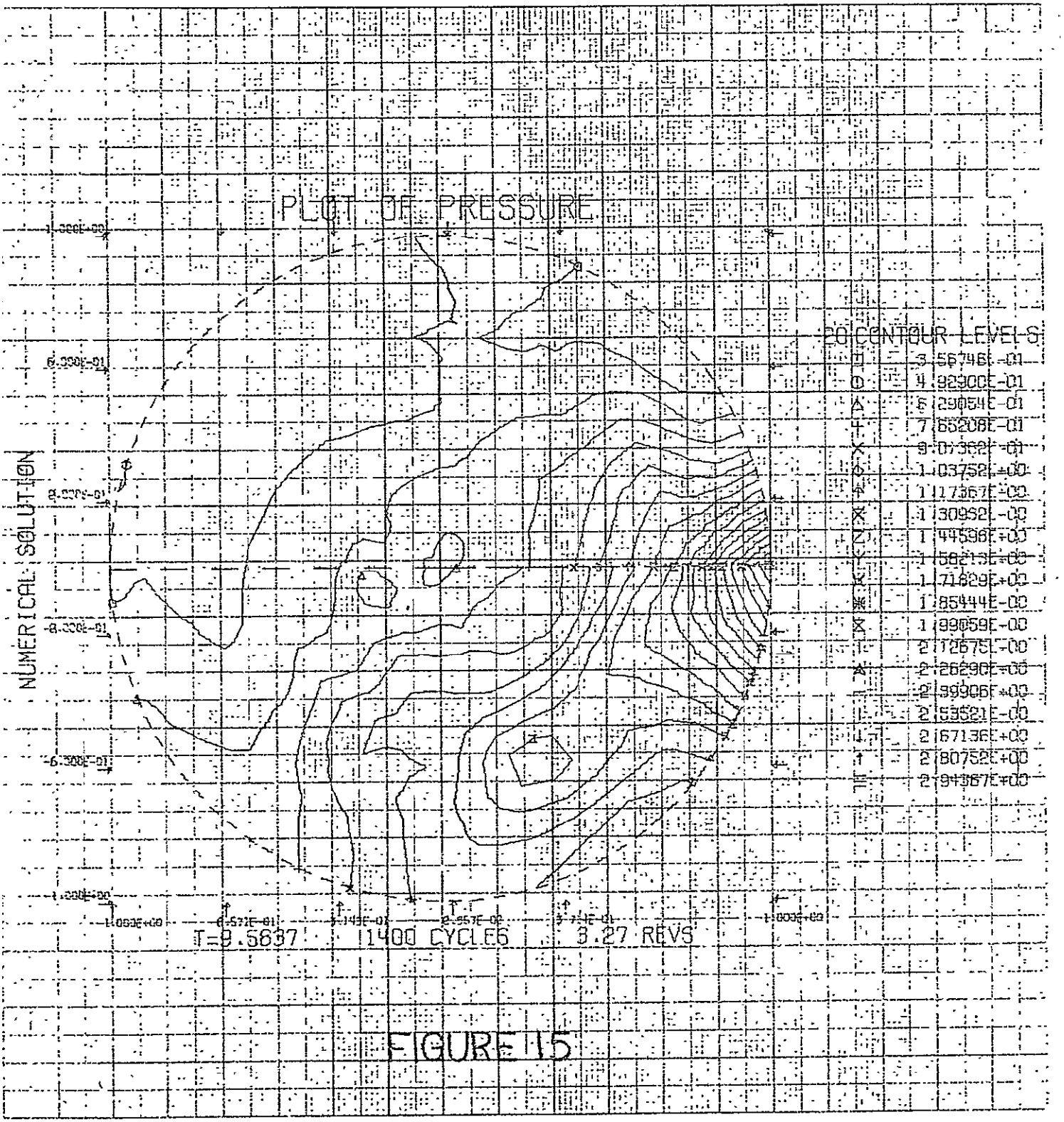
PLOT OF PRESSURE
NUMERICAL SOLUTION
20 CONTOUR LEVELS
3 5674E-01
4 9290E-01
6 2905E-01
7 6520E-01
9 0736E-01
1 0375E+00
1 1736E+00
1 3095E+00
1 4459E+00
1 5821E+00
1 7182E+00
1 8544E+00
1 9905E+00
2 1267E+00
2 2629E+00
2 3990E+00
2 5352E+00
2 6713E+00
2 8075E+00
2 9436E+00
T=9.5637
1400 CYCLES
3.27 REVS

FIGURE 15

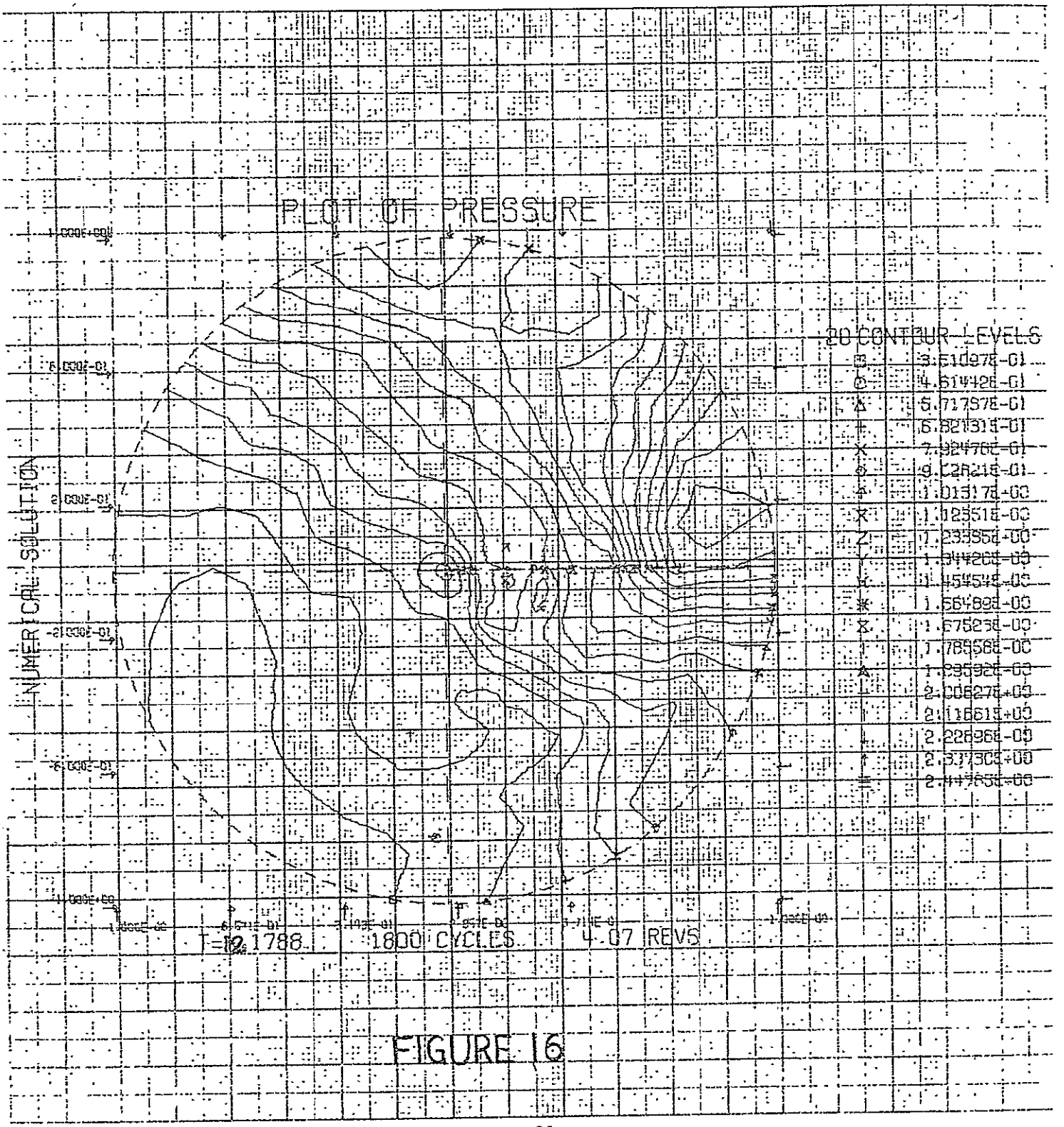
PLOT OF PRESSURE
NUMERICAL SOLUTION
20 CONTOUR LEVELS
T=12.1788
1800 CYCLES
4.07 REVS

FIGURE 16

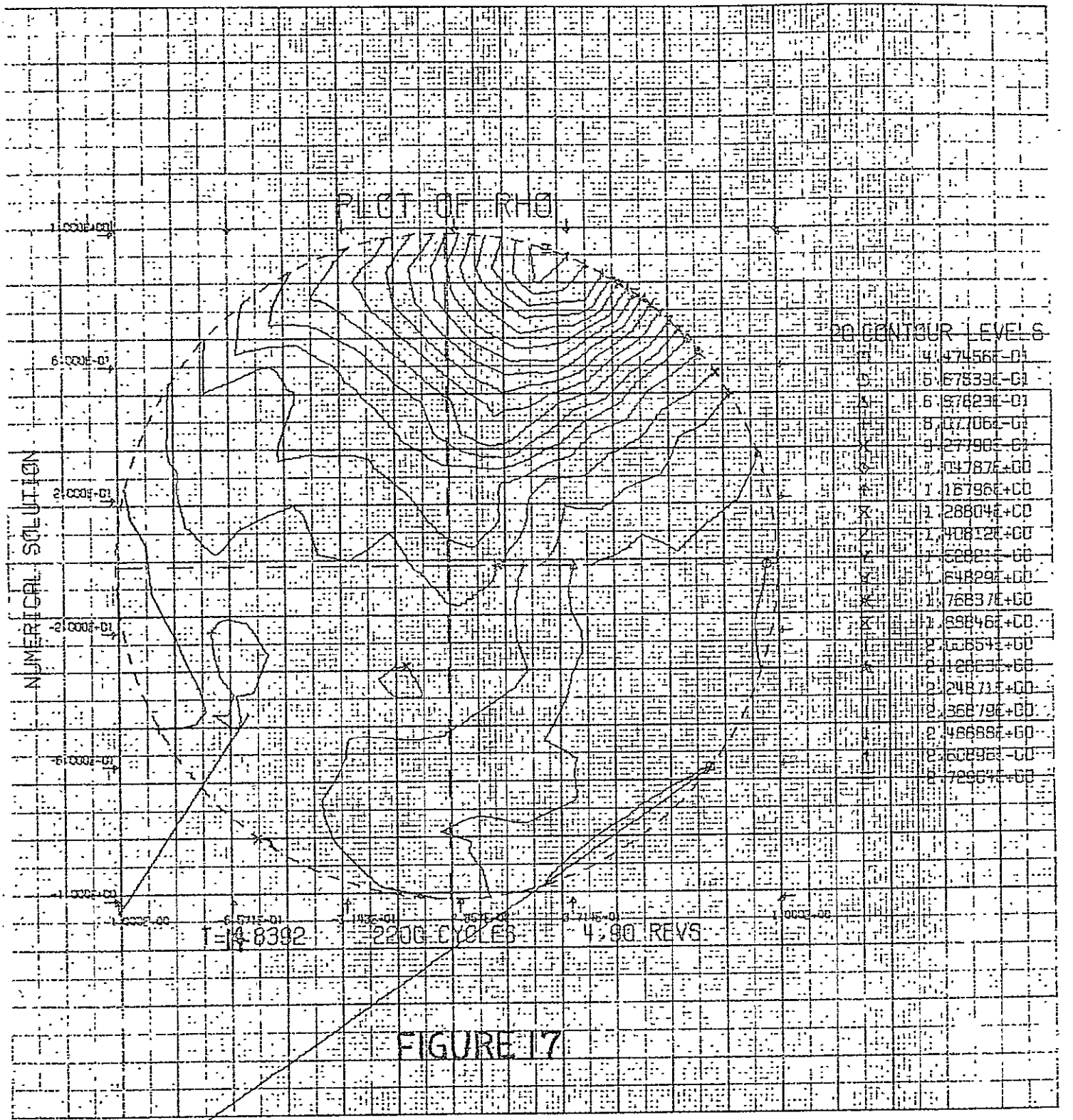
PLOT OF RHO
NUMERICAL SOLUTION
T=14.8392
2200 CYCLES
4.90 REVS
20 CONTOUR LEVELS

FIGURE 17

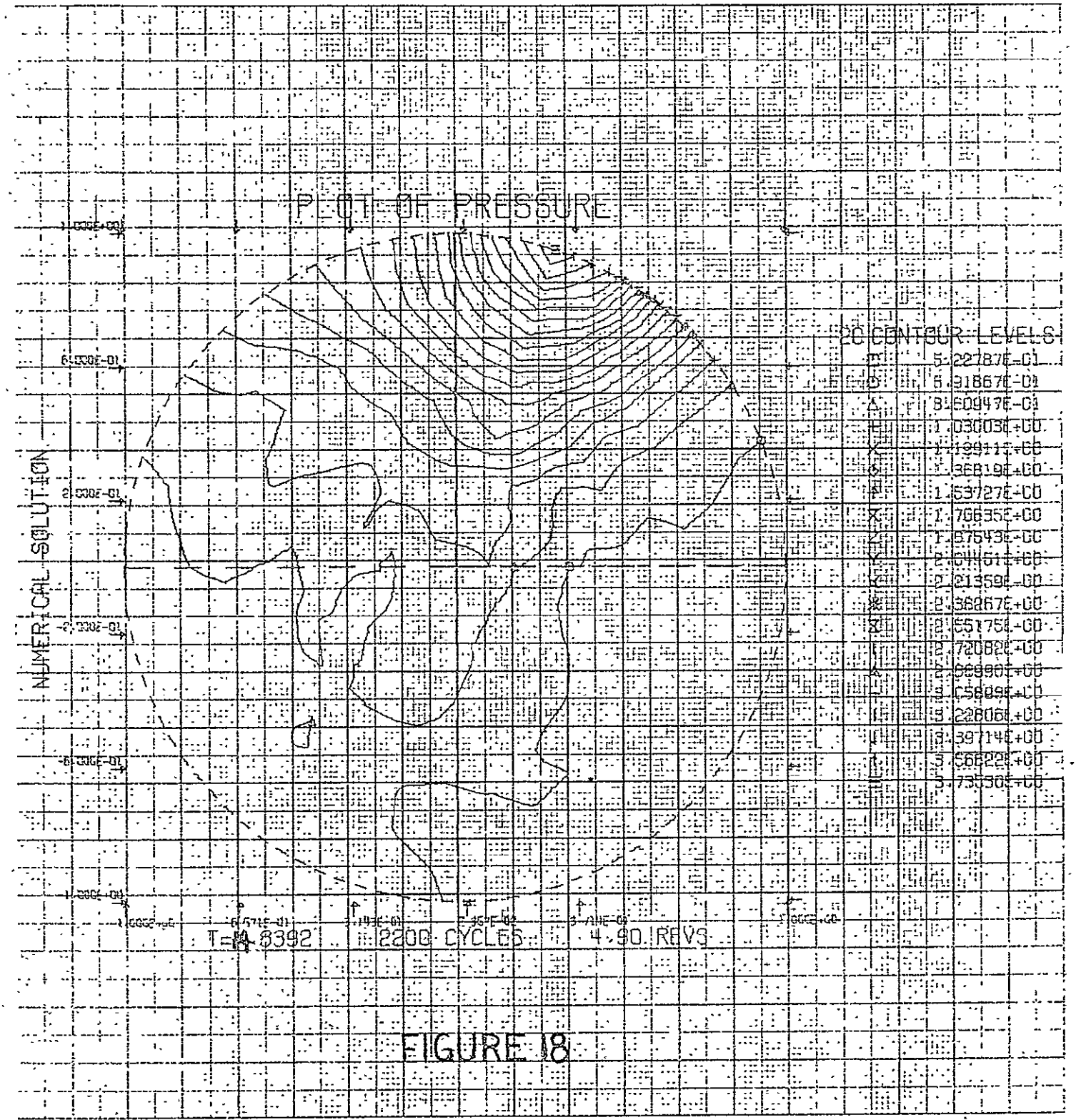
PLOT OF PRESSURE
NUMERICAL SOLUTION
20 CONTOUR LEVELS
T=14.8392
2200 CYCLES
4.90 REVS

FIGURE 18

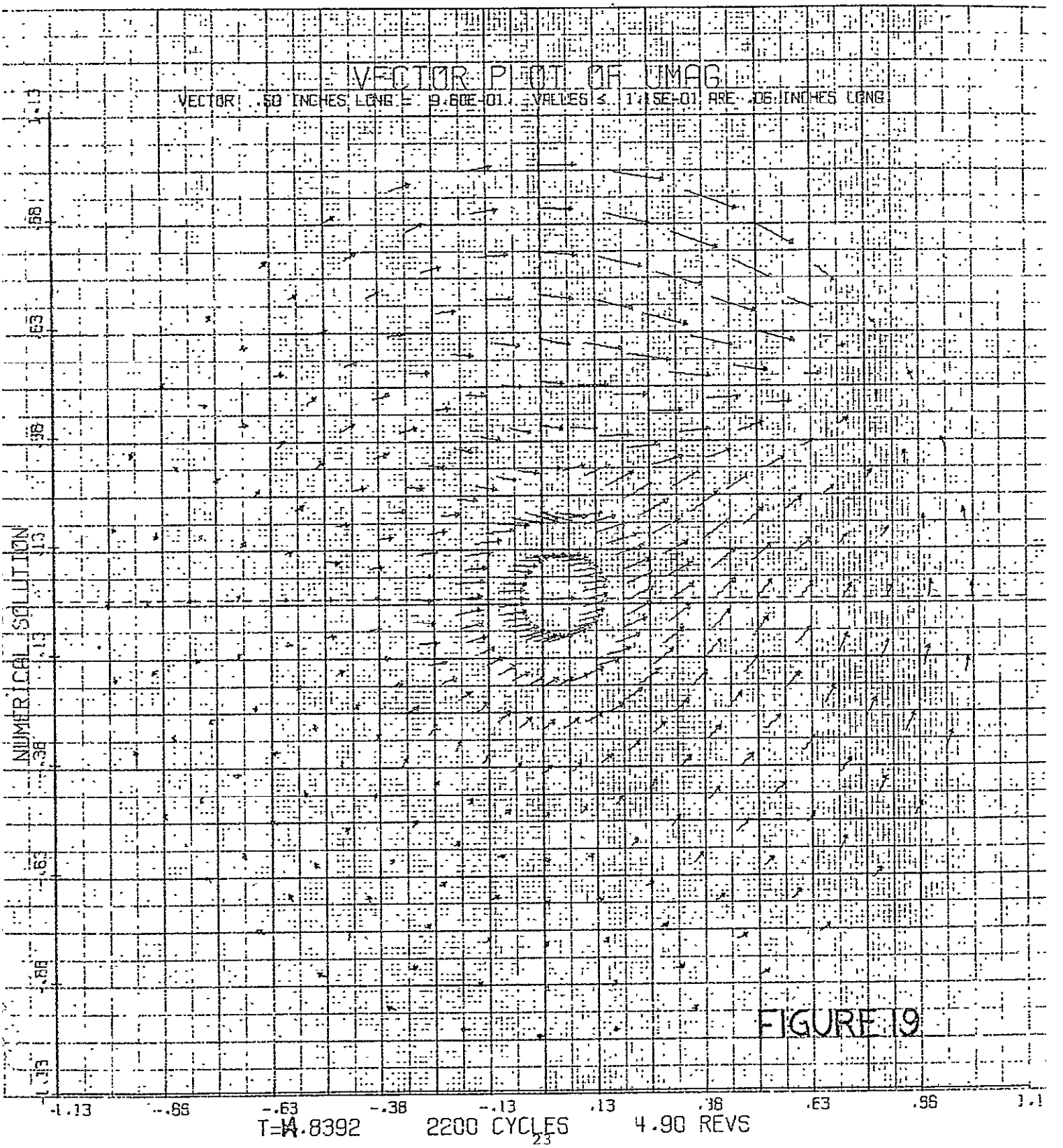
VECTOR PLOT OF UMAG
VECTOR = .50 INCHES LONG = 9.60E-01 VALUES ≤ 1.15E-01 ARE .06 INCHES LONG
NUMERICAL SOLUTION
-1.13
-.88
-.63
-.38
-.13
.13
.38
.63
.88
1.1
T=4.8392 2200 CYCLES 4.90 REVS

FIGURE 19

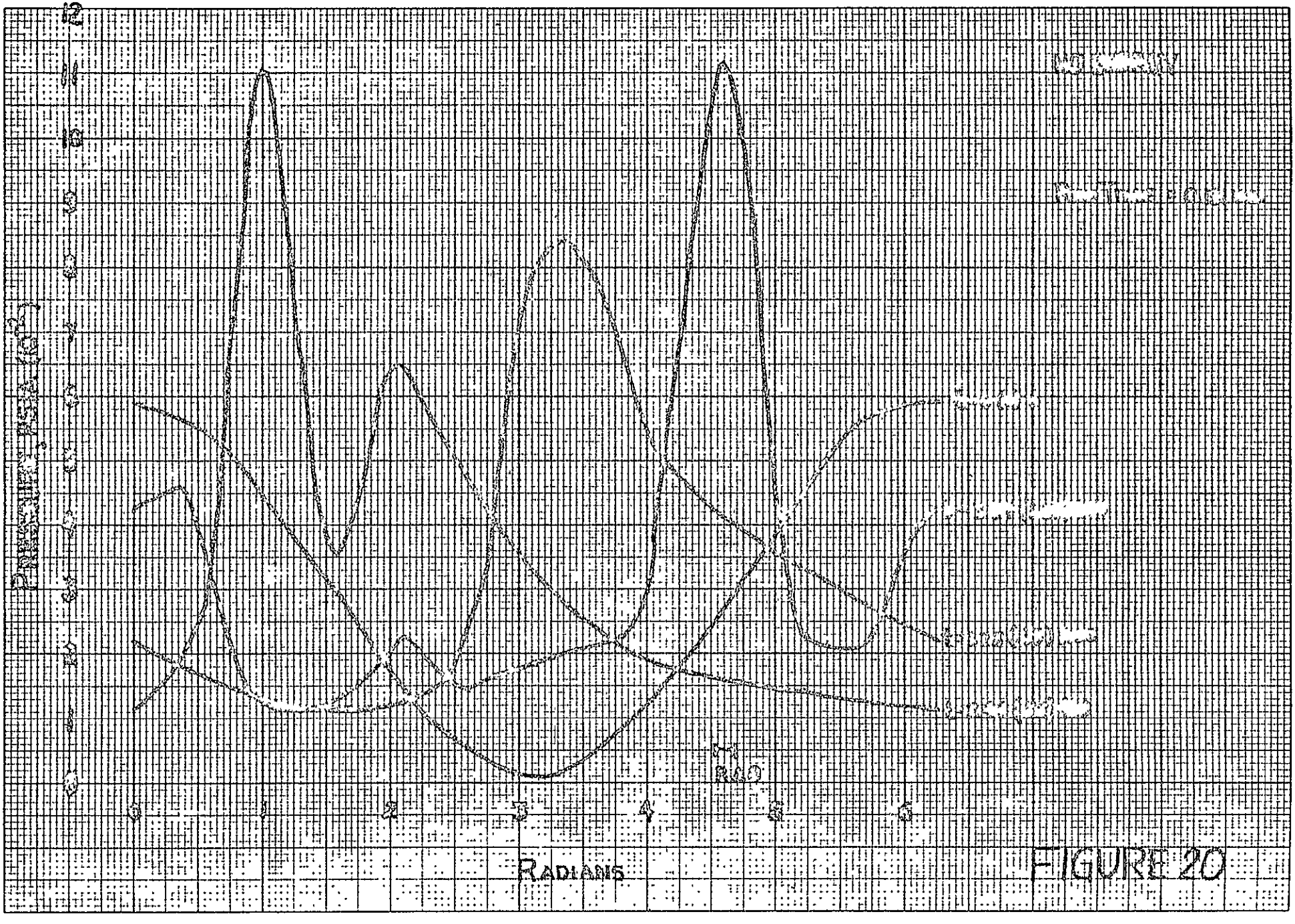

FIGURE 20

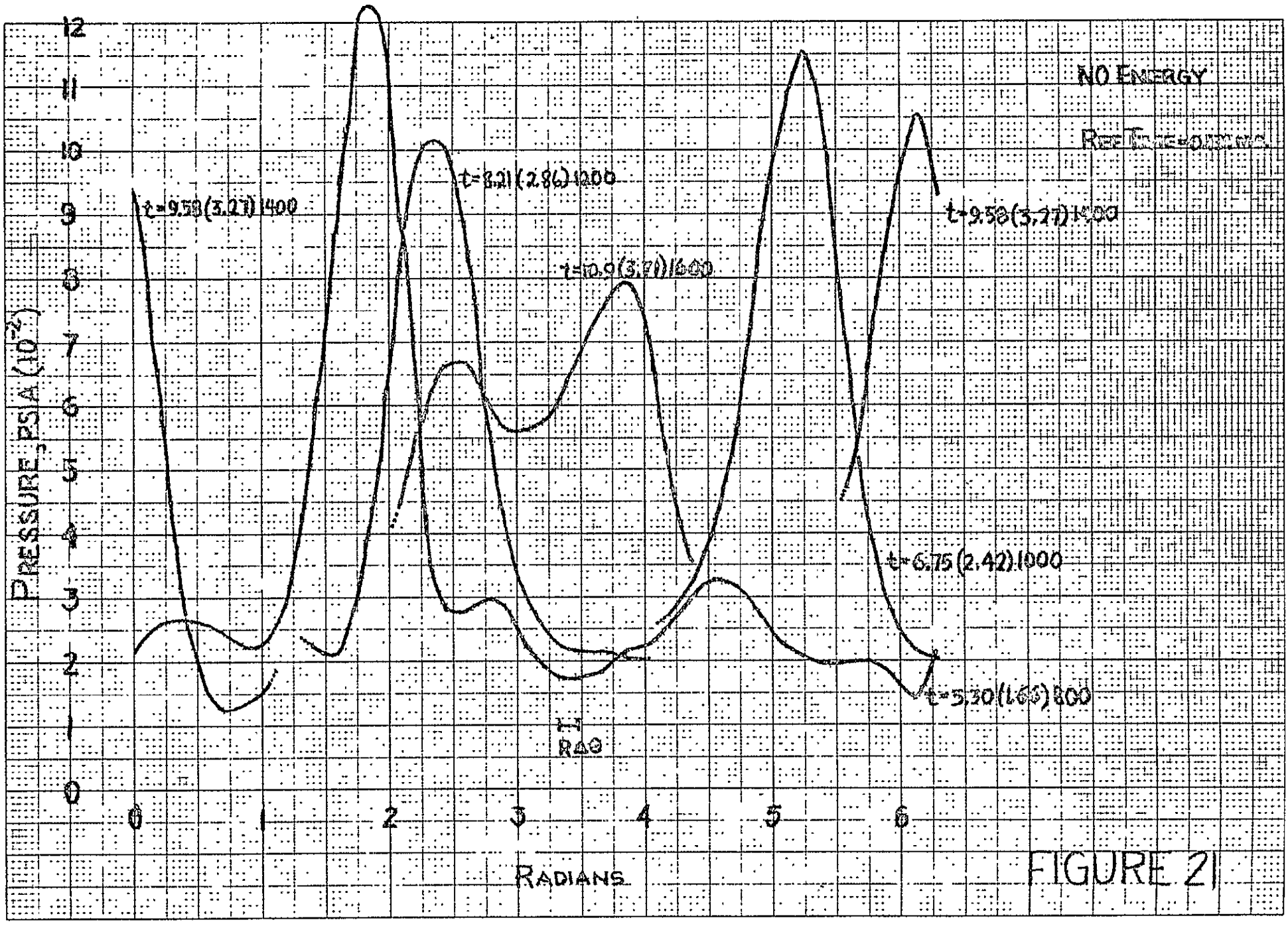
NO ENERGY
t=9.58(3.27)1400
t=8.21(2.86)1200
t=10.9(3.70)1600
t=9.58(3.27)1400
t=6.75(2.42)1000
t=5.30(1.63)800
PRESSURE, PSIA (10⁻²)
RADIANS
0
1
2
3
4
5
6
7
8
9
10
11
12

FIGURE 21

B. Energy Release in a Fluid with Finite Amplitude Waves, Simple Energy Source

We have carried out to completion the calculation started in the second quarterly report and described on page 26 of that report.

The calculation consists of adding an energy source term to the energy equation. There is no associated mass source term in the continuity equation. The energy term is dependent on the local pressure via

$$\dot{E} = \text{const}\,|(p-1)|^{\nu}\cdot\mu, \quad \nu=\tfrac{1}{2} \text{ if } p<1$$

$$\nu=1 \text{ otherwise}$$

It is also assumed that a velocity effect can be included by allowing μ to depend on the magnitude of the velocity $|\vec{u}| = (u^2+v^2)^{\frac{1}{2}}$ via

$$\mu = 1 \quad \text{if } |\vec{u}| \geq \delta$$

$$\mu = 0 \quad \text{otherwise}$$

We chose δ to be large enough so that the energy release occurred within the region of the pressure wave and nowhere else.

Finally, with the experience gained with the calculation described in section E of the second quarterly, we turn on the energy source slowly, i.e., the actual term used in the difference equation is $\omega\dot{E}$ where ω is monitonically increasing and satisfies $0\leq\omega\leq1$. We take ω to be the value of the 'rev' counter during the first rotation of the wave, it is taken as unity for all subsequent rotations.

The calculation starts off exactly as in the last section. Figures 22 and 23 show the extent of the development of the wave after about 1.8 rotations of the wave (note the velocity vector

at r = 0, the rev counter, has just passed the starting position $\theta = -\pi/2$ for the second time) and it is clear that the structure is quite similar to the non-reactive case. However, the peak pressure is 4350 psia. The velocity field is also similar to the non-reactive case. The maximum velocity in the wave corresponds to 9800 ft/sec. Of course, as the calculation proceeds, the pressure amplitude continues to grow reaching a value approximately thirty times the reference pressure while the maximum velocity reaches a value six times the reference sound speed after just four hundred more cycles of calculation.

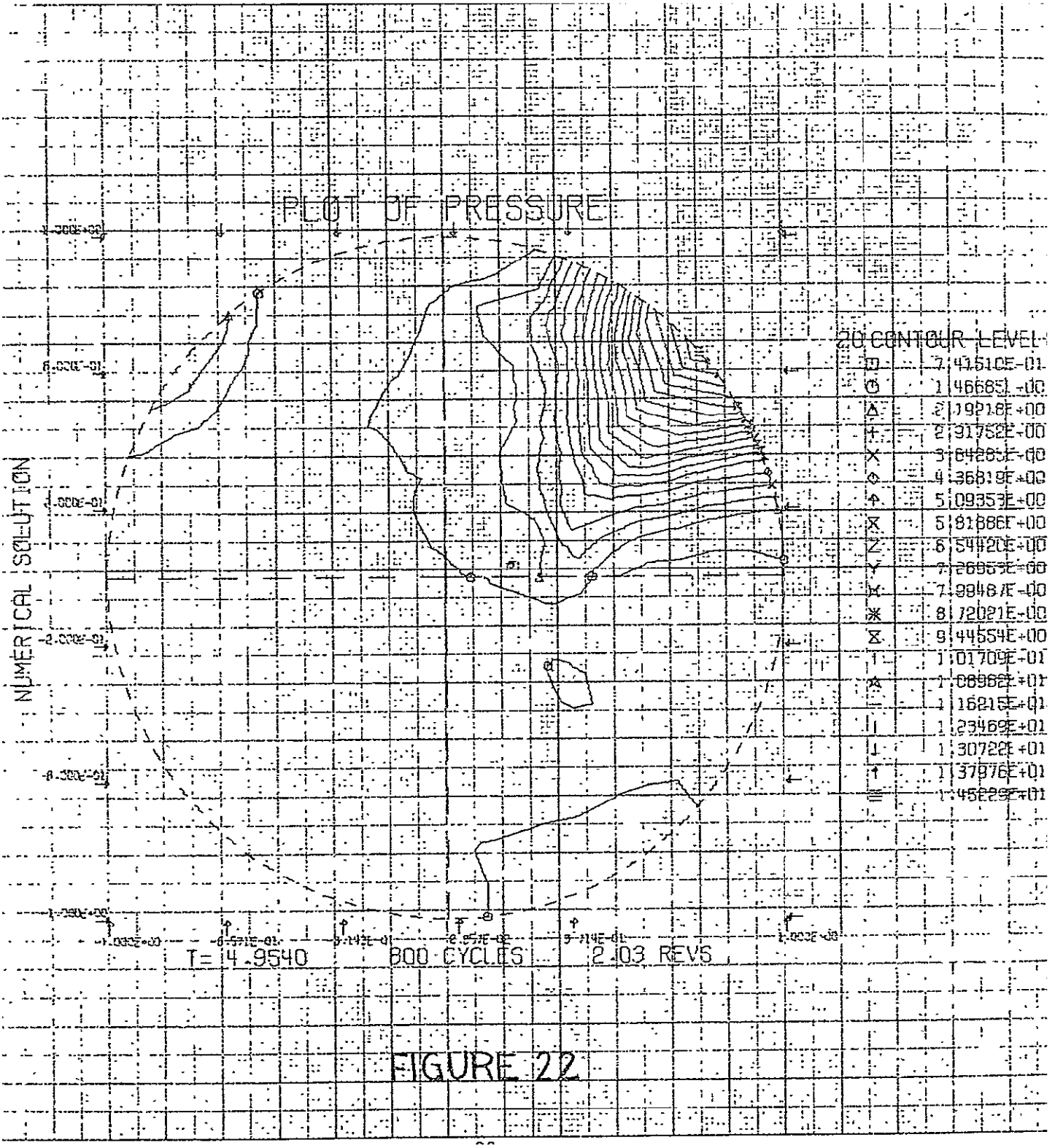
PLOT OF PRESSURE
NUMERICAL SOLUTION
20 CONTOUR LEVEL
7.41510E-01
1.46685E+00
1.99218E+00
2.31752E+00
3.64285E+00
4.36819E+00
5.09353E+00
5.81886E+00
6.54420E+00
7.26953E+00
7.99487E+00
8.72021E+00
9.44554E+00
1.01709E+01
1.08962E+01
1.16215E+01
1.23469E+01
1.30722E+01
1.37976E+01
1.45229E+01
T= 4.9540
800 CYCLES
2.03 REVS

FIGURE 22

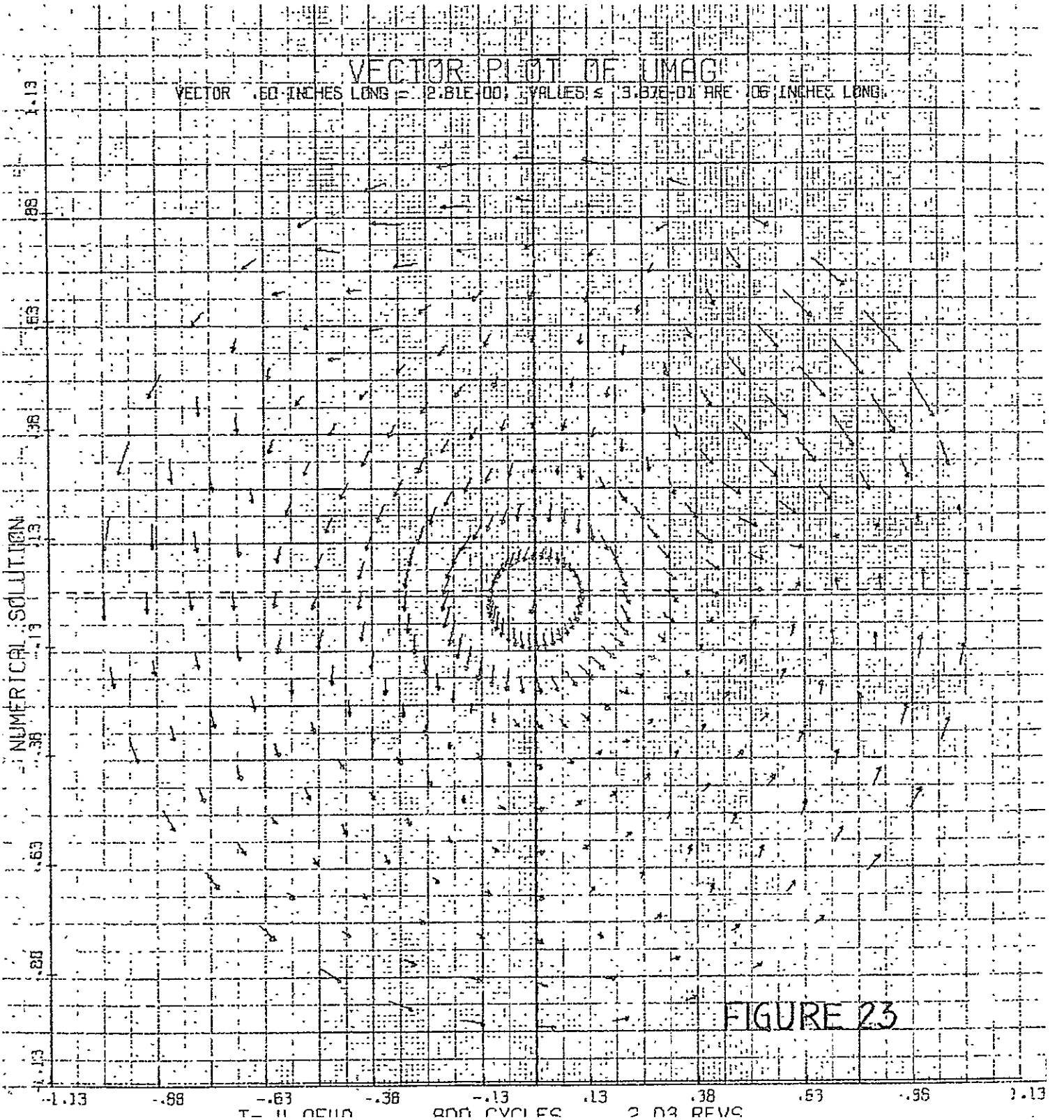
VECTOR PLOT OF UMAG
VECTOR .60 INCHES LONG = 2.81E-00 VALUES ≤ 3.83E-01 ARE .06 INCHES LONG
NUMERICAL SOLUTION
1.13
.88
.63
.38
.13
-.13
-.38
-.63
-.88
-1.13
-1.13
-.88
-.63
-.38
-.13
.13
.38
.63
.88
1.13

FIGURE 23

C. Energy Release in a Fluid with Finite Amplitude Waves (Including the Axial Flux Calculation)

It is clear from the last section that unless energy is allowed to leave the system convectively, the pressure (as well as the specific internal energy) will continue to increase monotonically. Program COMB was then modified to include, in an approximate way, a value for the axial flux of energy.

Several approximations were tried. The first method, and perhaps the most obvious, involved in essentially finding the total energy (and mass) contained in the r-θ plane for each cycle of computation. The excess due to accumulation is parceled equally so that at each mesh point there exists a contribution to outflow which will exceed the inflow by just the amount that is accumulated. It was found that this procedure seems to work for small amplitude waves where only slight spatial variations in the energy release exist. However, for finite amplitude waves which initiate locally large influxes of mass and energy (due to increased transport processes on the droplet spray) this procedure fails to work. Some regions of the flow field where little reaction occurs see, according to this procedure, a relatively large outflow of energy (or mass). If this occurs for a sufficient number of time steps, the flow pressure (or density) can become negative locally and indeed this has been our observation. It is clear that a weighting of the outflow according to the inflow would be more desirable.

This was done for the simple energy release model given in the last section; the results being given below. The energy that was input due to combustion was allowed to reside in the r, θ

plane for one time step and then it was immediately considered to contribute to the axial flux. The following table gives a quick comparison of the value of $p_{max}/\gamma p_\infty$ of three calculations. The first column is an inert calculation with no energy term, the second with the simple energy model including an energy flux in the axial direction, and finally the third calculation is with the simple energy model but no convective flux in the z direction, i.e., the energy is locked in.

Wave Amplitude ($P_{max}/\gamma P_\infty$)

Cycle	Inert Case	With Axial Flux	Trapped Case
0	1.63	1.63	1.63
600	3.25	3.73	7.18
1000	3.21	3.53	19.57
1200	3.05	3.45	29.65
1400	2.84	3.91	-----

The final row of data corresponds to approximately 3.27 rotations of the wave and it is clear that by including the axial flux, the rapid growth of the wave is controlled while the energy source itself supplies energy to the wave.

It was found that for values of ten times the constant in the energy law in section B, the solution could not be continued beyond 300 cycles. This value is consistent with a physically real energy release near the injector. It is clear that the evaluation of the axial flux is quite critical and indeed, the problem really requires a third dimension so as to mathematically pose the calculation correctly.

D. Finite Amplitude Waves and Simplified Modified Godsave Analysis

In this section we show the results of a tangential pressure wave interacting with a system of droplets (mean diameter = 75μ) which evaporates and burns according to the simplified Godsave analysis presented in Section II of this report. Hence, there is both an energy source for the energy equation as well as a mass source included in the continuity equation. However, there is no axial flux calculation included in this section.

The calculation consisted in specifying the flow field at $t = 0$. It is similiar to that given in figures 1 and 2 except that the maximum (minimum) pressure is 550 psia (50 psia). The calculation proceeds without energy addition for as long as it takes the wave to make one complete rotation. Then the calculation incorporates the relations developed in Section II of this report for the evaporation and combustion of the droplets. The energy and mass source is turned on completely just as the wave is starting its second period of rotation. Figures 24 and 25 give the fluid dynamic field just before the droplets start interacting (excuse the extraneous hash for this series of pictures which is due to a malfunctioning solenoid valve hooked onto the pen on the Calcomp Plotter). For this series of pictures the pressure is normalized with p_∞ (rather than γp_∞ as before). Figure 26 gives the dimensional pressure $p(R,\theta)$ at $t = 3.3259$ units at the outer wall of the chamber ($r = R$), again just before the energy is switched on. The wave is moving from right to left.

The next two figures, 27 and 28, show the initial transient as the energy is switched on. Due to large radial components, figure 28, the pressure pulse moves inward, but still undergoing rotation as the next four figures indicate (figures 29-32). The next sequence of figures (figures 33-38) show the transition to the compression/rarefaction pulse traveling along the chamber wall (except that strong radial motion flattens the pulse against the wall). This is seen from figure 39 to the final figure 44. As can be seen from figures 28 and 30, strong radial motion is generated by the large release of energy and persists as transverse motion is interacting with the tangential motion. The resultant 'steady' or time periodic pattern would require additional calculation.

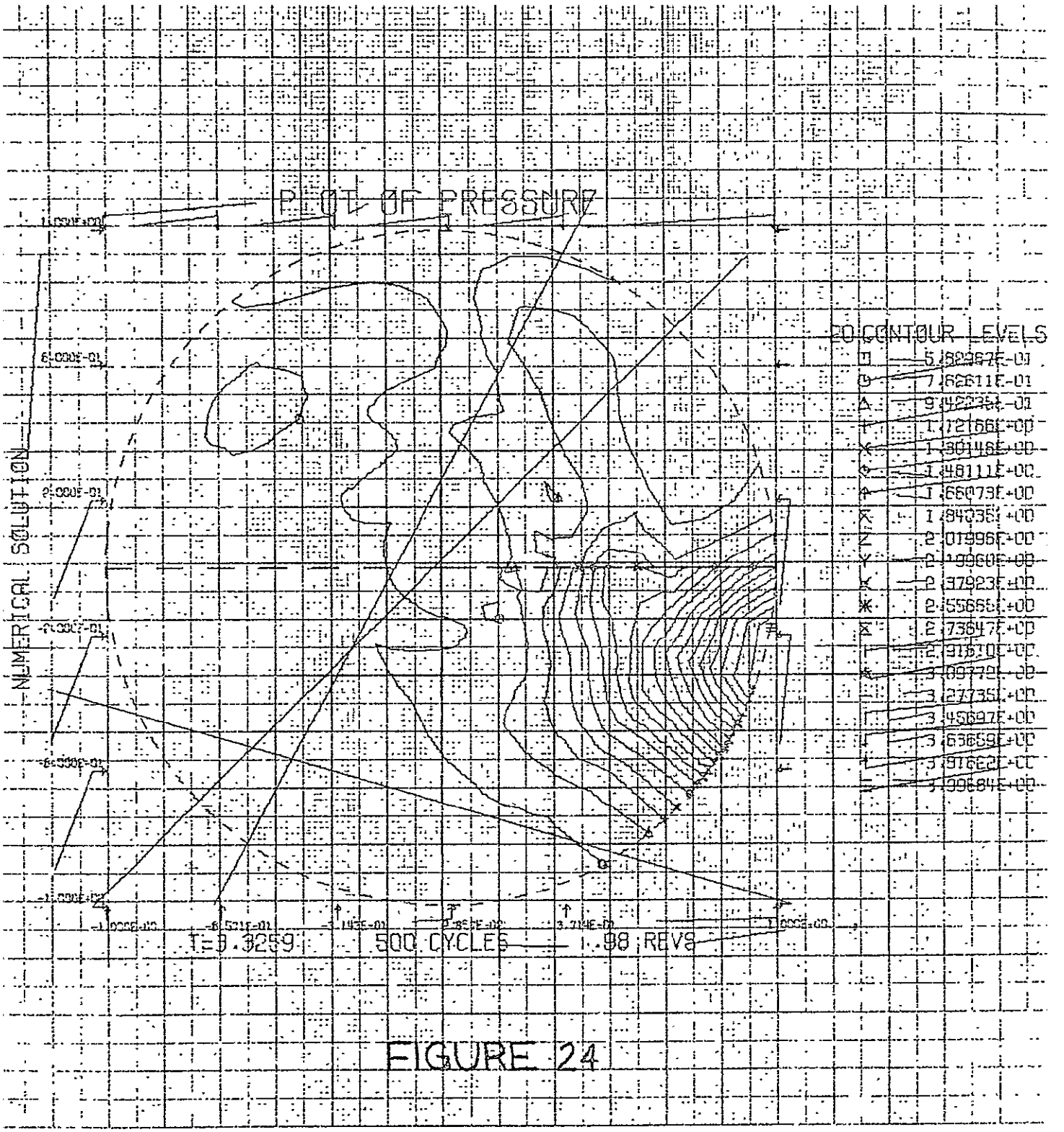
PLOT OF PRESSURE
NUMERICAL SOLUTION
20 CONTOUR LEVELS
T=9.3259
500 CYCLES
.98 REVS

FIGURE 24

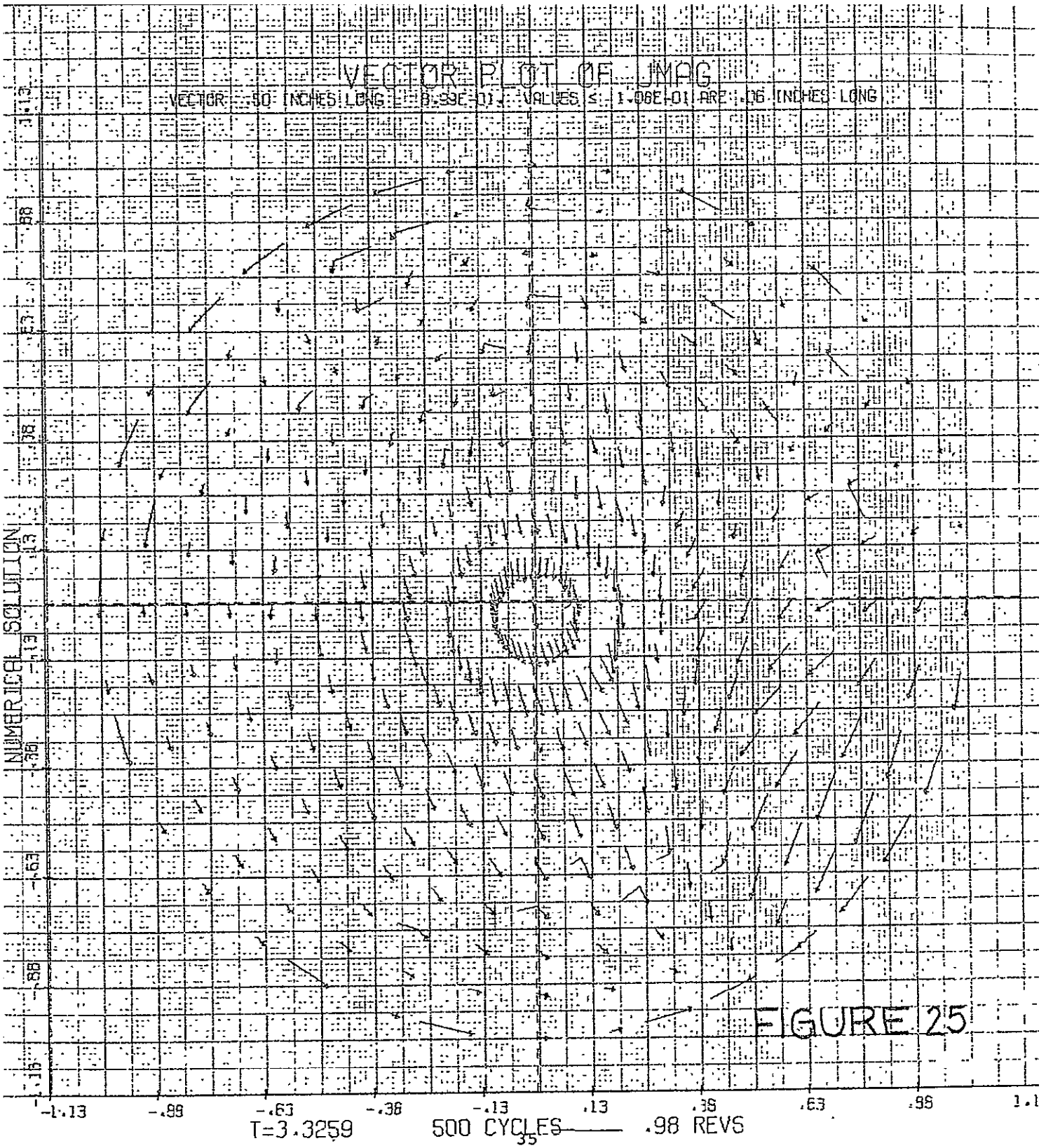
VECTOR PLOT OF JMAG
VECTOR = 50 INCHES LONG 8.93E-01 VALUES ≤ 1.06E-01 ARE .06 INCHES LONG
NUMERICAL SOLUTION
1.13
.88
.63
.38
.13
-.13
-.38
-.63
-.88
-1.13
-1.13
-.88
-.63
-.38
-.13
.13
.38
.63
.88
1.1
T=3.3259
500 CYCLES
.98 REVS

FIGURE 25

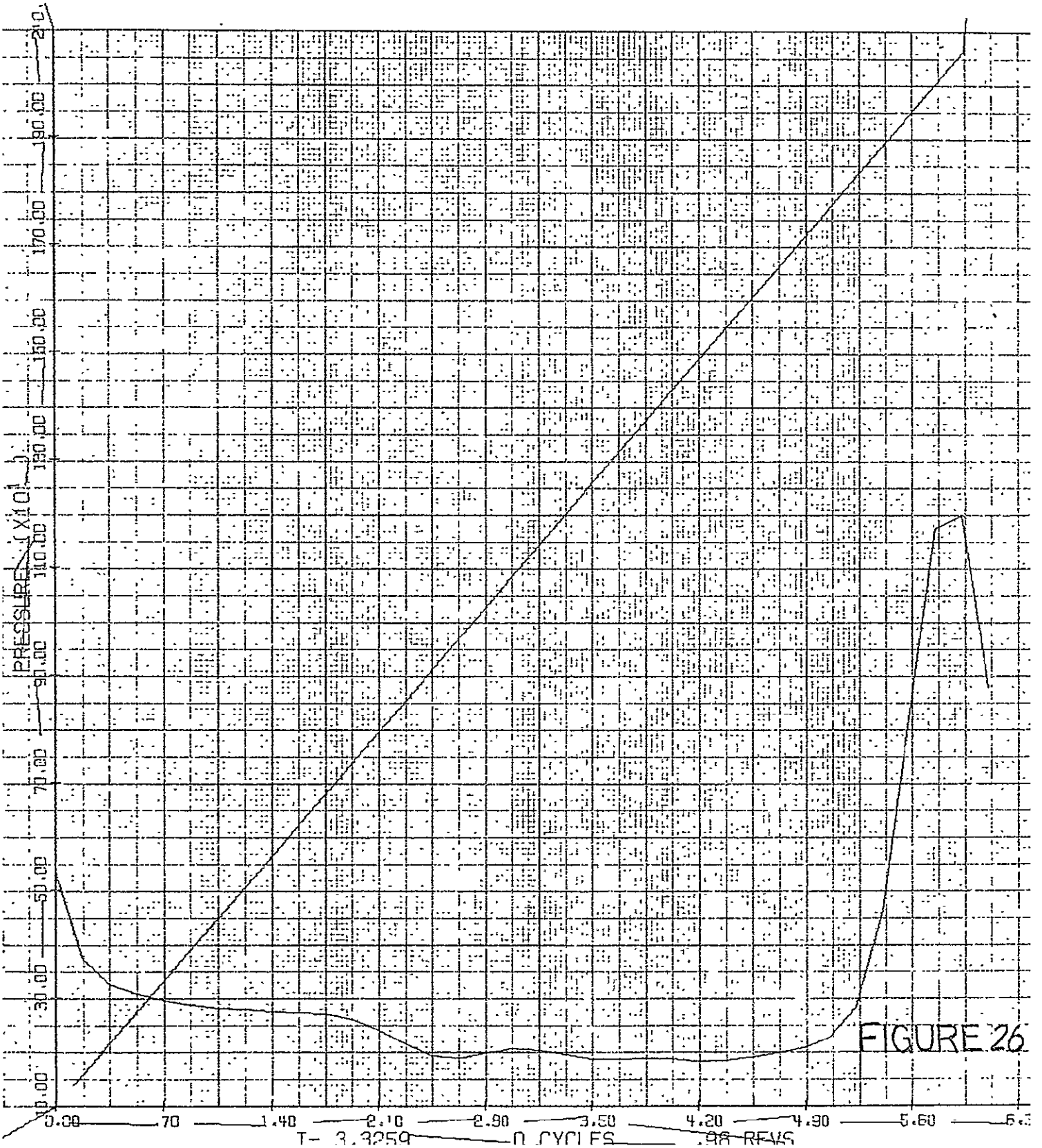
PRESSURE (X1 0)
210.00
190.00
170.00
150.00
130.00
110.00
90.00
70.00
50.00
30.00
10.00
0.00
.70
1.40
2.10
2.80
3.50
4.20
4.90
5.60
T= 3.3259
0 CYCLES
98 REVS

FIGURE 26

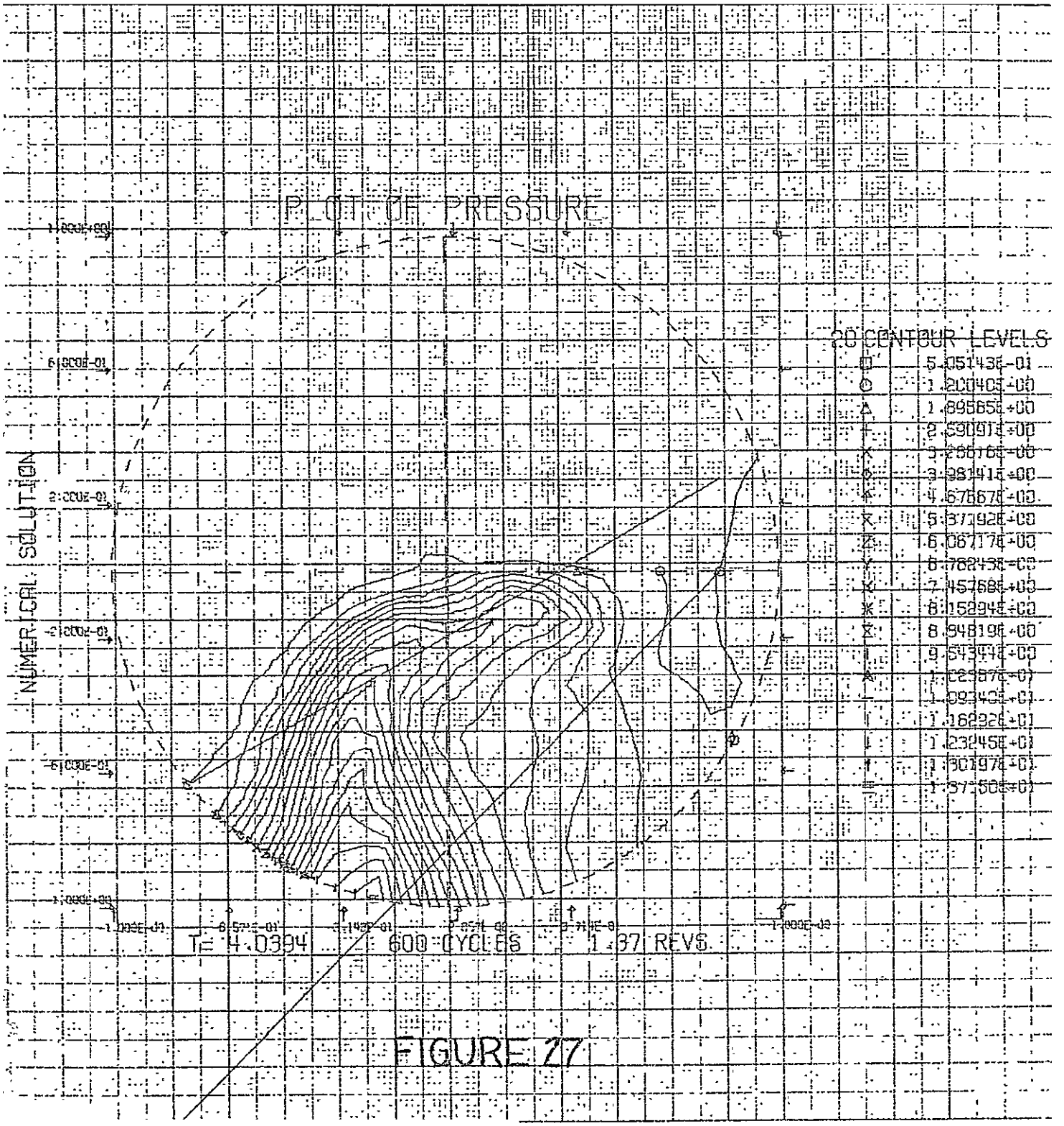
PLOT OF PRESSURE
NUMERICAL SOLUTION
20 CONTOUR LEVELS
5.051436E-01
1.200403E+00
1.895665E+00
2.590917E+00
3.286168E+00
3.981419E+00
4.676670E+00
5.371921E+00
6.067172E+00
6.762423E+00
7.457674E+00
8.152925E+00
8.848176E+00
9.543427E+00
1.023868E+01
1.093393E+01
1.162918E+01
1.232445E+01
1.301970E+01
1.371495E+01
T= 4.0394
600 CYCLES
1.37 REVS

FIGURE 27

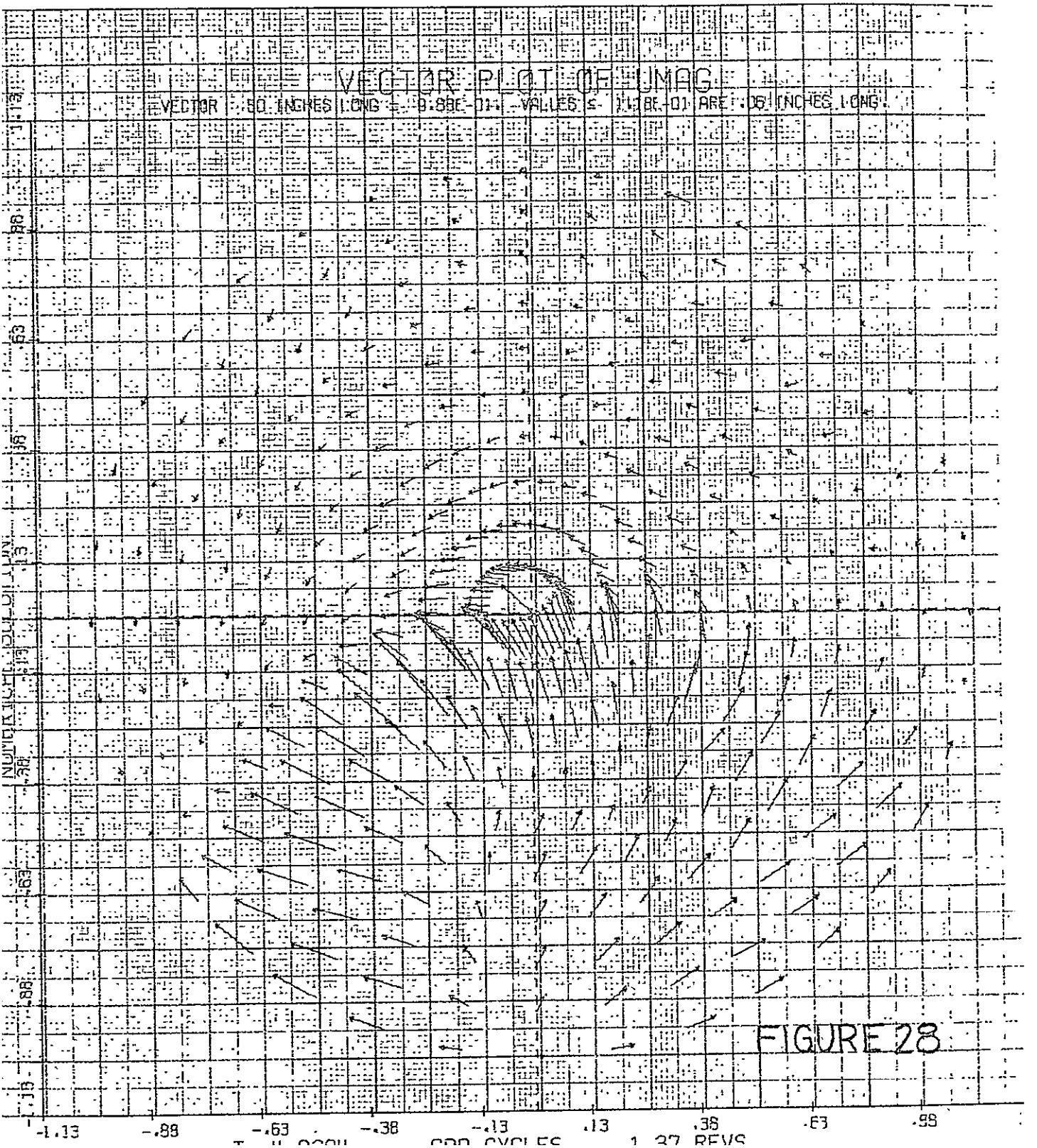
VECTOR PLOT OF UMAG
VECTOR = 50 INCHES LONG = 9.88E-01 VALUES = 1.18E-01 ARE .06 INCHES LONG
NUMERICAL SOLUTION
-1.13
-.88
-.63
-.38
-.13
.13
.38
.63
.88
1.13
1.37 REVS

FIGURE 28

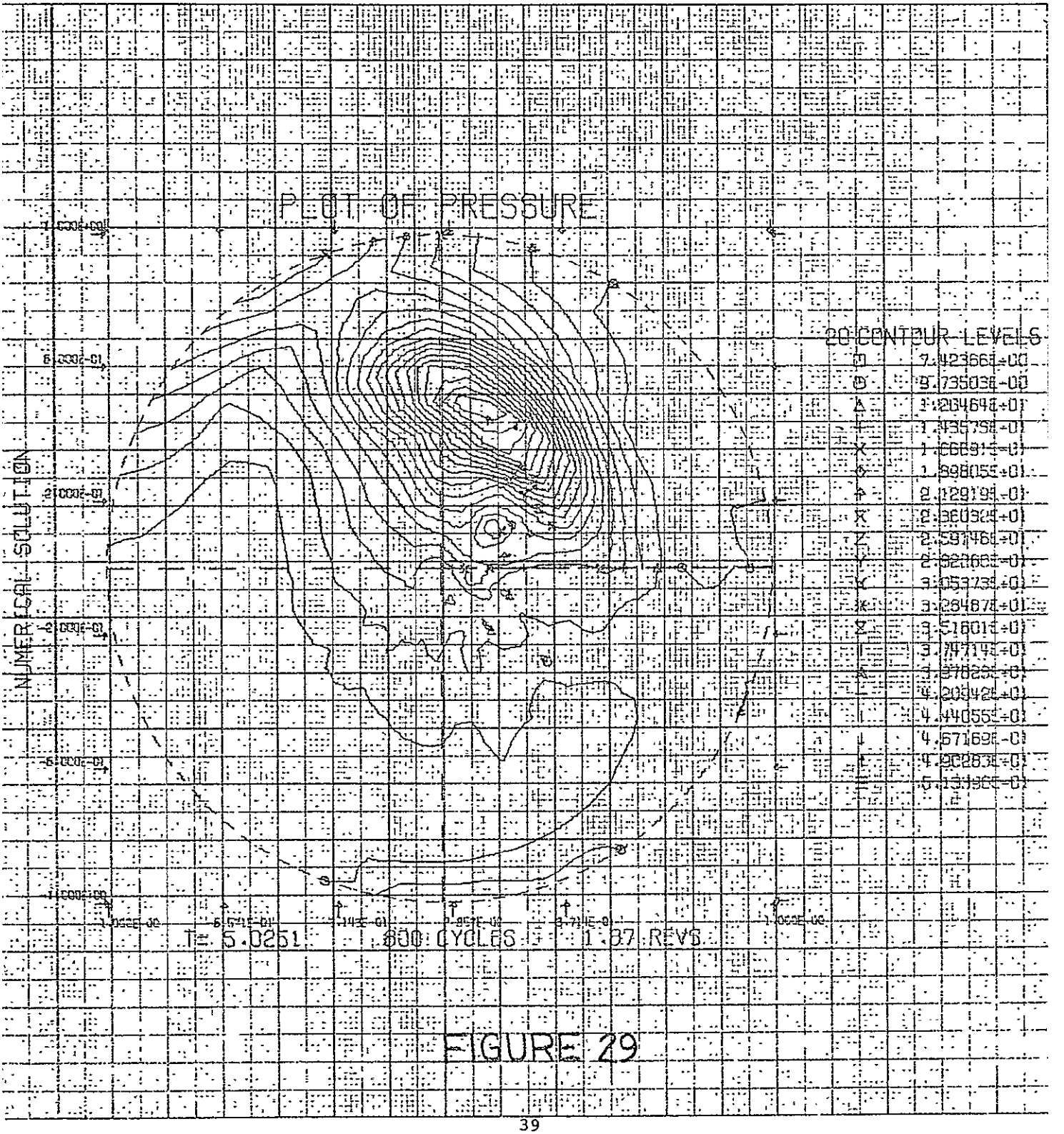
PLOT OF PRESSURE
20 CONTOUR LEVELS
NUMERICAL SOLUTION
T= 5.0251
800 CYCLES
1.87 REVS

FIGURE 29

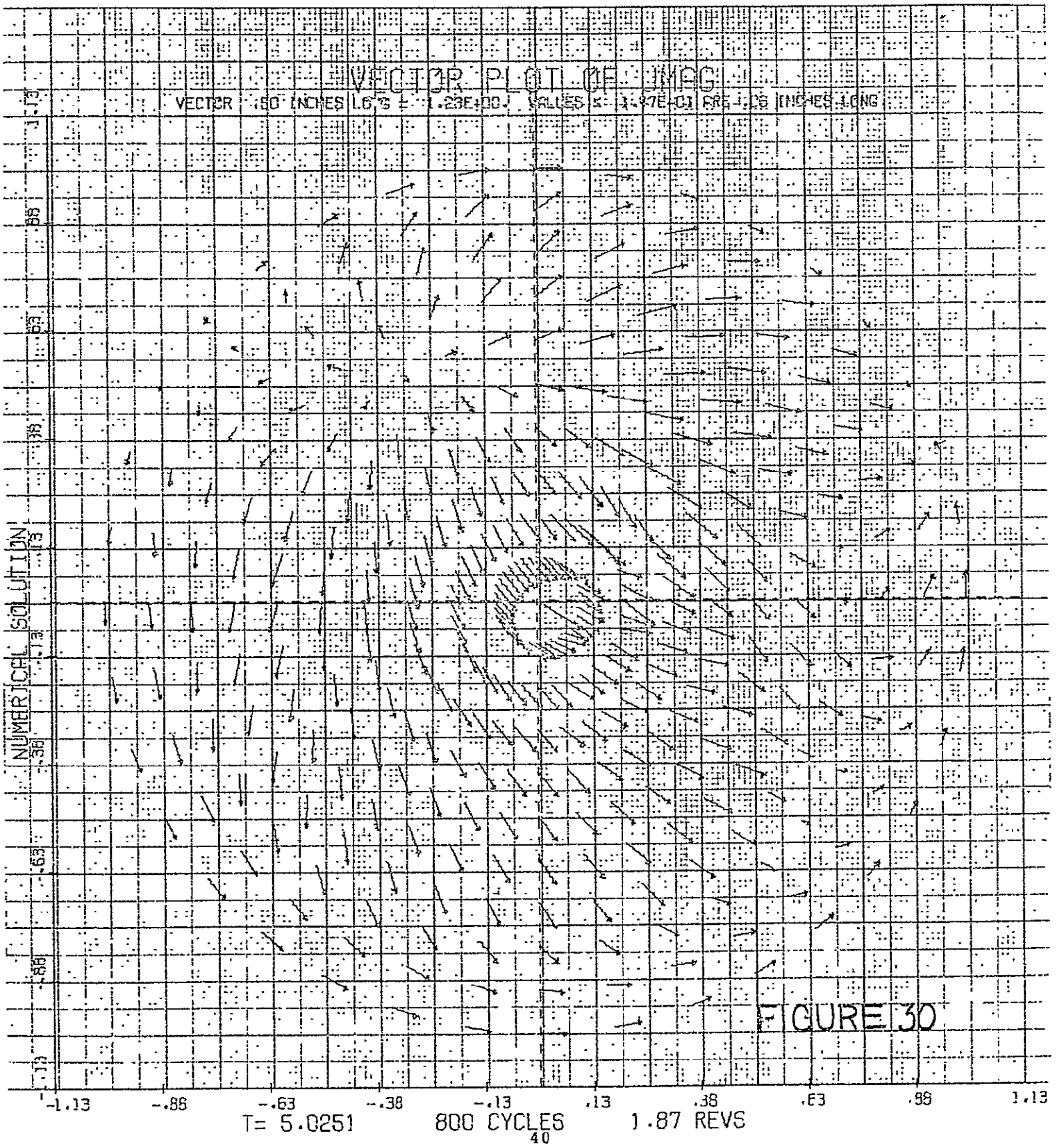
VECTOR PLOT OF VMAG
VECTOR = .50 INCHES LG'S = 1.23E+00 VALUES = 1.87E-01 PER .25 INCHES LONG
NUMERICAL SOLUTION
-1.13
-.88
-.63
-.38
-.13
.13
.38
.63
.88
1.13
T= 5.0251
800 CYCLES
1.87 REVS

FIGURE 30

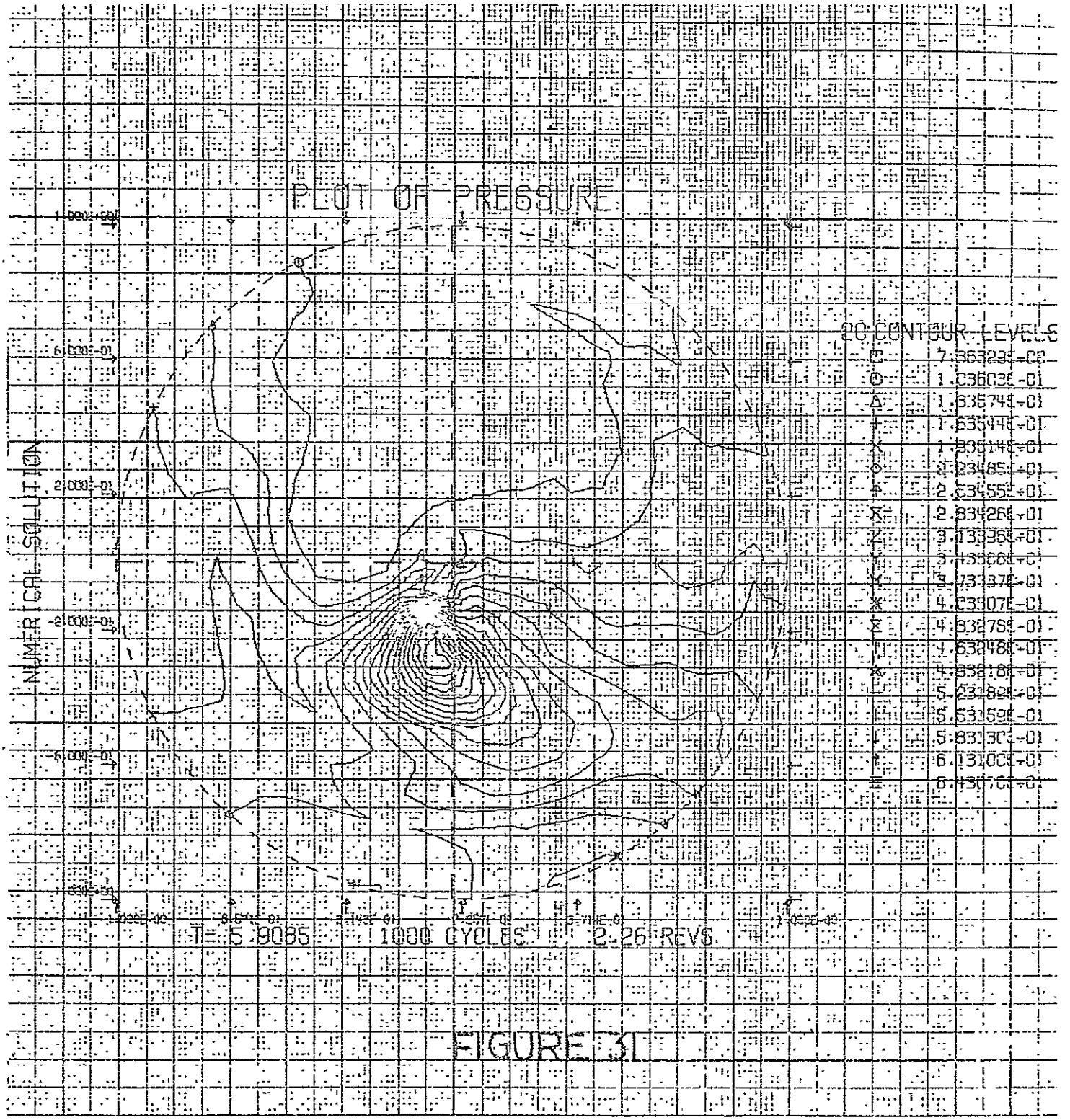
PLOT OF PRESSURE
NUMERICAL SOLUTION
20 CONTOUR LEVELS
7.363238E-02
1.036036E-01
1.335745E-01
1.635454E-01
1.935164E-01
2.234854E-01
2.534559E-01
2.834268E-01
3.133959E-01
3.433684E-01
3.733374E-01
4.033079E-01
4.332789E-01
4.632498E-01
4.932188E-01
5.231898E-01
5.531598E-01
5.831303E-01
6.131009E-01
6.430719E-01
TIME 5.9085
1000 CYCLES
2.26 REVS

FIGURE 31

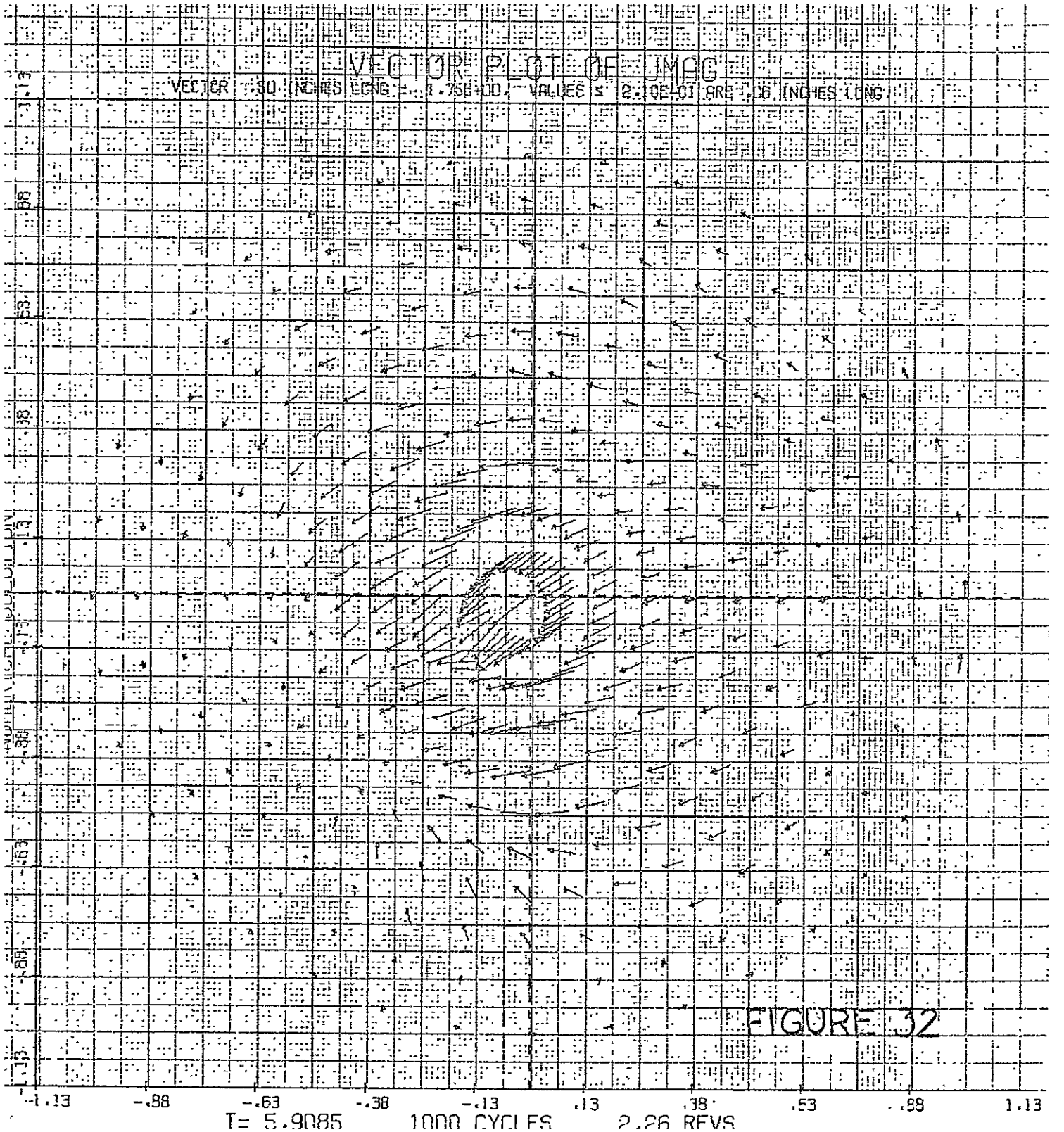
VECTOR PLOT OF JMCG
VECTOR .50 INCHES LONG = 1.75E+00 VALUES ≤ 2.10E-01 ARE .06 INCHES LONG
-1.13
-.88
-.63
-.38
-.13
.13
.38
.63
.88
1.13
T= 5.9085 1000 CYCLES 2.26 REVS

FIGURE 32

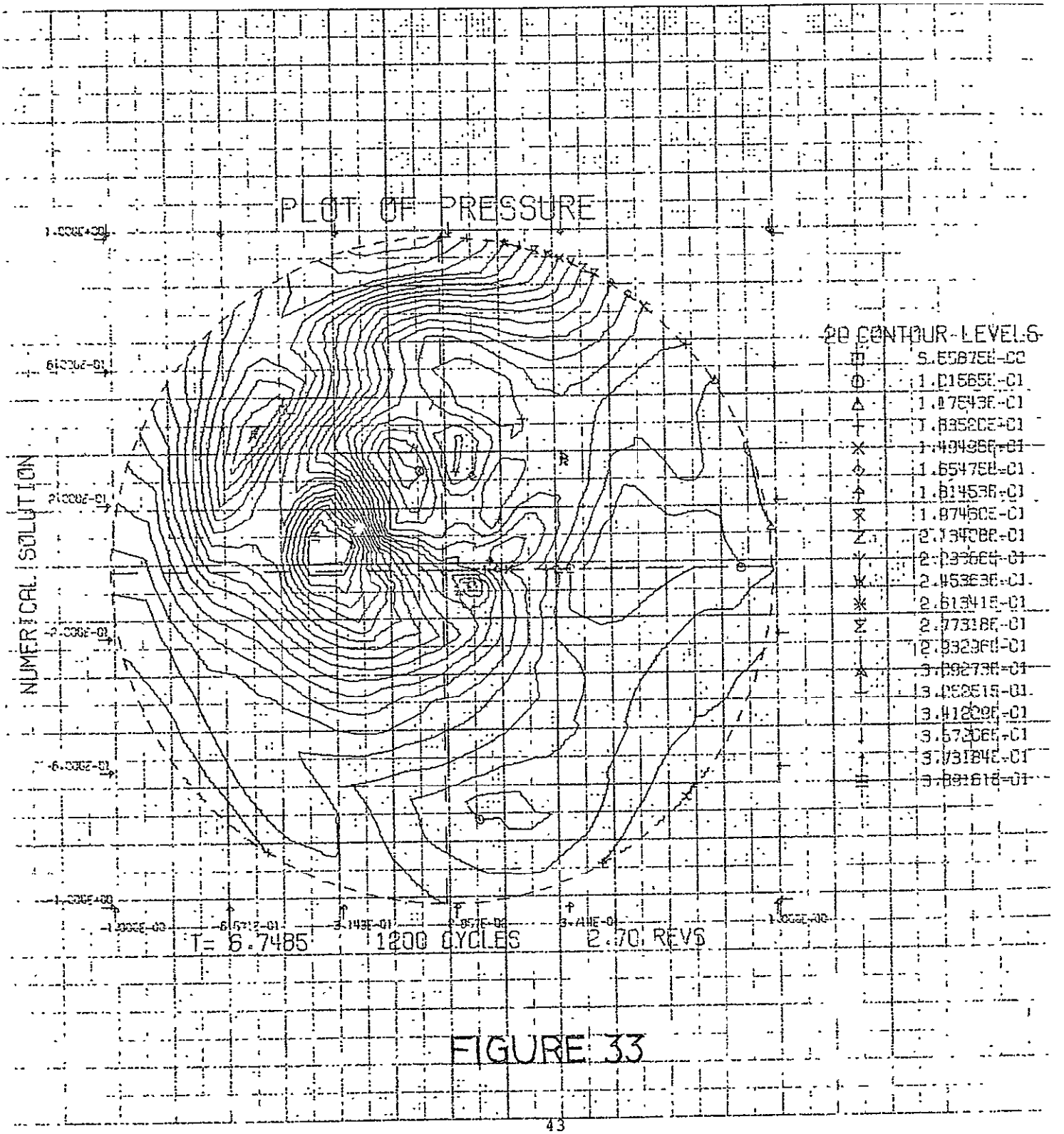
PLOT OF PRESSURE
NUMERICAL SOLUTION
20 CONTOUR LEVELS
T= 6.7485
1200 CYCLES
2.70 REVS

FIGURE 33

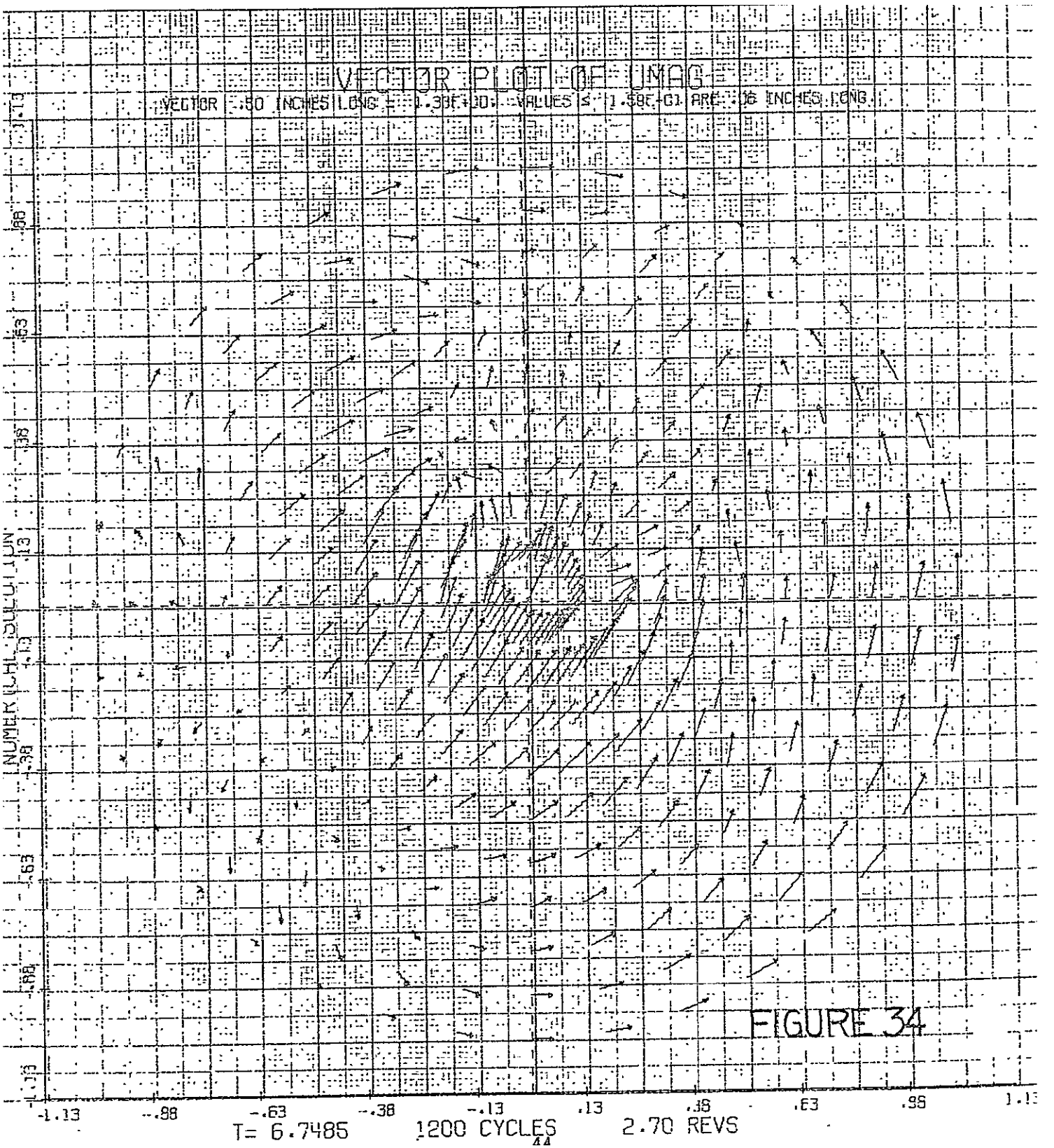
VECTOR PLOT OF UMAG
VECTOR .50 INCHES LONG = 1.38E+00 VALUES = 1.58E+01 ARE 16 INCHES LONG
NUMERICAL SOLUTION
-1.13
-.88
-.63
-.38
-.13
.13
.38
.63
.88
1.13
T= 6.7485 1200 CYCLES 2.70 REVS

FIGURE 34

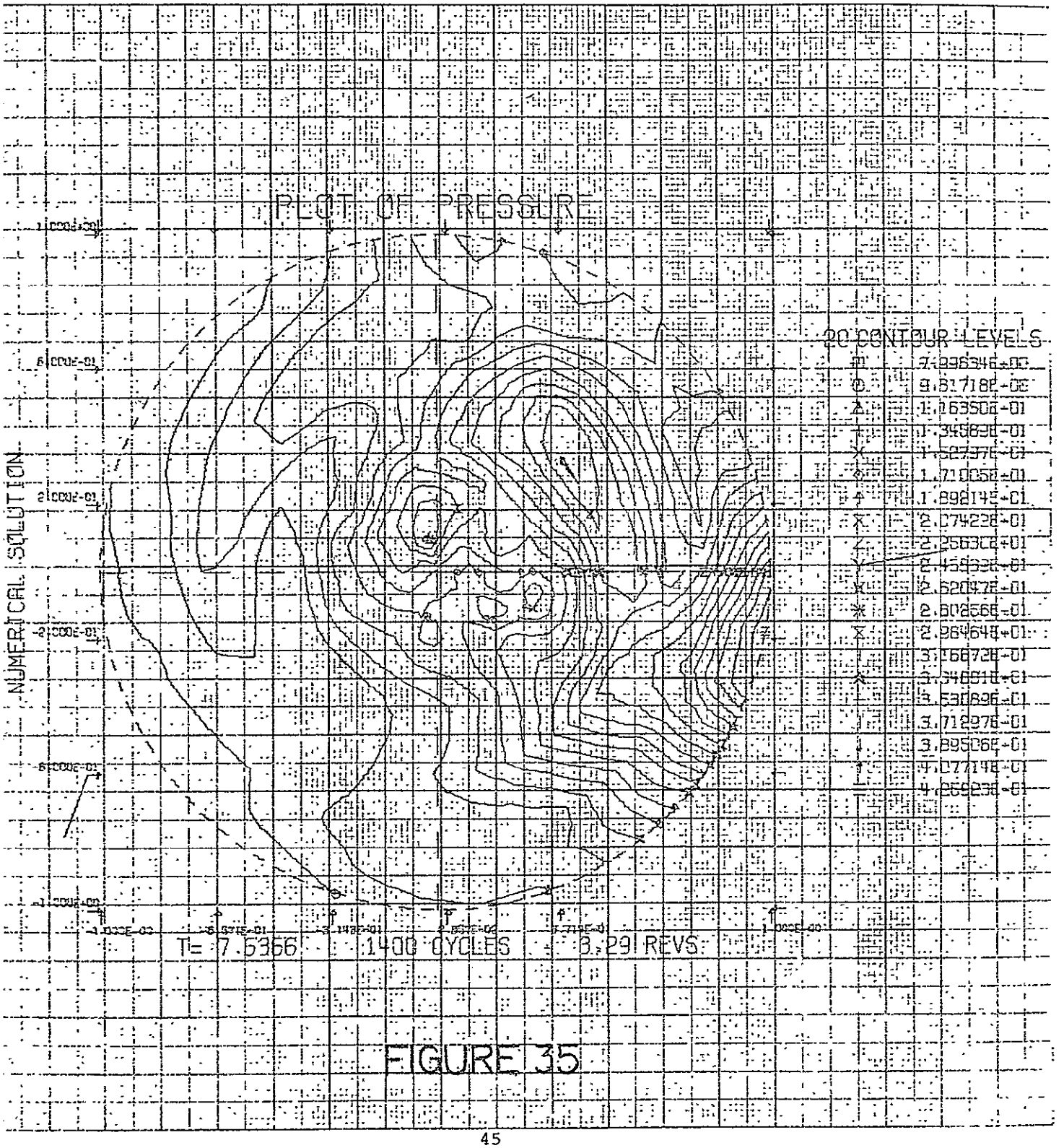
PLOT OF PRESSUR
NUMERICAL SOLUTION
20 CONTOUR LEVELS
7.898346E-02
9.817182E-02
1.163506E-01
1.345293E-01
1.527079E-01
1.708865E-01
1.890652E-01
2.074228E-01
2.256014E-01
2.437801E-01
2.619587E-01
2.801373E-01
2.983160E-01
3.166736E-01
3.348522E-01
3.530309E-01
3.712095E-01
3.893882E-01
4.077458E-01
4.259244E-01
T= 7.5366 1400 CYCLES 8.29 REVS

FIGURE 35

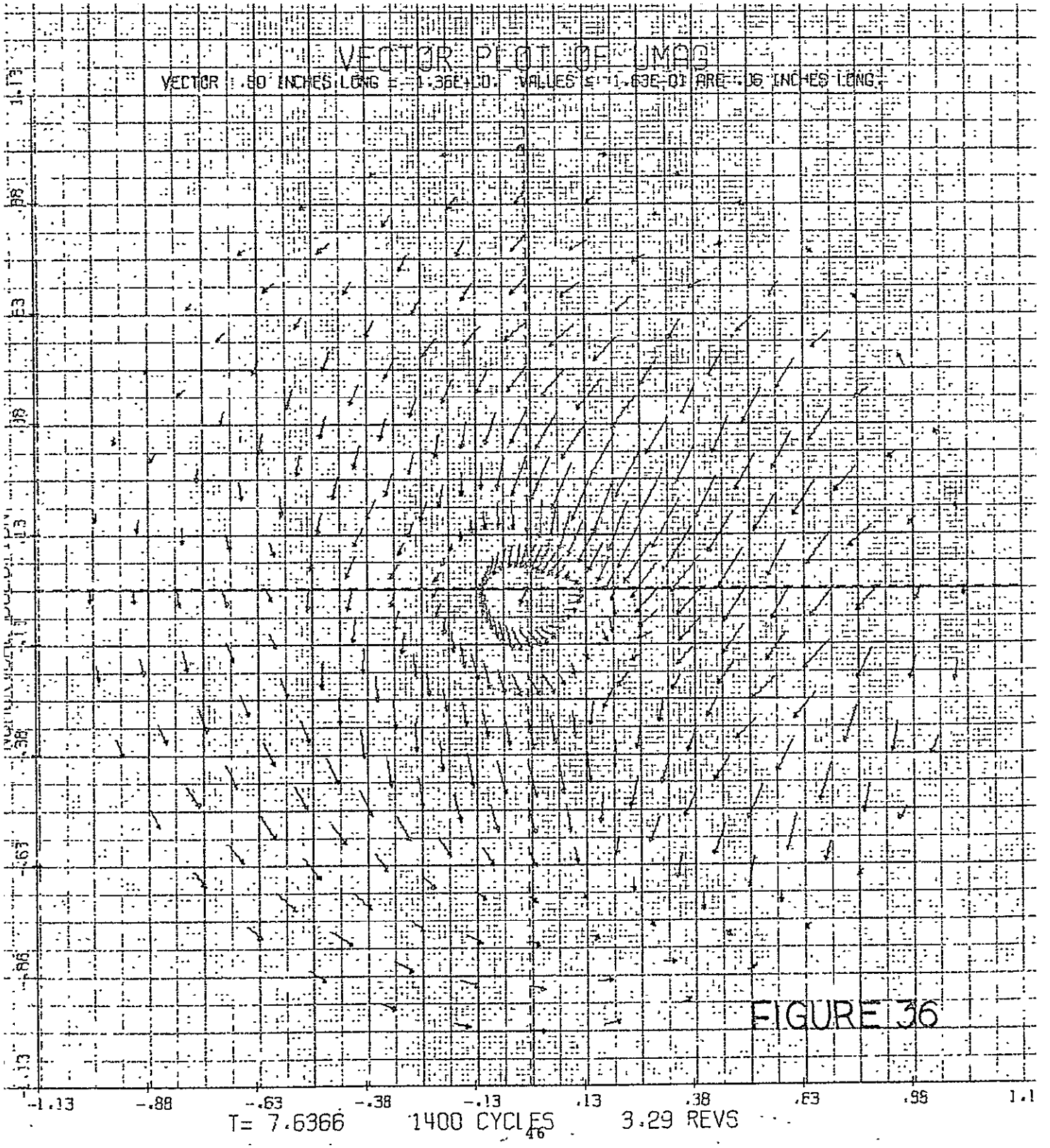
VECTOR PLOT OF UMAG
VECTOR = .80 INCHES LONG = 1.36E+00 VALUES = 1.63E-01 ARE .06 INCHES LONG
-1.13
-.88
-.63
-.38
-.13
.13
.38
.63
.88
1.1
T= 7.6366
1400 CYCLES
3.29 REVS

FIGURE 36

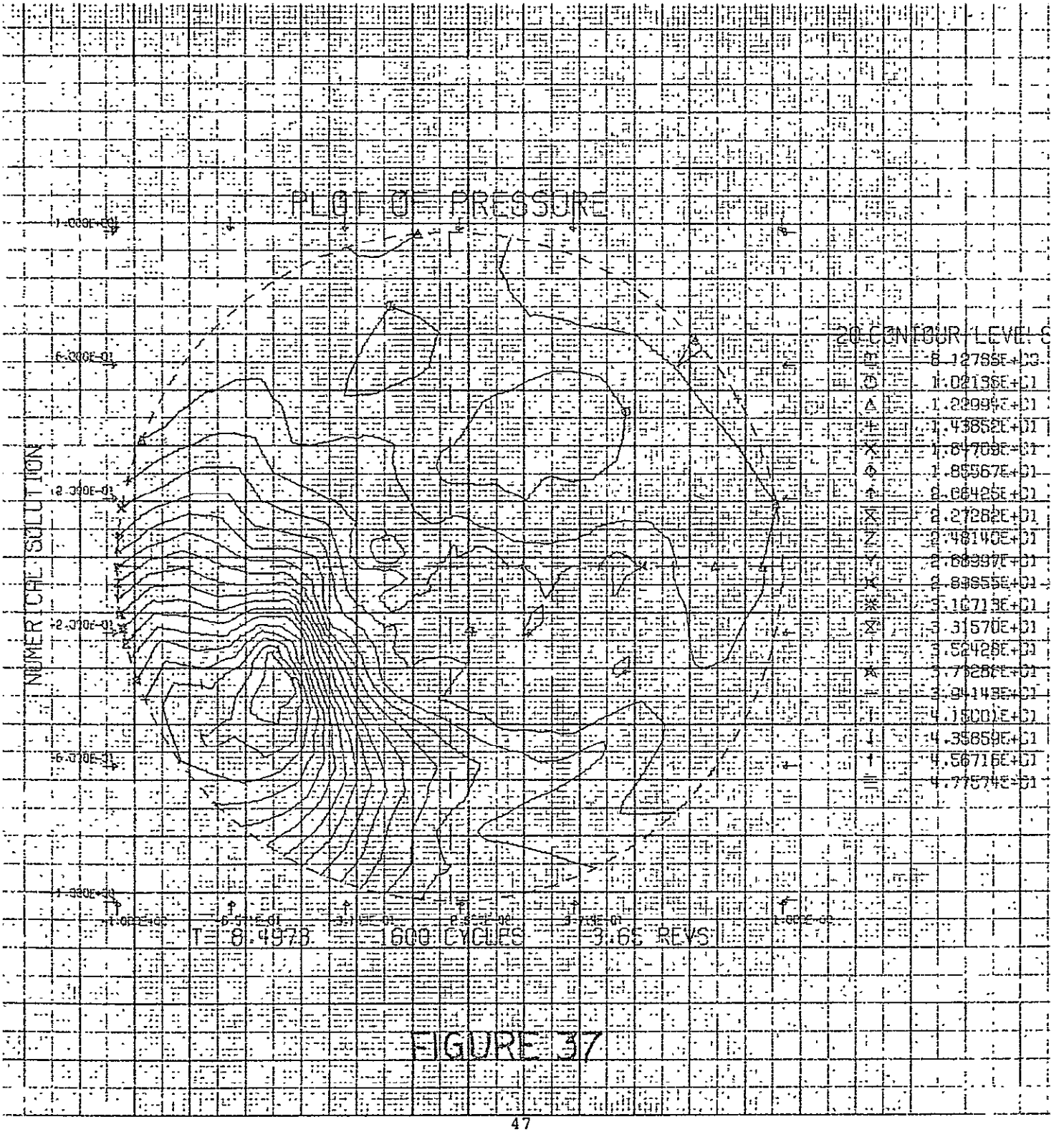
PLOT OF PRESSURE
NUMERICAL SOLUTION
20 CONTOUR LEVELS
8.12788E+00
1.02136E+01
1.22994E+01
1.43852E+01
1.64709E+01
1.85567E+01
2.06425E+01
2.27282E+01
2.48140E+01
2.68997E+01
2.89855E+01
3.10713E+01
3.31570E+01
3.52428E+01
3.73286E+01
3.94143E+01
4.15001E+01
4.35859E+01
4.56716E+01
4.77574E+01
T= 8.4978 1600 CYCLES 3.65 REVS

FIGURE 37

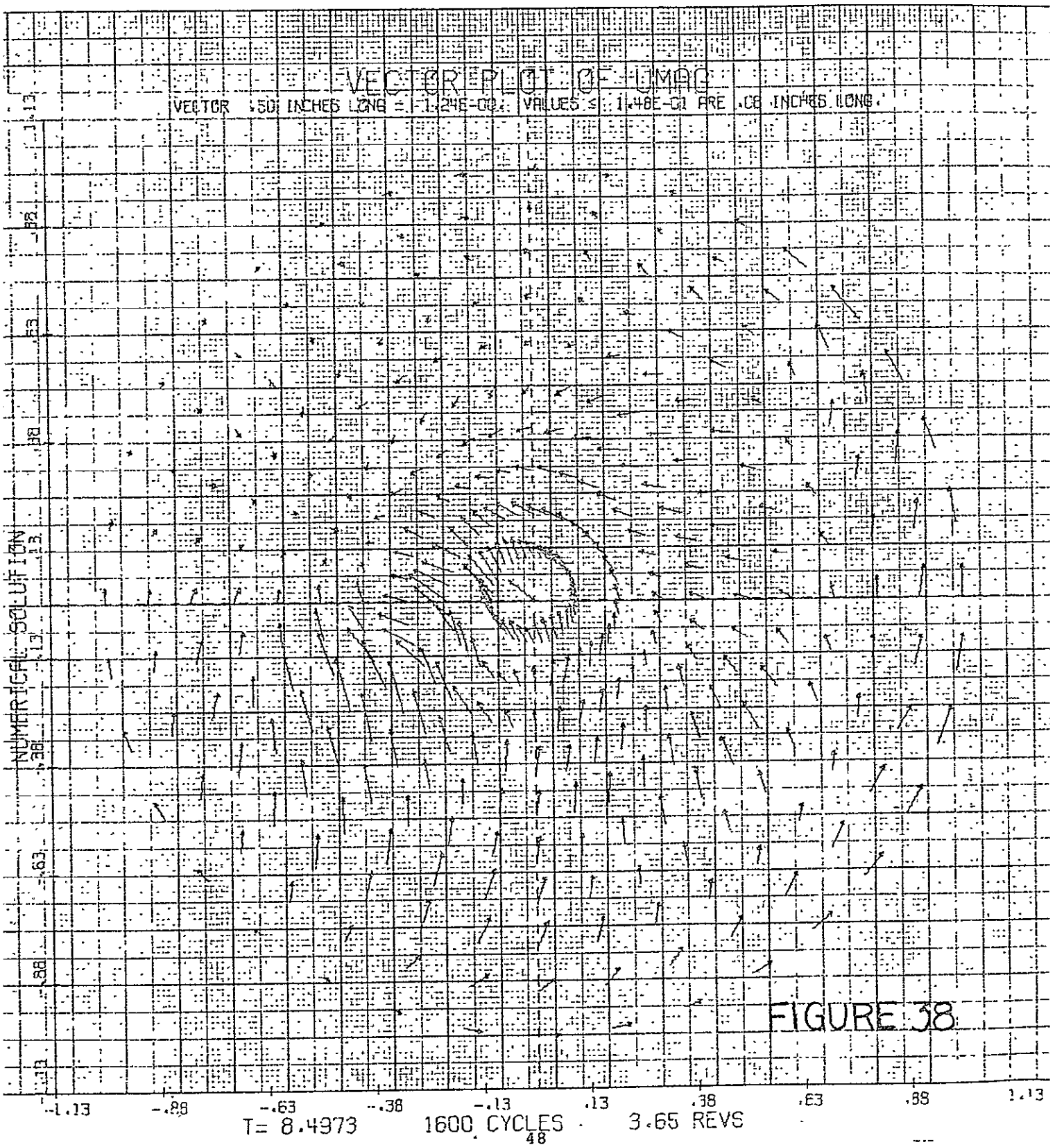
VECTOR PLOT OF UMOG
VECTOR .50 INCHES LONG = 1.24E-02. VALUES ≤ 1.48E-01 ARE .08 INCHES LONG.
NUMERICAL SOLUTION
-1.13
-.88
-.63
-.38
-.13
.13
.38
.63
.88
1.13
T= 8.4973 1600 CYCLES 3.65 REVS

FIGURE 38

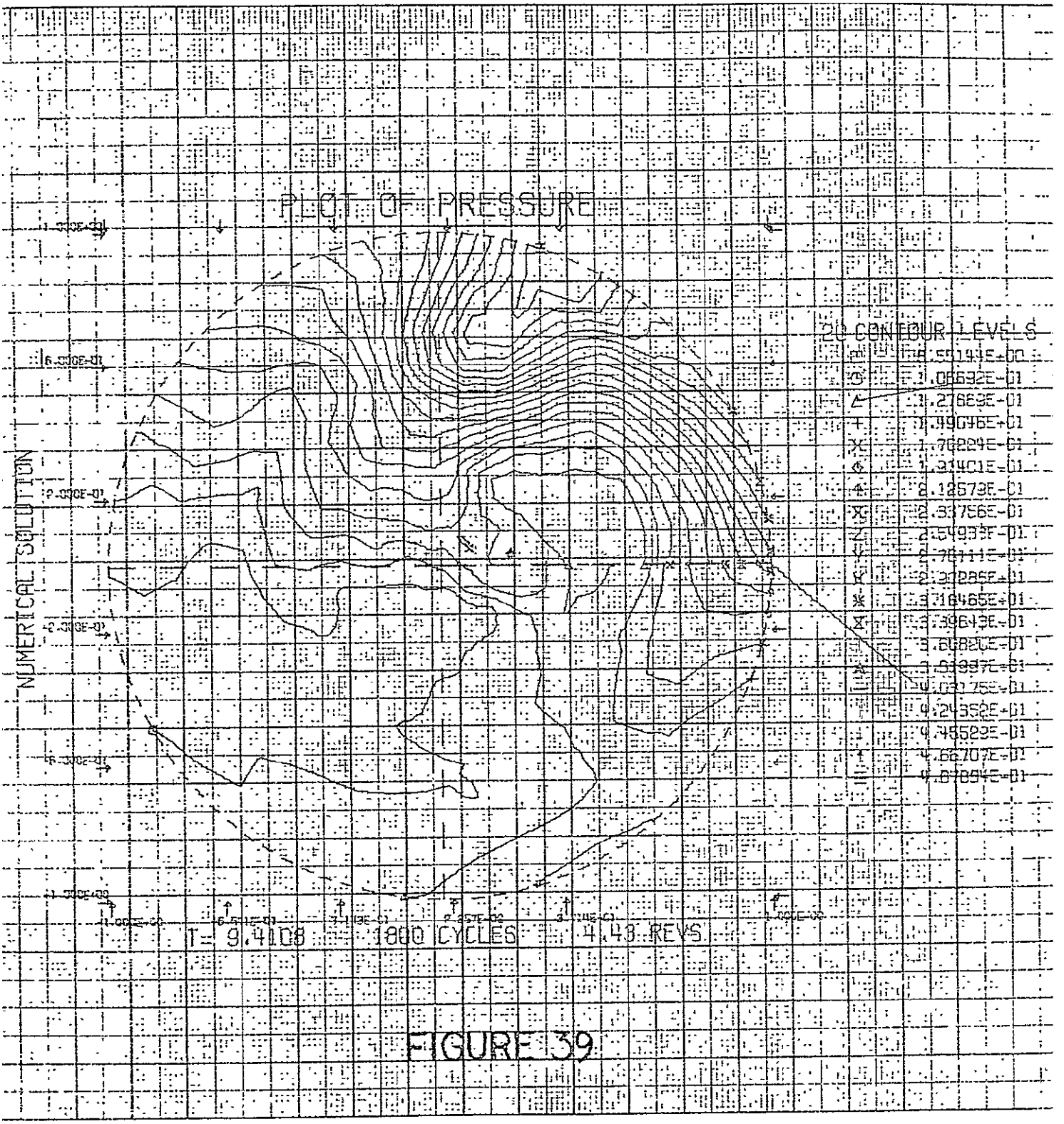
PLOT OF PRESSURE
NUMERICAL SOLUTION
20 CONTOUR LEVELS
T= 9.4108
1800 CYCLES
4.43 REVS

FIGURE 39

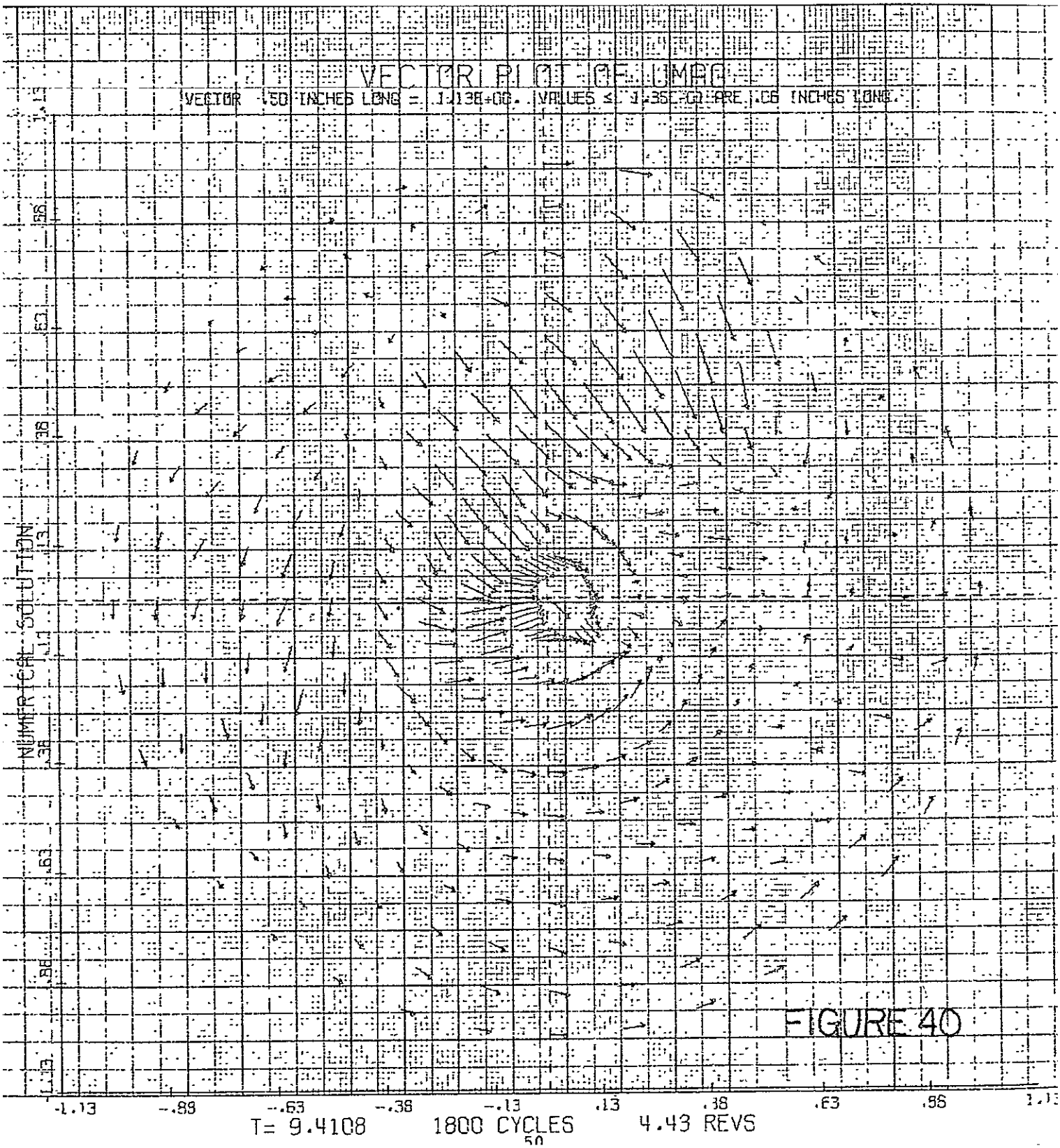
VECTOR PLOT OF UMRG
VECTOR =50 INCHES LONG = .1138+00. VALUES ≤ .1.35E-02 ARE .06 INCHES LONG.
NUMERICAL SOLUTION
-1.13
-.88
-.63
-.38
-.13
.13
.38
.63
.88
1.13
T= 9.4108
1800 CYCLES
4.43 REVS

FIGURE 40

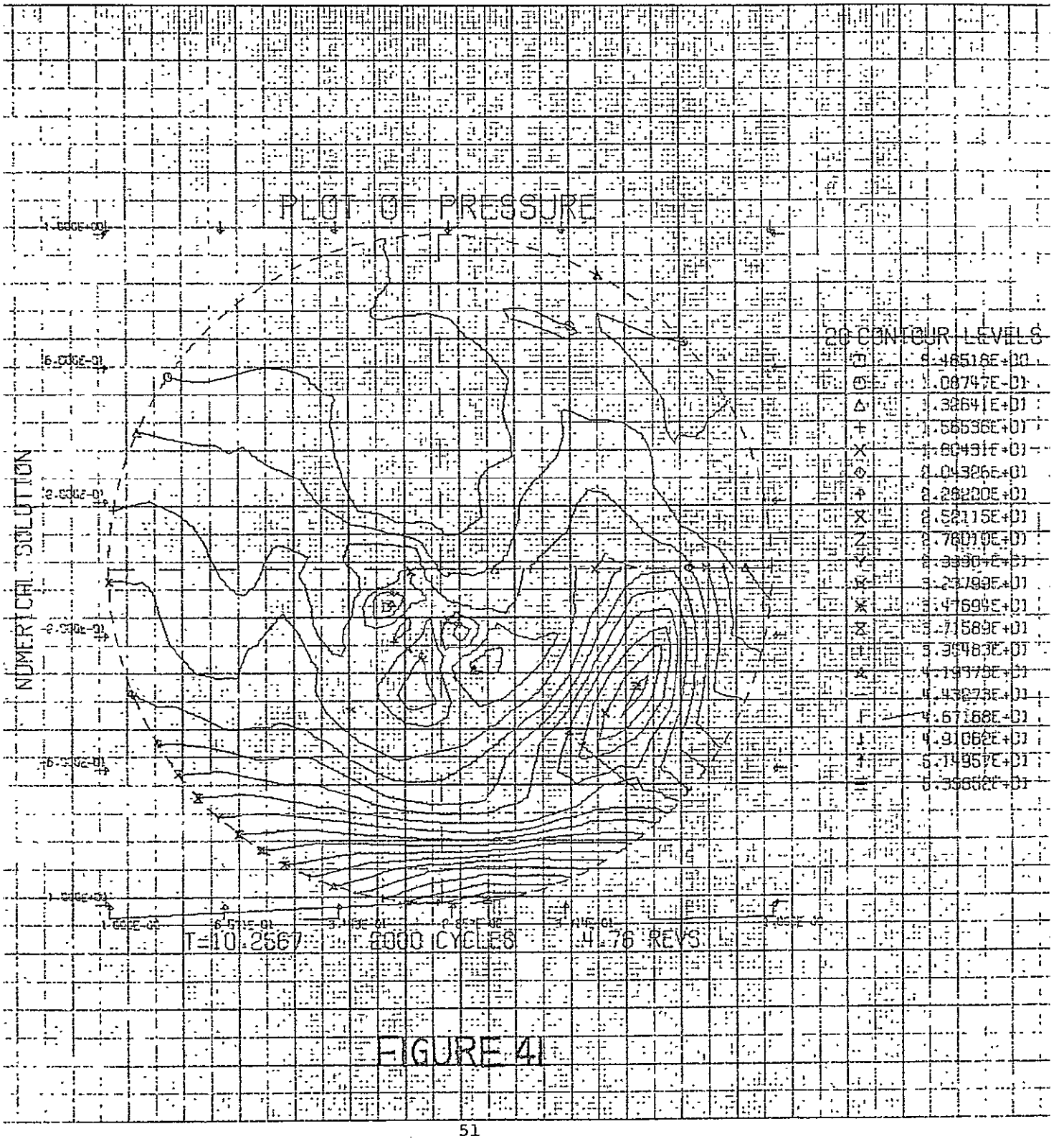
PLOT OF PRESSURE
NUMERICAL SOLUTION
20 CONTOUR LEVELS
8.48518E+00
1.08747E-01
1.38641E+01
1.56536E+01
1.80431E+01
2.04326E+01
2.28220E+01
2.52115E+01
2.76010E+01
3.23799E+01
3.47695E+01
3.71589E+01
3.95483E+01
4.43273E+01
4.67168E+01
4.91062E+01
5.14957E+01
T=10.2567
2000 CYCLES
4.76 REVS

FIGURE 4

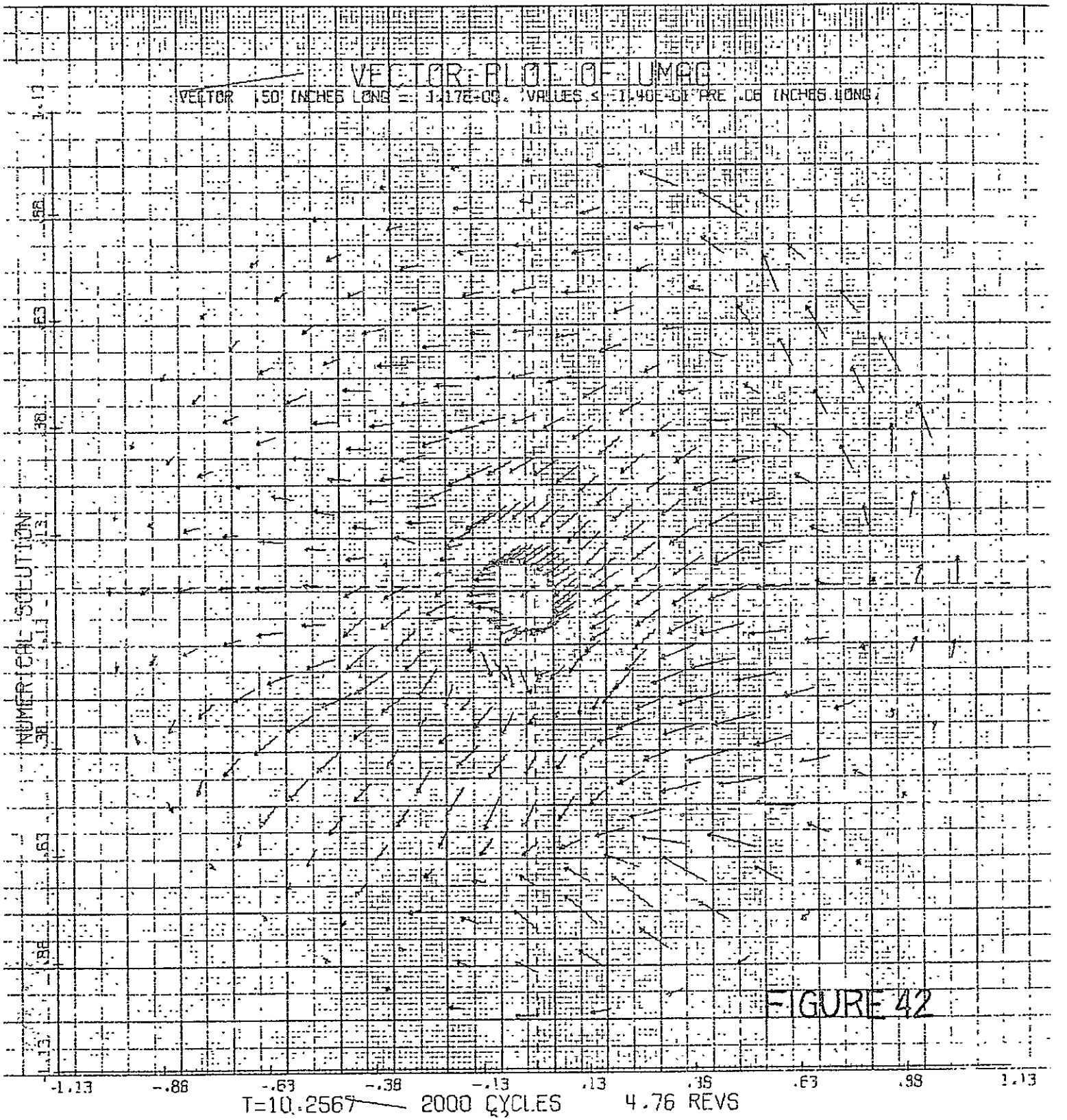
VECTOR PLOT OF UMAG
VECTOR 1.50 INCHES LONG = 1.17E+00. VALUES ≤ 1.40E-01 ARE .08 INCHES LONG.
NUMERICAL SOLUTION
-1.13
-.88
-.63
-.38
-.13
.13
.38
.63
.88
1.13
T=10.2567 2000 CYCLES 4.76 REVS

FIGURE 42

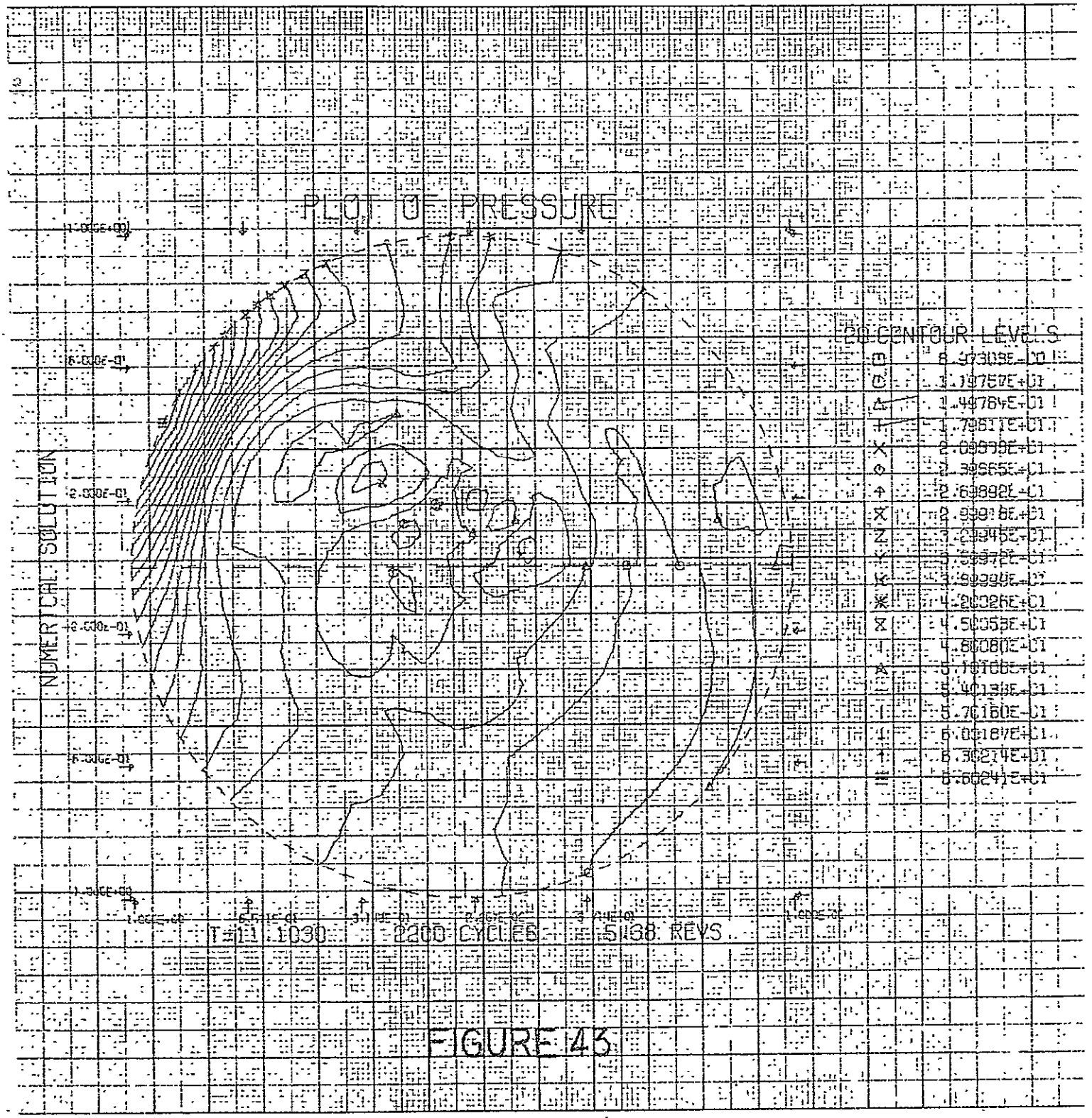
PLOT OF PRESSURE
NUMERICAL SOLUTION
T = 11.1030
2200 CYCLES
5.38 REVS
FIGURE 43

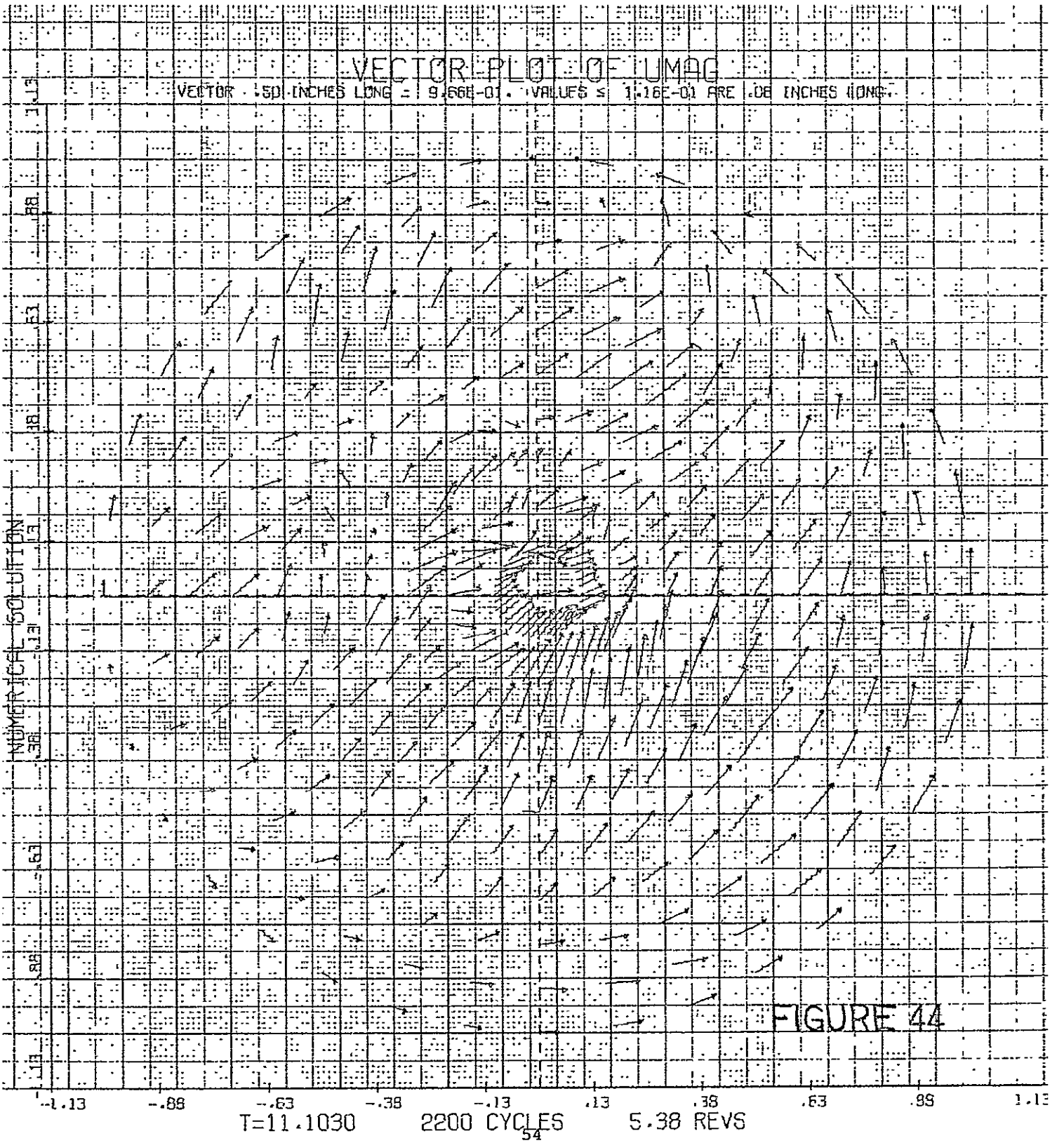
VECTOR PLOT OF UMAG
VECTOR .50 INCHES LONG = 9.66E-01. VALUES ≤ 1.16E-01 ARE .08 INCHES LONG.
NUMERICAL SOLUTION
-1.13
-.88
-.63
-.38
-.13
.13
.38
.63
.88
1.13
T=11.1030
2200 CYCLES
5.38 REVS

FIGURE 44

E. Program COMB Status

As is shown by figure 26, we have incorporated the ability to selectively plot the tangential pressure distribution at any value of radius and at any time. This feature adds flexibility to the program for ease in interpretation of the computed results.

It is anticipated that the final report will contain some instantaneous streakline pictures of 'particles' moving in the r-θ plane. The resultant motion is shown plotted as separate pictures after, say, one complete rotation of the wave. It is hoped that correlations can be made with these computed results and photographic techniques to be attempted by the JPL rocket combustion group.

The toroidal motor model is almost debugged. Tests are now being run to establish a steady state flow in the θ-z direction with given arbitrary initial data. A simple approach has been taken so as to simulate a converging diverging nozzle. That it is necessary to incorporate a supersonic boundary condition at the outflow plane of this toroidal geometry is evident. For a liquid propellant motor the only other required boundary condition is that the normal component of velocity shall vanish on the injector face. Plotting routines have been written which will be used to see isobars and vector fields in this geometry. Some preliminary results have been obtained at this time but are too incomplete in nature to present.

II. Droplet Evaporation and Combustion Analyses*

A. The Rate of the N_2H_4/N_2O_4 Reaction

It will be recalled that in order to utilize the modified flame surface analysis of Peskin and Wise (Ref. 1), some estimate is required of the overall (i.e., 'global') reaction rate constant for the N_2H_4/N_2O_4 reaction (Ref. 2). That is, assuming the reaction proceeds according to

$$N_2H_4 + NO_2 \xrightarrow{k_f} \frac{3}{2}N_2 + 2H_2O \qquad (1)$$

some estimate of k_f is required. (NO_2 is considered the oxidant rather than N_2O_4 as a result of the high level of dissociation of the latter under most engine operating conditions.)

This estimate can be obtained from the streamtube analysis developed in Ref. 2, wherein the relevant equations and assumptions are detailed. For reference purposes, the streamtube equations are summarized here as well:

Energy Conservation

$$\frac{dh}{dt} = 0\,,\ h = \text{constant} \qquad (2)$$

Species Conservation

$$\frac{dY_i}{dt} = \frac{r_i}{\rho} \qquad (3)$$

Equation of State

$$\rho = \frac{pM}{RT} \qquad (4)$$

* Figures in this section again start with the number 1.

Auxiliary Equations

$$h = \sum_i Y_i h_i \tag{5}$$

$$M = \left(\sum_i \frac{Y_i}{M_i} \right)^{-1} \tag{6}$$

$$h_i = \Delta_i + \bar{c}_{p_i} (T - T_{REF}) \tag{7}$$

where h_i = enthalpy (sensible plus chemical) of species i

r_i = rate of appearance (or disappearance) of species i

Y_i = mass fraction of species i

M_i = molecular weight of species i

ρ = mass density of the gas mixture

p = pressure of the mixture

T = temperature of the mixture

Δ_i = reference enthalpy of species i

$\bar{c}_{p_i}$ = average specific heat of species i

T_{REF} = reference temperature (1000°K)

t = time

Preliminary results were shown in Ref. 2. More complete results are presented in figure 1. Defining the ignition delay time (t_{ID}) qualitatively as the time required for the principal oxidation reactions to occur, figure 1 yields the anticipated result that t_{ID} is a strong function of the initial mixture temperature. On the other hand, these results indicate that in the range examined, t_{ID} is nearly independent of the pressure. As can be seen, at the higher pressures, the second-order reactions (which become more significant at higher pressures) produce an initial partial oxidation which results in a slight temperature increase. However, a leveling-off period is seen to subsequently

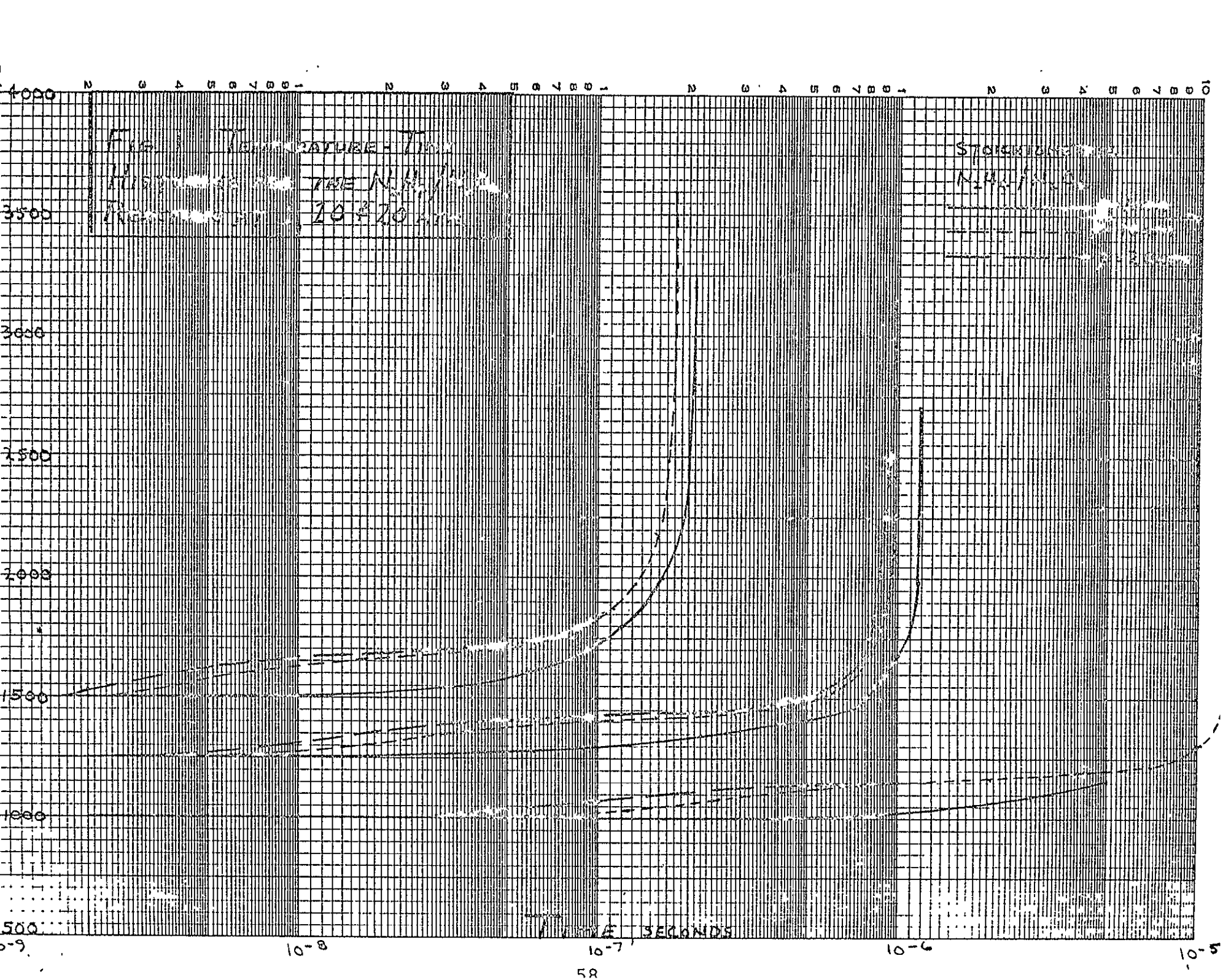
4000
3500
3000
2500
2000
1500
1000
500
10-9
10-8
10-7
10-6
10-5
TIME SECONDS

occur, followed by the principal, first-order oxidation processes which drive the reaction to completion.

As a result, the reaction may be said to be first-order, with ignition delay times (taken from figure 1) as shown in figure 2. In this latter figure, T_i is the initial mixture temperature. The approximate straight line behavior of ln t_{ID} when plotted against reciprocal initial temperature is in accordance with elementary chemical kinetic thoery which predicts a f ıction of the form

$$t_{ID} = \alpha \cdot \exp\ (E/RT_i) \tag{8}$$

where α is a constant and E is an overall activation energy. From figure 2, E was determined to be about 26,800 calories/mole.

As an initial estimate, the pre-exponential factor in the overall reaction rate constant was chosen to be the average of the pre-exponential factors for the N_2H_4 oxidation reactions as deduced by Sawyer (see Ref. 2, Table I). From this and the result obtained above, the initial estimate of the overall reaction rate constant was

$$k_f = 1.2 \times 10^{10}\ \exp\ (-26{,}800/RT) \tag{9}$$

To check this estimate, results using eq. 9 were checked against results obtained using the complete streamtube analysis. The comparison was made at high pressure (20 atm), where the first-order approximation and eq. 9 would be least accurate. The results are shown in figure 3, with the streamtube result labeled 'exact'. The global model does not, of course, predict the initial reactions or the leveling off period after the initial second-order.

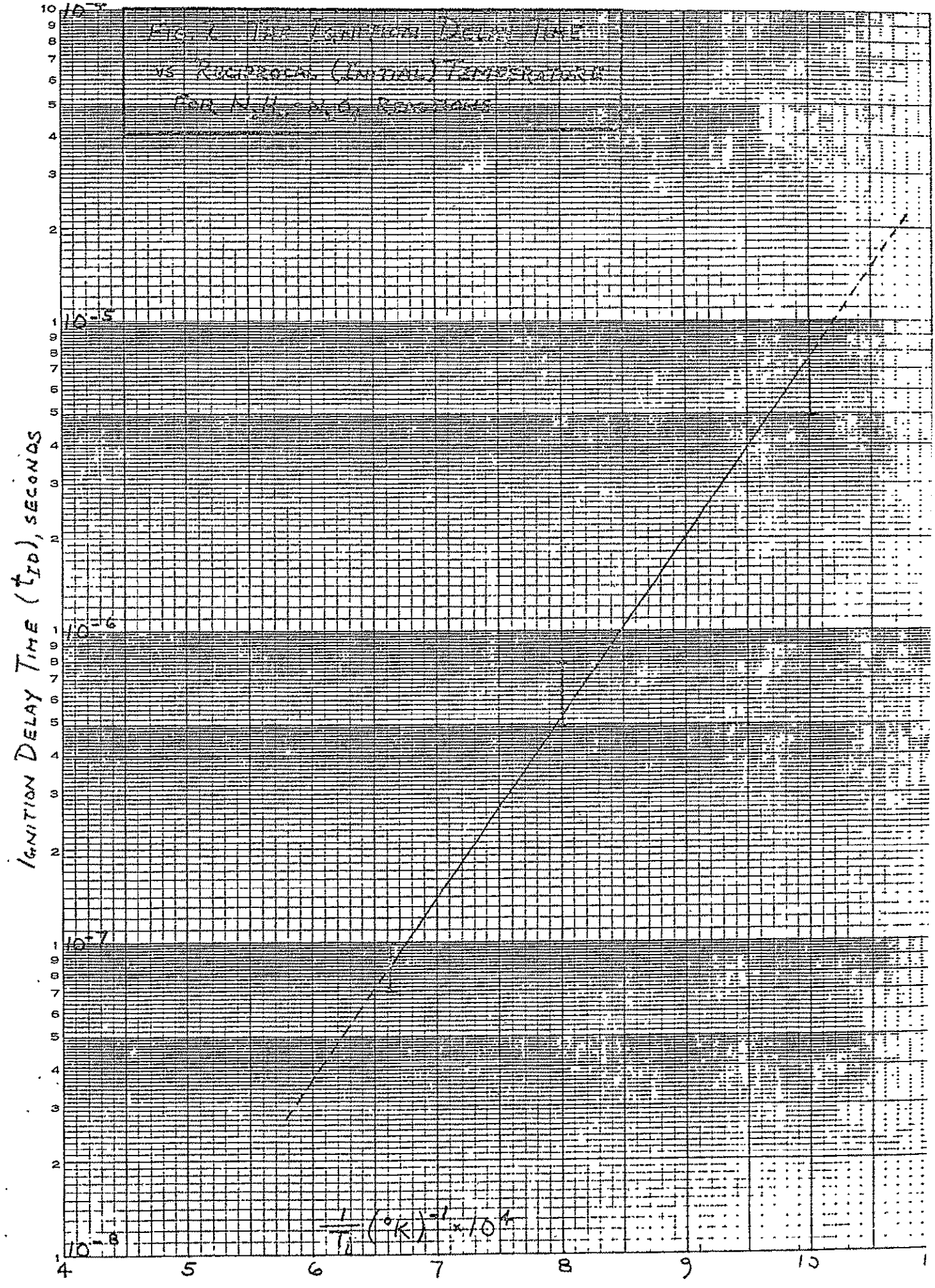
FIG. 1 IGNITION DELAY TIME VS RECIPROCAL (ABSOLUTE) TEMPERATURE FOR N_2H_4-N_2O_4 PROPELLANTS
IGNITION DELAY TIME (t_{ID}), SECONDS
10^{-4}
10^{-5}
10^{-6}
10^{-7}
10^{-8}
$\frac{1}{T_i}$ (°K)$^{-1}$ x 10^4
4
5
6
7
8
9
10

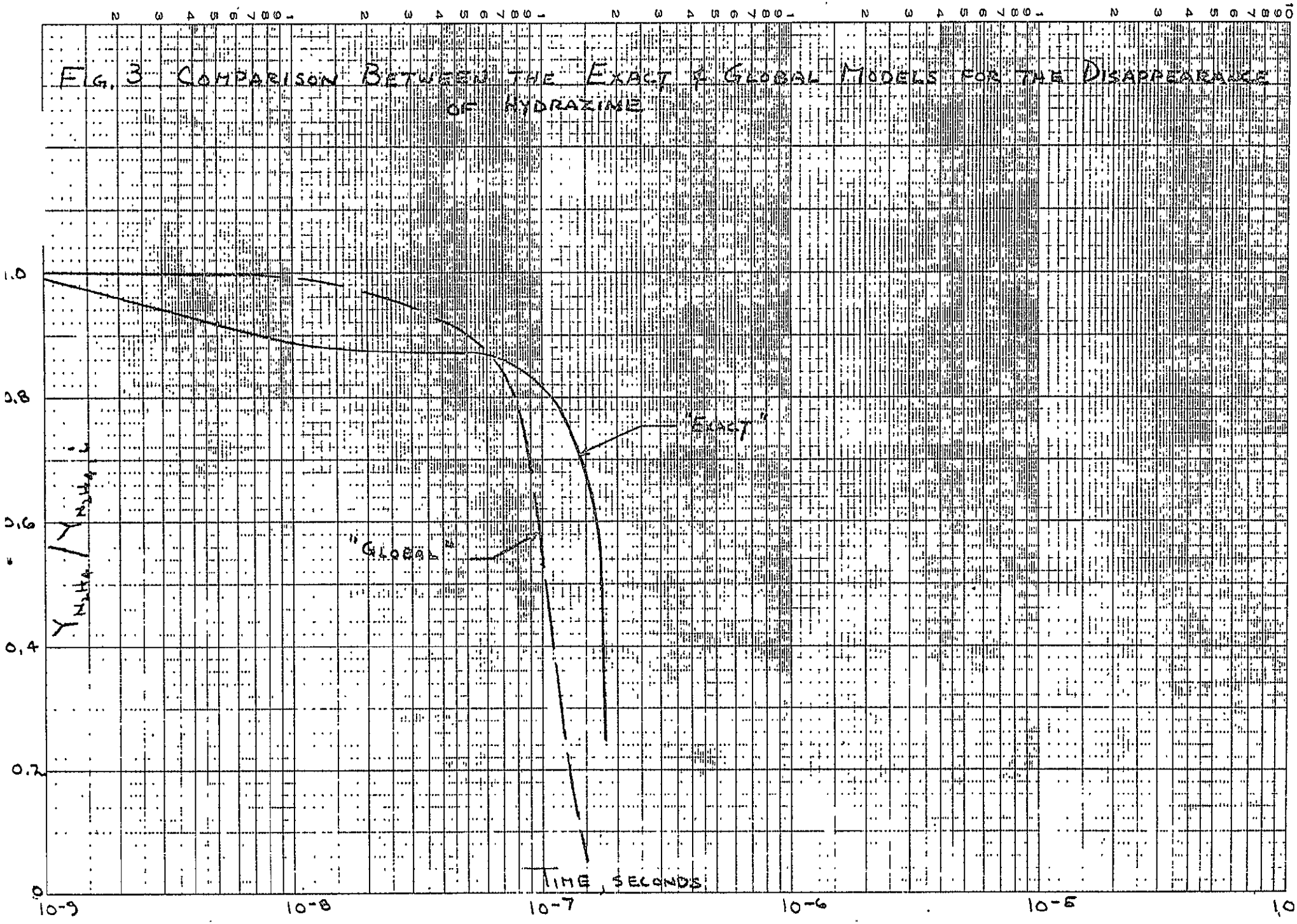
FIG. 3 COMPARISON BETWEEN THE EXACT & GLOBAL MODELS FOR THE DISAPPEARANCE OF HYDRAZINE
$Y_{N_2H_4} / Y_{N_2H_4}$
1.0
0.8
0.6
0.4
0.2
0
"EXACT"
GLOBAL
TIME, SECONDS
10^{-9}
10^{-8}
10^{-7}
10^{-6}
10^{-5}
1.0

reactions have occurred, but the general behavior and the delay time appears to be reasonable. Although the result for this particular case could have been improved by adjustment of the pre-exponential factor in eq. 9, this was felt to be unwarranted, and eq. 9 was selected as a suitably accurate overall reaction rate constant for inclusion in the modified flame surface analysis.

The Modified Flame Surface Analysis

Under the assumptions inherent in the modified flame surface analysis, as detailed in Refs. 2 and 3, the species conservation and energy equations were shown to reduce to

$$a\frac{dY_i}{d\eta} - \frac{d}{d\eta}\left(\eta^2 \frac{dY_i}{d\eta}\right) = - i_i \eta^2 b Y_F^{N_F} Y_O^{N_O} \qquad (10)$$

$$a\frac{dt}{d\eta} - \frac{d}{d\eta}\left(\eta^2 \frac{dt}{d\eta}\right) = \eta^2 b Y_F^{N_F} Y_O^{N_O} \qquad (11)$$

where a = dimensionless mass burning rate = $\dot{m}_F^o/(4\pi r_D k/c_p)$

$\dot{m}_F^o$ = mass burning rate in stagnant surrounding

r_D = fuel droplet radius

k = thermal conductivity

η = r/r_D

i_i = $\nu_i M_i/\nu_F M_F$

ν_i = stoichiometric coefficient of species i

N_F, N_O = reaction orders with respect to fuel and oxidizer

b = $k_f r_D^2/D$

D = binary diffusion coefficient

t = $(T-T_\infty)/(Q/c_p)$

Q = heat of reaction

T_∞ = temperature in the ambient gas mixture

On the basis of the conclusions drawn in the previous section, $N_O = 0$ and k_f is given by eq. 9. When eq. 10 is written first for the fuel and then for the oxidizer, and the resulting equations subtracted, an integrable ordinary differential equation results

subject to the following boundary conditions:

$$\frac{d}{d\eta} Y_O \Big]_{\eta=1} = a\, Y_O \Big]_{\eta=1}$$

$$\frac{d}{d\eta} Y_F \Big]_{\eta=1} = a\, Y_F \Big]_{\eta=1} - a$$

$$Y_F \Big]_{\eta\to\infty} = 0$$

When eq. 10 written for the fuel is added to eq. 11, another integrable ordinary differential equation results subject to these boundary conditions:

$$\frac{dt}{d\eta} \Big]_{\eta=1} = \frac{L}{Q}\, a$$

$$t \Big]_{\eta\to\infty} = 0$$

The resulting equations can be manipulated to yield the following expression for the dimensionless mass burning rate:

$$a = \ln \left[\frac{1 - \frac{L}{Q} + t_s}{1 - \frac{L}{Q} - Y_{F,s}} \right] \qquad (12)$$

where L = latent heat of vaporization of the fuel

t_s = dimensionless droplet surface temperature

$Y_{F,s}$ = mass fraction of fuel at the droplet surface

We now introduce the additional assumption that the flame zone of finite thickness can be replaced by an infinitessimal on represented by a Driac-delta function located such that the fuel and oxidant react stoichiometrically. As a consequence, the rig hand-sides of eqs. 10 (written for the fuel) and 11 become

$$\eta^2 b\, Y_F^* \cdot \delta(\eta-\eta^*)$$

where the asterisks refer to the values at the hypothetical flame surface, and δ is the delta function. (Note that the fact that $N_O = 0$ has been used in writing this term.)

Peskin (Ref. 1) shows that a solution to equation 10 with this right-hand-side is given by generalized function theory as

$$Y_F = \frac{b^*}{a}\, Y_F^*\, \eta^{*2}\, e^{-a/\eta} \begin{cases} 1-e^{a/\eta} & \text{for } \eta>\eta^* \\ 1-e^{a/\eta^*} & \text{for } \eta<\eta^* \end{cases} + 1-e^{-a/\eta} \tag{13}$$

Therefore, for $\eta=\eta^*$, $Y_F=Y_F$ and eq. 13 becomes

$$Y_F^* = \frac{(1-e^{-a/\eta^*})}{1+\frac{b^*}{a}\,\eta^{*2}(1-e^{-a/\eta^*})} \tag{14}$$

Now when eq. 13 is solved for $\eta=1$, $Y_F=Y_{FS}$, and eq. 14 is used, the result is

$$Y_{FS} = \frac{\frac{b^*}{a}\,\eta^{*2}\, e^{-a}\,(1-e^{a/\eta^*})\,(1-e^{-a/\eta^*})}{1+\frac{b^*}{a}\,\eta^{*2}\,(1-e^{-a/\eta^*})} + 1-e^{-a} \tag{15}$$

From the difference between eq. 10 written for the fuel and the oxidizer, and using the appropriate boundary conditions, the following expression is obtained for η^*:

$$\eta^* = \frac{a}{\ln\left[\dfrac{i_O\, Y_{FS} + Y_O\,(\infty)}{Y_O\,(\infty)\, e^{-a} + i_O\, Y_{FS}}\right]} \tag{16}$$

From the sum of equations 10 (written for the fuel) and 11, again subject to the appropriate boundary conditions, the following expression can be derived for t*:

$$t^* = \frac{(Y_{FS} + t_s)\ (e^{-a/\eta^*}-1)}{e^{-a}-1} - \frac{(1-e^{-a/\eta^*})}{1+\frac{b^*}{a}\eta^{*2}\ (1-e^{-a/\eta^*})} \qquad (17)$$

in which equation 14 was also used.

Finally, using the result of the previous section, b* can be written

$$b^* = \frac{r_D^2}{D}\ \left[1.2 \times 10^{10} \cdot \exp(-26{,}800/RT^*)\right] \qquad (18)$$

Equations 12, 15, 16, 17, and 18 constitute five equations in the five unknowns a, Y_{FS}, η^*, T*, and b*. (Unlike Peskin (Refs. 1, 4, 5), we are not interested here in species and temperature profiles surrounding the droplet, but in the mass burning rate a; as a consequence, the equations developed above are particularly suited to this purpose.)

Results using this analysis have been obtained for the following values of the parameters:

$Y_O(\infty) = 0.25$

$D = 10^{-4}\ \frac{ft^2}{sec}$

$i_o = \frac{23}{16}$ (see eq. 1)

Q was calculated from the enthalpies obtained from eq. 7; L was obtained from the Clausius-Clapeyron equation using the vapor pressure data in Ref. 6; in going from a to $\dot{m}_F^o$, k was obtained from Ref. 6 and c_p from Ref. 7.

Results are shown in figures 4, 5, and 6. In figure 4, the results are compared with the previous results obtained from the Godsav analysis (Ref. 2) and the experimental results of Ref. 8. As can be seen, the current analysis yields results which are about 80% higher over most of the range of r_D than the corresponding Godsav value. This is due, at least in part, to the values chosen for $Y_O(\infty)$ and D, as well as the differences inherent in the two approaches. It is interesting to note, however, that the line corresponding to $T = 1035^{\circ}K$, $p = 300$ psia (Curve B) passes right through the experimental points of Ref. 8. Unfortunately, Ref. 8 does not indicate the level of pressure at which these experiments were conducted, leaving this possible correlation unresolved. However, the linear dependence of the burning rate on droplet diameter is retained by the modified flame surface analysis, in accordance with the experimental results.

Figure 5 contrasts the ambient temperature dependence of this analysis and the Godsav analysis for the particular conditions noted. It was pointed out in Ref. 2, and can be seen in figure 5, that the Godsav analysis yields a very weak, almost linear ambient temperature dependence. Most experimental work indicates a stronger, non-linear dependence. The modified flame surface analysis does yield this latter type of dependence. It may be justifiably said, however, that the differences between the two analyses at these particular conditions are not sufficiently great to warrant using the current analysis in the fluid dynamics program. In particular, no evidence of extinction can be seen down

FIGURE 6 DEPENDENCE OF BURNING RATE ON THE DROPLET DIAMETER & AMBIENT PRESSURE

FIGURE 5, THE EFFECT OF AMBIENT TEMPERATURE ON THE BURNING RATE

to ambient temperatures near the boiling point of the fuel. If this same result is discovered at other values of the ambient pressure as well, this will constitute ample justification for the use of the simpler Godsav analysis.

The effect of ambient temperature on the values of Y_{FS}, n^* and T^* are shown in figure 6. The value of $Y_{FS} \to 1$ as T_∞ increases, in accordance with the assumption of the Godsav, diffusion-flame approximation ($Y_{FS=1}$). The hypothetical flame surface moves away from the droplet as T_∞ increases; this stems from the fact that in order to sustain a stoichiometric combustion process, the flame location must move away from the flame surface where a larger quantity of fuel vapor (Y_{FS}) is being produced. Finally, T^* exhibits a linear dependence on T_∞

FIGURE 6. THE EFFECT OF AMBIENT TEMPERATURE ON Y_{FS}, η_c AND T_{st}

C. The Reduced Godsav Analysis

Preliminary runs which coupled the complete Godsav analysis to the fluid dynamics program indicated that the running times were excessively long. (Roughly, five times slower than with the elementary energy term previously used.) As a consequence, the results obtained to date from the Godsav analysis (Ref. 2) were used to formulate the following simplified version of this analysis:

The weak, almost linear, temperature dependence of the dimensionless mass burning rate can be approximately expressed as

$$a_{300} = (3.73 \times 10^{-5}) \ (T_\infty) + 1.855 \tag{19}$$

where a_{300} is the dimensionless burning rate at a chamber pressure dependence is approximately given by

$$\frac{a_p}{a_{300}} = \left(\frac{p_\infty}{300}\right)^{0.0108} \tag{20}$$

Once a_p is computed, the burning rate in stationary surroundings is obtained from

$$\dot{m}_F^o = \frac{2\pi k}{c_p} \ d_L \ a_p \tag{21}$$

where d_L is the drop diameter, and the thermal conductivity and specific heat are functions of the liquid drop temperature.

The drop temperature, T_L, which is the boiling temperature at the chamber pressure, can be obtained to a good approximation from the integrated Clausius-Clapeyron equation

$$\ln \frac{p}{2131} = (8.7 \times 10^3)\left(\frac{1}{1176} - \frac{1}{T_L}\right) \tag{22}$$

where p is in psia, T_L is in ^{o}R, and the critical point conditions are 2131 psia, 1176 ^{o}R.

Knowing T_L, K is obtained from a linear curve fit of the data in Ref. 6:

$$K = \frac{1}{3600}\left[(-8.33 \times 10^{-5})\ (T_L - 460) + 0.2107\right] \tag{23}$$

and c_p is obtained from Ref. 7:

$$c_p = 0.138 + 0.527 \times 10^{-3}\ T_L - 0.120 \times 10^{-6}\ T_L^{\,2} \tag{24}$$

From $\dot{m}_F^o$, the burning rate in the convective environment is then obtained from (see Ref. 3, eq. 21):

$$\frac{\dot{m}_F}{\dot{m}_F^o} = 1 + 0.276\ (Re)^{\frac{1}{2}}\ (Pr)^{1/3} \tag{25}$$

Under the engine conditions of interest, the following constant values are reasonable:

$$Pr^{1/3} = 0.6$$

$$L_F = 540\ \frac{Btu}{lbm}$$

$$L_o = 178.2\ \frac{Btu}{lbm}$$

$$Q = 12{,}400\ \frac{Btu}{lbm}$$

where L_F is the latent heat of the fuel, L_o is the latent heat of the oxidizer, and Q is the heat of reaction. The appropriate terms in the ψ-vector of the fluid dynamics program may now be obtained as shown in Ref. 3 (eq. 22). Results obtained using this approximate formulation are shown elsewhere in this report.

REFERENCES

1. Peskin, R. L. and Wise, H., AIAA Journal, 4, 1646 (1966)

2. Burstein, S. Z. and Chinitz, W., "Nonlinear Combustion Instability in Liquid-Propellant Rocket Motors", 2nd Quarterly Report, Mathematical Applications Group, Inc. January 30, 1968.

3. IBID, 1st Quarterly Report, October 30, 1967.

4. Peskin; R. L., et.at., AIAA Journal, 5, 2173 (1967).

5. Polymeropoulos, C. E. and Peskin, R. L., "Theoretical Calculations of Fuel Drop Ignition and Extinction", Paper USCI-67-5, Western States Section/The Combustion Institute, April, 1967.

6. Aerojet-General Corporation Report on Properties of Propellants

7. Haws, J. L. and Harden, D. G., J. Spacecraft and Rockets 2, 972 (1965).

8. Dynamic Science Report No. SN-95-4, Monthly Progress Report under Contract No. NAS7-567, 1967.